

DTIC FILE COPY

(2)  
NCS TIB 87-14



## NATIONAL COMMUNICATIONS SYSTEM

### TECHNICAL INFORMATION BULLETIN 87-14

#### MAGNETOHYDRODYNAMIC (MHD) NUCLEAR WEAPONS EFFECTS ON SUBMARINE CABLE SYSTEMS

#### VOLUME I: EXPERIMENTS AND ANALYSIS

AD-A198 749

This document has been approved  
for public release and sale; its  
distribution is unlimited.

DTIC  
ELECTE  
AUG 9 1988  
S A D

JUNE 1987

88 8 08 041

Unclassified

SECURITY CLASSIFICATION OF THIS PAGE

## REPORT DOCUMENTATION PAGE

Form Approved  
OMB No. 0704-0188

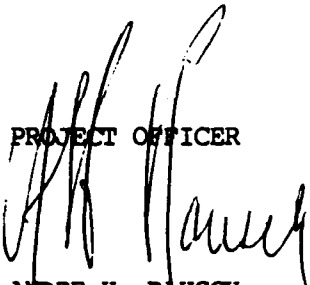
1a REPORT SECURITY CLASSIFICATION Unclassified			1b RESTRICTIVE MARKINGS		
2a SECURITY CLASSIFICATION AUTHORITY			3 DISTRIBUTION/AVAILABILITY OF REPORT Approved for public release; distribution unlimited		
2b DECLASSIFICATION/DOWNGRADING SCHEDULE					
4 PERFORMING ORGANIZATION REPORT NUMBER(S) NCS TIB 87-14			5 MONITORING ORGANIZATION REPORT NUMBER(S)		
6a NAME OF PERFORMING ORGANIZATION AT&T Bell Laboratories	6b OFFICE SYMBOL (If applicable)	7a NAME OF MONITORING ORGANIZATION			
6c ADDRESS (City, State, and ZIP Code) Crawfords Corner Road Holmdel, NJ 07733		7b ADDRESS (City, State, and ZIP Code)			
8a NAME OF FUNDING/SPONSORING ORGANIZATION National Communications System	8b OFFICE SYMBOL (If applicable) NCS-TS	9 PROCUREMENT INSTRUMENT IDENTIFICATION NUMBER DCA100-85-C-0060			
8c ADDRESS (City, State, and ZIP Code) Office of Technology & Standards Washington, D.C. 20305-2010		10 SOURCE OF FUNDING NUMBERS			
		PROGRAM ELEMENT NO 33127K	PROJECT NO	TASK NO 001	WORK UNIT ACCESSION NO
11 TITLE (Include Security Classification) Magnetohydrodynamic (MHD) Nuclear Weapons Effects on Submarine Cable Systems, Volume I: Experiments and Analysis					
12 PERSONAL AUTHOR(S)					
13a. TYPE OF REPORT Final	13b TIME COVERED FROM _____ TO _____	14 DATE OF REPORT (Year, Month, Day) June 1987		15 PAGE COUNT 302	
16 SUPPLEMENTARY NOTATION					
17 COSATI CODES			18 SUBJECT TERMS (Continue on reverse if necessary and identify by block number)		
FIELD	GROUP	SUB-GROUP	MHD		
			Submarine Cable Systems		
			Nuclear Weapons Effects		
19 ABSTRACT (Continue on reverse if necessary and identify by block number) This report presents a study of the nuclear weapons magnetohydrodynamic (MHD) effects on submarine communications cables. The study consisted of the analysis and interpretation of currently available data on submarine cable systems TAT-4, TAT-6, and TAT-7. The primary result of the study is that decrease of the effective resistivity with frequency over the available experimental range, coupled with the model results, leads to quite small effective resistivities at the MHD characteristic frequencies, and hence small earth potential differences. Thus, it appears that submarine cable systems are less susceptible to an MHD threat than their land-based counter-parts.					
20 DISTRIBUTION/AVAILABILITY OF ABSTRACT <input checked="" type="checkbox"/> UNCLASSIFIED/UNLIMITED <input type="checkbox"/> SAME AS REPORT <input type="checkbox"/> OTHER USERS			21 ABSTRACT SECURITY CLASSIFICATION Unclassified		
22a NAME OF RESPONSIBLE INDIVIDUAL J. Orndorff			22b REPORT NUMBER (Include Area Code) 200-692-2124		22c OFFICE SYMBOL NCS-TS

NCS TECHNICAL INFORMATION BULLETIN 87-14

MAGNETOHYDRODYNAMIC (MHD) NUCLEAR WEAPONS  
EFFECTS ON SUBMARINE CABLE SYSTEMS

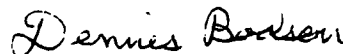
VOLUME I: EXPERIMENTS AND ANALYSIS

PROJECT OFFICER



ANDRE H. RAUSCH  
Electronics Engineer  
Office of NCS Technology  
and Standards

APPROVED FOR PUBLICATION:



DENNIS BODSON  
Assistant Manager  
Office of NCS Technology  
and Standards

FOREWORD

The National Communications System (NCS) is an organization of the Federal Government whose membership is comprised of 22 Government entities. Its mission is to assist the President, National Security Council, Office of Science and Technology Policy, and Office of Management and Budget in:

- o The exercise of their wartime and non-wartime emergency functions and their planning and oversight responsibilities.
- o The coordination of the planning for and provision of National Security/Emergency Preparedness communications for the Federal Government under all circumstances including crisis or emergency.

In support of this mission the NCS has initiated and manages the Electromagnetic Pulse (EMP) Mitigation Program. The major objective of this program is to significantly reduce the vulnerability of the U.S. telecommunications infrastructure to disabling damage due to nuclear weapon effects in direct support of the survivability and endurability objectives addressed by Executive Order 12472 and National Security Decision Directive 97. Nuclear weapon effects include EMP, magnetohydrodynamic EMP (MHD-EMP), and fallout radiation from atmospheric detonations. The purpose of this Technical Information Bulletin is to provide the reader with information relating to specific areas of EMP which are being investigated in support of the NCS EMP Mitigation Program.

Comments on this TIB are welcome and should be addressed to:

Office of the Manager  
National Communications System  
ATTN: NCS-TS  
Washington, DC 20305-2010  
(202) 692-2124

[illegible]





## TABLE OF CONTENTS

LIST OF ABBREVIATIONS .....	i.7
FIGURE CAPTIONS .....	i.9
EXECUTIVE SUMMARY .....	E.1
CHAPTER 1 - GENERAL INTRODUCTION.....	1.1
CHAPTER 2 - SUBMARINE CABLE EXPERIMENTS .....	2.1
2.1 - TAT-6 Unpowered Data.....	2.1
2.2 - TAT-7 Unpowered Data.....	2.2
2.3 - TAT-7 Powered Data .....	2.3
2.4 - TAT-4 Unpowered Data.....	2.4
2.5 - TAT-3 Powered Data .....	2.4
2.6 - Alias Filters .....	2.5
CHAPTER 3 - DATA ANALYSIS .....	3.1
3.1 - Details of the Data Analysis .....	3.1
3.2 - Least-Squares Fitting .....	3.4
3.3 - Results for a Typical Data Segment - (TAT-6).....	3.8
3.4 - Results for Complete TAT-6, TAT-7 Data Set .....	3.10
3.5 - Results for TAT-4 Data at Faster Sampling Rate.....	3.13
CHAPTER 4 - SUMMARY OF INTERPRETATION OF THE DATA.....	4.1
4.1 - General Summary .....	4.1
4.2 - Measurements at Higher Frequency .....	4.3
4.3 - High Frequency Oscillations.....	4.4
CHAPTER 5 - MODELING SUMMARY .....	5.1

CHAPTER 6 - NUMERICAL MODELING RESULTS .....	6.1
6.1 - The Semi-Analytic Land/Ocean Model.....	6.1
6.2 - The Finite Element Code .....	6.6
6.3 - Conclusions for the Modeling Effort .....	6.7
CHAPTER 7 - A WORST-CASE SCENARIO FOR SUBMARINE CABLES .....	7.1
CHAPTER 8 - EQUIVALENT MHD COUPLING AND CIRCUIT THEORY .....	8.1
8.1 - General Remarks.....	8.1
8.2 - Branching Power Supplies .....	8.4
8.3 - Repeater Powering and Failure.....	8.5
8.4 - Zener Diode Operation.....	8.6
8.5 - Repeater Operation Tolerance .....	8.7
8.6 - Steel Armor .....	8.8
CHAPTER 9 - PROTECTION .....	9.1
SUMMARY AND RECOMMENDATIONS .....	S.1
APPENDIX A - SEMI-ANALYTIC MODEL .....	A.1
A.1 - Introduction .....	A.1
A.2 - General Remarks .....	A.3
A.2a - The Textbook "Trivial Solutions" .....	A.4
A.2b - Inclusion of Vertical Boundaries.....	A.7
A.3 - Formalism for the Approximation .....	A.10
A.4 - Numerical Evaluation Procedure .....	A.13
APPENDIX B - FINITE ELEMENT CODE.....	B.1
B.1 - Remarks on the Finite Element Method .....	B.1

APPENDIX C - THE EARTH POTENTIAL AND THE MHD CIRCUIT LIMIT ..C.1

C.1 - Review of Transmission Line Formalism .....	C.1
C.2 - The Earth Potential and the Circuit Limit.....	C.5
C.3 - MHD Coupling to a Submarine Cable.....	C.8



## LIST OF ABBREVIATIONS

MHD - Magnetohydrodynamics  
HABW - High Altitude Blast Wave  
EMP - Electromagnetic Pulse  
TAT-3 - Transatlantic Cable 3  
TAT-4 - Transatlantic Cable 4  
TAT-6 - Transatlantic Cable 6  
TAT-7 - Transatlantic Cable 7  
D - East-West magnetic field  
H - North-South magnetic field  
Z - Vertical magnetic field  
V - Cable voltage  
f - frequency  
 $\omega$  - radian frequency  
 $\rho_{\text{eff}}$  - effective resistivity  
Hz - hertz  
km - kilometer  
EM - electromagnetic  
msc - magnitude squared coherence  
L4/L5 - land based communications system  
NJ - New Jersey  
RI - Rhode Island  
Cray X-MP - a vector computer at AT&T Bell Laboratories

*Other symbols with technical interpretations are defined in the text.*



## FIGURE CAPTIONS

### CHAPTER 1

Fig. 1.1. Mechanism for the MHD HABW (High Altitude Blast Wave) effect.

Fig. 1.2. Mechanism for the MHD Heave effect.

### CHAPTER 2

Fig. 2.1. Positions of the TAT-6 and TAT-7 transoceanic cables.

Fig 2.2. Experimental set-up. The center conductor of the coaxial cable is grounded on land through the voltmeter resistance  $R_{VM}$  and grounded at sea through the sea ground.

Fig 2.3. The Atlantic Ocean seabed around  $40^\circ$  N latitude.

### CHAPTER 3

Fig. 3.1. Coordinate system for the magnetic field. The components H, D, and Z point in the +North, +East, and down directions respectively.

Fig. 3.2. Time series for a typical six-hour segment for the cable voltage V and the ambient magnetic field components H, D, and Z for TAT-6 at 225 km.

Fig 3.3a. Effective resistivity  $\rho_D$  (6 hrs, TAT-6 at 225 km).

Fig. 3.3b. Effective resistivity  $\rho_H$  (6 hrs, TAT-6 at 225 km).

Fig. 3.3c. Effective resistivity  $\rho_Z$  (6 hrs, TAT-6 at 225 km).

Fig. 3.4a. Magnitude of transfer function  $\alpha_D$  (6 hrs, TAT-6 at 225 km).

Fig. 3.4b. Phase of transfer function  $\alpha_D$  (6 hrs, TAT-6 at 225 km).

Fig. 3.4c. Real part of transfer function  $\alpha_D$  (6 hrs, TAT-6 at 225 km).

Fig. 3.4d. Imaginary part of transfer function  $\alpha_D$  (6 hrs, TAT-6 at 225 km).

Fig. 3.5a. Magnitude of transfer function  $\alpha_H$  (6 hrs, TAT-6 at 225 km).



Fig. 3.5b. Phase of transfer function  $\alpha_H$  (6 hrs, TAT-6 at 225 km).

Fig. 3.5c. Real part of transfer function  $\alpha_H$  (6 hrs, TAT-6 at 225 km).

Fig. 3.5d. Imaginary part of transfer function  $\alpha_H$  (6 hrs, TAT-6 at 225 km).

Fig. 3.6a. Magnitude of transfer function  $\alpha_Z$  (6 hrs, TAT-6 at 225 km).

Fig. 3.6b. Phase of transfer function  $\alpha_Z$  (6 hrs, TAT-6 at 225 km).

Fig. 3.6c. Real part of transfer function  $\alpha_Z$  (6 hrs, TAT-6 at 225 km).

Fig. 3.6d. Imaginary part of transfer function  $\alpha_Z$  (6 hrs, TAT-6 at 225 km).

Fig. 3.7a. Magnitude squared coherence for V and D (6 hrs, TAT-6 at 225 km).

Fig. 3.7b. Magnitude squared coherence for V and H (6 hrs, TAT-6 at 225 km).

Fig. 3.7c. Magnitude squared coherence for V and Z (6 hrs, TAT-6 at 225 km).

Fig. 3.8. Composite F test (6 hrs, TAT-6 at 225 km).

Fig. 3.9a. Effective resistivity  $\rho_D$  for TAT-6 at 225 km, all data.

Fig. 3.9b. Effective resistivity  $\rho_D$  for TAT-6 at 3140 km, all data.

Fig. 3.10a. Effective resistivity  $\rho_H$  for TAT-6 at 225 km, all data.

Fig. 3.10b. Effective resistivity  $\rho_H$  for TAT-6 at 3140 km, all data.

Fig. 3.11a. Effective resistivity  $\rho_Z$  for TAT-6 at 225 km, all data.

Fig. 3.11b. Effective resistivity  $\rho_Z$  for TAT-6 at 3140 km, all data.

Fig. 3.12a. Effective resistivity  $\rho_D$  for TAT-7 at 1500 km, all data.

Fig. 3.12b. Effective resistivity  $\rho_D$  for TAT-7 at 3000 km, all data.

Fig. 3.12c. Effective resistivity  $\rho_D$  for TAT-7 at 4400 km, all data.

Fig. 3.13a. Effective resistivity  $\rho_H$  for TAT-7 at 1500 km, all data.

Fig. 3.13b. Effective resistivity  $\rho_H$  for TAT-7 at 3000 km, all data.

Fig. 3.13c. Effective resistivity  $\rho_H$  for TAT-7 at 4400 km, all data.

Fig. 3.14a. Effective resistivity  $\rho_Z$  for TAT-7 at 1500 km, all data.

Fig. 3.14b. Effective resistivity  $\rho_Z$  for TAT-7 at 3000 km, all data.

Fig. 3.14c. Effective resistivity  $\rho_z$  for TAT-7 at 4400 km, all data.

Fig. 3.15a. Magnitude of transfer function  $\alpha_D$  for TAT-6 at 225 km, all data.

Fig. 3.15b. Magnitude of transfer function  $\alpha_D$  for TAT-6 at 3140 km, all data.

Fig. 3.16a. Magnitude of transfer function  $\alpha_H$  for TAT-6 at 225 km, all data.

Fig. 3.16b. Magnitude of transfer function  $\alpha_H$  for TAT-6 at 3140 km, all data.

Fig. 3.17a. Magnitude of transfer function  $\alpha_z$  for TAT-6 at 225 km, all data.

Fig. 3.17b. Magnitude of transfer function  $\alpha_z$  for TAT-6 at 3140 km, all data.

Fig. 3.18a. The ratio of the magnitudes of the TAT-6 transfer function  $\alpha_D$  at 3140 km relative to 225 km, all data.

Fig. 3.18b. The ratio of the magnitudes of the TAT-6 transfer function  $\alpha_H$  at 3140 km relative to 225 km, all data.

Fig. 3.18c. The ratio of the magnitudes of the TAT-6 transfer function  $\alpha_z$  at 3140 km relative to 225 km, all data.

Fig. 3.19a. Phase of transfer function  $\alpha_D$  for TAT-6 at 225 km, all data.

Fig. 3.19b. Phase of transfer function  $\alpha_D$  for TAT-6 at 3140 km, all data.

Fig. 3.20a. Phase of transfer function  $\alpha_H$  for TAT-6 at 225 km, all data.

Fig. 3.20b. Phase of transfer function  $\alpha_H$  for TAT-6 at 3140 km, all data.

Fig. 3.21a. Phase of transfer function  $\alpha_z$  for TAT-6 at 225 km, all data.

Fig. 3.21b. Phase of transfer function  $\alpha_z$  for TAT-6 at 3140 km, all data.

Fig. 3.22a. Magnitude of transfer function  $\alpha_D$  for TAT-7 at 1500 km, all data.

Fig. 3.22b. Magnitude of transfer function  $\alpha_D$  for TAT-7 at 3000 km, all data.

Fig. 3.22c. Magnitude of transfer function  $\alpha_D$  for TAT-7 at 4400 km, all data.

Fig. 3.23a. Magnitude of transfer function  $\alpha_H$  for TAT-7 at 1500 km, all data.

Fig. 3.23b. Magnitude of transfer function  $\alpha_H$  for TAT-7 at 3000 km, all data.

Fig. 3.23c. Magnitude of transfer function  $\alpha_H$  for TAT-7 at 4400 km, all data.

Fig. 3.24a. Magnitude of transfer function  $\alpha_z$  for TAT-7 at 1500 km, all data.

Fig. 3.24b. Magnitude of transfer function  $\alpha_z$  for TAT-7 at 3000 km, all data.

Fig. 3.24c. Magnitude of transfer function  $\alpha_z$  for TAT-7 at 4400 km, all data.

Fig. 3.25a. Phase of transfer function  $\alpha_D$  for TAT-7 at 1500 km, all data.

Fig. 3.25b. Phase of transfer function  $\alpha_D$  for TAT-7 at 3000 km, all data.

Fig. 3.25c. Phase of transfer function  $\alpha_D$  for TAT-7 at 4400 km, all data.

Fig. 3.26a. Phase of transfer function  $\alpha_H$  for TAT-7 at 1500 km, all data.

Fig. 3.26b. Phase of transfer function  $\alpha_H$  for TAT-7 at 3000 km, all data.

Fig. 3.26c. Phase of transfer function  $\alpha_H$  for TAT-7 at 4400 km, all data.

Fig. 3.27a. Phase of transfer function  $\alpha_z$  for TAT-7 at 1500 km, all data.

Fig. 3.27b. Phase of transfer function  $\alpha_z$  for TAT-7 at 3000 km, all data.

Fig. 3.27c. Phase of transfer function  $\alpha_z$  for TAT-7 at 4400 km, all data.

Fig. 3.28. Temperature fluctuations in the Tuckerton station exhibiting the air conditioning unit cycling related to the noise problems for the powered TAT-7 data taken in late 1986.

Fig. 3.29a. Effective resistivity  $\rho_D$  (2 hrs, TAT-4 at 25 km).

Fig. 3.29b. Effective resistivity  $\rho_H$  (2 hrs, TAT-4 at 25 km).

Fig. 3.29c. Effective resistivity  $\rho_Z$  (2 hrs, TAT-4 at 25 km).

Fig. 3.30a. Magnitude squared coherence for V and D (2 hrs, TAT-4 at 25 km).

Fig. 3.30b. Magnitude squared coherence for V and H (2 hrs, TAT-4 at 25 km).

Fig. 3.30c. Magnitude squared coherence for V and Z (2 hrs, TAT-4 at 25 km).

Fig. 3.31a. Smoothed effective resistivity  $\rho_D$  (day 279, TAT-4 at 25 km).

Fig. 3.31b. Smoothed effective resistivity  $\rho_H$  (day 279, TAT-4 at 25 km).

Fig. 3.31c. Smoothed effective resistivity  $\rho_Z$  (day 279, TAT-4 at 25 km).

Fig. 3.32a. Smoothed effective resistivity  $\rho_D$  (day 280, TAT-4 at 25 km).

Fig. 3.32b. Smoothed effective resistivity  $\rho_H$  (day 280, TAT-4 at 25 km).

Fig. 3.32c. Smoothed effective resistivity  $\rho_Z$  (day 280, TAT-4 at 25 km).

Fig. 3.33a. Smoothed effective resistivity  $\rho_D$  and  $\pm 1$  standard deviation lines (2 hrs. TAT-4 at 25 km - new program).

Fig. 3.33b. Smoothed effective resistivity  $\rho_H$  and  $\pm 1$  standard deviation lines (2 hrs. TAT-4 at 25 km - new program).

Fig. 3.33c. Smoothed effective resistivity  $\rho_Z$  and  $\pm 1$  standard deviation lines (2 hrs. TAT-4 at 25 km - new program).

Fig. 3.34a. Phase of transfer function  $\alpha_D$  (2 hrs, TAT-4 at 25 km - new program).

Fig. 3.34b. Phase of transfer function  $\alpha_H$  (2 hrs, TAT-4 at 25 km - new program).

Fig. 3.34c. Phase of transfer function  $\alpha_Z$  (2 hrs, TAT-4 at 25 km - new program).

#### CHAPTER 4

Fig. 4.1. Study of the high-frequency oscillations. The three-dimensional plots exhibit (a) the spectra of the TAT-4 induced voltage and (b) the D-component of the magnetic field, plotted against a window center position in time.

#### CHAPTER 5

Fig. 5.1a. Results for the effective resistivity for the semi-analytic fitted solution as a function of frequency for two barrier conductivities ( $\sigma_{\text{barrier}} = 0.01, 0.1$  mho/m). Also shown are the data for  $\rho_D$  for TAT-6 at 225 km.

Fig. 5.1b. Same as Fig. 5.1a plotted with the data for  $\rho_H$  for TAT-7 at 3000 km.

Fig. 5.2. The effective resistivity for the semi-analytic fitted solution as a function of frequency out to 1 Hz for two barrier conductivities ( $\sigma_{\text{barrier}} = 0.1, 0.01$  mho/m).

Fig. 5.3. The effective resistivity from the finite element code solution as a function of frequency out to 1 Hz for two barrier conductivities ( $\sigma_{\text{barrier}} = 0.1, 0.01$  mho/m).

#### CHAPTER 6

Fig. 6.1. The simple three-layer geometry air/ocean/barrier. The fields depend only on the z-coordinate.

Fig. 6.2a.  $H_x$  for the air/ocean/barrier layered geometry (ocean depth = 0.2 km). The dashed (solid) line is the least-squares fit (exact result).

Fig. 6.2b.  $E_y$  for the air/ocean/barrier layered geometry (ocean depth = 0.2 km). The dashed (solid) line is the least-squares fit (exact result).

Fig. 6.2c.  $J_y$  for the air/ocean/barrier layered geometry (ocean depth = 0.2 km). The dashed (solid) line is the least-squares fit (exact result). The two solutions are almost identical.

Fig. 6.3a.  $H_x$  for the air/ocean/barrier layered geometry (ocean depth = 4.0 km). The dashed (solid) line is the least-squares fit (exact result). The two solutions are essentially identical.

Fig. 6.3b.  $E_y$  for the air/ocean/barrier layered geometry (ocean depth = 4.0 km). The dashed (solid) line is the least-squares fit (exact result). The solutions are almost identical.

Fig. 6.3c.  $J_y$  for the air/ocean/barrier layered geometry (ocean depth = 4.0 km). The dashed (solid) line is the least-squares fit (exact result). The solutions are essentially identical.

Fig. 6.4. Geometry used for modeling the land/ocean environment.

Fig. 6.5a. The effective resistivity for the semi-analytic solution as a function of frequency for two different barrier conductivities ( $\sigma_{\text{barrier}} = 0.01, 0.1$  mho/m). Also shown are the data for  $\rho_D$  for TAT-6 at 225 km.

Fig. 6.5b. Same as Fig. 6.5a plotted with the data for  $\rho_H$  for TAT-7 at 3000 km.

Fig. 6.6a. Same as Fig. 6.5a except the "trivial" 2-layer/3-layer model results are shown.

Fig. 6.6b. Same as Fig. 6.5b except the "trivial" 2-layer/3-layer model results are shown.

Fig. 6.7a. The effective resistivity for the semi-analytic solution as a function of frequency out to 1 Hz.

Fig. 6.7b. The effective resistivity for the "trivial" 2-layer/3-layer solution as a function of frequency out to 1 Hz.

Fig. 6.8. The geometry for the plots 6.9 - 6.14 showing the cuts along which the various fields are plotted. Figs. 6.9 - 6.14 all have  $\sigma = 0.1$  mho/m for the barrier conductivity and are evaluated at a frequency of 0.1 Hz. The continuity conditions are that  $H_x$ ,  $E_y$ , and  $\tilde{J}_z$  are supposed to be continuous across horizontal boundaries, while  $H_x$ ,  $\tilde{J}_y$ , and  $E_z$  are supposed to be continuous across vertical boundaries.

Fig. 6.9a. The magnetic field  $H_x$  from the fitted semi-analytic solution at  $y = 1$  km.

Fig. 6.9b. The magnetic field  $H_x$  from the semi-analytic solution at  $y = -1$  km.

Fig. 6.9c. The magnetic field  $H_x$  from the semi-analytic solution at  $y = 0.1$  km.

Fig. 6.9d. The magnetic field  $H_x$  from the semi-analytic solution at  $y = -0.1$  km.

Fig. 6.10a. The electric field  $E_y$  from the semi-analytic solution at  $y = 1$  km.

Fig. 6.10b. The electric field  $E_y$  from the semi-analytic solution at  $y = -1$  km.

Fig. 6.10c. The electric field  $E_y$  from the semi-analytic solution at  $y = 0.1$  km.

Fig. 6.10d. The electric field  $E_y$  from the semi-analytic solution at  $y = -0.1$  km.

Fig. 6.11a. The total current  $\tilde{J}_z$  from the semi-analytic solution at  $y = 1$  km.

Fig. 6.11b. The total current  $\tilde{J}_z$  from the semi-analytic solution at  $y = -1$  km.  
(Ordinate label of  $n^{-m}$  means current of  $n \times 10^{-m}$  amps/m<sup>2</sup>.)

Fig. 6.11c. The total current  $\tilde{J}_z$  from the semi-analytic solution at  $y = 0.1$  km.

Fig. 6.11d. The total current  $\tilde{J}_z$  from the semi-analytic solution at  $y = -0.1$  km.

Fig. 6.12a. The magnetic field  $H_x$  from the semi-analytic solution at  $z = -0.21$  km.

Fig. 6.12b. The magnetic field  $H_x$  from the semi-analytic solution at  $z = -0.19$  km.

Fig. 6.12c. The magnetic field  $H_x$  from the semi-analytic solution at  $z = -0.01$  km.

Fig. 6.13a. The electric field  $E_z$  from the semi-analytic solution at  $z = -0.21$  km.

Fig. 6.13b. The electric field  $E_z$  from the semi-analytic solution at  $z = -0.19$  km.

Fig. 6.13c. The electric field  $E_z$  from the semi-analytic solution at  $z = -0.01$  km.

Fig. 6.14a. The total current  $\tilde{J}_y$  from the semi-analytic solution at  $z = -0.21$  km.

Fig. 6.14b. The total current  $\tilde{J}_y$  from the semi-analytic solution at  $z = -0.19$  km.

Fig. 6.14c. The total current  $\tilde{J}_y$  from the semi-analytic solution at  $z = -0.01$  km.

Fig. 6.15a.  $H_x$  for the air/ocean/barrier layered geometry; ocean depth = 0.2 km. The dashed (solid) line is the finite element code (exact) result. The frequency is 0.1 Hz and  $\sigma_{\text{barrier}} = 0.1$  mho/m.

Fig. 6.15b.  $E_y$  for the air/ocean/barrier layered geometry; ocean depth = 0.2 km. The dashed (solid) line is the finite element code (exact) result.

Fig. 6.16. The effective resistivity from the finite element code as a function of frequency out to 1 Hz for two barrier conductivities ( $\sigma_{\text{barrier}} = 0.1, 0.01$  mho/m).

Fig. 6.17a. The magnetic field  $H_x$  solution from the finite element code at  $y = 10$  km. Figs. 6.17- 6.22 all have  $\sigma = 0.1$  mho/m for the barrier conductivity and are evaluated at a frequency of 0.1 Hz. The continuity conditions are that  $H_x$ ,  $E_y$ , and  $\tilde{J}_z$  are supposed to be continuous across horizontal boundaries, while  $H_x$ ,  $\tilde{J}_y$ , and  $E_z$  are supposed to be continuous across vertical boundaries.

Fig. 6.17b. The magnetic field  $H_x$  from the finite element code at  $y = -12.5$  km.

Fig. 6.17c. The magnetic field  $H_x$  from the finite element code at  $y = 0.1$  km.

Fig. 6.17d. The magnetic field  $H_x$  from the finite element code at  $y = -0.1$  km.

Fig. 6.18a. The electric field  $E_y$  from the finite element code at  $y = 10$  km.

Fig. 6.18b. The electric field  $E_y$  from the finite element code at  $y = -12.5$  km.

Fig. 6.18c. The electric field  $E_y$  from the finite element code at  $y = 0.1$  km.

Fig. 6.18d. The electric field  $E_y$  from the finite element code at  $y = -0.1$  km.

Fig. 6.19a. The total current  $\tilde{J}_z$  from the finite element code at  $y = 10$  km.

Fig. 6.19b. The total current  $\tilde{J}_z$  from the finite element code at  $y = -12.5$  km.

Fig. 6.19c. The total current  $\tilde{J}_z$  from the finite element code at  $y = 0.1$  km.

Fig. 6.19d. The total current  $\tilde{J}_z$  from the finite element code at  $y = -0.1$  km.

Fig. 6.20a. The magnetic field  $H_x$  from the finite element code at  $z = -0.225$  km.

Fig. 6.20b. The magnetic field  $H_x$  from the finite element code at  $z = -0.175$  km.

Fig. 6.20c. The magnetic field  $H_x$  from the finite element code at  $z = -0.1$  km.

Fig. 6.21a. The electric field  $E_z$  from the finite element code at  $z = -0.225$  km.

Fig. 6.21b. The electric field  $E_z$  from the finite element code at  $z = -0.175$  km.

Fig. 6.21c. The electric field  $E_z$  from the finite element code at  $z = -0.1$  km.

Fig. 6.22a. The total current  $\tilde{J}_y$  from the finite element code at  $z = -0.225$  km.

Fig. 6.22b. The total current  $\tilde{J}_y$  from the finite element code at  $z = -0.175$  km.

Fig. 6.22c. The total current  $\tilde{J}_y$  from the finite element code at  $z = -0.1$  km.

## CHAPTER 7

Fig. 7.1. Effective resistivity found in Ref. [1] for the L4/L5 land-based system. The two lines are 95% confidence bounds.

## CHAPTER 8

Fig. 8.1. Equivalent circuit for a submarine cable communications system with an earth potential present.

Fig. 8.2. The approximate straight-line-segment V-I curve for the power supply of a submarine cable.

Fig. 8.3. The power supply characteristics after shutdown occurs. On the vertical segment marked (SC), a short circuit overcurrent shutdown situation for aiding earth potential voltages occurs. On the horizontal segment marked (OC) an open circuit overvoltage shutdown situation occurs for bucking earth potential voltages.

Fig. 8.4. The power-supply characteristics for a fast overvoltage shutdown. At point (A), shunt gas tubes fire at a power-supply voltage of 9000 volts, thereby connecting 1000 ohms in parallel with the power output. At point (B), 9 amperes of current exist in the reverse direction. At point (C), the power supply voltage is 100 volts. A 1000-ohm slope connects points (B) and (C). In the quadrant (ABC) the reverse current is limited mainly by the resistance of the cable power conductor.

Fig. 8.5. A configuration of a branching into two legs with a total of three power supplies.

Fig. 8.6. The characteristics of a Zener diode in a submarine cable repeater. The maximum allowable surge power is plotted vs. pulse width of the surge. The surges are assumed to be square pulses. The DC power rating is 10 watts.

Fig. 8.7. The equivalent circuit for a repeater on the continental shelf with two strings of diodes.



## APPENDIX A

Fig. A1. Idealized geometry for the land/ocean model treated in the text.

Fig. A2. A simpler version of Fig. A1 containing several layers, but without the complications of the continental edge effects.

Fig. A3. An idealized land/ocean geometry showing the possibility of leakage fields coming down through the land and around to the bottom of the ocean floor as well as diffusion fields coming down through the ocean.

Fig. A4. The hypothesized leakage barrier which serves to help attenuate the leakage fields at higher frequencies, consistent with the falloff in the effective resistivity with frequency.

Fig. A5. The model evaluated in this report with a homogeneous barrier substance beneath the ocean on the continental shelf.

## APPENDIX C

Fig. C1. The equivalent circuit for the cable and ocean along with a global return path deep in the earth. The common-mode current for the cable and ocean is called  $I_c$  and the small differential-mode current is  $I_d$ .

Fig. C2. The path of a submarine cable from point A (earth station) to point B (sea ground or other ground). Point C represents the local ground at the earth station.

Fig. C3. The hypothetical circuit path ABCA used to deduce the approximate result that the voltage measured at the earth station between the cable end point A and the local ground point C is equal to the line integral of the unperturbed electric field along the path of the cable from point A to point B.

## MAGNETOHYDRODYNAMIC (MHD) NUCLEAR WEAPONS EFFECTS ON SUBMARINE CABLE SYSTEMS

### EXECUTIVE SUMMARY

This report presents a study of the nuclear weapons magnetohydrodynamic (MHD) effects on submarine communications cables. The study consisted of the analysis and interpretation of currently available data on submarine cable systems TAT-4, TAT-6, and TAT-7. The primary result of the study is that decrease of the effective resistivity with frequency over the available experimental range, coupled with the model results, leads to quite small effective resistivities at the MHD characteristic frequencies, and hence small earth potential differences. Thus, it appears that submarine cable systems are less susceptible to an MHD threat than their land-based counterparts.

The effective resistivity curves for submarine cables, however, showed more complicated behavior than those from land-based cable systems. This complexity is caused by the land/ocean interface crossed by the undersea cables and is exhibited by frequency dependent behavior of the effective resistivity. This makes any extrapolation procedure difficult and decreases confidence in the ability to predict the susceptibility of submarine cables to be laid in other regions. The extent to which the surrounding geology can affect the MHD threat to undersea cable systems is thus an important question which remains to be clarified. Another requirement for characterization of the reaction of various undersea systems to MHD effects is to extend measurements to frequencies of 1 Hz and somewhat higher, which corresponds more closely to the characteristic frequency of MHD from nuclear weapons.

## CHAPTER 1

### GENERAL INTRODUCTION

The disruption of communications systems due to large solar-activity-induced magnetic storms has been observed several times. Examples include noise and distortion of communications of the AT&T transatlantic cable from Newfoundland to Scotland in 1958 and the failure for about half an hour of a link between Illinois and Iowa in 1972. These disturbances led to the identification of possible communication disruption and damage as a result of nuclear weapons-produced magnetic disturbances at low frequency. The potential disturbance, termed MHD, or the Magnetohydrodynamic effect (also called MHD EMP), is distinct from other nuclear weapons effects [1].

MHD is actually a complex set of phenomena. Typical dominant frequencies in the spectra are 1 Hz or less, much lower than the megahertz scale of the early-time EMP disturbance [2]. For this reason, the effect couples to communications systems in a different fashion than for EMP. At MHD frequencies, the skin depth in the earth is typically on the order of kilometers, so that cables buried in the earth are not immune. For the ocean, at 1 Hz the skin depth is about 1/4 km, on the order of the depth of water over the continental shelf. Hence coupling to submarine cables on the continental shelf can occur easily.

At least two general MHD phenomena are distinguished. The first, and more important, is called the HABW (High Altitude Blast Wave) effect. The second is called the Heave effect. The HABW effect is illustrated in Fig. 1.1, taken from Ref. [1] (unclassified drawing). The mechanism for the HABW effect is that the expanding debris produces a sort of magnetic bubble by creating a

dipole-like field outside a volume of several hundred km radius which distorts the ambient geomagnetic field. The mechanism for this is a shock front created by blast debris interacting with the earth's magnetic field. Alfven waves, which depend on the magnetic field of the earth and charged particles due to the blast, are produced. The shock distorts the ambient earth magnetic field lines and passes through the "F-region" of the ionosphere, about 300 km in altitude, and then through the "D" and "E" regions at around 100 km. Finally, an electromagnetic wave propagates down to the earth. The resulting pulse lasts several seconds, with typical frequency content on the scale of 0 - 1 Hz. The Heave effect is illustrated in Fig. 1.2, another unclassified drawing from Ref. [1]. The mechanism for the Heave effect is that the atmosphere in a "debris patch" is heated by various ions resulting from the explosion which travel in helical paths around the geomagnetic field lines (Fig. 1.2a). The resulting hot air rises. As it rises, it cuts across the ambient geomagnetic field lines, thereby inducing an East-West EMF along with ionospheric currents (Fig. 1.2b). These currents then produce an electromagnetic disturbance on the earth whose time scale is on the order of tens of seconds, with a corresponding frequency scale on the order of 0 - 0.1 Hz. These summary descriptions should not obscure the fact that both effects are extremely complex plasma-physics and atomic-physics problems. Large computer codes are necessary to deal with an estimation of the threat.

In order to try to estimate the MHD effect on communications systems, an indirect method which has been adopted in the past shall be followed here. Geophysics measurements of cable voltage fluctuations induced by fluctuations  $\delta B_{\text{earth}}$  in the earth's magnetic induction field are made [3,4]. Once analyzed,

the response of the same system to an MHD disturbance can be obtained by scaling up the measured voltages under the assumption that the system response is linear in the imposed electromagnetic field. Extension to other systems can be made if the ratios of the responses of the other systems to the system on which the measurements were made are known.

An analysis of these effects was performed in Ref. [5] for the L4/L5 coaxial cable system on the continental United States. The nature of the possible disruptions on a transoceanic cable are the subject of this report. The methodology of Ref. [5] is closely followed here. First, experimental results correlating ambient (solar-induced) magnetic field fluctuations with undersea cable voltage fluctuations are examined. Then, given a definition of the MHD magnetic field threat, the assumed linearity of the system can, in principle, be used to predict the cable voltage fluctuations due to a nuclear weapon.

Two difficulties emerge with respect to this procedure. First, appropriate experimental measurements may not exist for the cable of interest. Second, the sampling times of the measurements are such that the fields and voltages may not be available at the frequencies of interest for the MHD effects. In the L4/L5 study, measurements were made directly on that system. The extrapolation in frequency also seemed particularly simple. Here the situation is more complex. More analysis is necessary, including a substantial modeling effort.

The extrapolation of the data to the 1 Hz frequency region is the most serious issue. Such an extrapolation depends on the geological structure in the vicinity of the communication system. This structure is often complex and more to the point, often unknown. Indeed, it is a classic geophysics procedure to

deduce information about geological structure using such data [6]. In the absence of experimental data up to 1 Hz, a co-ordinated effort in analyzing the data, modeling the electromagnetic fields for a given geological structure, and calculating the coupling to a given communications system is called for in the analysis of the MHD threat.

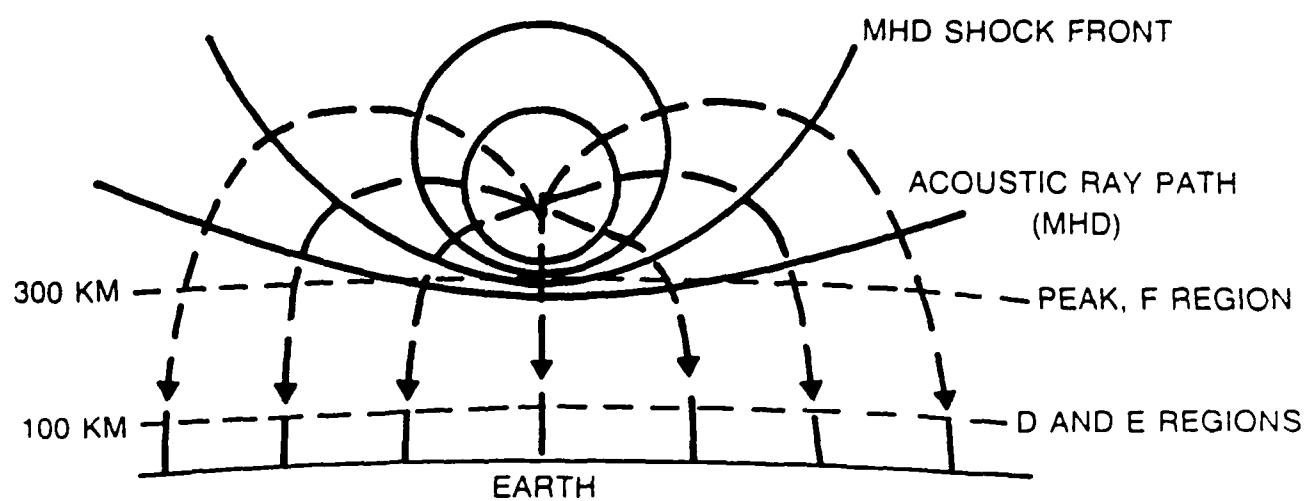
A second problem is connected with the nature of the measurement itself. Usually, the magnetic field fluctuations  $\delta B_{\text{earth}}$  are measured at a given point, or a few points, on the land. It is difficult to measure  $\delta B_{\text{earth}}$  at sea due to random movements of boats. On the other hand, an induced voltage on a cable results from the non-local integration of the electric field tangential to the cable along its length, with appropriate correction made for the transfer function of the electric field into the cable itself. For submarine cables, this means that the electric field at the sea floor is being correlated with the magnetic field at sea level. While this is indeed the desired correlation, the problem of extrapolation in frequency then implies involvement with the geological structure underneath the sea-floor, including the complex structure of the continental shelf. Further, since  $\delta B_{\text{earth}}$  is not measured over the ocean, some assumptions about the spatial variation of  $\delta B_{\text{earth}}$  have to be made. It is known that  $\delta B_{\text{earth}}$  does vary over large spatial scales, and therefore this method can really only be useful if the nonlocal integration of the electric field producing the cable voltage fluctuations takes place over distances smaller than the spatial scale of variation of the fluctuations of the earth's magnetic field. Luckily, for the submarine cable measurements, it will be seen that most of the coupling occurs on the continental shelf. The width of the continental shelf is on the order of a few hundreds of kilometers, within the scale of spatial variation of  $\delta B_{\text{earth}}$ .

This first volume deals with the general aspects of the experiments and analysis. Volume 2 (classified) presents the details of the threat and the consequences for submarine cable systems.

## REFERENCES (Chapter 1)

1. N. J. Carron and C. L. Longmire, "Magnetohydrodynamic EMP Environments (U)", Mission Research Corporation Report MRC-R-724 Revised, DNA-TR-82-25 (February, 1982).
2. See, e.g., "EMP Interaction: Principles, Techniques, and Reference Data (A Compleat Concatenation) ", K.S.H. Lee, editor , Air Force Weapons Laboratory Report TR-80-402, Kirtland AFB, NM (1980).
3. L. J. Lanzerotti, D. J. Thomson, A. Meloni, L. V. Medford, and C. G. MacLennan, "Electromagnetic Study of the Atlantic Continental Margin Using a Section of a Transatlantic Cable", J. Geoph. Res. Vol 91, 7417 (1986); A. Meloni, L. J. Lanzerotti, and G. P. Gregori, Reviews of Geophysics and Space Physics, Vol. 21, 795 (1983); L. V. Medford, A. Melonis, L. J. Lanzerotti, and G. P. Gregori, Nature, Vol. 290, 329 (1981)
4. L. J. Lanzerotti, L. Medford, D. J. Thomson, and C. MacLennan. private communication.
5. D. L. Lin, "Solar-Induced and Nuclear Magnetohydrodynamic Effects on Coaxial Carrier Transmission Systems", 1984.
6. I. I. Rokityansky, "Goelectromagnetic Investigation of the Earth's Crust and Mantle", Springer-Verlag ( 1982).
7. A. Beilis, J. W. Dash, and A. Farrow, "Analytic " $\alpha$  - Pole" Approach to an Electromagnetic Scattering Problem", IEEE Transactions EMC Vol. 29, No. 2, pp. 175-185 (1987).





MHD — HABW EFFECT

Fig. 1.1. Mechanism for the MHD HABW (High Altitude Blast Wave) effect.

# MHD — HEAVE EFFECT

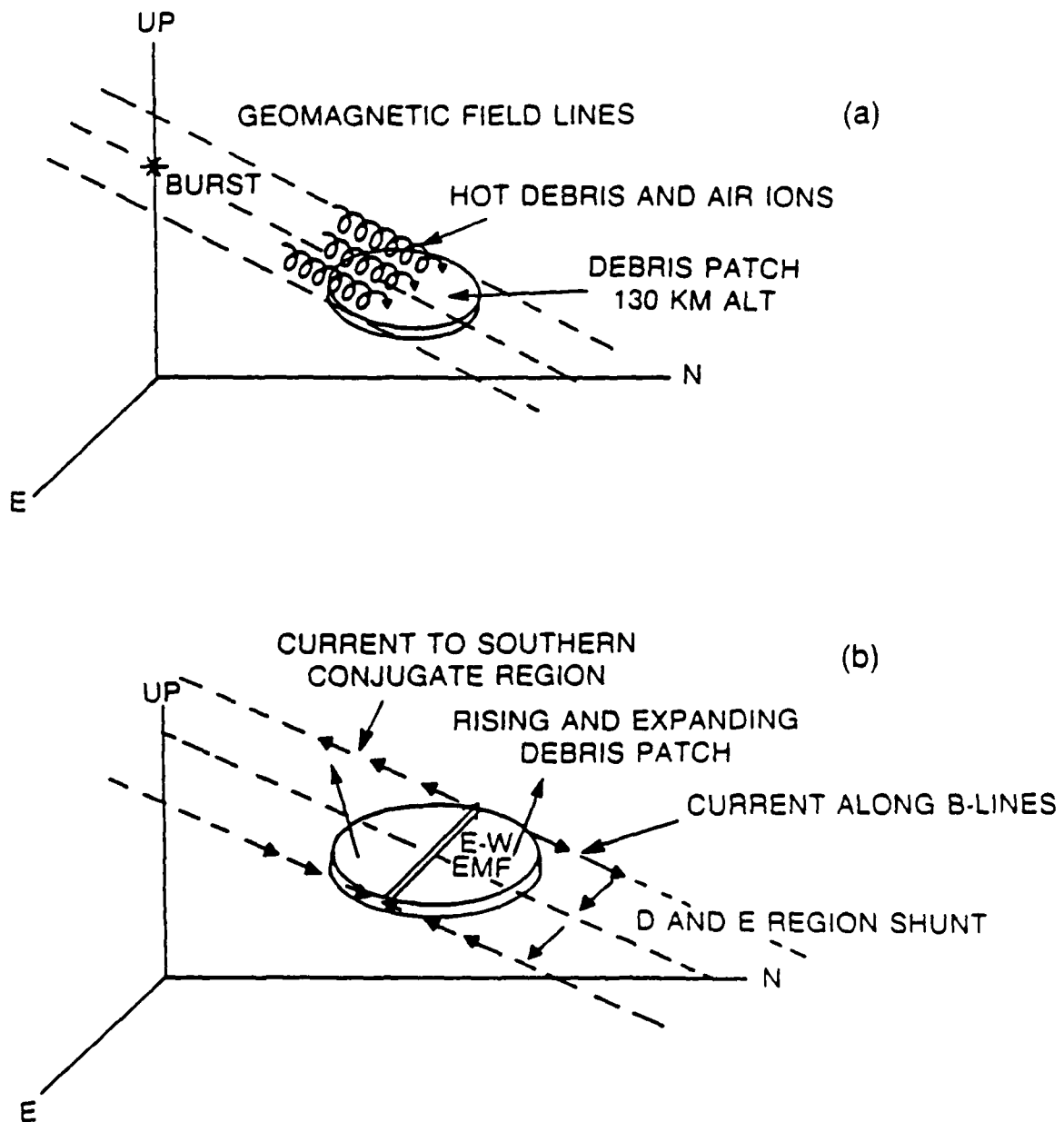


Fig. 1.2. Mechanism for the MHD Heave effect.

## CHAPTER 2

### SUBMARINE CABLE EXPERIMENTS

This section describes details of the experiments done by the AT&T geophysics group [1] on the TAT-3, TAT-4, TAT-6 and TAT-7 coaxial cable transoceanic communication systems (see Fig. 2.1). The data taken were under two conditions - unpowered and powered. For reasons described below, the unpowered data contain the more useful information.

#### 2.1 - TAT-6 UNPOWERED DATA

The TAT-6 experiment was done while repairs were being made to the system, originally placed in service in 1976. Seawater penetration of a flexible joint had led to corrosion and noise problems, necessitating repeater retrieval and repair. Since the power supply at the terminal in Green Hill, Rhode Island was positive, a sacrificial metal ground was made directly from the end of the center conductor to the sea water to prevent electrolysis of the repeater housings during powered testing of the cable under repair. Figure 2.2 shows the set-up. The experiment used a voltmeter marked  $R_{VM}$  in the figure to measure the voltage between the cable center conductor and the local ground at the station. Appendix C contains a theoretical discussion of the relation of this measurement with the earth potential (cf Chapter 8) needed to obtain the MHD threat estimates.

Measurements on the TAT-6 system were made for two lengths as repairs were made at different points. The lengths of cable measured from the terminal in Rhode Island were 225 and 3140 km. Fortunately, the 225-km length corresponds to a position only just past the continental shelf. This allows

comparison of the coupling on the continental shelf to the coupling on the ocean bottom for the longer lengths. For the 225-km length, the depth of the water at the anode end was 980 fathoms, or around 2000 m, corresponding to about 40% of the depth of the bottom of the ocean at the "abyssal plane". Fig. 2.3 exhibits the profile of the seabed of the Atlantic Ocean around 40° N. latitude where the submarine cables run.

## 2.2 - TAT-7 UNPOWERED DATA

Measurements on the TAT-7 system were performed during installation before the system was placed in service in 1983. The AT&T geophysics group arranged for the power to be turned off so that quiescent conditions could be obtained (the power is normally turned on to test the repeaters while the system is being laid). The end of the partial cable was on the ocean bottom and was grounded in the following manner: the center conductor of the coaxial cable was shorted to the sheath, or outer conductor. The latter had a direct electrical connection to the last repeater housing before the cable end. Finally, the repeater housing, of a Be/Cu construction, was grounded to the sea water. Since the TAT-7 power supply was negative at the originating end, electrolytic metal loss was not a problem and no anode was used.

Measurements for TAT-7 were taken at lengths approximately 1500, 3000, and 4400 km as measured from the terminal at Tuckerton, New Jersey.

The TAT-7 data taken early in the experiment suffered from "glitches", occasional random spikes in the data which were introduced by an analog to digital converter being operated at too high a clock rate. These effects had to be

subtracted out by hand during the data analysis. Spikes were at known count levels in the conversion process. Some data at the nominal 3000-km length for TAT-7 actually corresponded to an effective length of around 1200 km, due to an anomalous short between the pigtail coaxial connection and the case of a repeater. This short occurred within hours after completion of the 3000-km lay. These data were not used. Several days of 3000-km data were obtained after repair of the short. Finally, some TAT-7 data at 1500 km with a 5-sec sampling rate seemed inconsistent (as described in the next chapter) and are therefore not exhibited in this report.

### 2.3 - TAT-7 POWERED DATA

Powered TAT-7 data were also obtained. These data were obtained for various lengths under the normal installation conditions with the power being supplied at the terminal out to the last repeater housing before the cable end in the sea water, and also for the full length. Unfortunately, these data were contaminated by voltage variations in the powering equipment induced by ambient building temperature fluctuations from the cooling system cycling. (The heat generated by the equipment requires year-round cooling, either by air conditioning or by cycled cold air from outside in winter). Moreover, the increased current in the system (relative to the unpowered configuration) produced another noise problem due to an electrochemical effect between the last repeater housing and the sea water. The induced signals, being small, were therefore unacceptably contaminated by noise.

An experiment was performed in late 1986 when the outside temperature was cold enough so that the air conditioning noise problem could be a-priori

hopefully judged to be less severe. These measurements were also performed with a faster sampling rate in an attempt to facilitate the extrapolation. The results show that, unfortunately, the air conditioning was still a significant problem, and therefore these data were also unacceptably corrupted by noise.

As a result, all TAT-7 powered data were judged unsuitable for incorporation into this report.

#### 2.4 - TAT-4 UNPOWERED DATA

Late in 1986 the TAT-4 cable was accidentally cut just past the first repeater by a boat, and the section from the terminal to the cut was thus available for measurement in an unpowered state. The length of this section was about 25 km, a very short length. Data were obtained for this system at a sampling rate of 2 sec/measurement. These data are incorporated in this report.

#### 2.5 - TAT-3 POWERED DATA

Data on the TAT-3 system (an old vacuum tube system) were taken early in the experimental effort before the other cables were available. The experimentalists judge the quality of these data as inferior [1]. Since these TAT-3 data were duplicated by better quality data taken later on other systems, they were judged as serving no useful purpose.

In 1986 the old TAT-3 cable experienced multiple repeater failures and was decommissioned ahead of schedule. The possibility thus existed for measurements of the partial cable in an unpowered state. Unfortunately the

cable was soon damaged just offshore by a trawler, resulting in a noisy leakage to sea ground, and the cable was therefore abandoned for consideration.

Therefore, no TAT-3 data are incorporated into this report.

## 2.6 - ALIAS FILTERS

Alias filters were used by the AT&T geophysics group to reduce the effects of the band limitations in their measurements. The problem is that higher frequency effects get reflected or "aliased" as an artificial increase in the lower frequencies of the spectrum. Since the geophysics group was primarily interested in frequencies  $f < 0.05\text{Hz}$ , filtering was necessary. The filters were Butterworth filters, "maximally flat" out to around 0.035 Hz and then falling off at 24 dB/octave at higher frequencies. A phase "lag/lead" change was also present. Nominally, the spectrum should be divided by this filter shape to recover the raw data for the voltage and magnetic field spectra. However, for the ratios of these spectra, the alias filters (which were identical for all field and voltage measurements) cancel out. Other faster filters were used for the measurements at the faster sampling rates on TAT-4, TAT-7.

REFERENCE (Chapter 2)

1. L. J. Lanzerotti, L. V. Medford, D. J. Thomson, and C. MacLennan, private communication. See L. J. Lanzerotti, D. J. Thomson, A. Meloni, L. V. Medford, and C. G. MacLennan, "Electromagnetic Study of the Atlantic Continental Margin Using a Section of a Transatlantic Cable", J. Geoph. Res. Vol 91, pp. 7417-27, 1986.



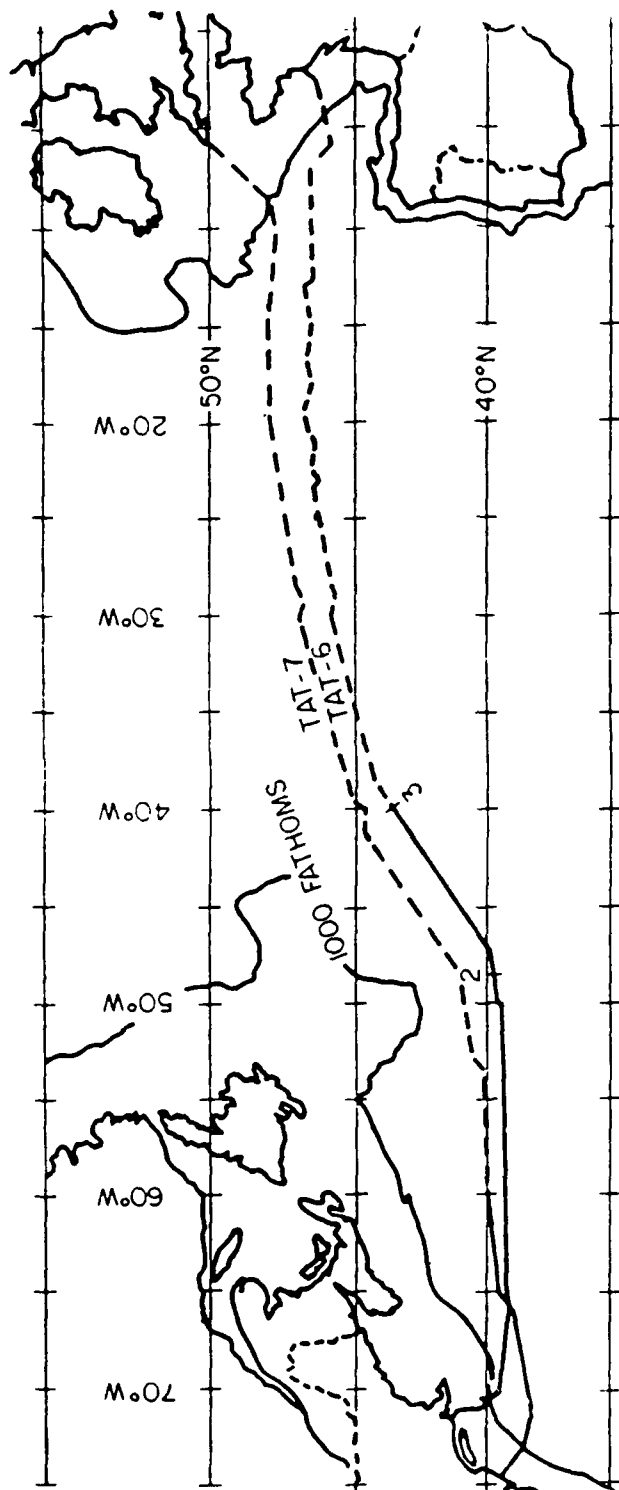


Fig. 2.1. Positions of the TAT-6 and TAT-7 transoceanic cables.

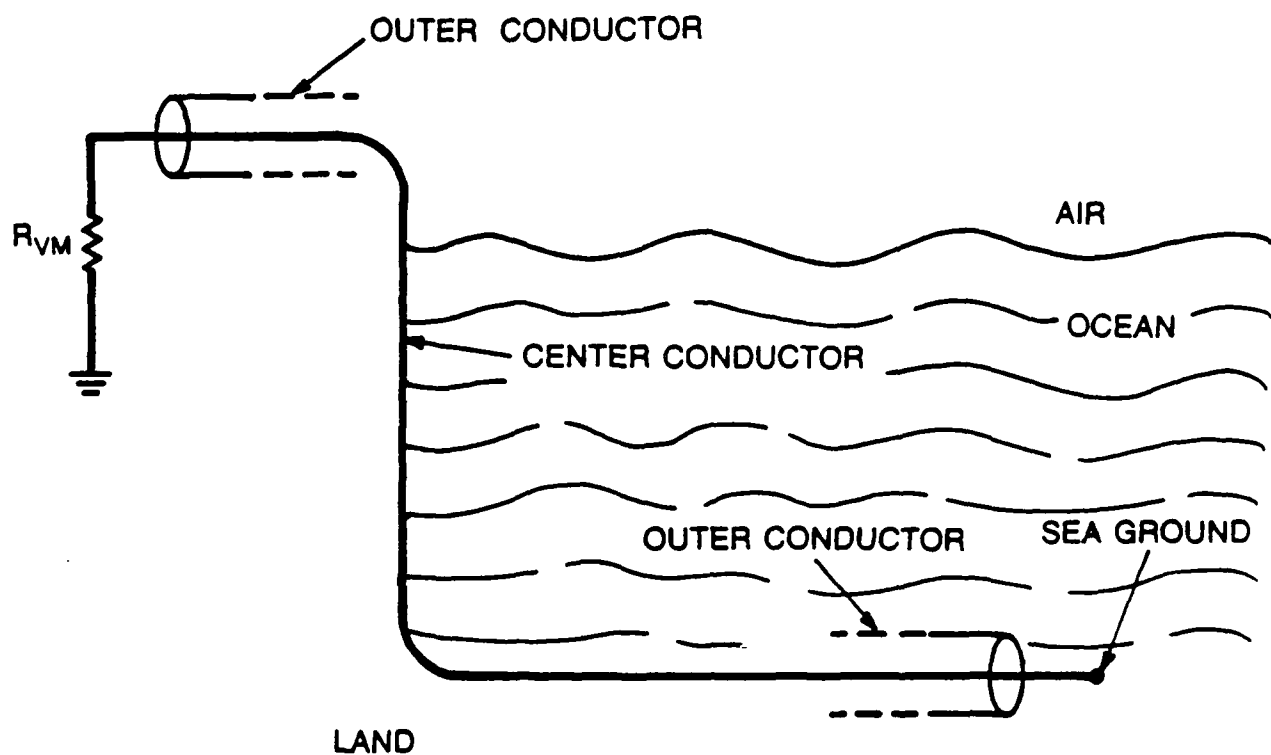


Fig. 2.2. Experimental set-up. The center conductor of the coaxial cable is grounded on land through the voltmeter resistance  $R_{VM}$  and grounded at sea through the sea ground.

# BOTTOM PROFILE

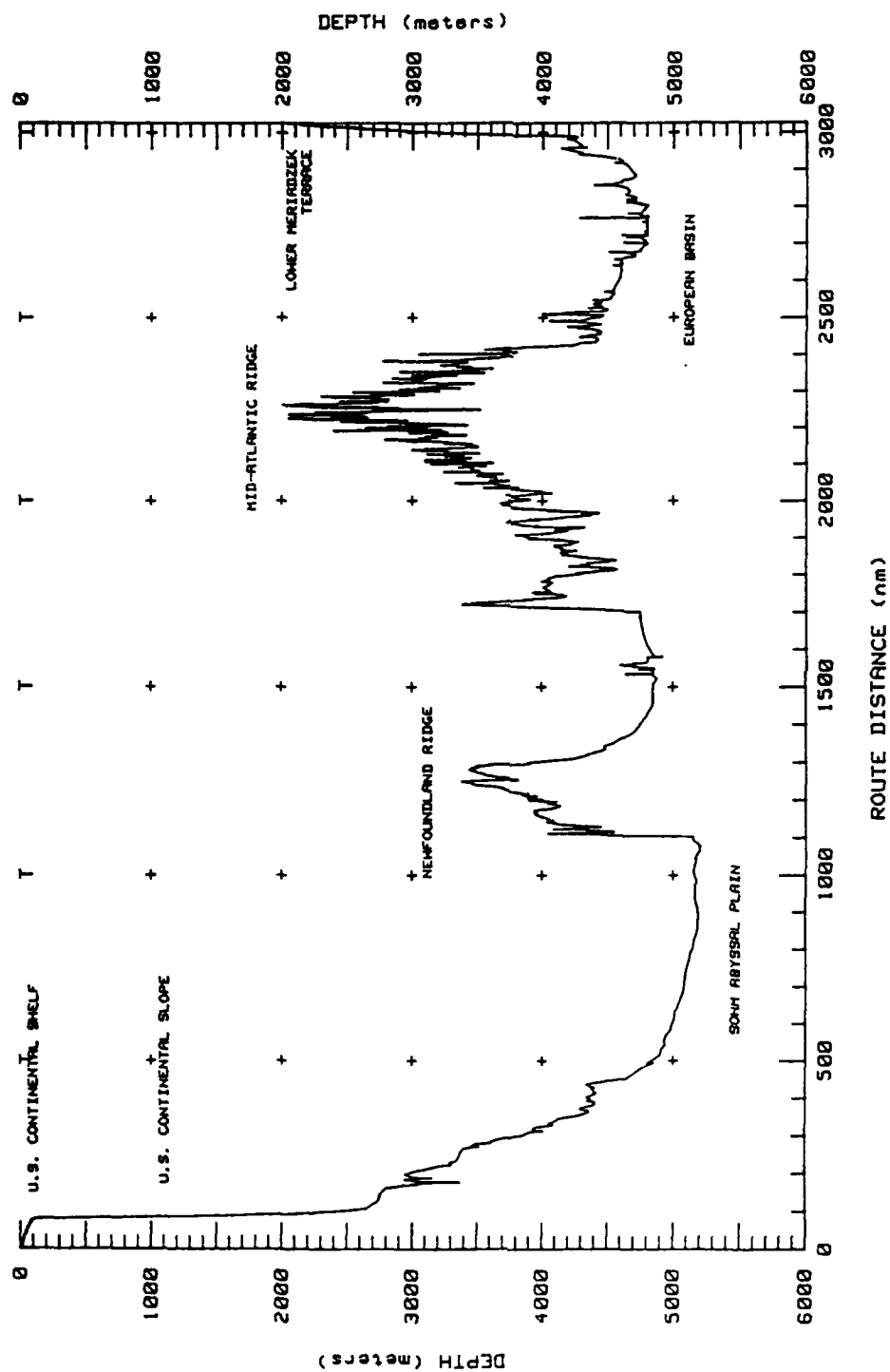


Fig. 2.3. The Atlantic Ocean seabed around 40° N latitude.

## CHAPTER 3

### DATA ANALYSIS

The data from the experiments described above were processed using the computer programs of D. J. Thomson [1] on the Cray X-MP computer at AT&T Bell Laboratories, Murray Hill, NJ. Altogether, over 250,000 measurements of the cable voltage and magnetic induction field, or over 1,000,000 data points, were processed. The transfer functions between the experimental cable voltage fluctuations and the sea-level magnetic field fluctuations were then obtained up to the Nyquist, or maximum, frequency corresponding to the measurement sampling rate. Details of the extrapolation in frequency are discussed in subsequent sections.

The three components of the magnetic field  $\delta B_{\text{earth}}$  called H, D, and Z are defined in Fig. 3.1. Thus, D describes east-west magnetic field fluctuations, while H describes north-south fluctuations, and Z describes vertical fluctuations. The Fourier transforms of these components are designated as  $H(\omega)$ ,  $D(\omega)$ ,  $Z(\omega)$ . Here  $\omega = 2\pi f$  is the radian frequency. While the transoceanic cables basically run east-west, significant departures from this orientation occur close to shore, and this is an important feature in the analysis.

#### 3.1 - DETAILS OF THE DATA ANALYSIS

The raw data tapes were read into the system. These data consisted of time waveforms of the cable voltage and magnetic induction. Some data points were missing. Missing data points were corrected for in a routine which put a flag on the missing data, and then calculated an autocorrelation function for five time lags, using all lagged products for which no data were missing. A

Wiener least-squares interpolator was then generated to give the best estimate of the missing point from the five adjacent points on each side.

The programs then computed the spectra of the voltage  $V(\omega)$  and of the three components of the magnetic field  $H(\omega)$ ,  $D(\omega)$ ,  $Z(\omega)$ . Actually, the time series are windowed with prolate spheroidal functions. Prolate spheroidal functions provide optimal windows, and their properties are presented in detail in Ref. 2. Thus, the data are multiplied in the time domain by the  $k$ th-order prolate spheroidal function, where  $k = 0, 1, \dots, 7$  was used. These windowed data then were Fourier-transformed. The Fourier transforms of the windowed voltage and magnetic fields are denoted by  $V^{(k)}(\omega)$ ;  $D^{(k)}(\omega)$ ,  $H^{(k)}(\omega)$ ,  $Z^{(k)}(\omega)$ . Next the magnitude squared coherence functions were computed. Some statistical tests were also computed. These quantities are now described.

The cross spectrum between the voltage and one of the components of the magnetic field (say  $D$ ) is defined as follows (where  $*$  denotes complex conjugate),

$$\langle V(\omega)D(\omega)^* \rangle \approx \frac{1}{N_{\text{windows}}} \sum_{k=1}^{N_{\text{windows}}} V^{(k)}(\omega)D^{(k)}(\omega)^* \quad (3.1)$$

where  $N_{\text{windows}}$  is the number of prolate spheroidal windows. The sum also includes a weight term which depends on both  $k$  and  $\omega$ , and which automatically decreases coefficients where "leakage" from adjacent frequencies is significant. In the calculations reported here, leakage is insignificant and the weights are effectively equal to 1.

The "magnitude squared coherence" (msc) between V and D is then defined as the real ratio

$$M_{VD} = \frac{| \langle V(\omega)D(\omega)^* \rangle |^2}{\langle V(\omega)V(\omega)^* \rangle \langle D(\omega)D(\omega)^* \rangle} \quad (3.2)$$

and the "coherence phase"  $\Phi_{VD}(\omega)$  is then

$$\Phi_{VD}(\omega) = \tan^{-1} \frac{\text{Im}(\langle V(\omega)D(\omega)^* \rangle)}{\text{Re}(\langle V(\omega)D(\omega)^* \rangle)} \quad (3.3)$$

The "delay" is defined as the derivative of the coherence phase, and corresponds roughly to a delay time, because time translation by an amount  $t_0$  corresponds to an exponential  $\exp(i\omega t_0)$  in the Fourier transform. Here the delay is in the coherence function, and therefore represents a relative time delay  $T_{\text{delay}}$ . For example, between V and D the relative time delay is defined as

$$T_{\text{delay}_{VD}} = \frac{d\Phi_{VD}(\omega)}{d\omega} \quad (3.4a)$$

In practice  $T_{\text{delay}}$  is calculated as

$$T_{\text{delay}} = \frac{\text{Re Im}' - \text{Im Re}'}{\text{Re}^2 + \text{Im}^2} \quad (3.4b)$$

where Re and Im mean the real and imaginary parts of  $\langle V(\omega)D(\omega)^* \rangle$  while the prime means differentiation with respect to  $\omega$ . This is because while both Re and Im are essentially bandlimited functions, so that their numerical derivatives are well behaved,  $\Phi_{VD}$  is not.

The F test is defined as

$$F_{\text{test}} = \frac{\frac{1}{6} |V(\omega)_{\text{reg}}|^2}{\frac{1}{(2N_{\text{windows}} - 6)} |V(\omega) - V(\omega)_{\text{reg}}|^2} \quad (3.5)$$

where  $V(\omega)_{\text{reg}}$  is the fit from the regression to the voltage. The normalizations follow from the fact that with  $N_{\text{windows}}$  windows and 3 input magnetic components, 6 and  $2N_{\text{windows}} - 6$  are the number of degrees of freedom in the fit and residuals, respectively. Similar definitions are made for the magnetic field components. The F-test roughly speaking can be thought of as the ratio of "explained" power to "residual" power.

### 3.2 - LEAST-SQUARES FITTING

The least squares fitting is used to obtain the transfer functions between the voltage and magnetic field components. The windowed voltage and magnetic fields  $V^{(k)}(\omega)$ ;  $D^{(k)}(\omega)$ ,  $H^{(k)}(\omega)$ ,  $Z^{(k)}(\omega)$  are used. Symbolically, the transfer functions  $\alpha_D(\omega)$ ,  $\alpha_H(\omega)$ ,  $\alpha_Z(\omega)$  can be written as

$$A_{\text{transfer}} = V H^{-1} \quad (3.6)$$

Specifically, it is assumed that for each window

$$V^{(k)}(\omega) = \alpha_D(\omega)D^{(k)}(\omega) + \alpha_H(\omega)H^{(k)}(\omega) + \alpha_Z(\omega)Z^{(k)}(\omega) + \epsilon^{(k)}(\omega) \quad (3.7)$$

where  $\epsilon^{(k)}(\omega)$  is the error for this kth-windowed formula. Then the quantity  $\Delta(\omega)$ , a measure of the overall mean-squared discrepancy, is minimized with respect to  $\alpha_H(\omega)$ ,  $\alpha_D(\omega)$ ,  $\alpha_Z(\omega)$ . Specifically,

$$\Delta(\omega) = \sum_{k=1}^{N_{\text{windows}}} |\epsilon^{(k)}(\omega)|^2 \quad (3.8)$$

and this determines the optimal values of  $\alpha_H(\omega)$ ,  $\alpha_D(\omega)$ ,  $\alpha_Z(\omega)$ .

The program LINPACK [3], a standard software package, was employed to perform the least-squares fitting. This package employs a technique known as a "Q-R" decomposition that is efficient and stable.

A caveat on this, and similar methods, is that the observations are assumed to be stationary. With geophysical data this is not, of course, strictly true, so that the results are less reliable than they would be with strictly stationary, Gaussian data.

Now the transfer functions can be used to define an "effective resistivity" matrix. In order to motivate this, consider the textbook example of a spatially



uniform conducting medium with a uniform incident plane wave with polarization  $E_y$  and magnetic field  $H_x$ . The ratio  $Z_{xy} = E_y/H_x$  with both fields evaluated at a given spatial point is the impedance, or transfer function per unit length in this simple case. It can be written

$$Z_{xy} = \frac{(1 - i)}{\tilde{\sigma}\delta} \quad (3.9)$$

where  $\tilde{\sigma} = \sigma - i\omega\epsilon \approx \sigma$  is the complex conductivity, equal to the conductivity to the extent that the displacement current measured by the second term in  $\tilde{\sigma}$  can be neglected. Also,  $\delta$  is the skin depth. Solving for  $\rho = 1/\sigma$  produces

$$\rho = \frac{|Z_{xy}|^2}{\mu\omega} \quad (3.10)$$

which is the resistivity. Typical values are  $\rho = 500 \Omega\text{-m}$  for land and  $\rho = \frac{1}{4} \Omega\text{-m}$  for seawater. Actually, since there are three transfer functions  $\alpha_D(\omega)$ ,  $\alpha_H(\omega)$ ,  $\alpha_Z(\omega)$  there are three resistivities  $\rho_D$ ,  $\rho_H$ ,  $\rho_Z$ . Now for a complex system involving both land and seawater, which is the case here, it would not be expected that one of the resistivities defined using the above formula would produce a simple result. Nonetheless, it is convenient to parametrize the data in terms of these quantities. For example, if an effective electric field  $E_{eff}$  were defined via an effective length  $L_{eff}$  as

$$E_{\text{eff}} = V/L_{\text{eff}} \quad (3.11)$$

then

$$\rho_D = \frac{|\alpha_D(\omega)|^2}{\mu\omega L_{\text{eff}}^2} \quad (3.12)$$

Two remarks are in order. First,  $\alpha_D(\omega)$  gives the transfer function between the magnetic D field component measured at sea-level and the voltage, which is the integrated electric field along the undersea cable position. Therefore, the fields are not measured at the same spatial point. Second,  $\rho_D$  reflects the composite structure of the land and ocean. However it is useful to consider this quantity because it is the closest thing to a physically interpretable parameter that is present. It is therefore anticipated that physical insight as to the geological structure as well as the manner of extrapolation to the higher frequency region of 1 Hz will be enhanced by consideration of  $\rho_D$  as well as the effective resistivities  $\rho_H$ ,  $\rho_Z$  for the other components.

The definition of  $L_{\text{eff}}$  needs clarification.  $L_{\text{eff}}$  is the effective length over which the electric field couples to the cable. It is an effective parameter because it is anticipated that the real electric field is not spatially constant. Here, the coupling is mostly on the continental shelf, so  $L_{\text{eff}} \approx 200$  km. Further discussion of this point appears below.

### 3.3 - RESULTS FOR A TYPICAL DATA SEGMENT - (TAT-6)

The above quantities were computed for each 6 hour segment of data and the results were collected. The most useful data turn out to be the TAT-6 data for the partial cable of length 225 km. These data are also very clean. These data have  $\Delta t = 10$  sec. between measurement points. They correspond to days 112, 113, 116, and 117 (1985). The waveforms for one six-hour segment of data are shown in Fig. 3.2. In the waveforms of Fig. 3.2, the units of magnetic field are emu gammas ( $\gamma$  emu) which are translated into MKS units by the formula

$$\vec{H} [\text{amps/m}] = \frac{1}{10^9 \mu_0} \vec{H} [\gamma \text{ emu}] \quad (3.13)$$

where  $\mu_0 = 4\pi \times 10^{-7}$  ohm-sec/meter. One important point to note is that visual correlations of the data can be misleading. It is seen that, for example, Fig. 3.2 shows a peak around 9:00 UT (Universal Time) in the voltage which appears well correlated with corresponding peaks in the magnetic fields. However, the width of this peak of over 10 minutes corresponds to a frequency of under 0.002 Hz, which is very low frequency. Thus, visual peaks of this sort are of no particular interest in this analysis. Rather, correlations of the rapidly varying part of the data (on this scale) which correspond to frequencies close to the Nyquist frequency  $1/(2\Delta t) = 0.05$  Hz are of interest.

Figs. 3.3a-c present the results for the resistivities  $\rho_D$ ,  $\rho_H$ ,  $\rho_Z$  for this six-hour segment of data. The word "uncorrected" is on the plots because there has been no attempt to correct the experimental data for any effects (e.g. noise).

Note that the magnetic field was measured on land while the electric field producing the cable voltage was at the cable position. It will be seen later that most of the coupling is on the continental shelf, and depth corrections are not significant for such small ocean depths. It is seen that the resistivities decrease with frequency out to the Nyquist, or maximum, frequency of 0.05 Hz, corresponding to the sampling rate for these data of 10 sec.

Figs. 3.4 a-d exhibit the transfer function  $\alpha_D(\omega)$  which produced the resistivity  $\rho_D$  in Fig. 3.3a. The magnitude, phase, and real and imaginary parts of  $\alpha_D(\omega)$  are shown. Note that the phase is roughly flat out to around 0.04 Hz, aside from jumps of  $2\pi$  which are of no physical significance. Thus the voltage and D component of the magnetic field are highly correlated at least out to 0.04 Hz. Figs. 3.5a-d and 3.6a-d exhibit the same information for  $\alpha_H(\omega)$  and  $\alpha_Z(\omega)$ , respectively. It is seen that the coherence measured by the phase is not as strong, and seems to disappear by around 0.03 Hz.

Correlations can also be measured by the magnitude squared coherence (msc). Figs. 3.7a-c show the msc for the three transfer functions for the same 6-hour segment. Again it is seen that higher coherence occurs at lower frequencies, and that the D component has the largest msc with the voltage. The msc test seems to indicate less correlation than the simple phase test, and this may in turn be related to the weighting of the higher-order prolate spheroidal windows in the msc definition, which oscillate rapidly and pick up information about the fluctuations which are more pronounced at the higher frequencies.

Fig. 3.8 presents the composite F-test for this data sample. The composite F-test measures the "explained" over "residual" power, and is therefore large when the correlations between the voltage and magnetic field components are high. Again, this is largest at lower frequencies where these correlations are most pronounced.

### 3.4 - RESULTS FOR COMPLETE TAT-6 , TAT-7 DATA SET

The effective resistivities for the whole data sample on a given cable at one length were then averaged over all the 6 hour data segments. For the purposes of plotting the data, as described above, the length  $L_{eff} = 200$  km was used in the definition of the resistivity. No depth corrections or other model-dependent corrections were applied. Practically all data had a 10-sec sampling rate except for some data which shall be discussed at the end.

The results for the resistivity  $\rho_D$  from the TAT-6 data at 225 km and at 3140 km are shown in Figs. 3.9a,b. For all resistivity plots,  $L_{eff}$  in Eq. 3.12 has been defined as 200 km, the approximate width of the continental shelf off the U.S. The consistency of this assumption will be examined shortly, being based on the length-independence of resistivities for lengths longer than the continental shelf width. Figs. 3.10a,b and 3.11 a,b exhibit  $\rho_H$  and  $\rho_Z$  from the TAT-6 data at 225 and 3140 km.

The resistivities from the unpowered TAT-7 data are presented in Figs. 3.12-3.14. Figs. 3.12a-c contain  $\rho_D$  from the 1500, 3000, and 4400 km lengths. Figs. 3.13a-c and 3.14a-c exhibit  $\rho_H$  and  $\rho_Z$ .

The resistivities given in Figs. 3.9-14 are all seen to have a similar shape with a maximum at very low frequencies, a plateau of some width depending on the details, and a distinct falloff at higher frequencies. This falloff is quite pronounced, and appears to be of at least 2 orders of magnitude. This corresponds to an order of magnitude decrease of the electric field relative to a situation with the same magnetic field but where the resistivity is a constant, since the electric field is proportional to the square root of the resistivity. This is because the impedance  $Z_{xy} = E_y/H_x = -ik/\bar{\sigma}$  and  $k = (i\omega\mu_0\bar{\sigma})^{1/2}$  in the simple one-dimensional case, leading to  $E_y = \text{const}\sqrt{\rho}$  in conductors.

The transfer functions leading to the above results for the resistivities are exhibited in Figs. 3.15-3.17 for the TAT-6 data. Figs. 3.15a,b contain the magnitudes of  $\alpha_D(\omega)$  at 225 km and 3140 km, while Figs. 3.16a,b and 3.17a,b exhibit the magnitudes of  $\alpha_D(\omega)$  and  $\alpha_Z(\omega)$ .

The length independence of the effective resistivities for frequencies above around 0.01 Hz is easily seen. Fig. 3.18a exhibits the ratio of the magnitudes of the transfer functions  $\alpha_D(\omega)$  for D at the two lengths 3140 km and 225 km. If there were a length dependence to the effective resistivity  $\rho_D$ , it would show up in a larger magnitude of  $\alpha_D(\omega)$  at 3140 km relative to 225 km. However, the data are consistent with a ratio of almost exactly one above frequencies of 0.01 Hz. This means that the coupling to the cable is almost entirely at distances equal to or less than the smaller 225 km cable length, and hardly any coupling to the part of the cable from 225 to 3140 km occurs, at least at frequencies above around 0.01 Hz. Similar statements hold for the H and Z ratios of transfer functions for TAT-6 shown in Figs. 3.18b,c. Below 0.01 Hz,

an increase in the ratios above one is seen, but even here the ratio does not generally increase to the value  $3140/225 = 14$  that would be expected if the coupling of the electric field at the cable position were uniform along its length. The exception is  $\alpha_H(\omega)$  at very low  $f < 0.002$  Hz, where the ratio is compatible with uniform coupling. It is concluded that the effective length  $L_{eff}$  to be used in calculating the resistivities in Eq. 3.12 which corresponds to the effective length of cable over which appreciable coupling occurs should be less than or equal to 225 km. As mentioned above, 200 km has been chosen to reflect a nominal width for the continental shelf. The 225 km cable actually ended part way down the slope from the continental slope to the abyssal plain of the ocean bottom.

Figs. 3.19a,b exhibit the phases of  $\alpha_D(\omega)$  for the TAT-6 complete data set at 225 and 3140 km. Again, good correlations are seen in the nearly constant phases out to around 0.03-0.04 Hz. Similar results hold for the phases of  $\alpha_H(\omega)$  and  $\alpha_Z(\omega)$  shown in Figs. 3.20a,b and Figs. 3.21a,b.

The transfer functions from the TAT-7 data are shown in Figs. 3.22-3.24. Figs. 3.22a-c show the magnitude of  $\alpha_D(\omega)$  from the 1500, 3000, and 4400 km lengths. Figs. 3.23a-c and 3.24a-c exhibit the magnitudes of  $\alpha_H(\omega)$  and  $\alpha_Z(\omega)$ . The corresponding phases for  $\alpha_D(\omega)$ ,  $\alpha_H(\omega)$ , and  $\alpha_Z(\omega)$  are presented in Figs. 3.25a-c, 3.26a-c, and 3.27a-c.

The TAT-7 data at 3000 km were actually taken with a 5-sec sampling rate. Some 1500-km TAT-7 data, not exhibited in this report, were also taken with a 5-sec sampling. For this sampling rate the maximum frequency is 0.1 Hz. It would seem from these data that the transfer functions have begun to flatten

out at frequencies 0.05-0.1 Hz. Moreover, the transfer functions of some of the 1500-km 5-sec data exhibited a rise with frequency. However, system problems were present around the time that these 1500-km data were taken, and this situation along with the limited statistics of these 5-sec data, imply that we should not give much emphasis to this rise.

Finally in late 1986, powered TAT-7 data were taken at a faster sampling rate (2 sec/measurement) with the goal of obtaining information at higher frequencies. Fig. 3.28 exhibits the temperature fluctuations inside the Tuckerton station, reflecting the air conditioning cycling. The air conditioning was thus a constant problem. Hence, these powered TAT-7 data could not be regarded as reliable due to the noise introduced by the air conditioning system, and these data were therefore not used for further consideration.

### 3.5 - RESULTS FOR TAT-4 DATA AT FASTER SAMPLING RATE

The partial unpowered TAT-4 system was measured at the same time in late 1986 as the powered TAT-7 mentioned above, also using the faster sampling rate (2 sec/measurement).

Figs. 3.29a-c exhibit the resulting effective resistivities  $\rho_D$ ,  $\rho_H$ , and  $\rho_Z$  assuming an effective length of 25 km for the partial TAT-4 system. Data for a two hour segment are plotted. Two hours of these data, measured with a sampling rate of 2 sec/measurement, have the same number of data points as 10 hours of data with the sampling rate of 10 sec/measurement. The characteristic drop-off with frequency is seen here out to the 0.05-0.1 Hz range of the other measurements.



Figs. 3.30a-c exhibit the magnitude squared coherences for this data segment. The small values of these quantities past around 0.05 Hz indicate that noise becomes a problem for frequencies higher than this value.

Figs. 3.31a-c exhibit the data for one day. Here, the data for each two hour segment were first smoothed using a moving window technique in the time [1]. Afterwards, the data for all two hour segments in the day were averaged. As before, this latter averaging was done separately for the real and imaginary parts of the transfer functions. Equal weights were given to each segment. Finally the averaged effective resistivities were calculated from these (doubly) averaged transfer functions. It is seen that these results seem to indicate a further drop-off of the effective resistivities even past 0.1 Hz to very low values at 0.25 Hz, on the order of 0.001 ohm-m, or about an order of magnitude below the effective resistivities indicated by the unsmoothed 2 hour plots of Figs. 3.29. Figs. 3.32a-c show the same quantities for the next day (day 280); it is seen that the results seem qualitatively reproducible from one day to the next.

Figs. 3.33a-c exhibit data from a two hour segment of another day, this time averaged with a more sophisticated moving window average technique. The  $\pm 1$  standard deviation levels are also shown. It is seen that the results for these averaged effective resistivities seem to level off around 0.001 ohm-m, consistent with Figs. 3.29. Figs. 3.34a-c exhibit the corresponding smoothed transfer function phases. The phases seem roughly constant out to 0.05-0.1 Hz.

## REFERENCES (Chapter 3)

1. D. J. Thomson, private communication. The data processing was performed by D. R. Macauley, A. Farrow, and C. G. MacLennan.
2. D. J. Thomson, "Spectrum Estimation and Harmonic Analysis", IEEE Proceedings, Vol. 70, p 1055 (1982).
3. J. J. Dongarra, J. R. Bunch, C. B. Moler, G. W. Stewart "LINPACK Users' Guide" Siam, 1979.
4. A. D. Chave, D. J. Thomson, and M. E. Anders, in press, J. Geoph. Res.

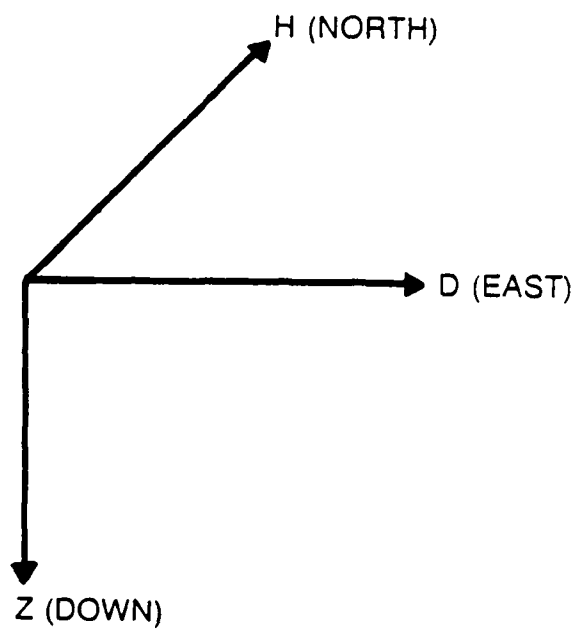


Fig. 3.1. Coordinate system for the magnetic field. The components H, D, and Z point in the +North, +East, and down directions respectively.

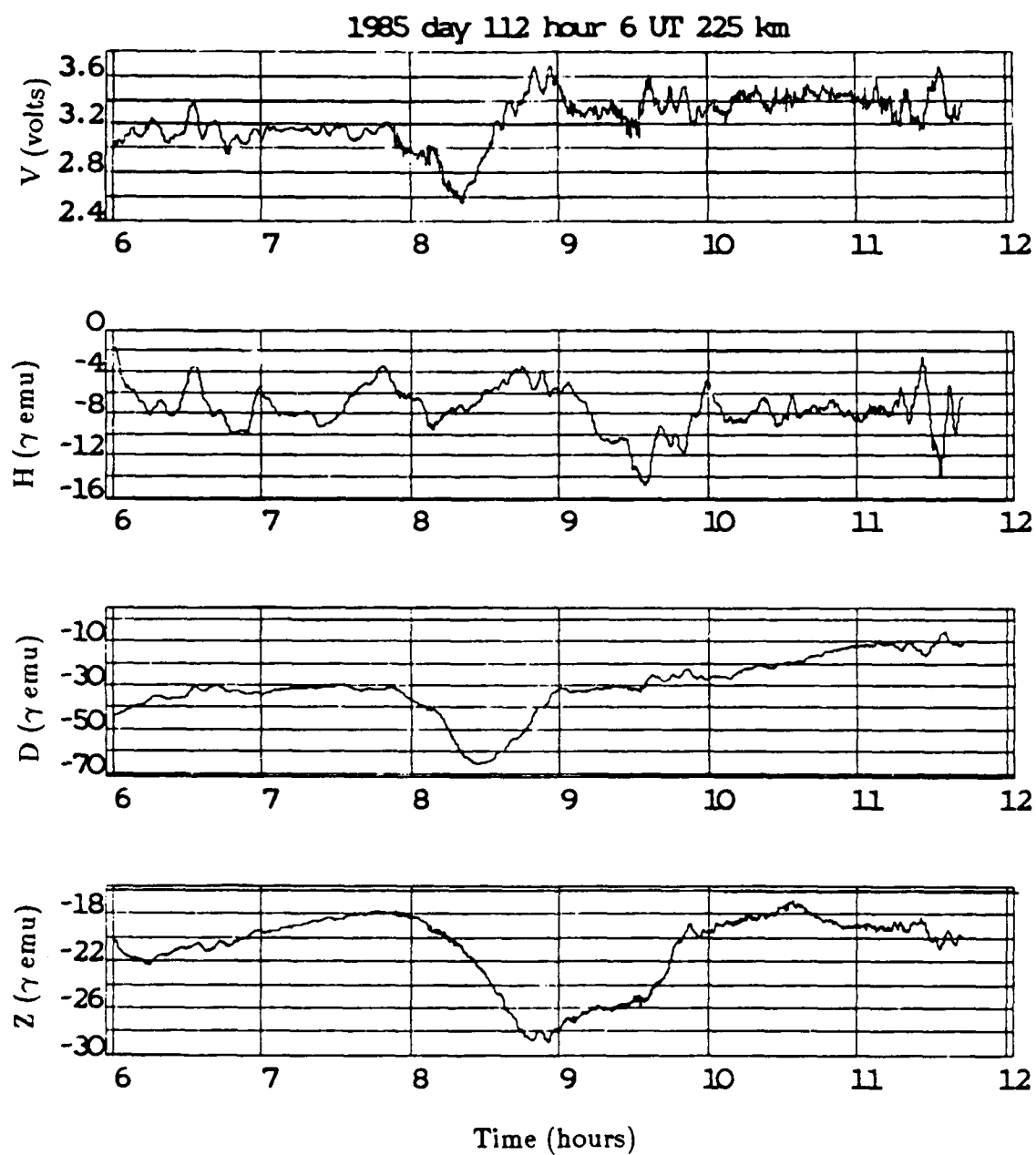


Fig. 3.2. Time series for a typical six-hour segment for the cable voltage  $V$  and the ambient magnetic field components  $H$ ,  $D$ , and  $Z$  for TAT-6 at 225 km.

Edited TAT-6 D (+East), 10 second, 1985.112.6-12, 225km

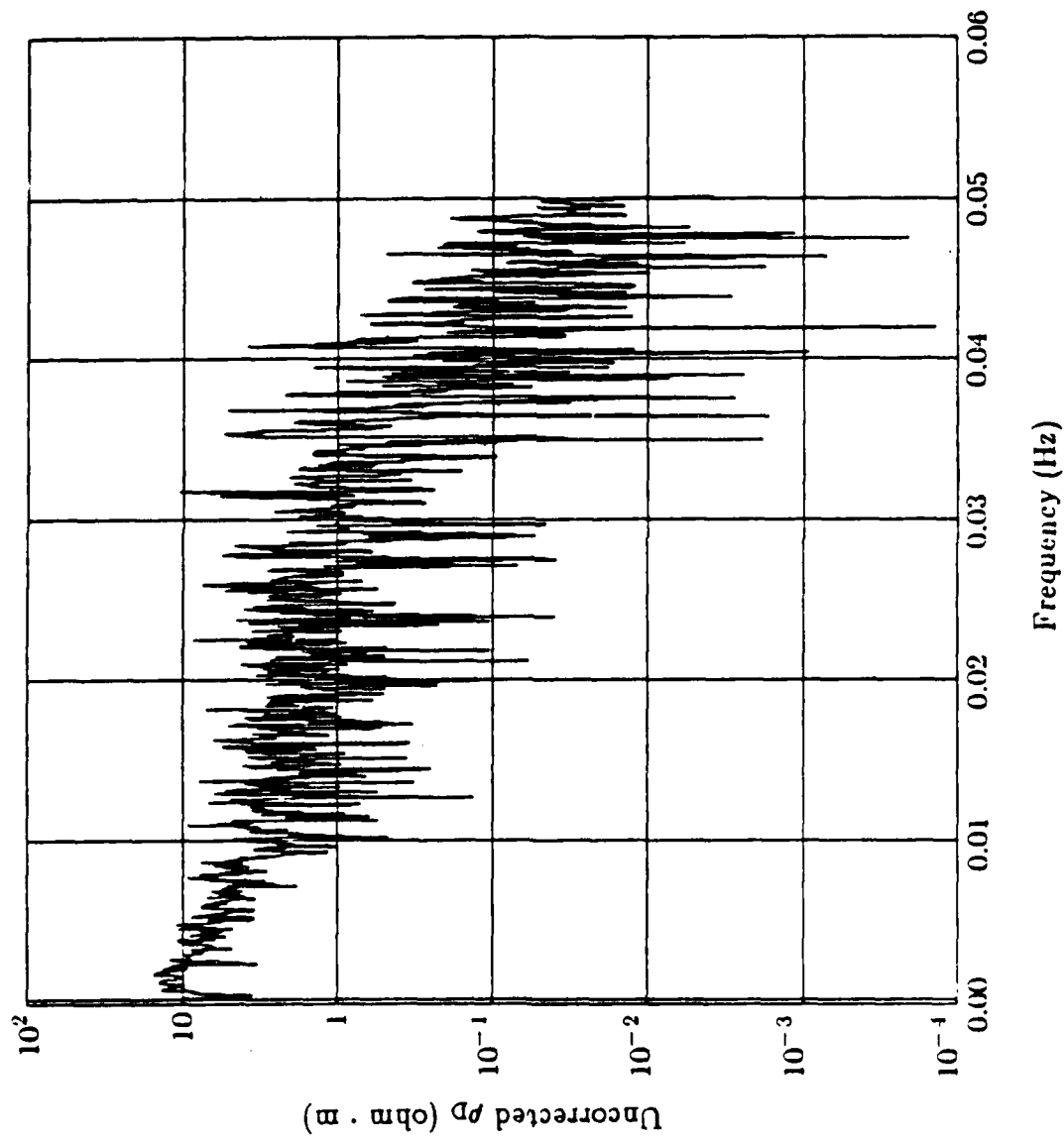


Fig. 3.3a. Effective resistivity  $\rho_D$  (6 hrs, TAT-6 at 225 km).

Edited TAT-6 H (+North), 10 second, 1985.112.6-12, 225m

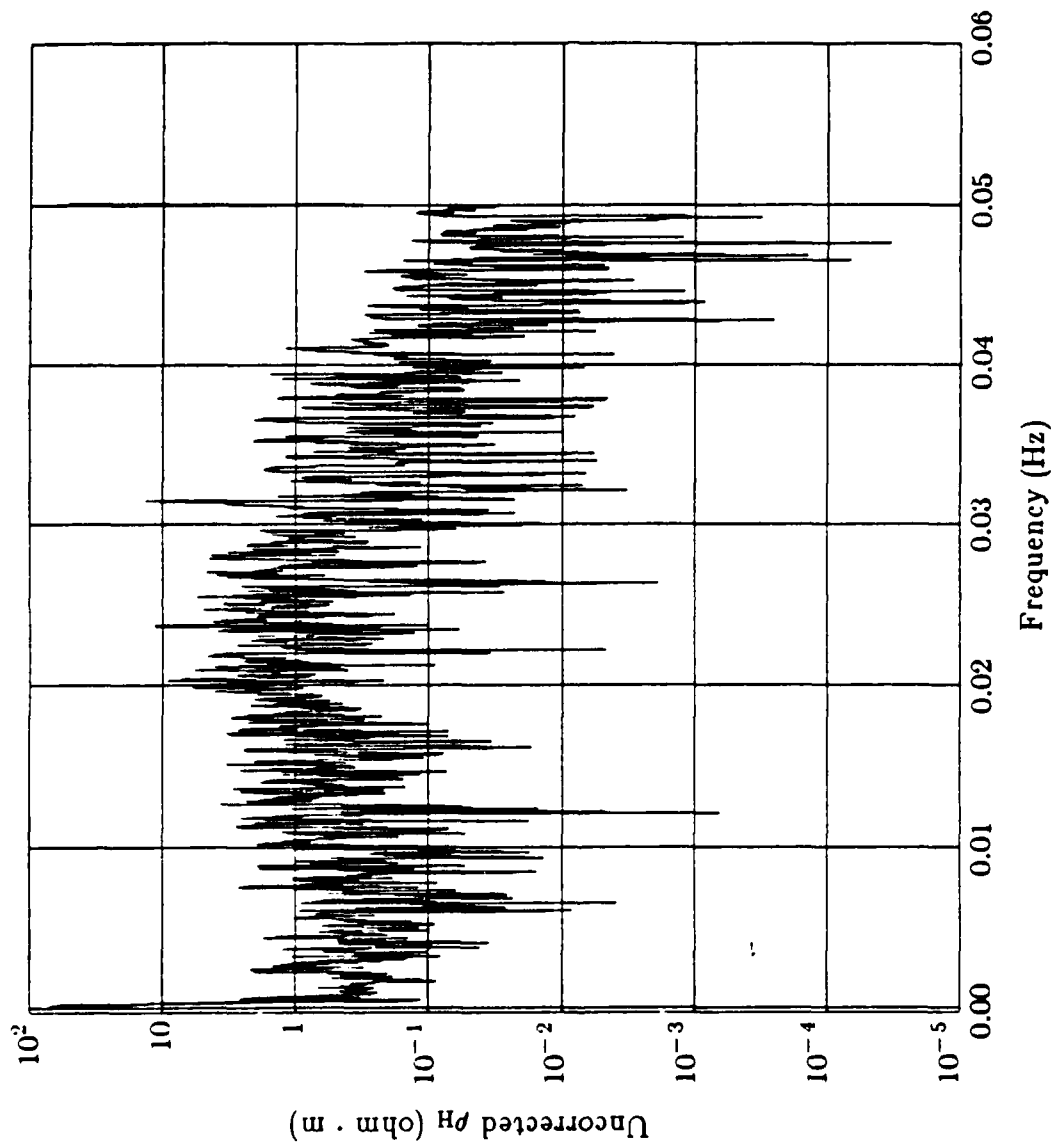


Fig. 3.3b. Effective resistivity  $\rho_H$  (6 hrs, TAT-6 at 225 km).

Edited TAT-6 Z (+Down), 10 second, 1985.112.6-12, 225km

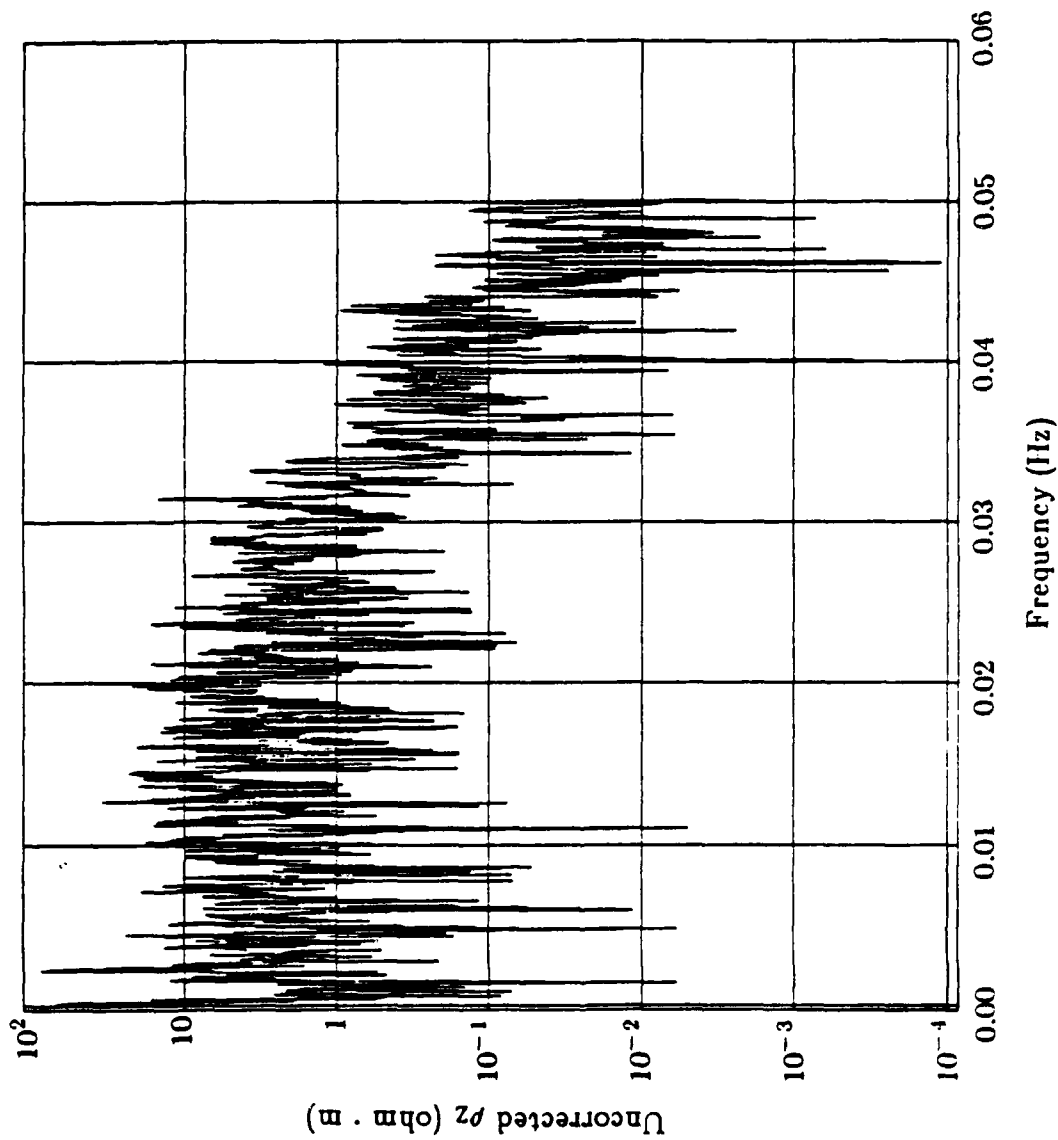


Fig. 3.3c. Effective resistivity  $\rho_z$  (6 hrs, TAT-6 at 225 km).

Edited TAT-6 D (+East), 10 second, 1985.112.6-12, 225km

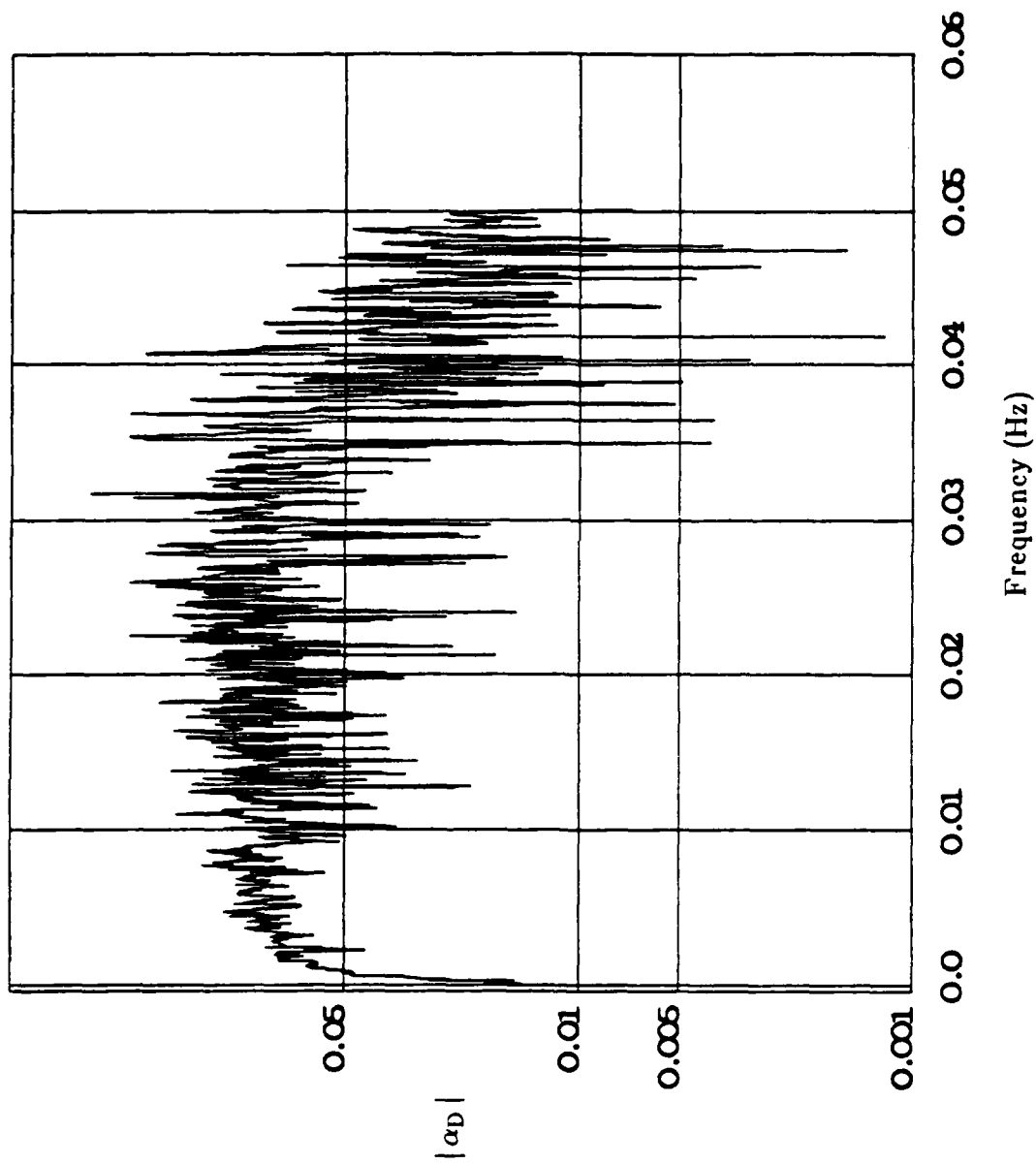


Fig. 3.4a. Magnitude of transfer function  $\alpha_D$  (6 hrs, TAT-6 at 225 km).



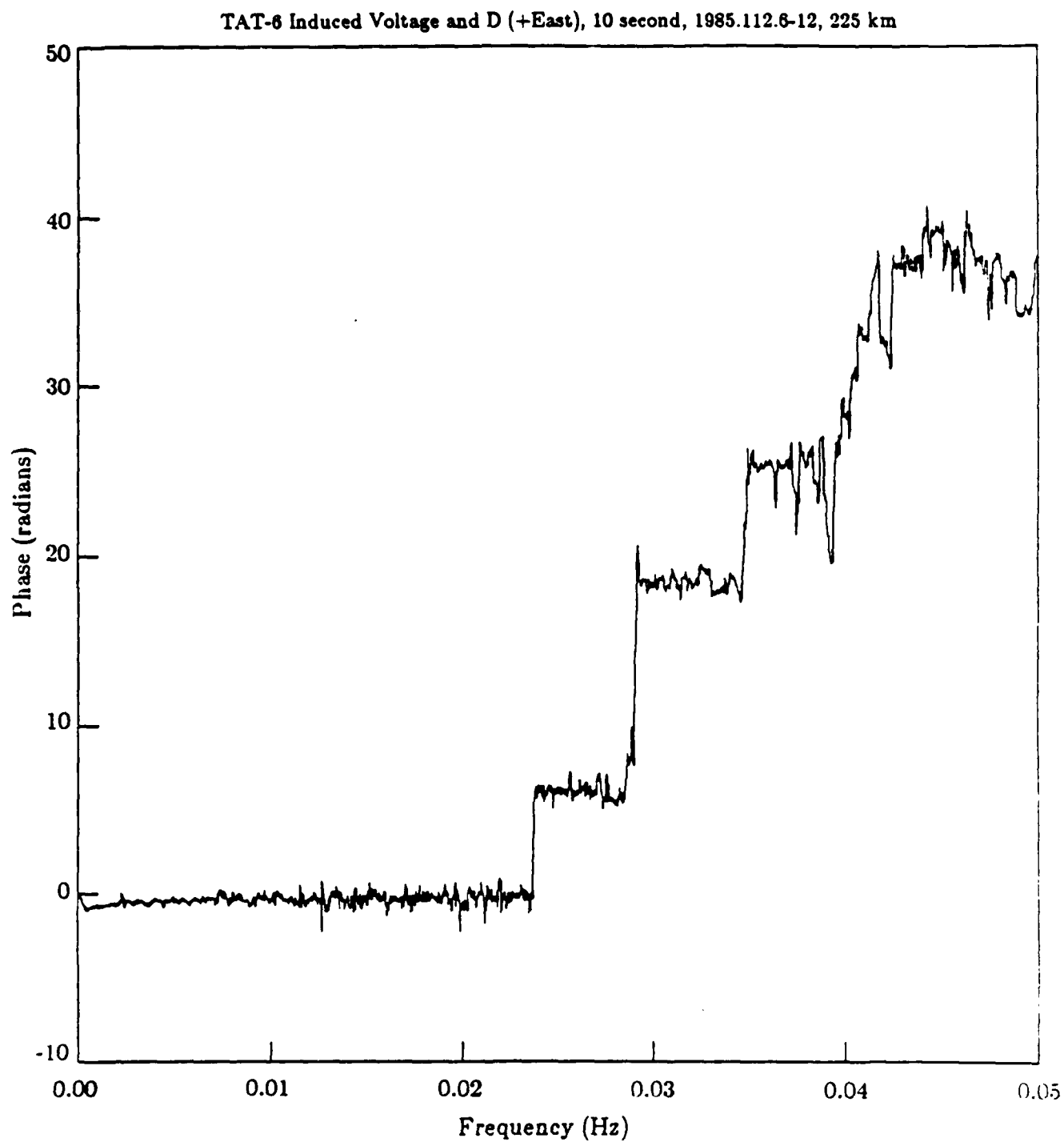


Fig. 3.4b. Phase of transfer function  $\alpha_D$  (6 hrs, TAT-6 at 225 km).

Edited TAT-6 D (+East), 10 second, 1985.112.6-12, 225km

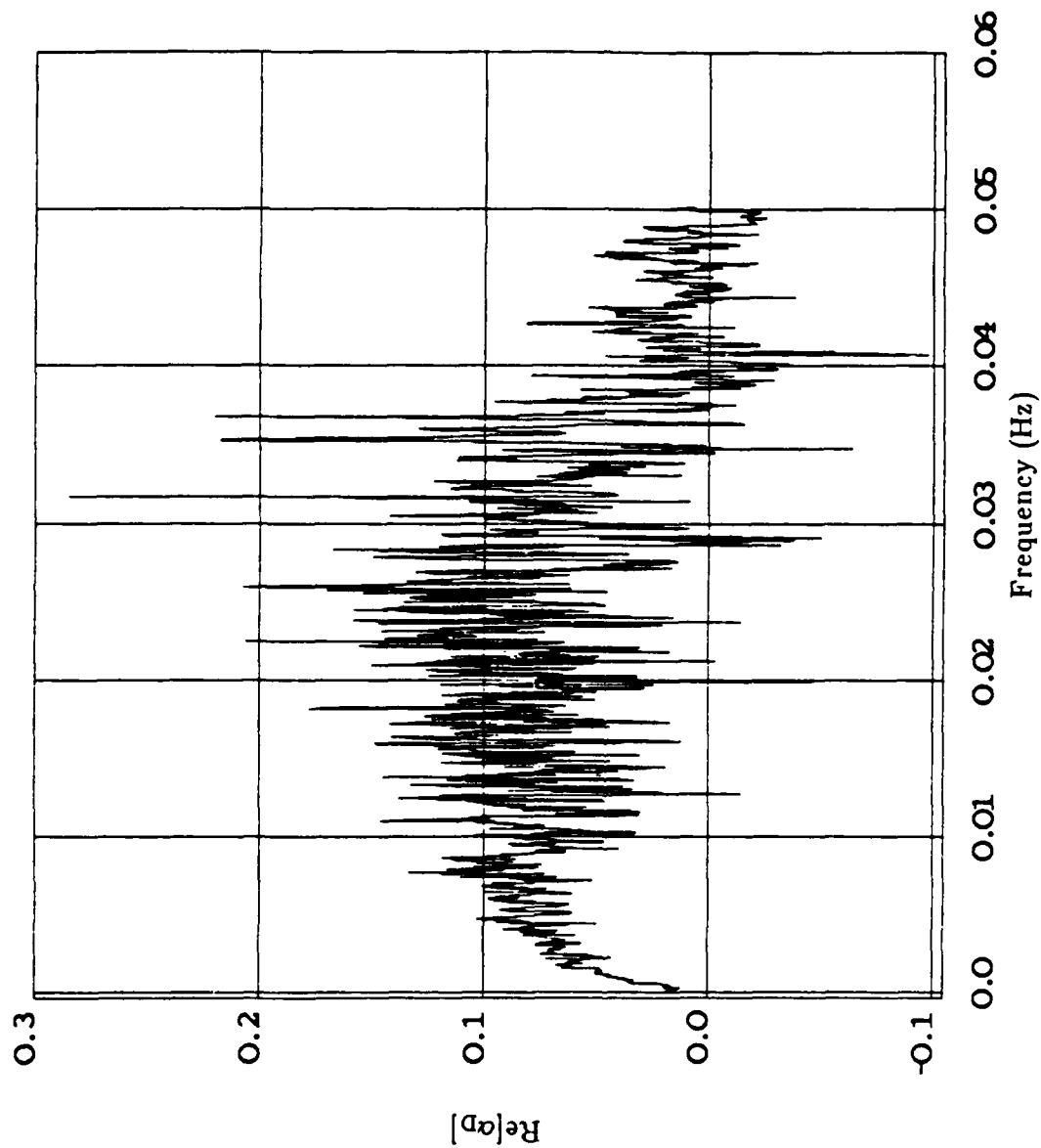


Fig. 3.4c. Real part of transfer function  $\alpha_D$  (6 hrs, TAT-6 at 225 km).

Edited TAT-6 D (+East), 10 second, 1985.112.6-12, 225km

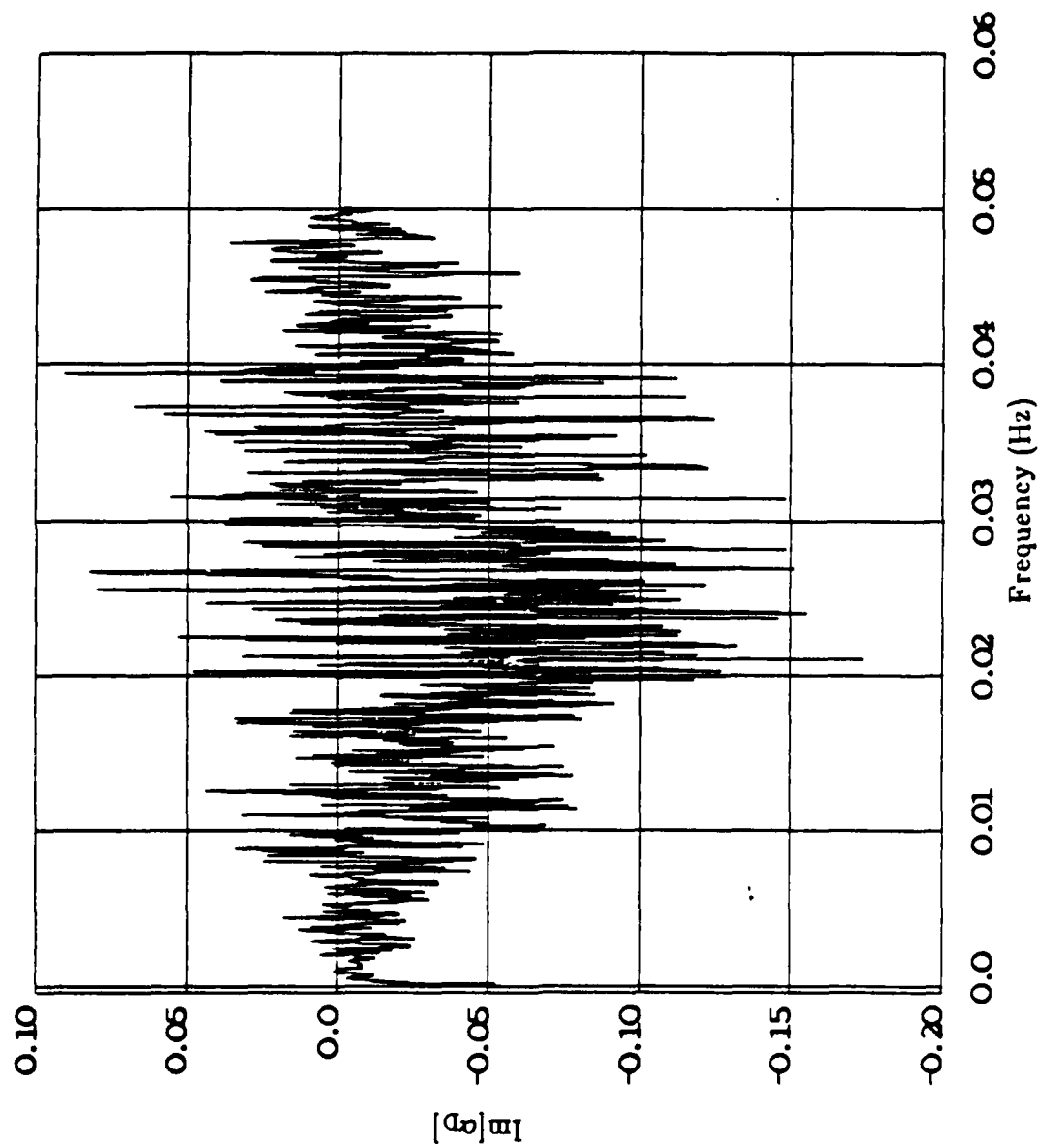


Fig. 3.4d. Imaginary part of transfer function  $\alpha_D$  (6 hrs, TAT-6 at 225 km).

Edited TAT-6 H (+North), 10 second, 1985.112.6-12, 225km

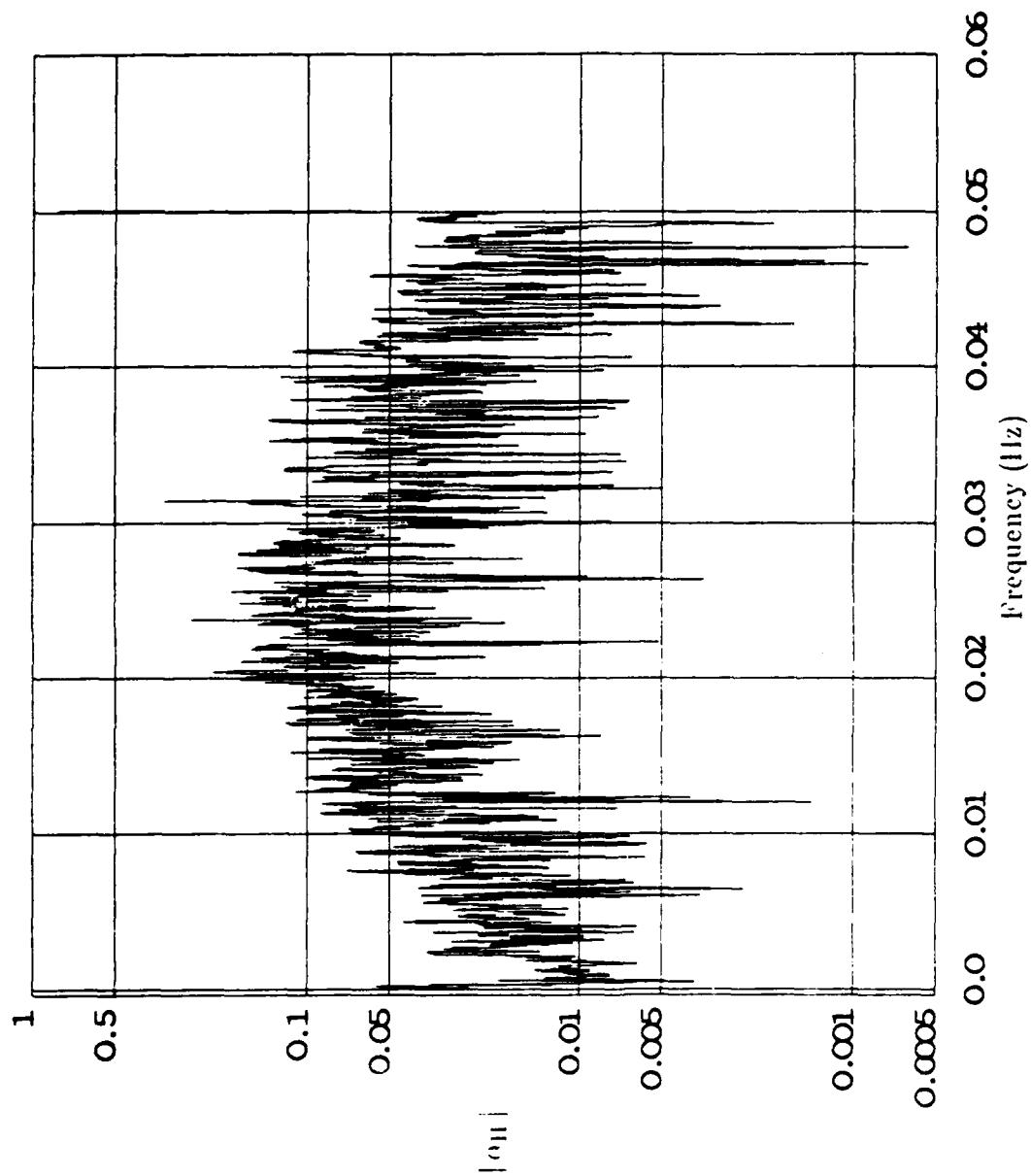


Fig. 3.5a. Magnitude of transfer function  $a_H$  (6 hrs, TAT-6 at 225 km).

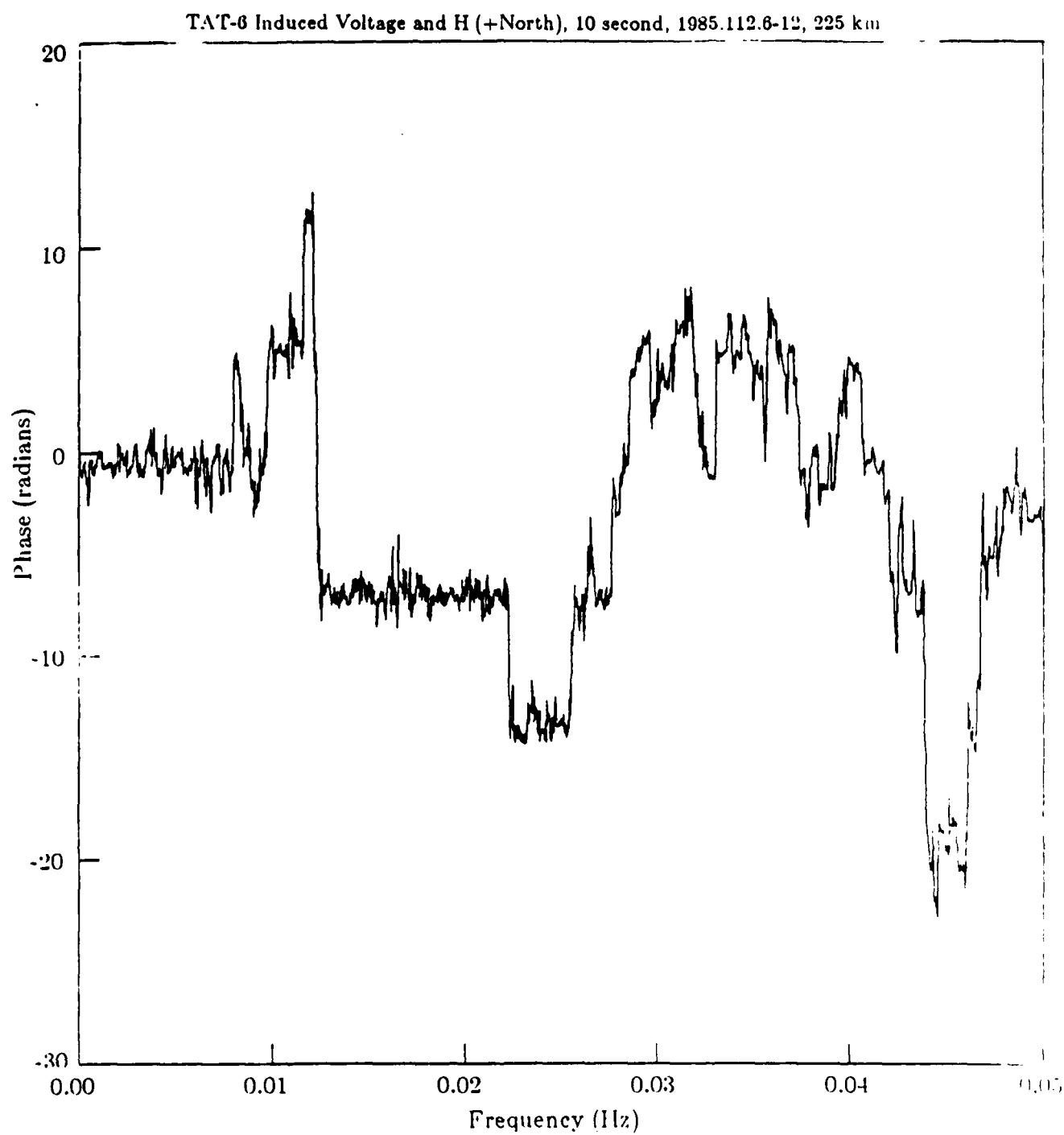


Fig. 3.5b. Phase of transfer function  $\alpha_H$  (6 hrs. TAT-6 at 225 km).

Edited TAT-6 H (+North), 10 second, 1985.112.6-12, 225m

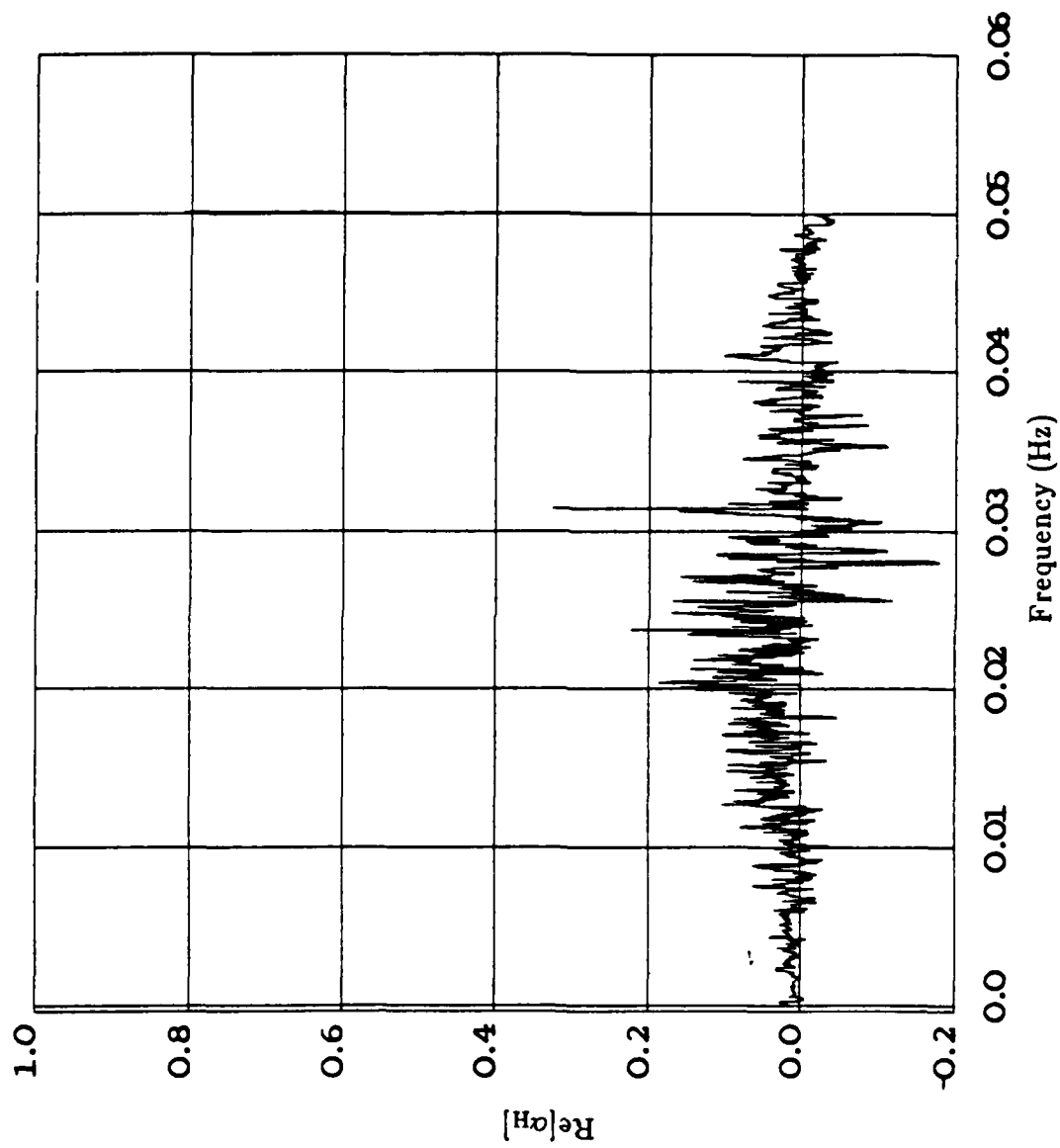


Fig. 3.5c. Real part of transfer function  $\alpha_H$  (6 hrs, TAT-6 at 225 km).

Edited TAT-6 H (+North), 10 second, 1985.112.6-12, 225m

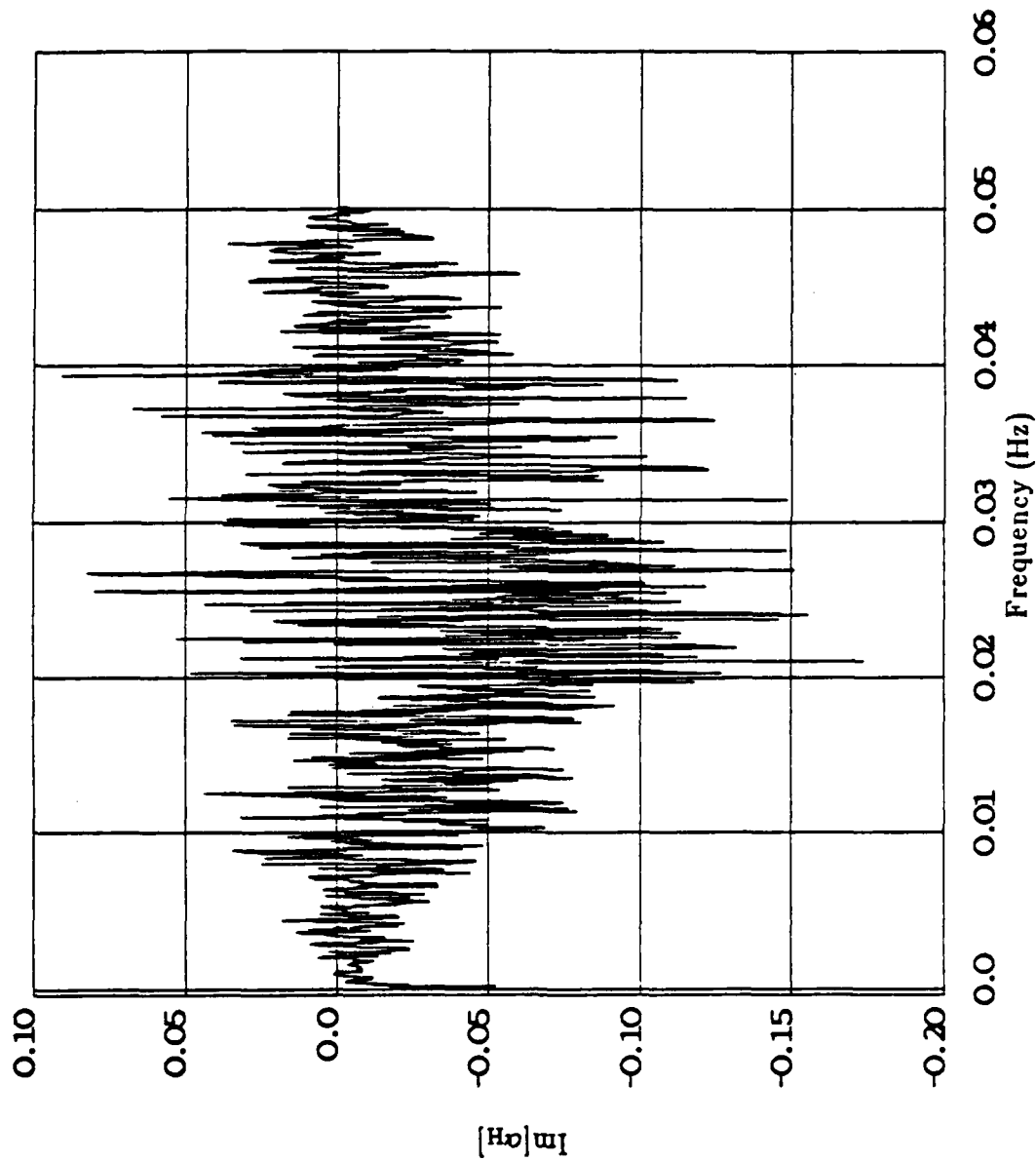


Fig. 3.5d. Imaginary part of transfer function  $\alpha_{11}$  (8 hrs, TAT-6 at 225 km).

Edited TAT-6 Z (+Down), 10 second, 1985.112.6-12, 225km

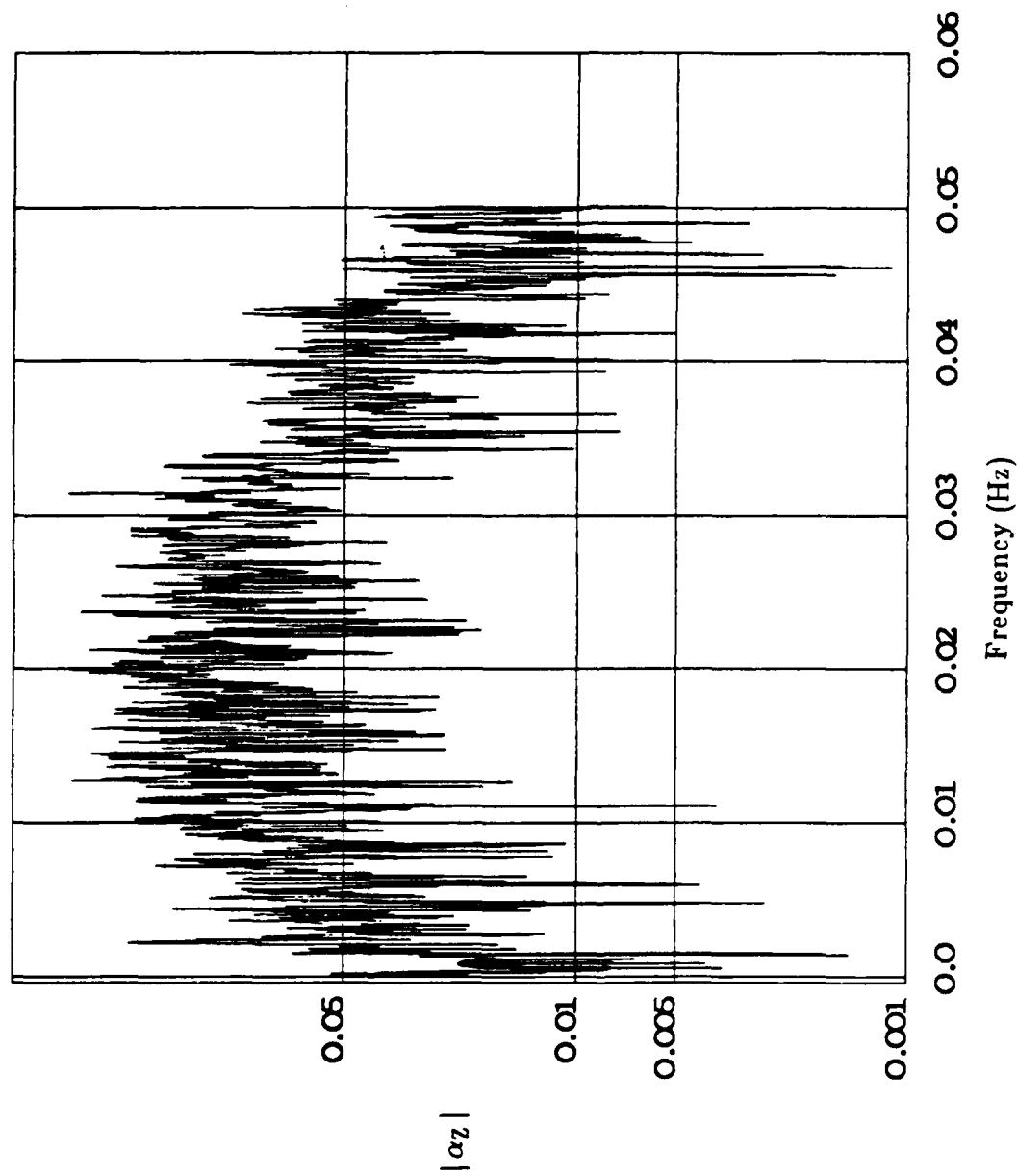


Fig. 3.6a. Magnitude of transfer function  $\alpha_z$  (6 hrs, TAT-6 at 225 km).



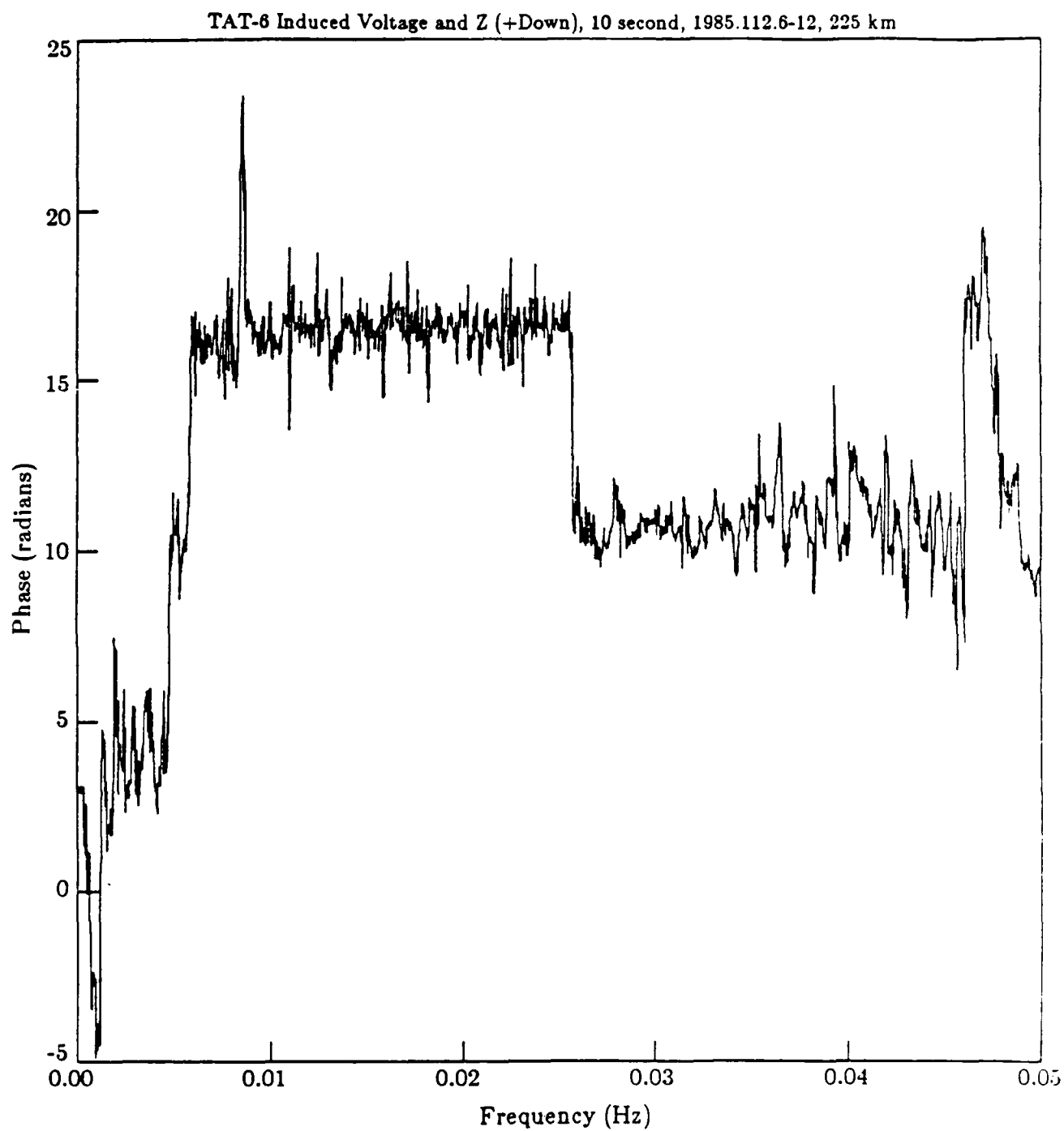


Fig. 3.8b. Phase of transfer function  $\alpha_z$  (6 hrs, TAT-6 at 225 km).

Edited TAT-6 Z (+Down), 10 second, 1985.112.6-12, 225km

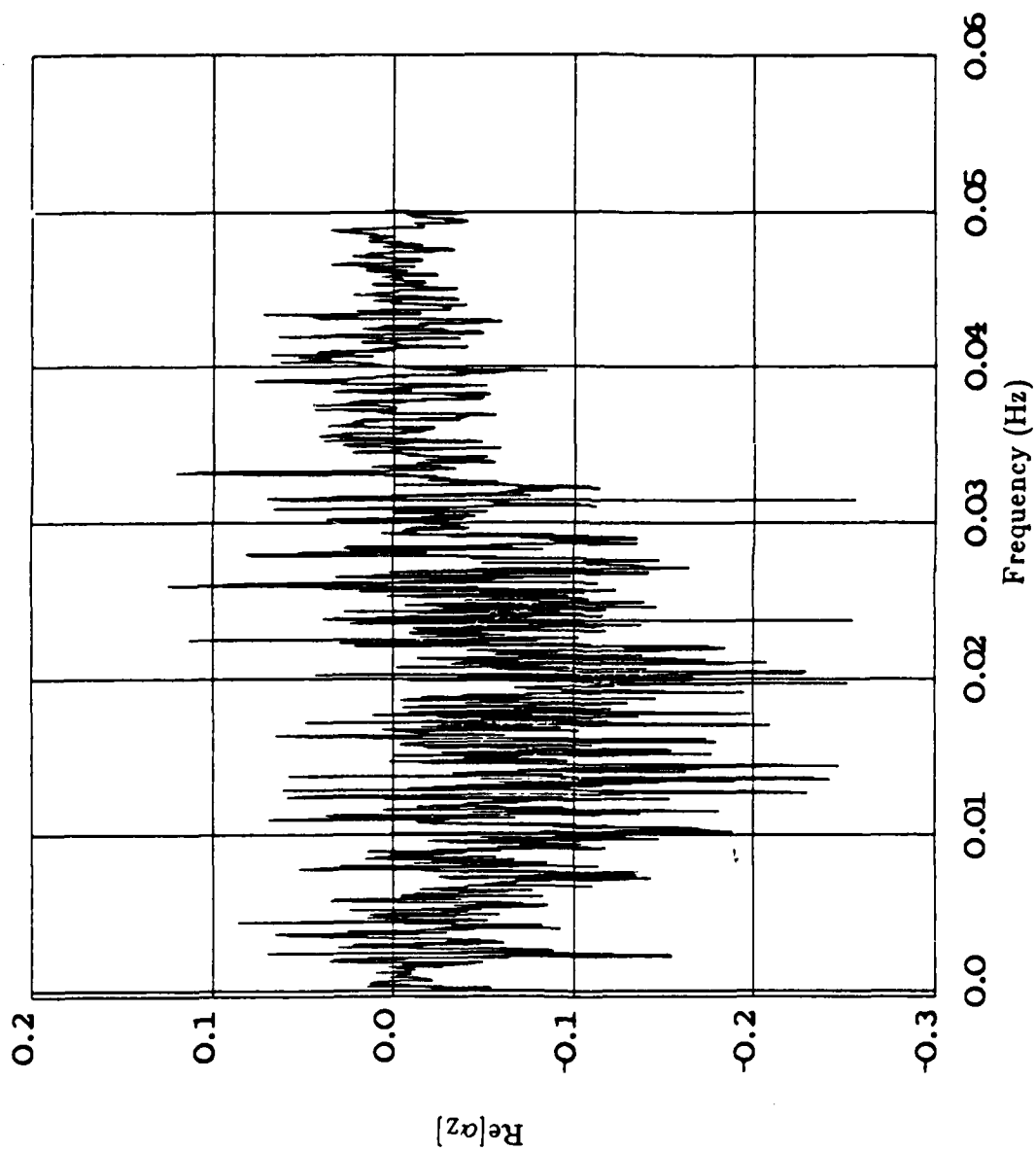


Fig. 3.6c. Real part of transfer function  $\alpha_z$  (6 hrs, TAT-6 at 225 km).

Edited TAT-6 Z (+Down), 10 second, 1985.112.6-12, 225km

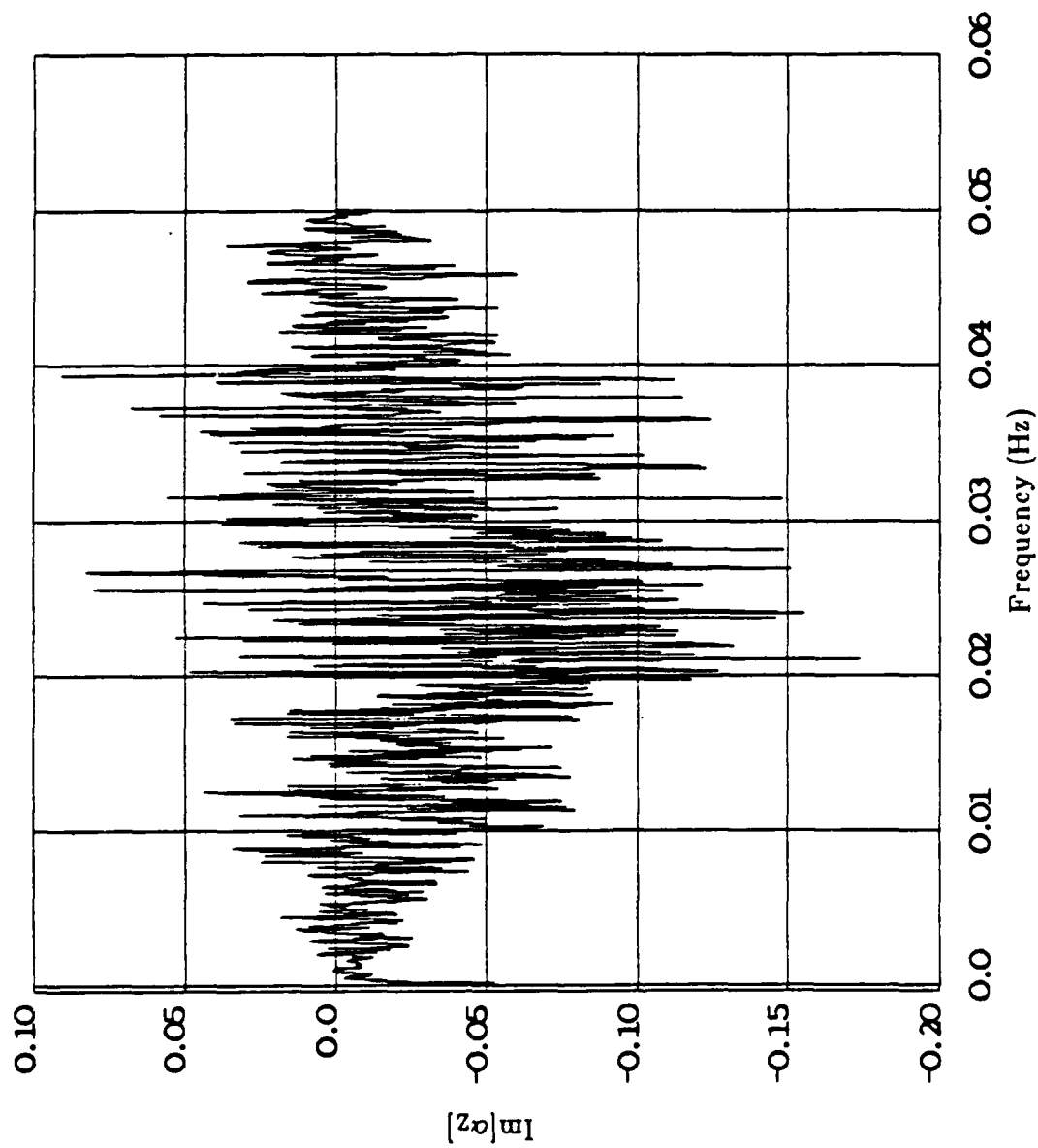


Fig. 3.6d. Imaginary part of transfer function  $\alpha_z$  (6 hrs, TAT-6 at 225 km).

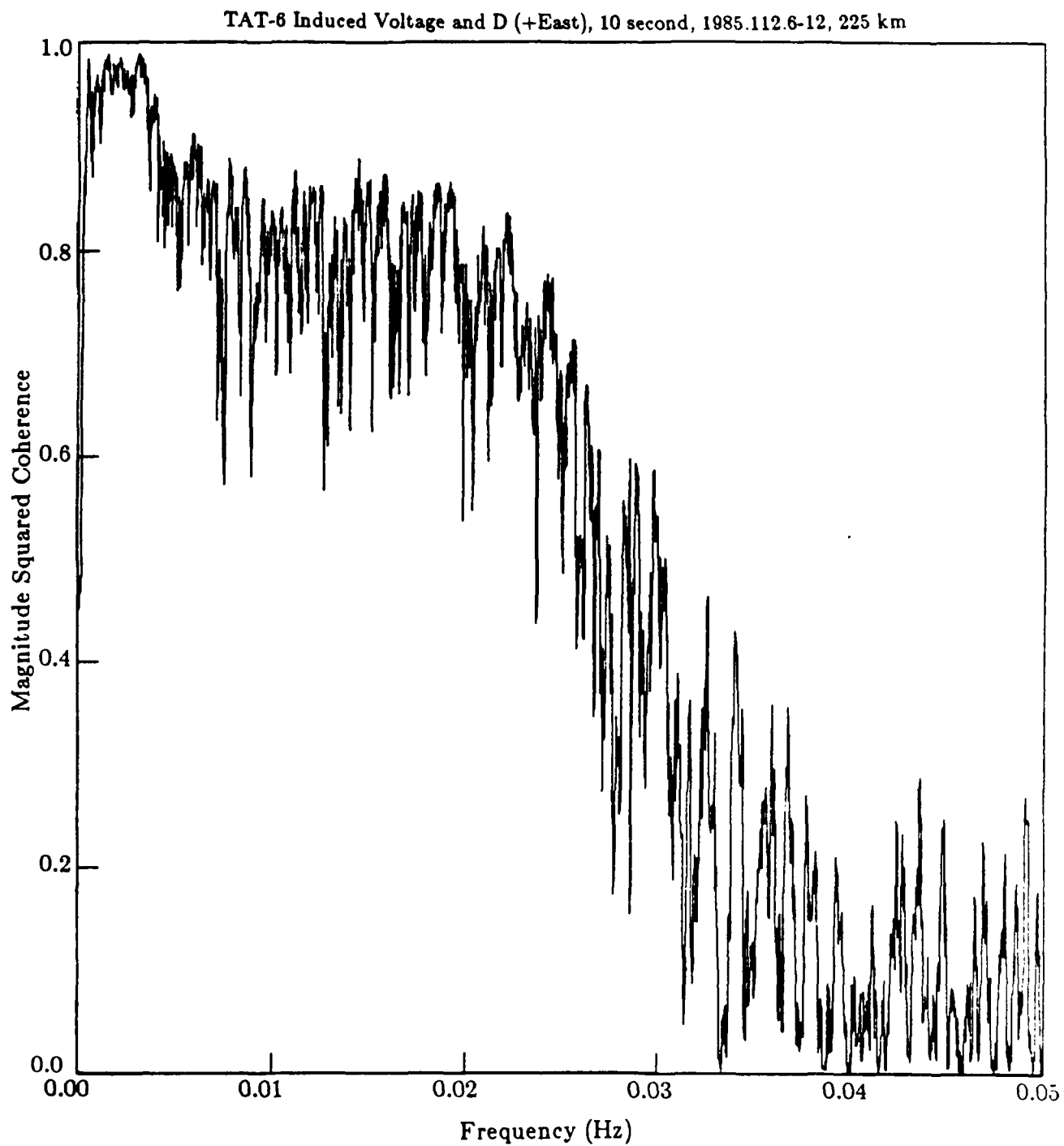


Fig. 3.7a. Magnitude squared coherence for V and D (6 hrs, TAT-6 at 225 km).

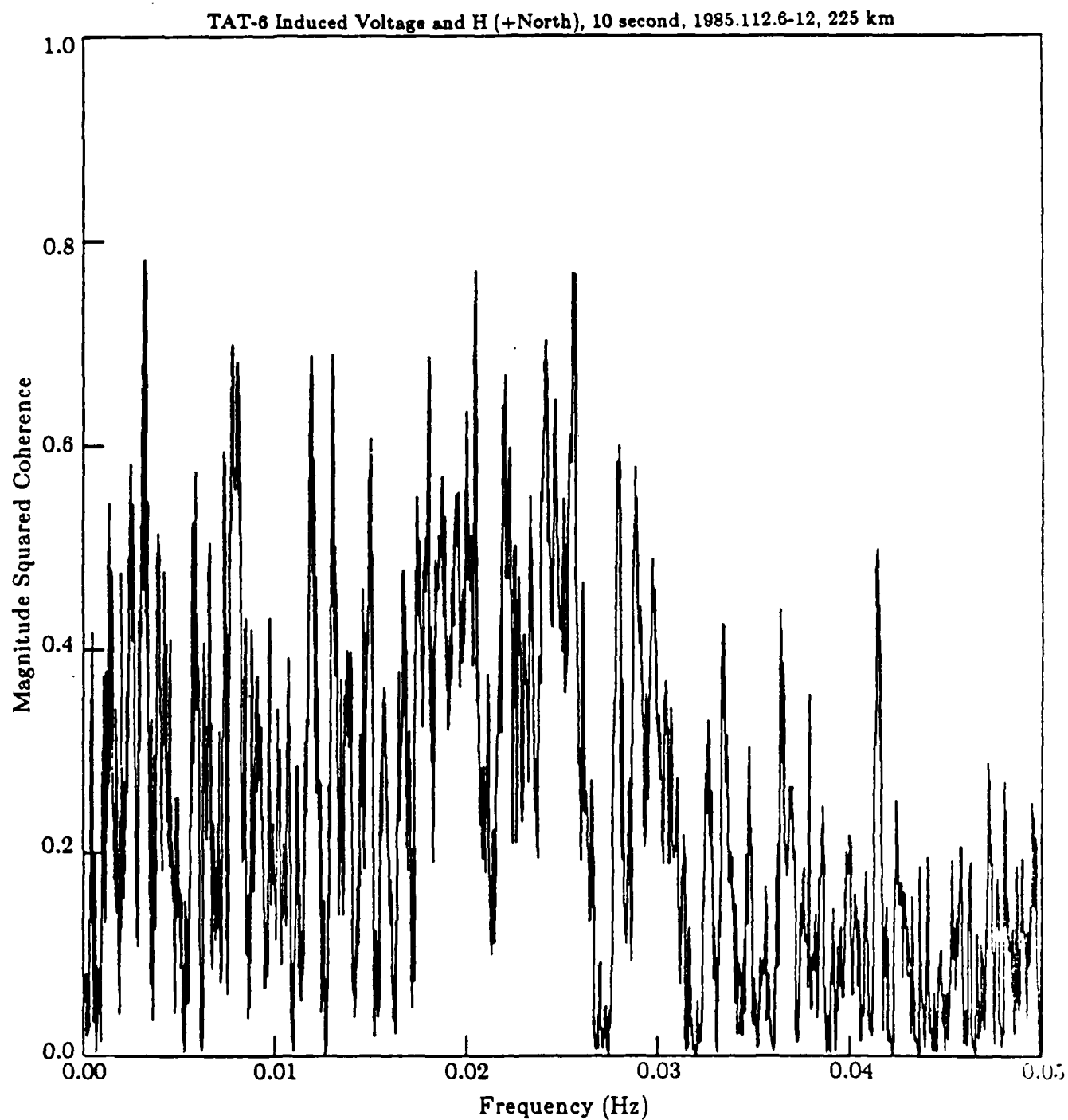


Fig. 3.7b. Magnitude squared coherence for V and H (6 hrs, TAT-6 at 225 km).

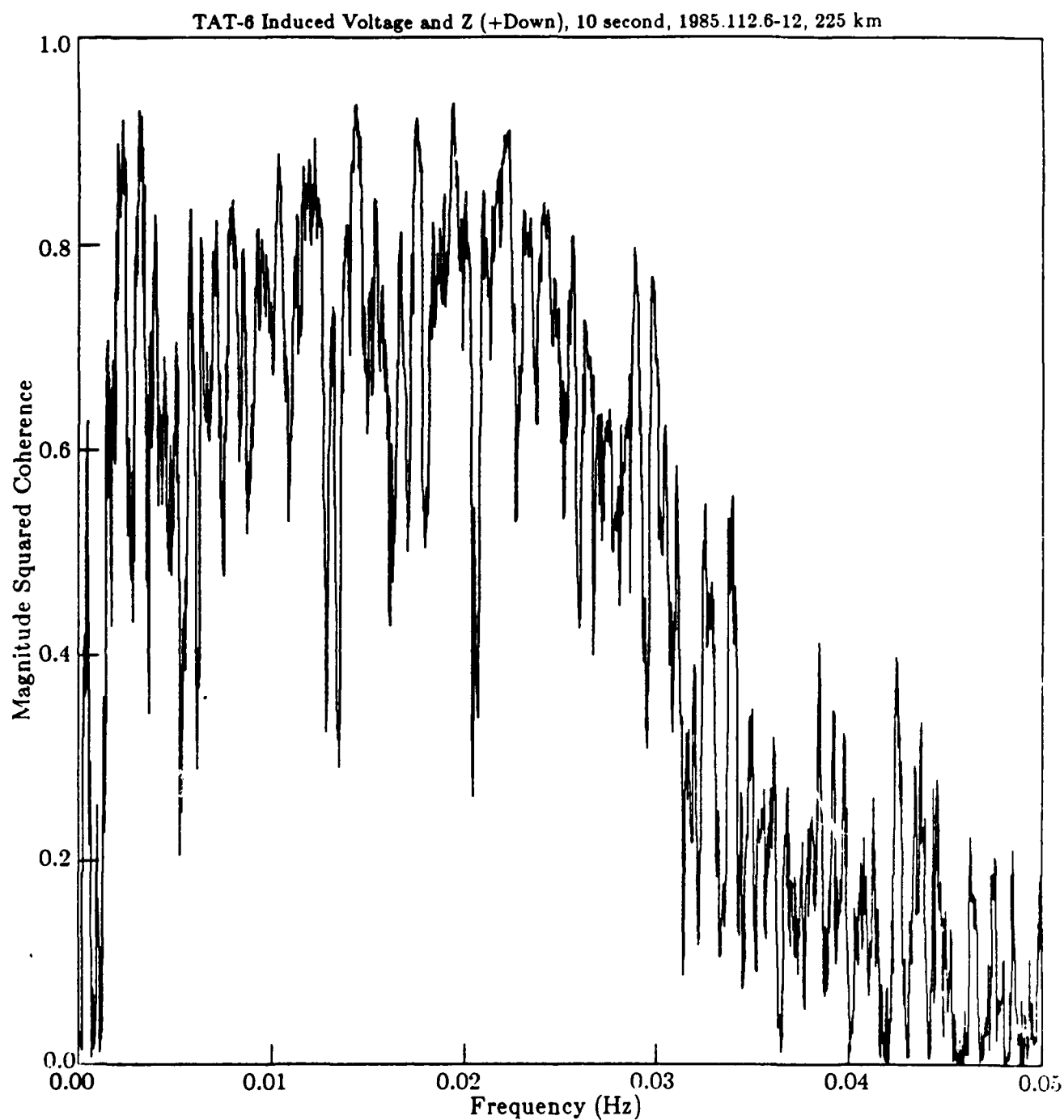


Fig. 3.7c. Magnitude squared coherence for V and Z (6 hrs, TAT-6 at 225 km).

TAT-6 Induced Voltage, 10 second, 1985.112.6-12, 225 km  
Simultaneous Regression of V on H, D, and Z

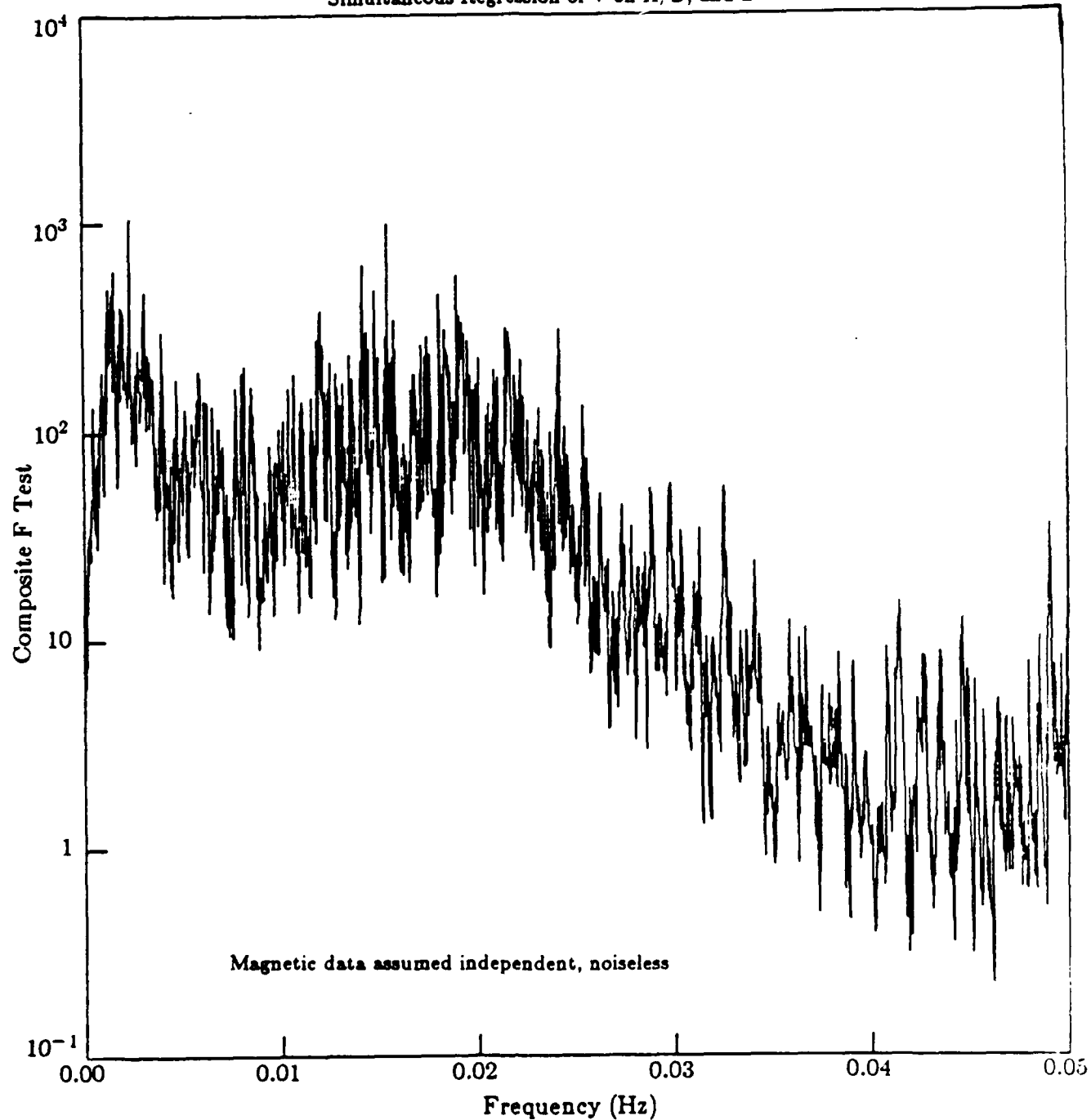


Fig. 3.8. Composite F test (6 hrs, TAT-6 at 225 km).

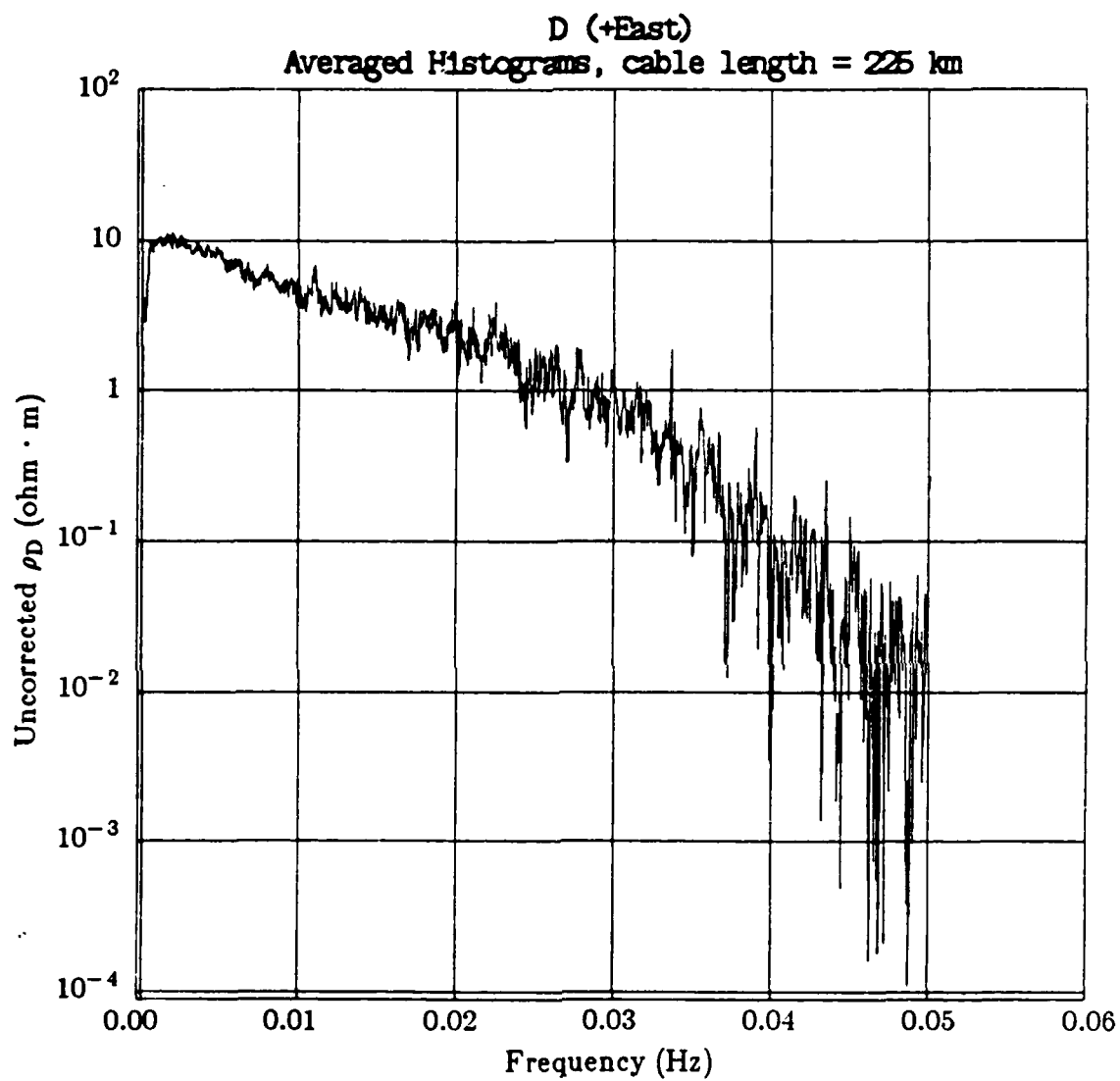


Fig. 3.9a. Effective resistivity  $\rho_D$  for TAT-6 at 225 km, all data.



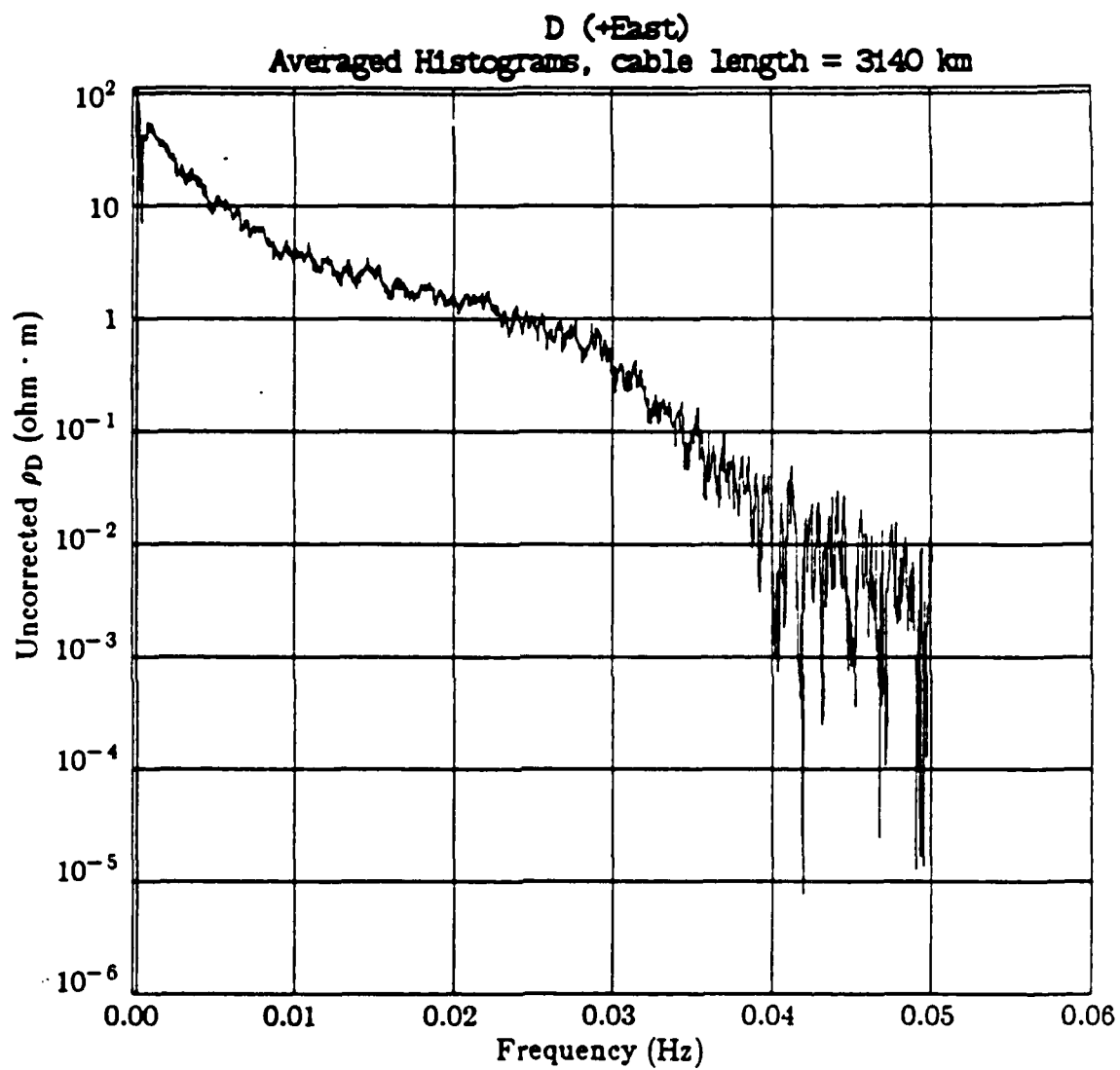


Fig. 3.9b. Effective resistivity  $\rho_D$  for TAT-6 at 3140 km, all data.

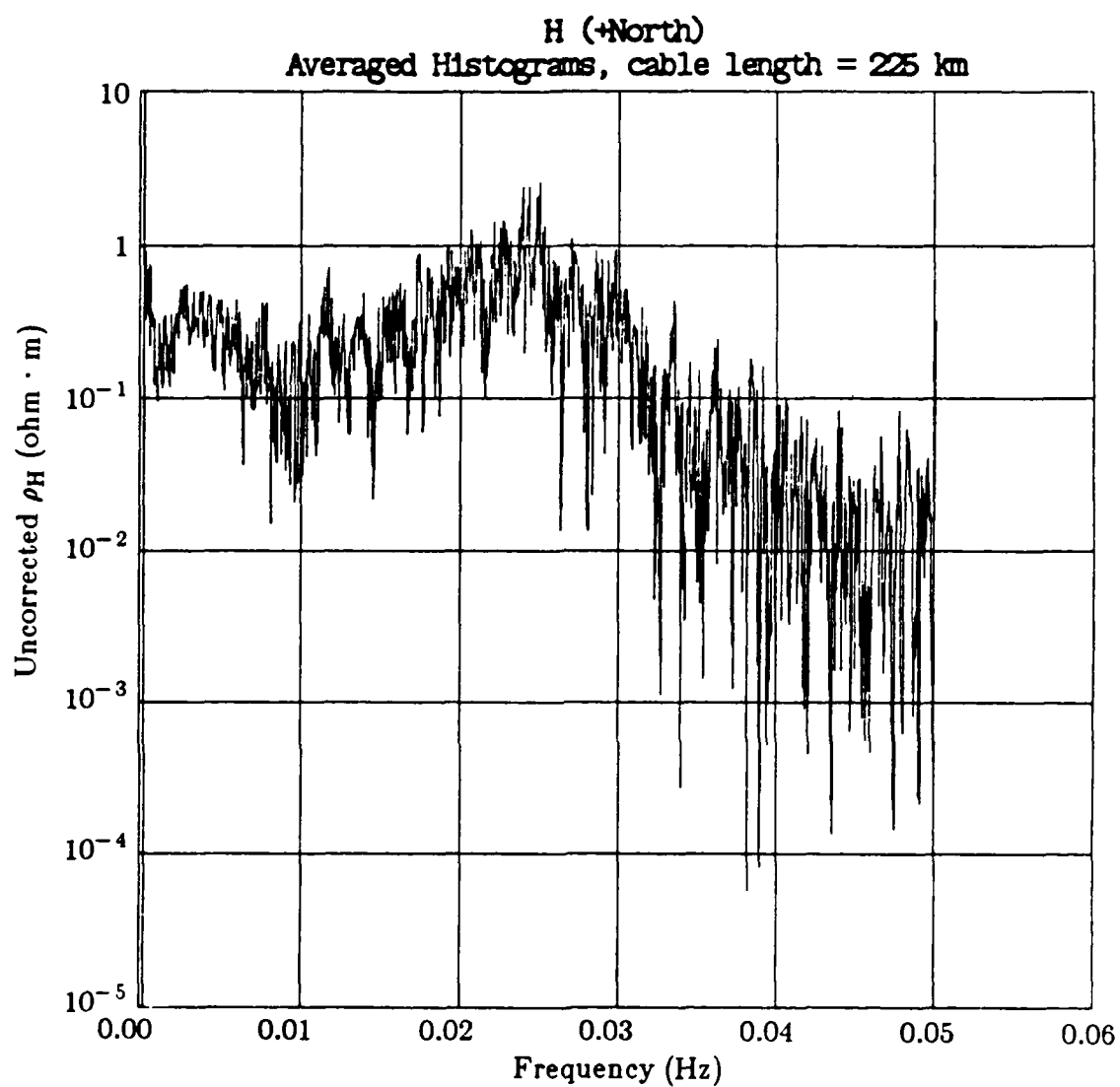


Fig. 3.10a. Effective resistivity  $\rho_H$  for TAT-6 at 225 km, all data.

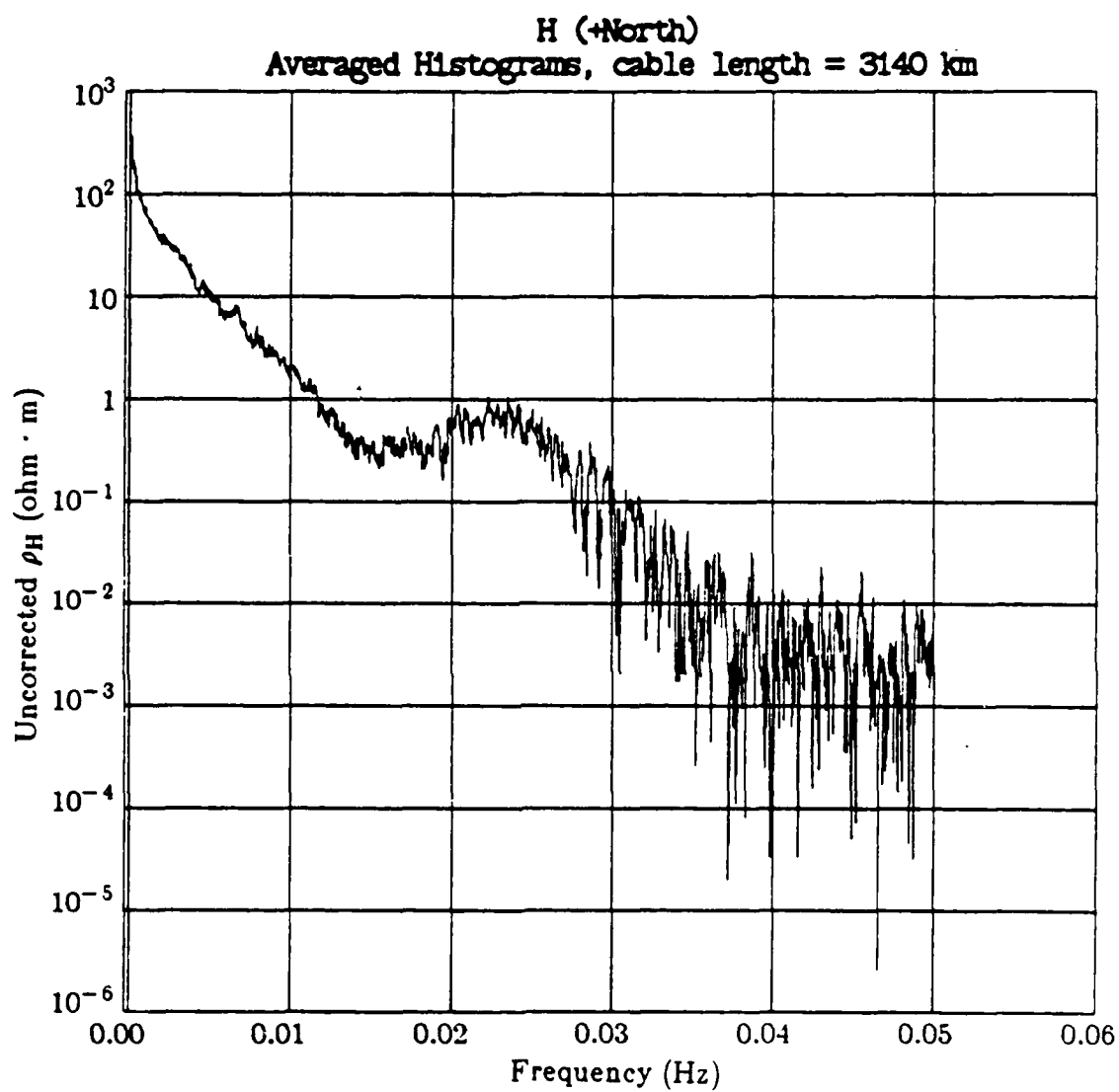


Fig. 3.10b. Effective resistivity  $\rho_H$  for TAT-6 at 3140 km, all data.

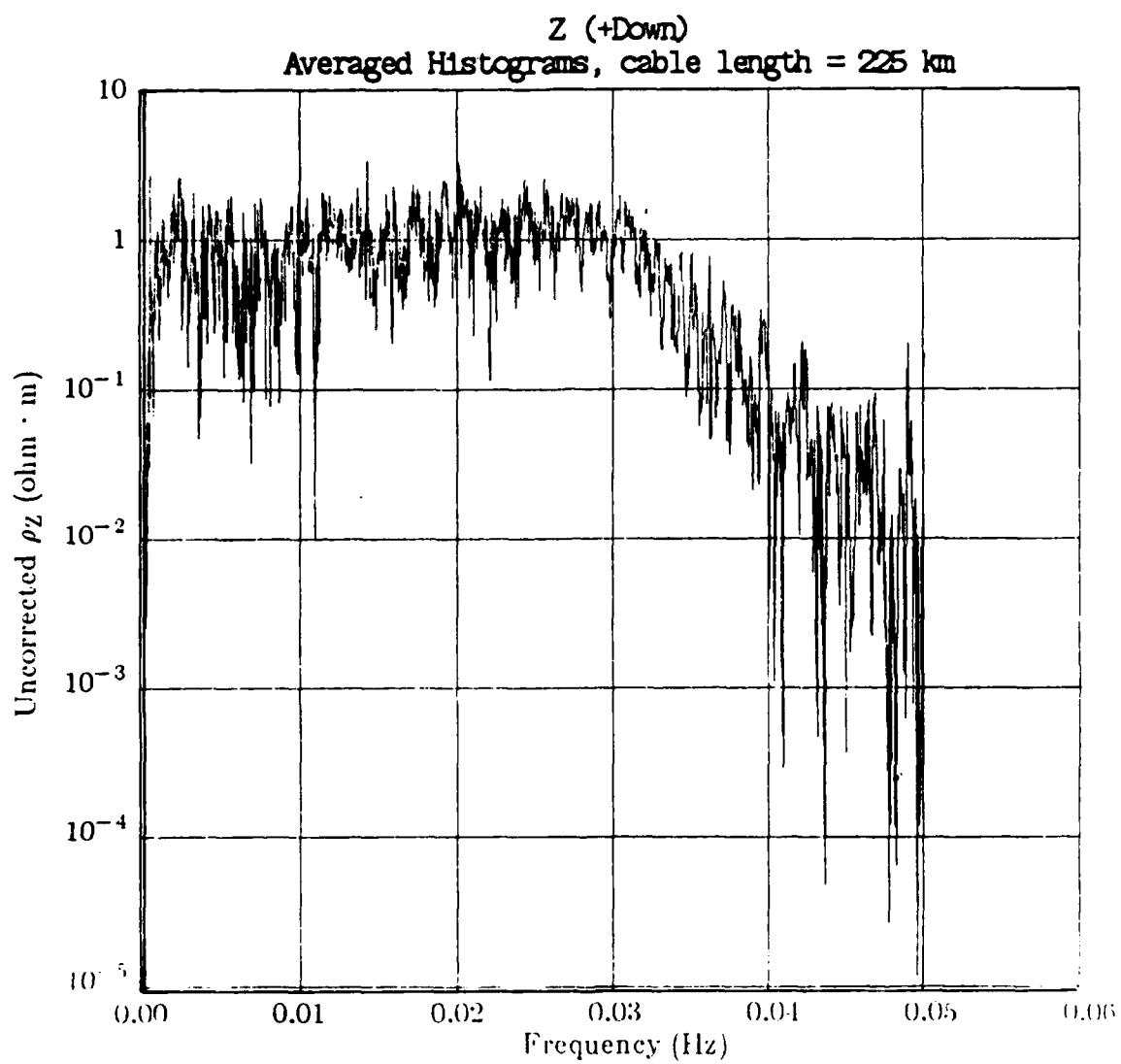


Fig. 3.11a. Effective resistivity  $\rho_z$  for TAT-6 at 225 km. all data.

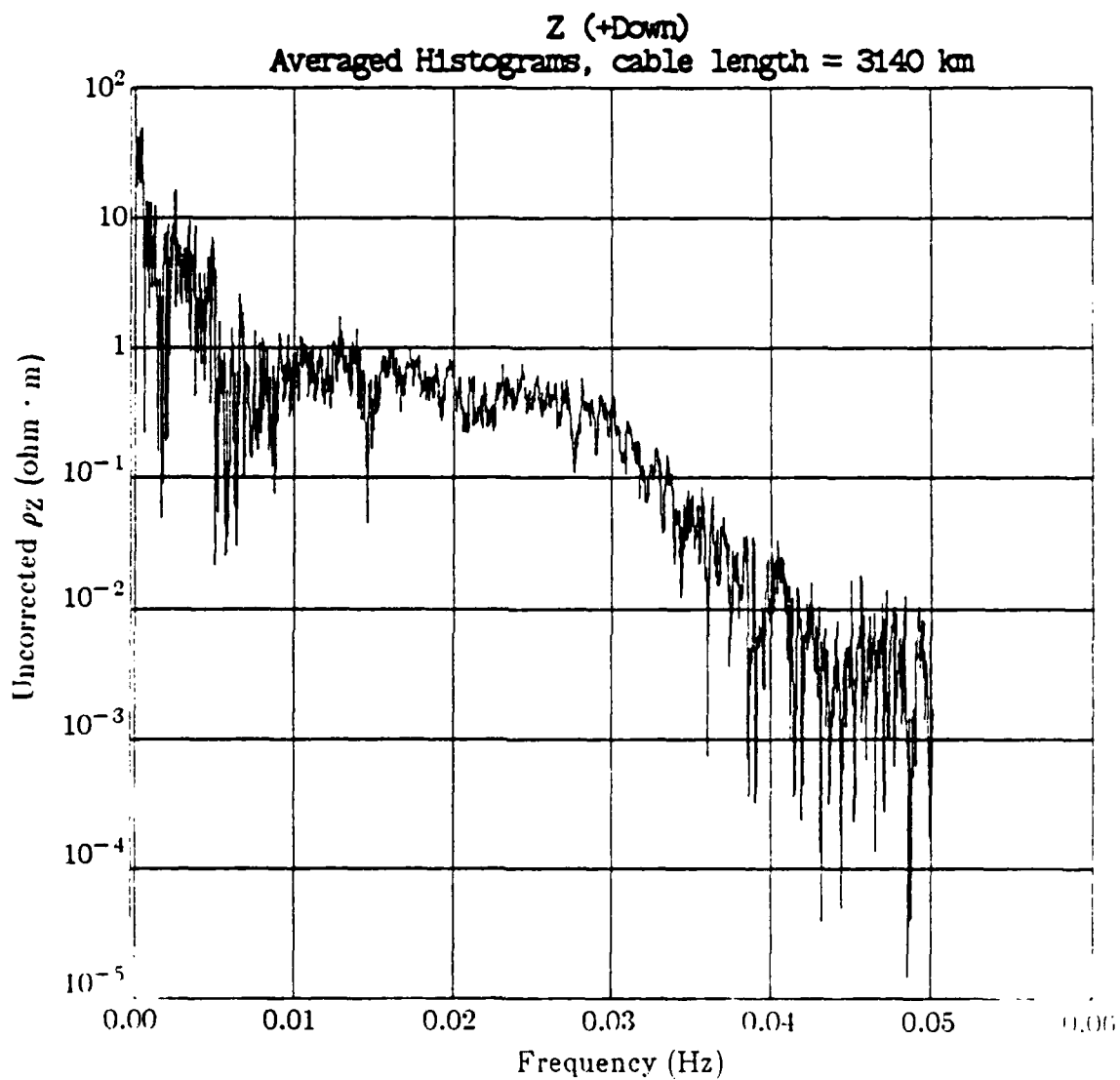


Fig. 3.11b. Effective resistivity  $\rho_z$  for TAT-6 at 3140 km. all data.

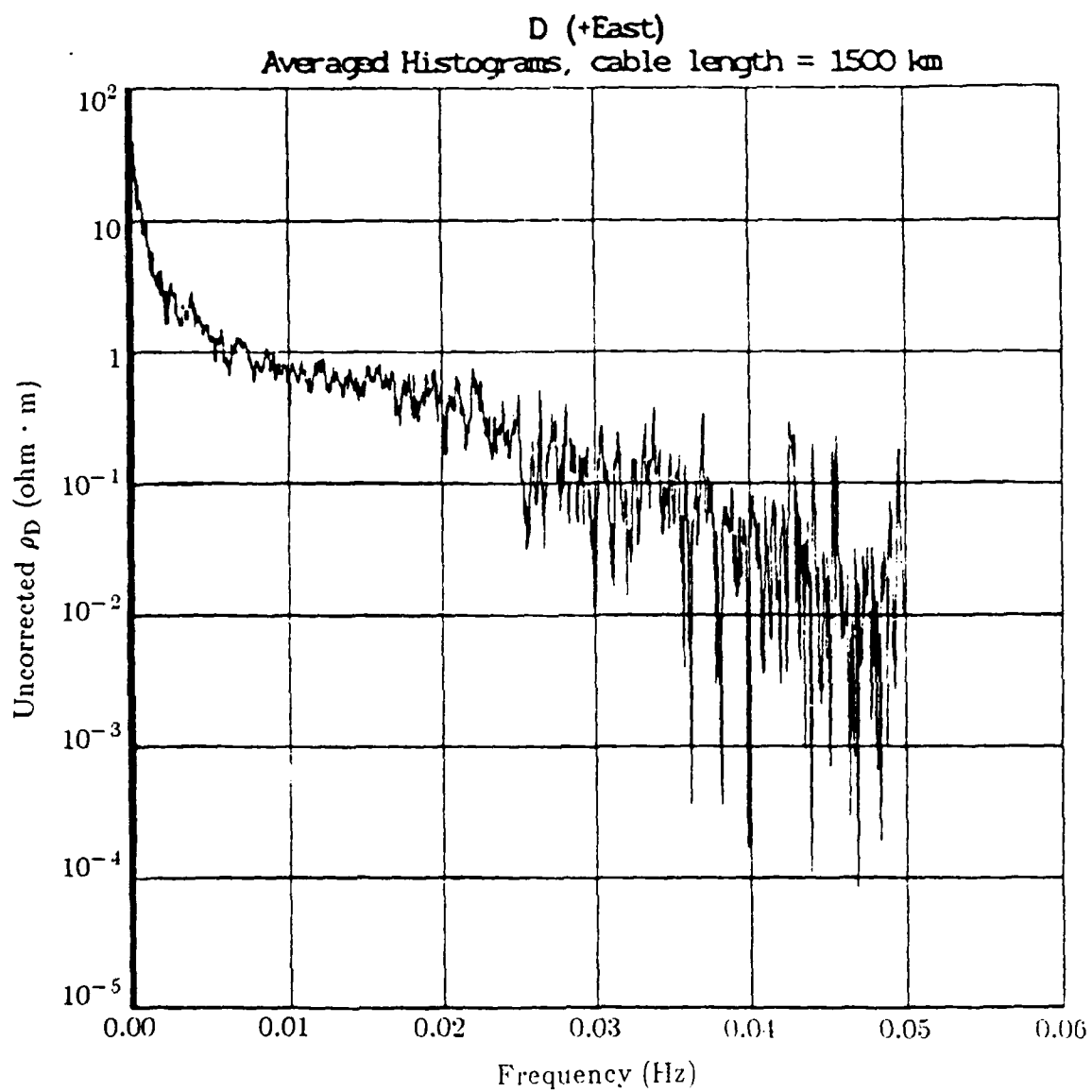


Fig. 3.12a. Effective resistivity  $\rho_D$  for TAT-7 at 1500 km. all data.

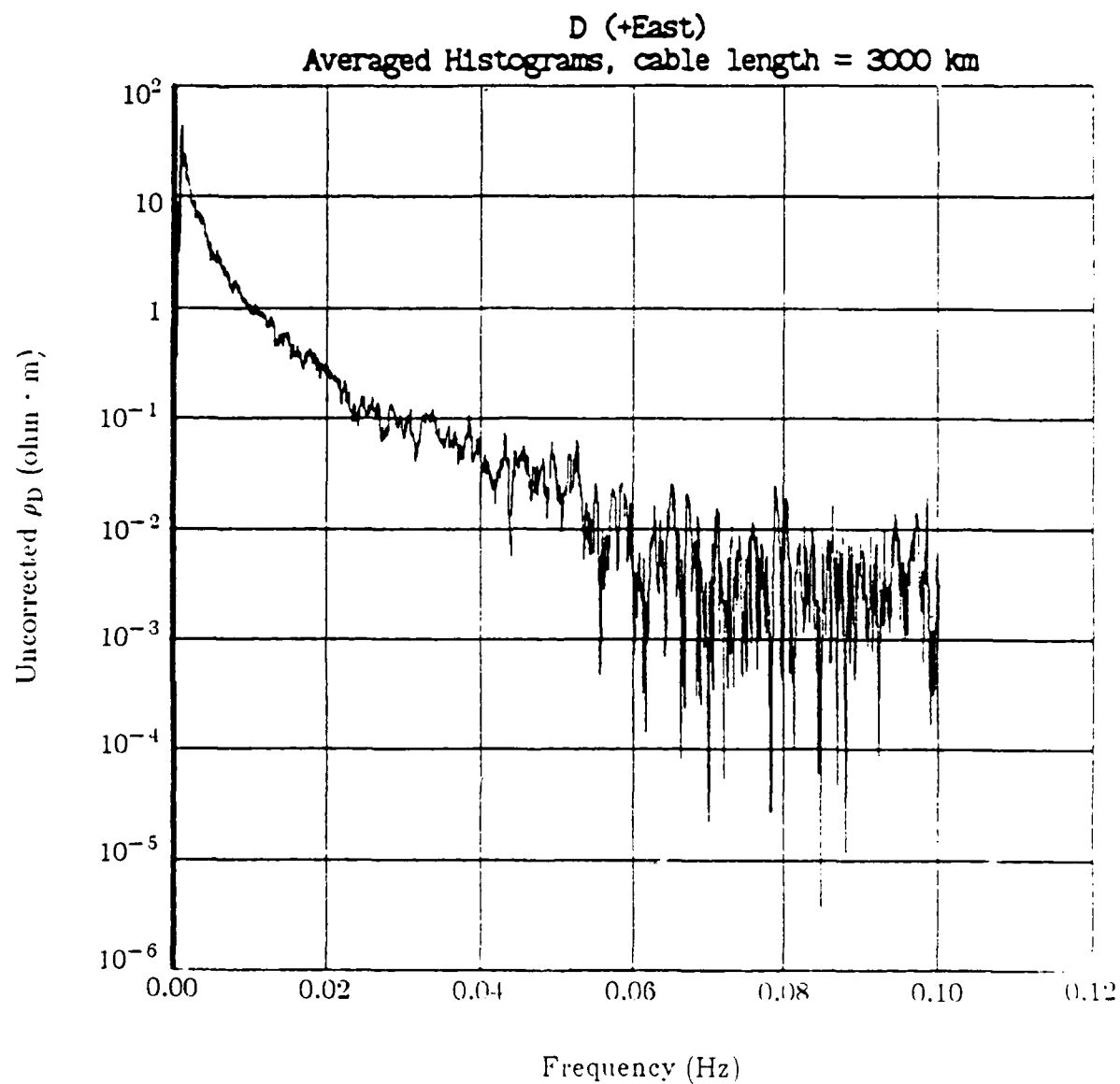


Fig. 3.12b. Effective resistivity  $\rho_D$  for TAT-7 at 3000 km, all data.

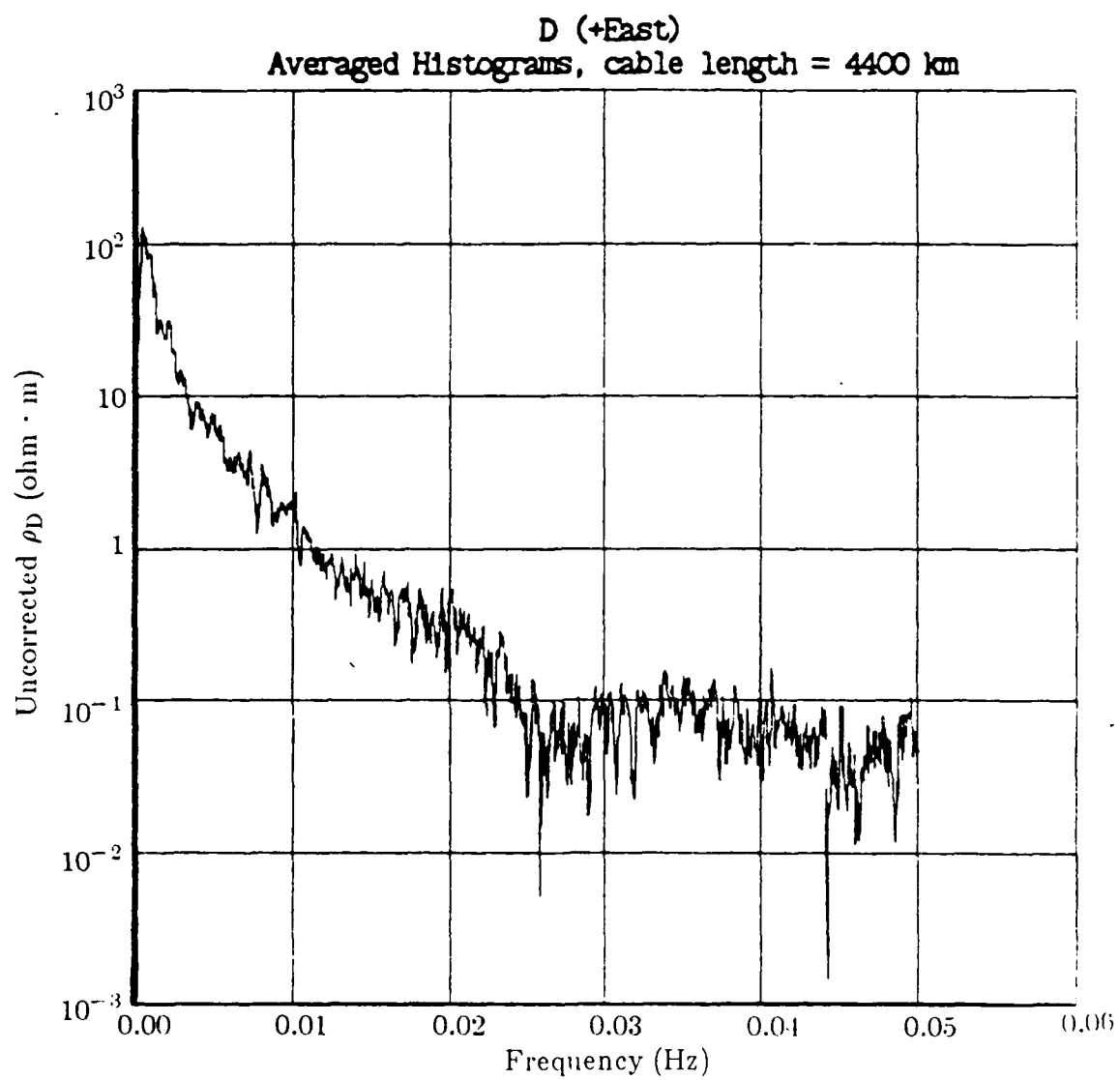


Fig. 3.12c. Effective resistivity  $\rho_D$  for TAT-7 at 4400 km. all data.



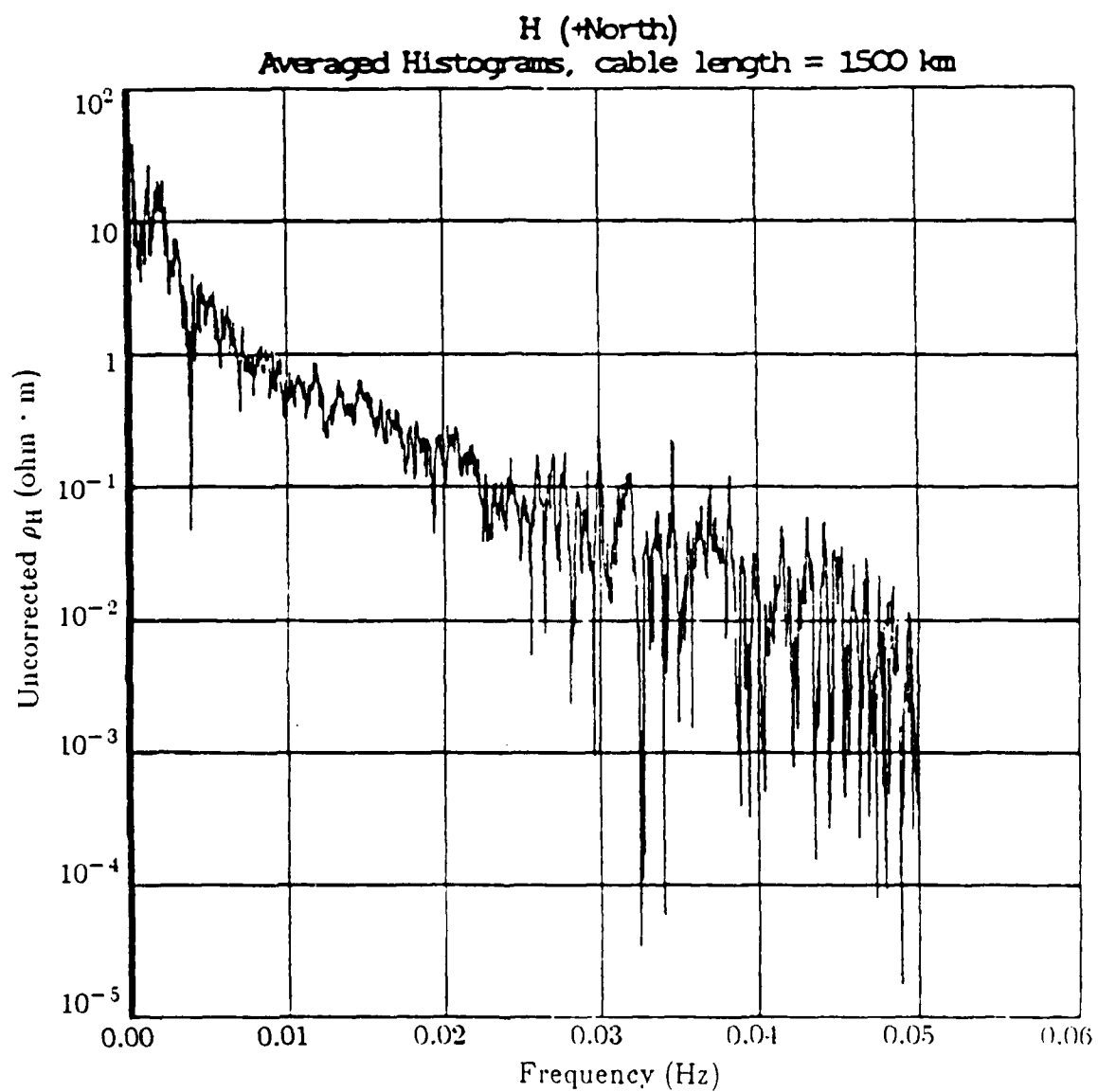


Fig. 3.13a. Effective resistivity  $\rho_H$  for TAT-7 at 1500 km, all data.

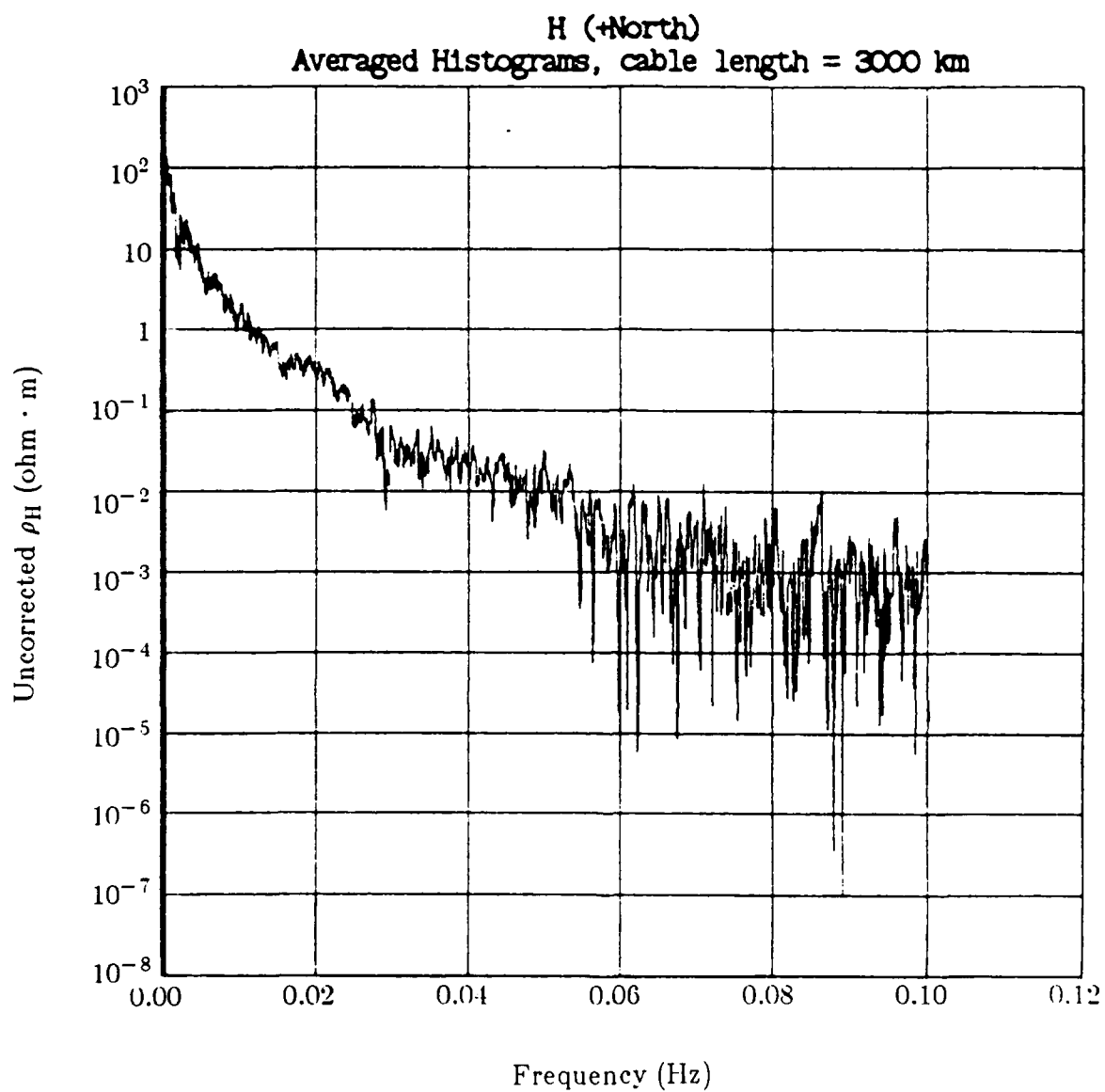


Fig. 3.13b. Effective resistivity  $\rho_H$  for TAT-7 at 3000 km. all data.

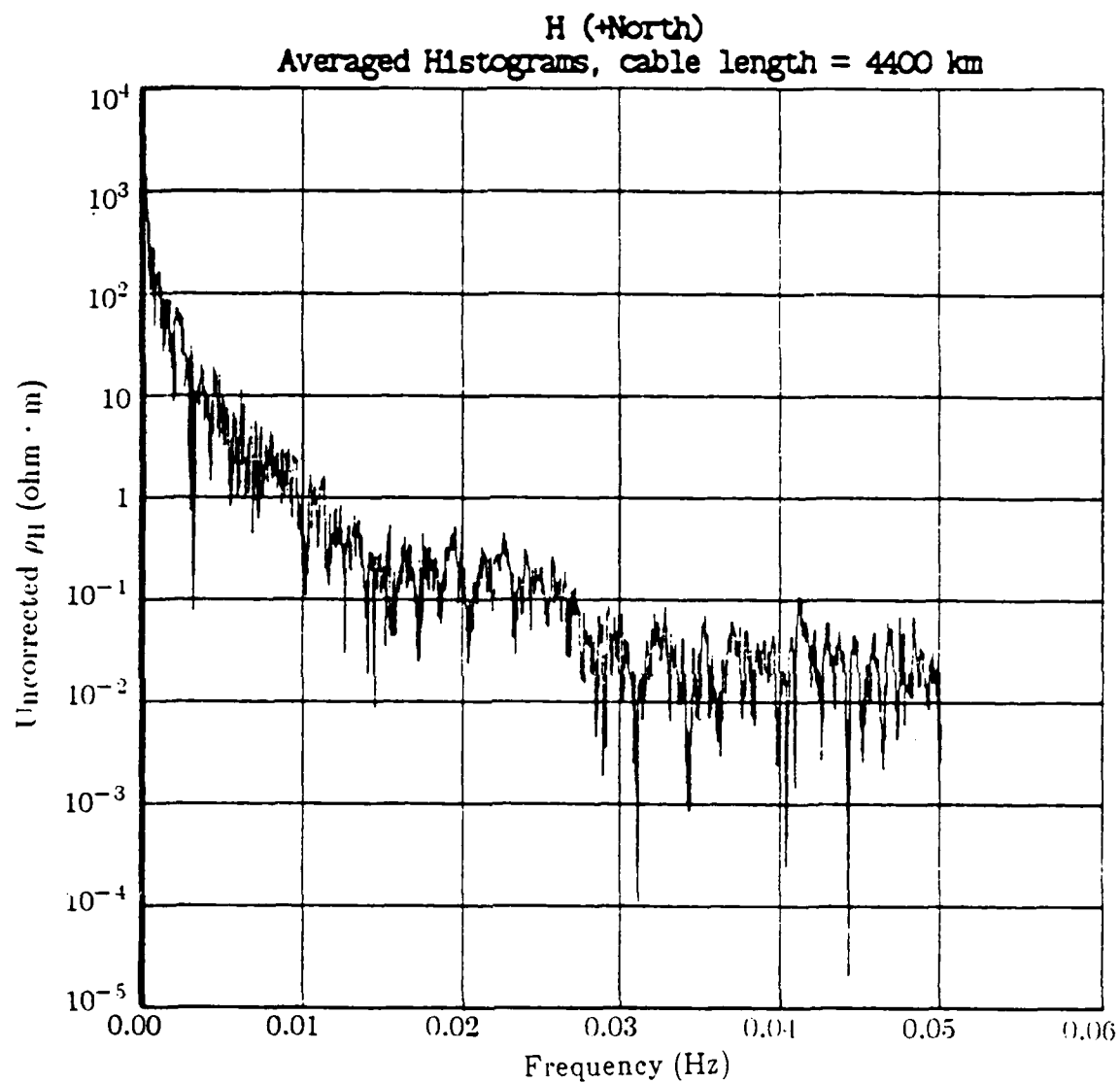


Fig. 3.13c. Effective resistivity  $\rho_H$  for TAT-7 at 4400 km, all data.

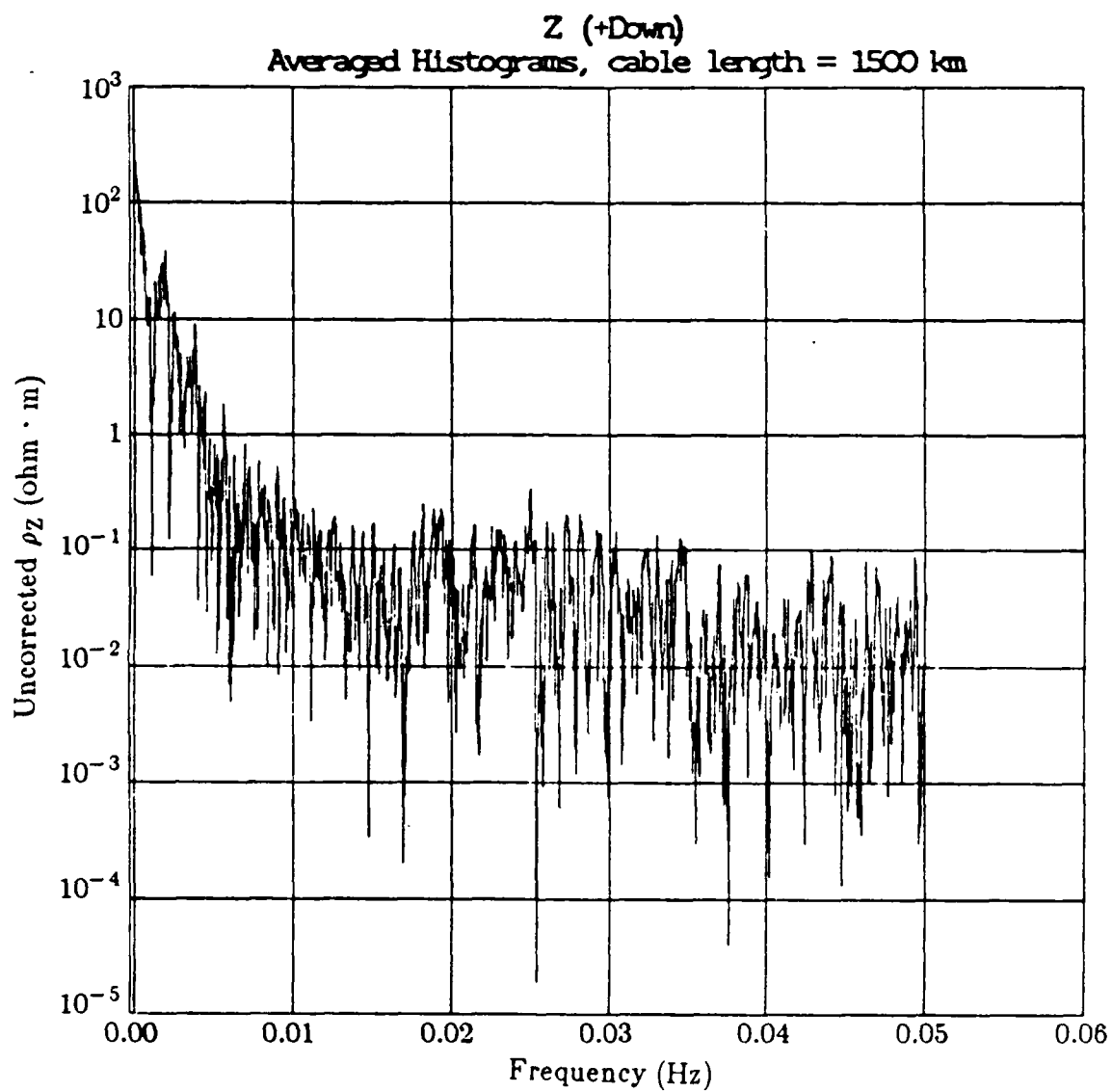


Fig. 3.14a. Effective resistivity  $\rho_Z$  for TAT-7 at 1500 km, all data.

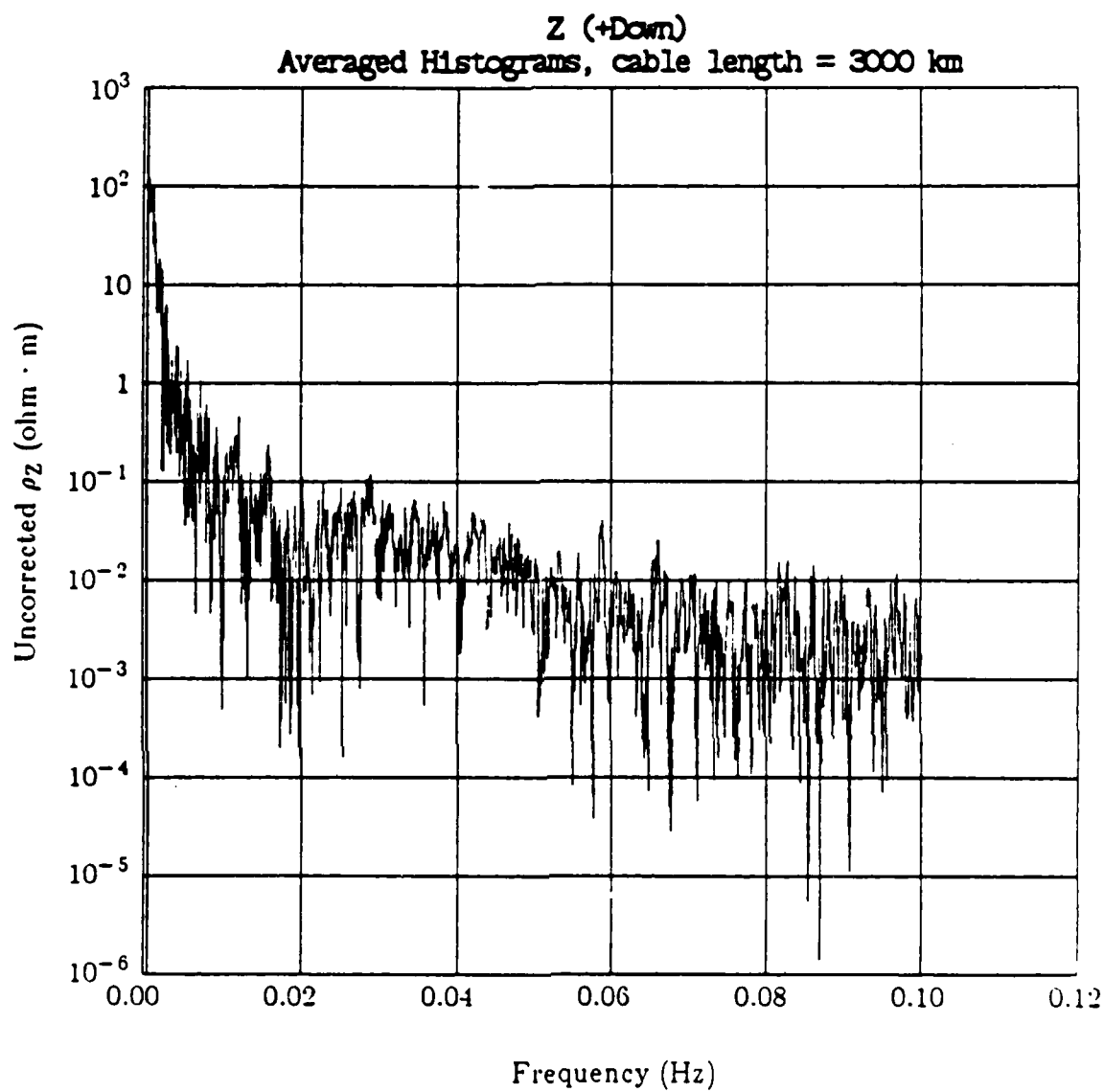


Fig. 3.14b. Effective resistivity  $\rho_z$  for TAT-7 at 3000 km, all data.

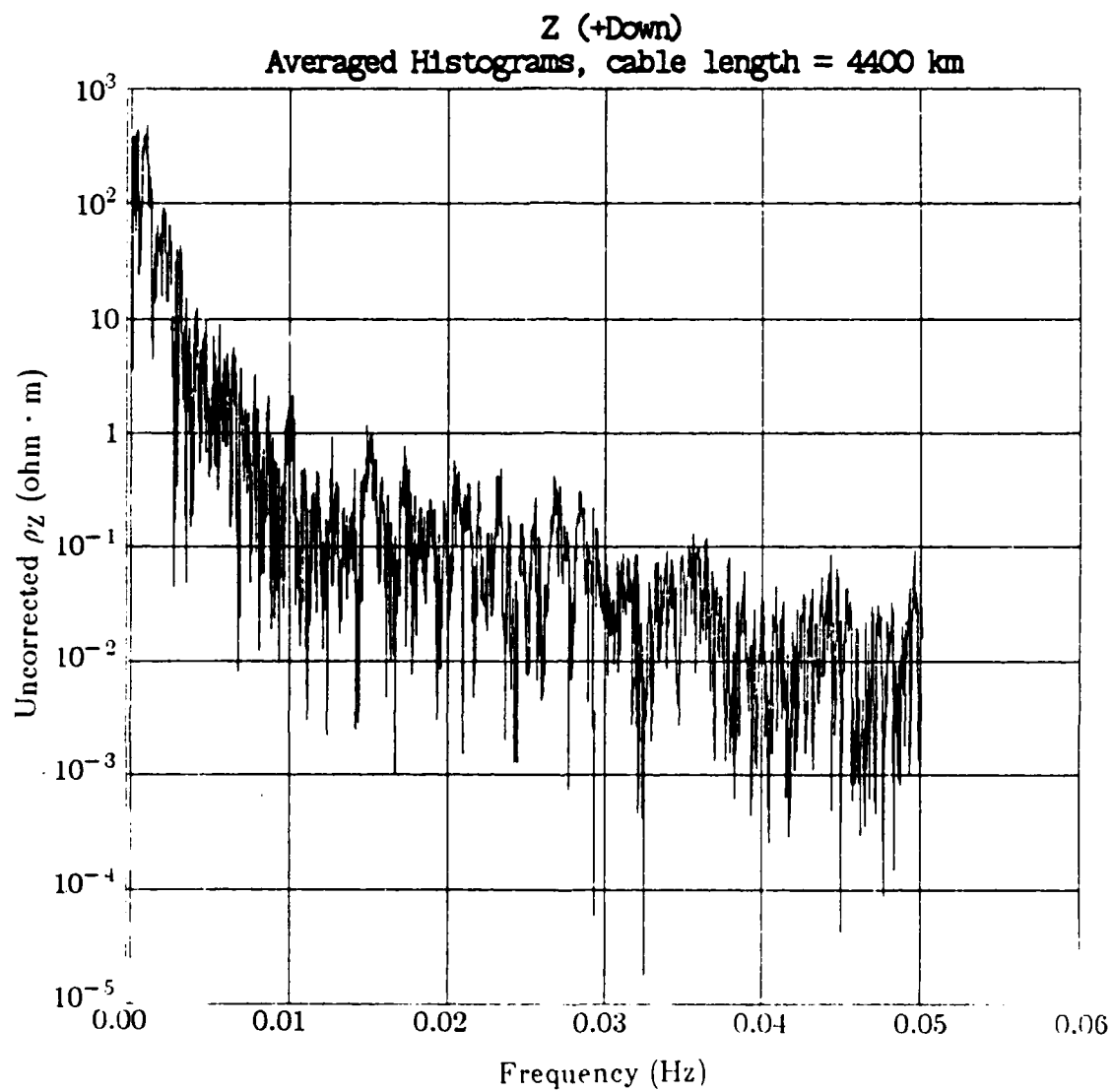


Fig. 3.14c. Effective resistivity  $\rho_z$  for TAT-7 at 4400 km. all data.

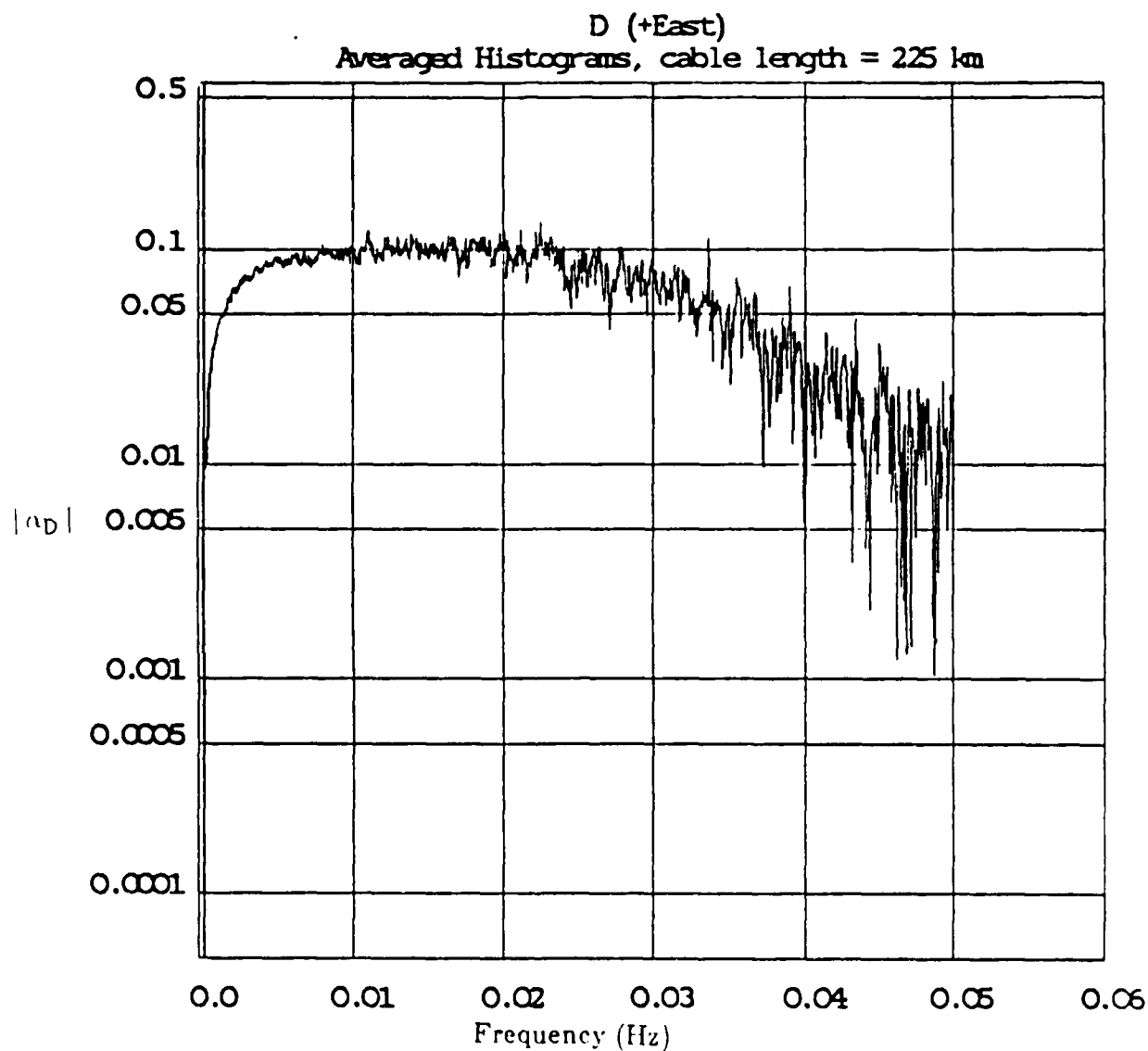


Fig. 3.15a. Magnitude of transfer function  $\alpha_D$  for TAT-6 at 225 km. all data.

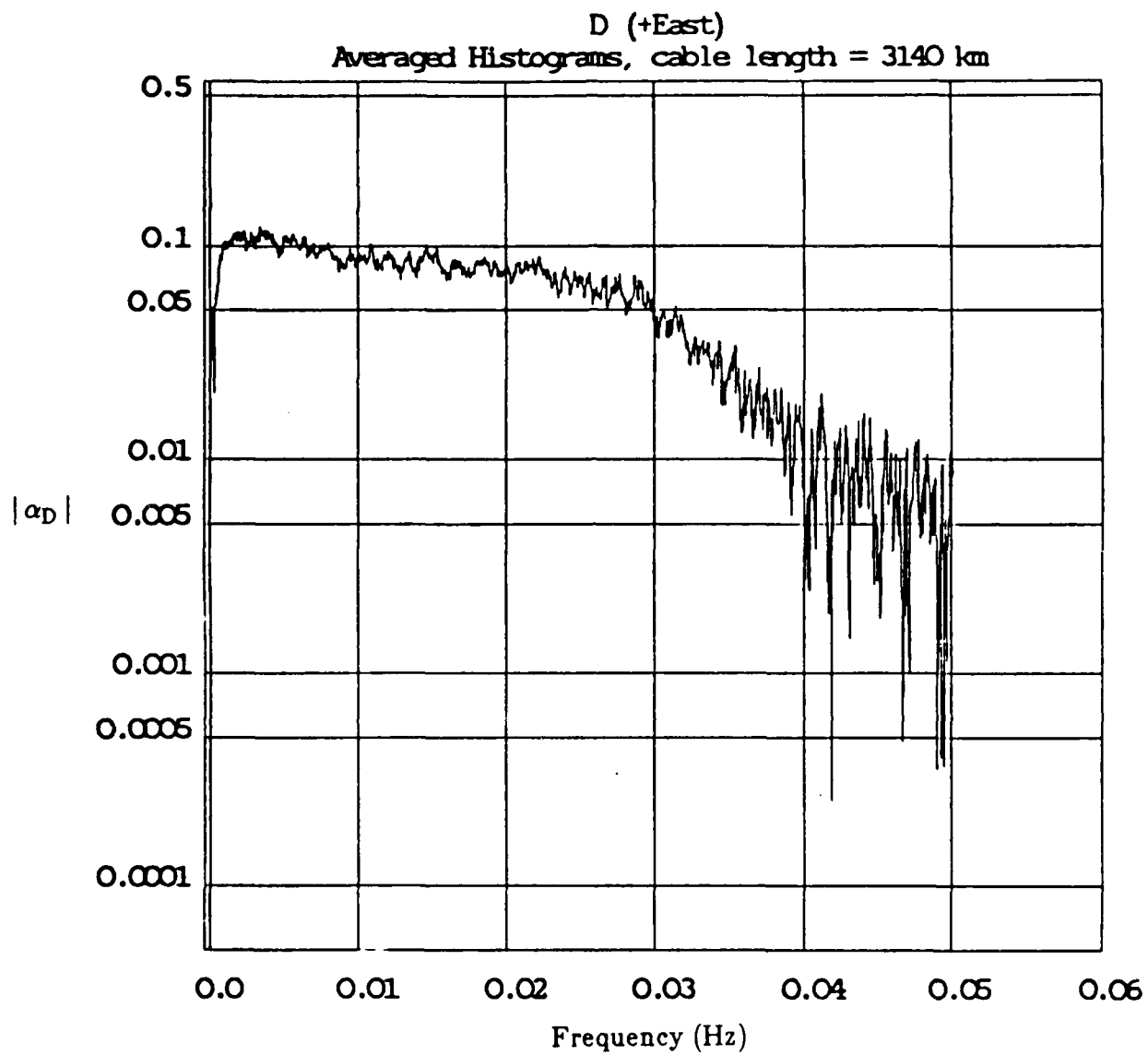


Fig. 3.15b. Magnitude of transfer function  $\alpha_D$  for TAT-6 at 3140 km, all data.



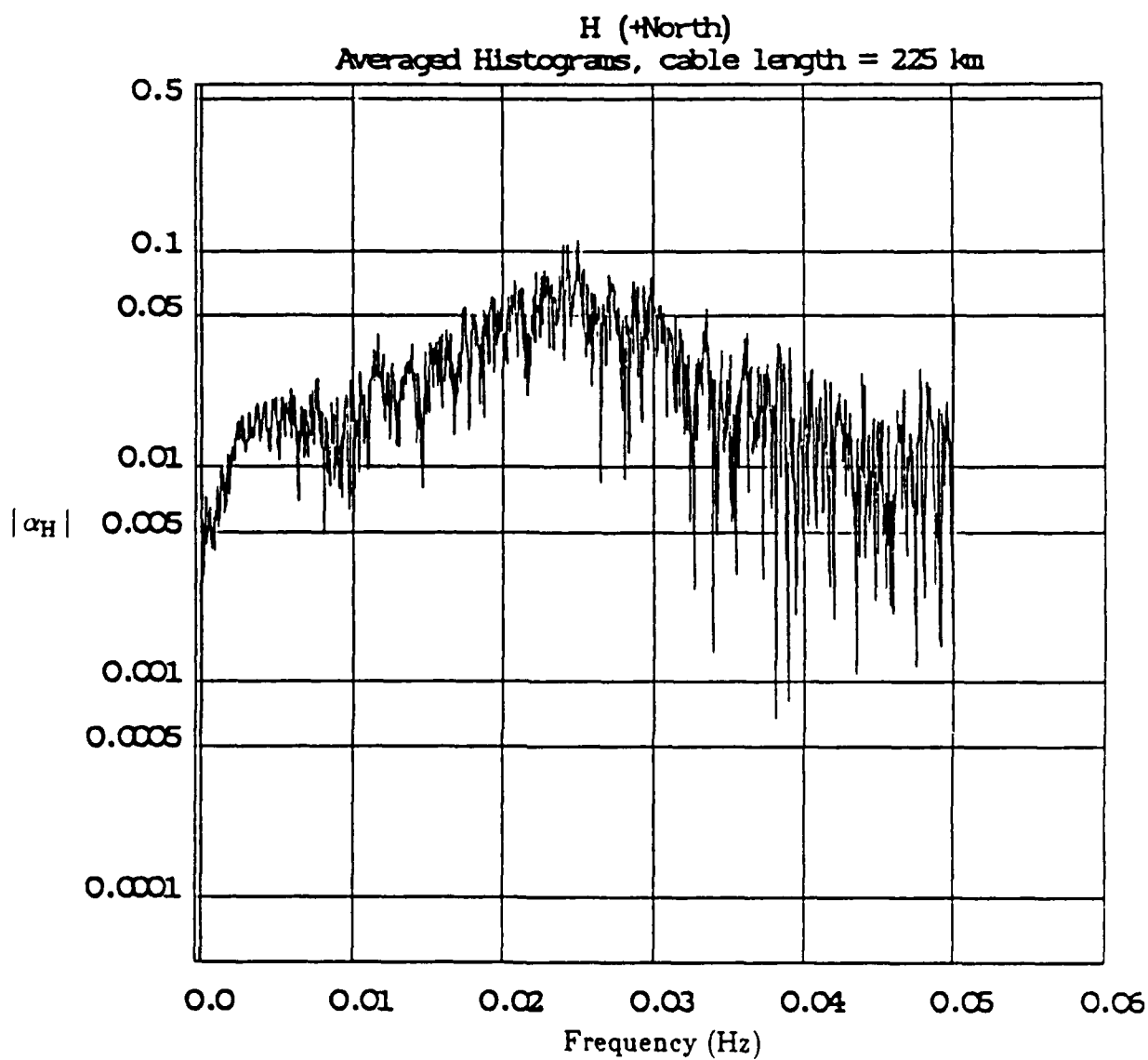


Fig. 3.16a. Magnitude of transfer function  $\alpha_H$  for TAT-6 at 225 km, all data.

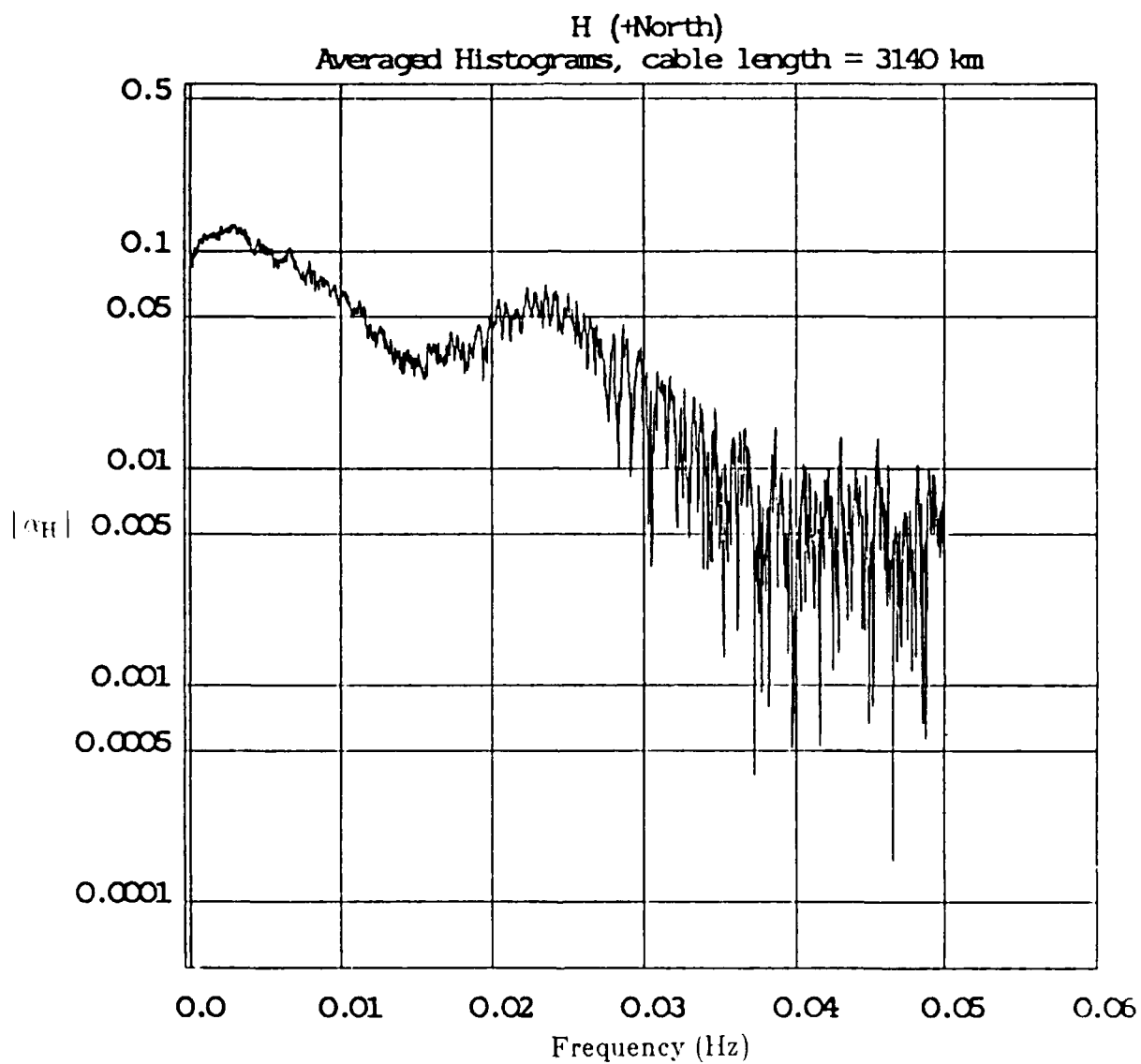


Fig. 3.16b. Magnitude of transfer function  $\alpha_H$  for TAT-6 at 3140 km. all data.

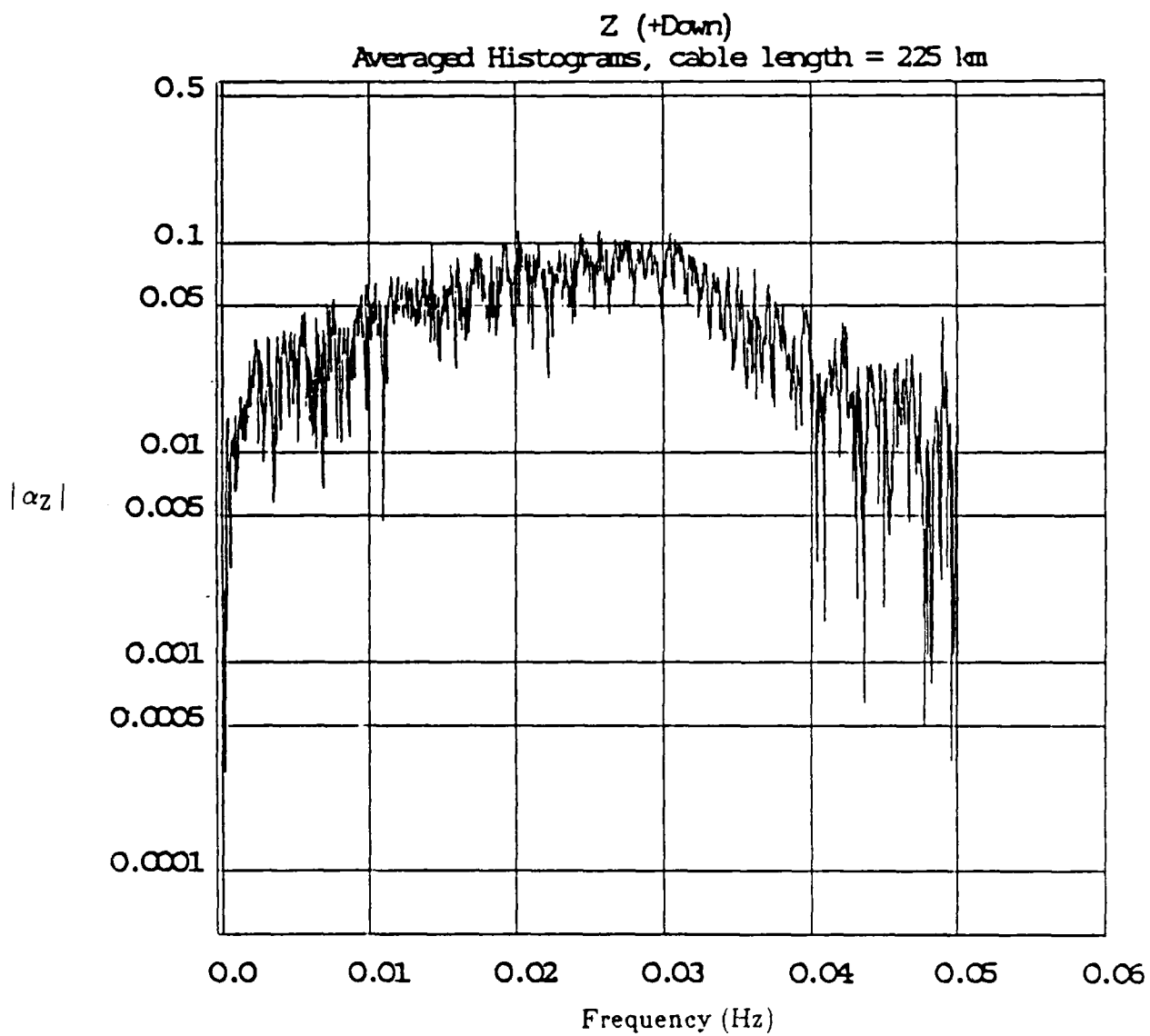


Fig. 3.17a. Magnitude of transfer function  $\alpha_z$  for TAT-6 at 225 km. all data.

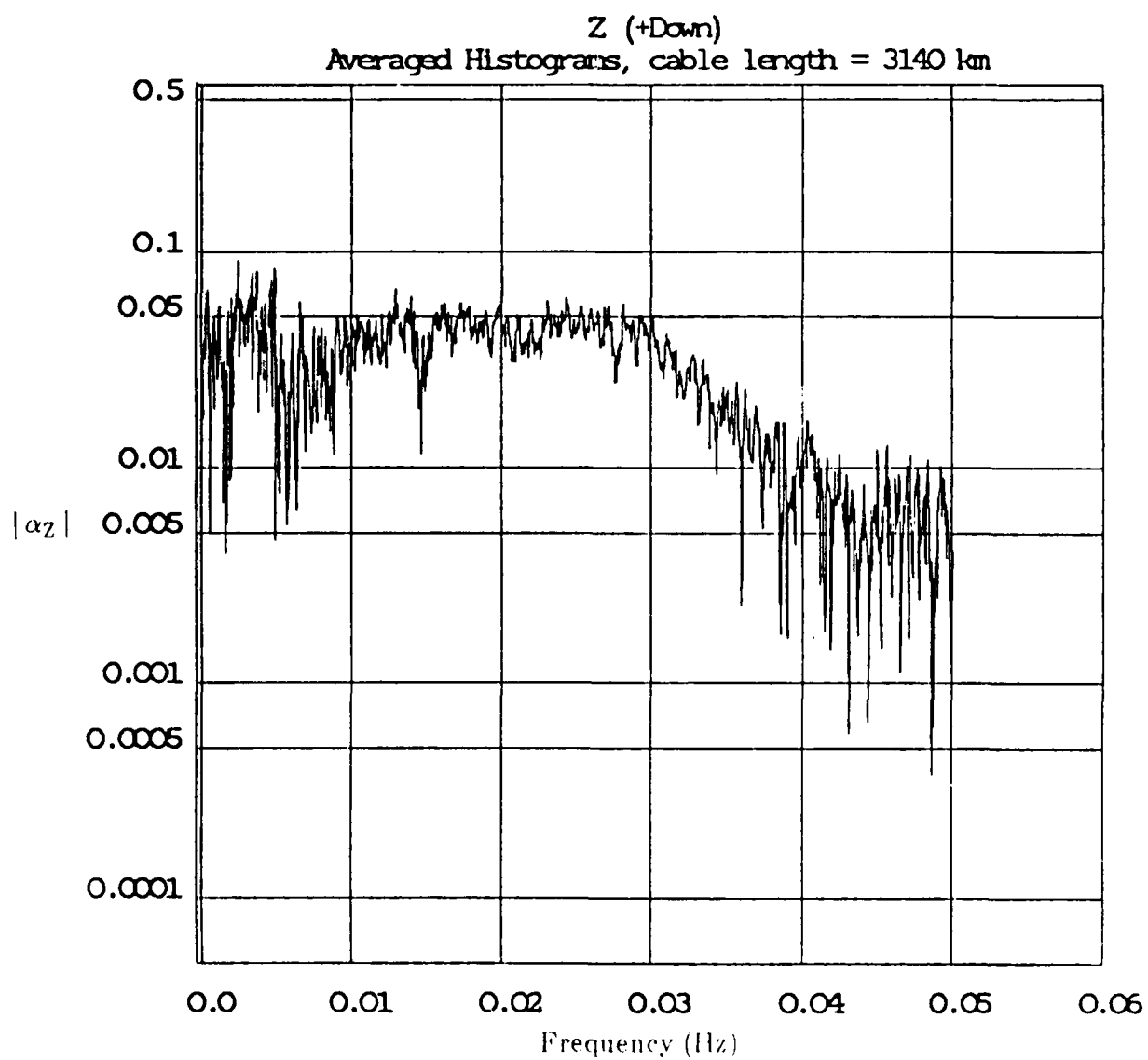


Fig. 3.17b. Magnitude of transfer function  $\alpha_z$  for TAT-6 at 3140 km, all data.

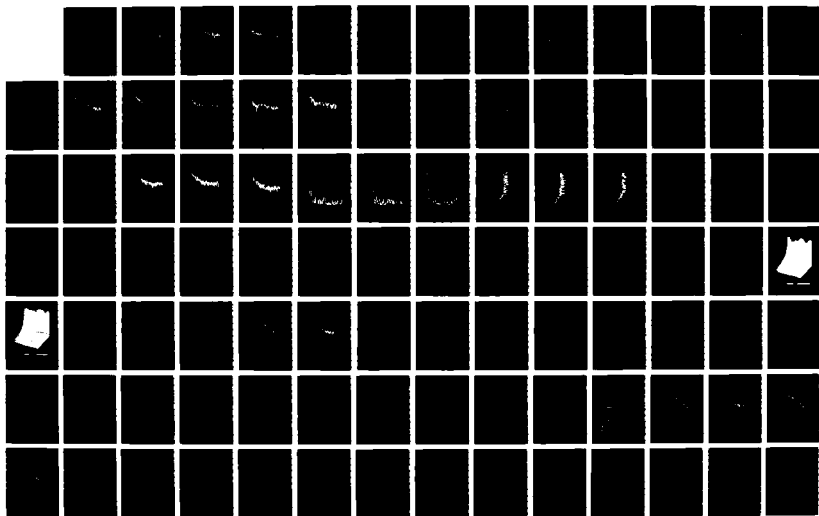
NO-A190-749

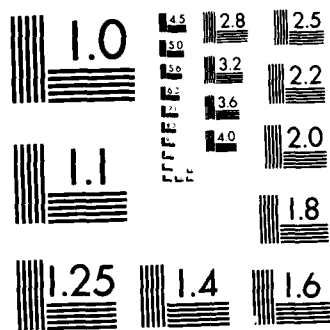
MAGNETOHYDRODYNAMIC (MHD) NUCLEAR WEAPONS EFFECTS ON  
SUBMARINE CABLE SVST. (U) AT AND T BELL LABS HOLMDEL NJ  
JUN 87 MCS-TIB-87-14-VOL-1 DCR100-85-C-0068

UNCLASSIFIED

F/G 28/14

NL





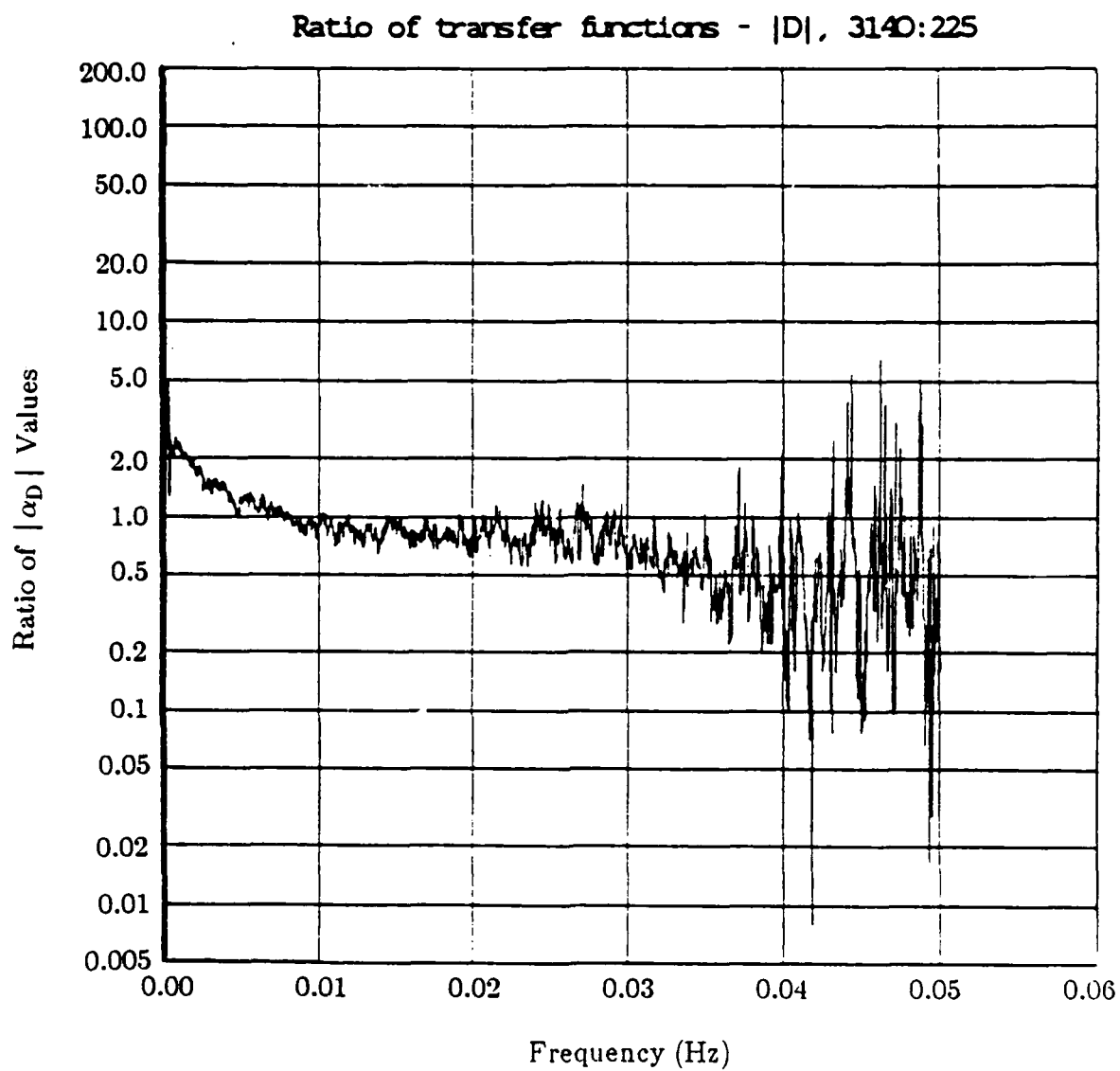


Fig. 3.18a. The ratio of the magnitudes of the TAT-6 transfer function  $\alpha_D$  at 3140 km relative to 225 km, all data.

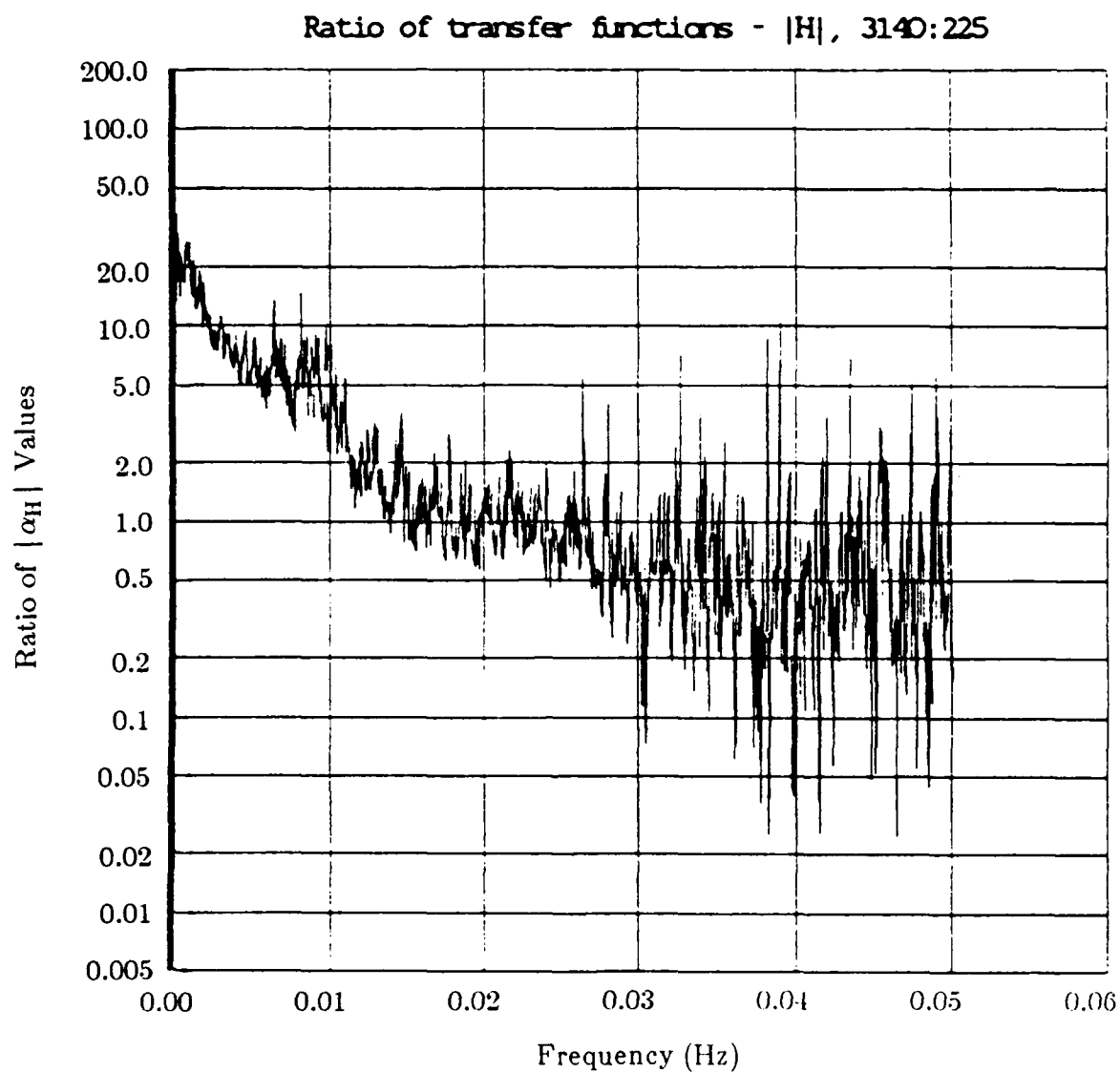


Fig. 3.18b. The ratio of the magnitudes of the TAT-6 transfer function  $a_H$  at 3140 km relative to 225 km, all data.



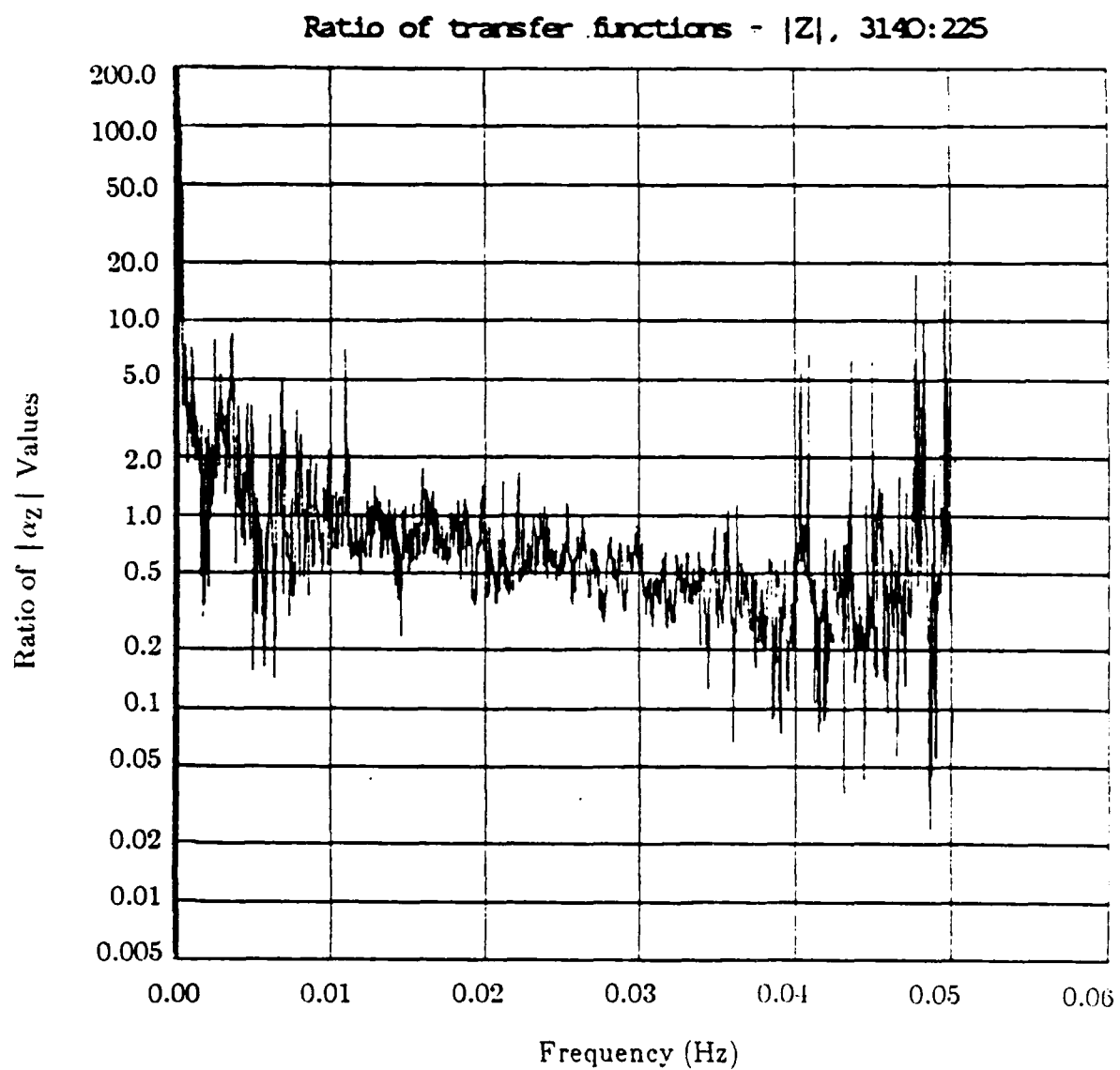


Fig. 3.18c. The ratio of the magnitudes of the TAT-6 transfer function  $\alpha_z$  at 3140 km relative to 225 km, all data.

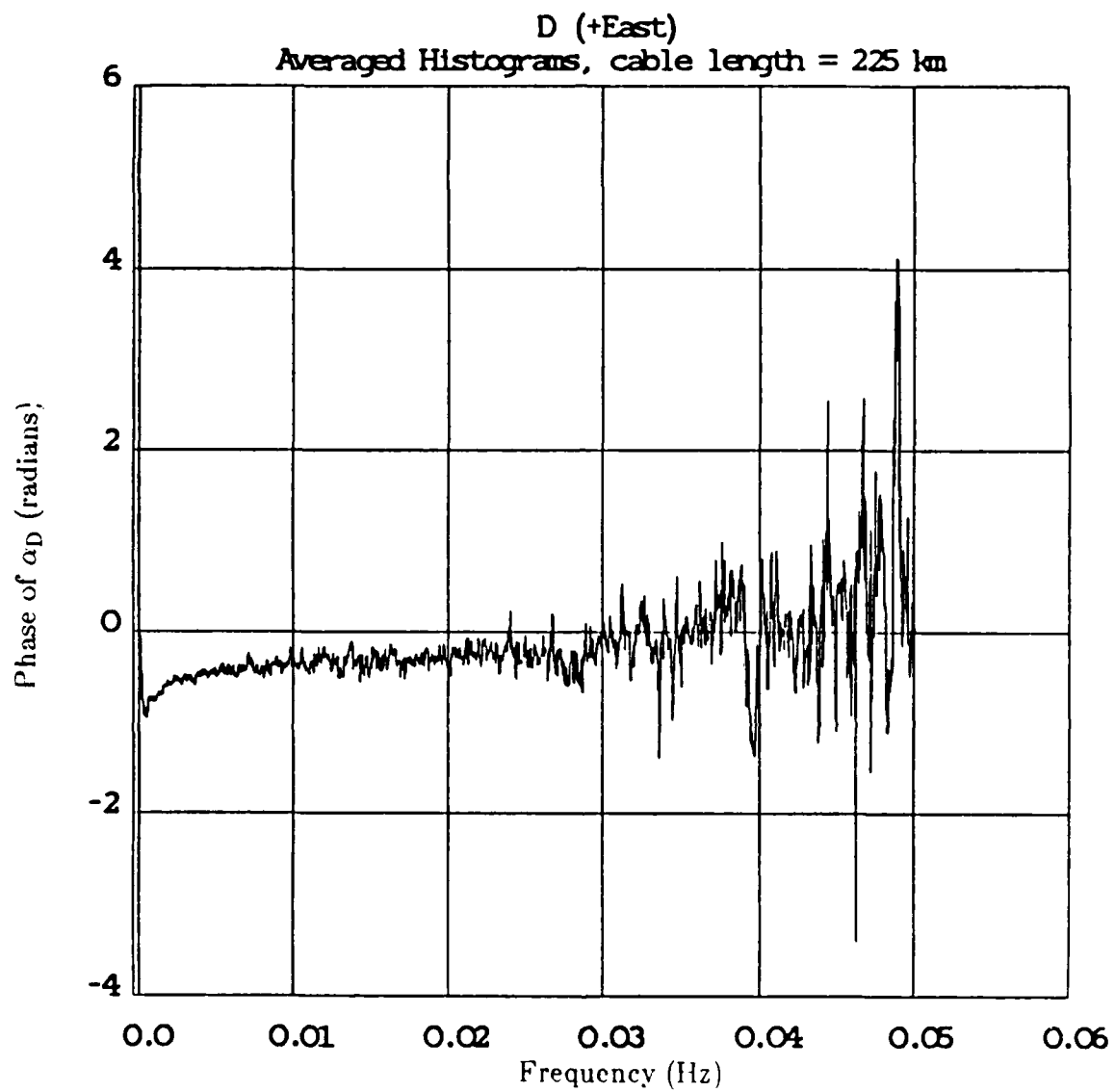


Fig. 3.19a. Phase of transfer function  $\alpha_D$  for TAT-6 at 225 km. all data.

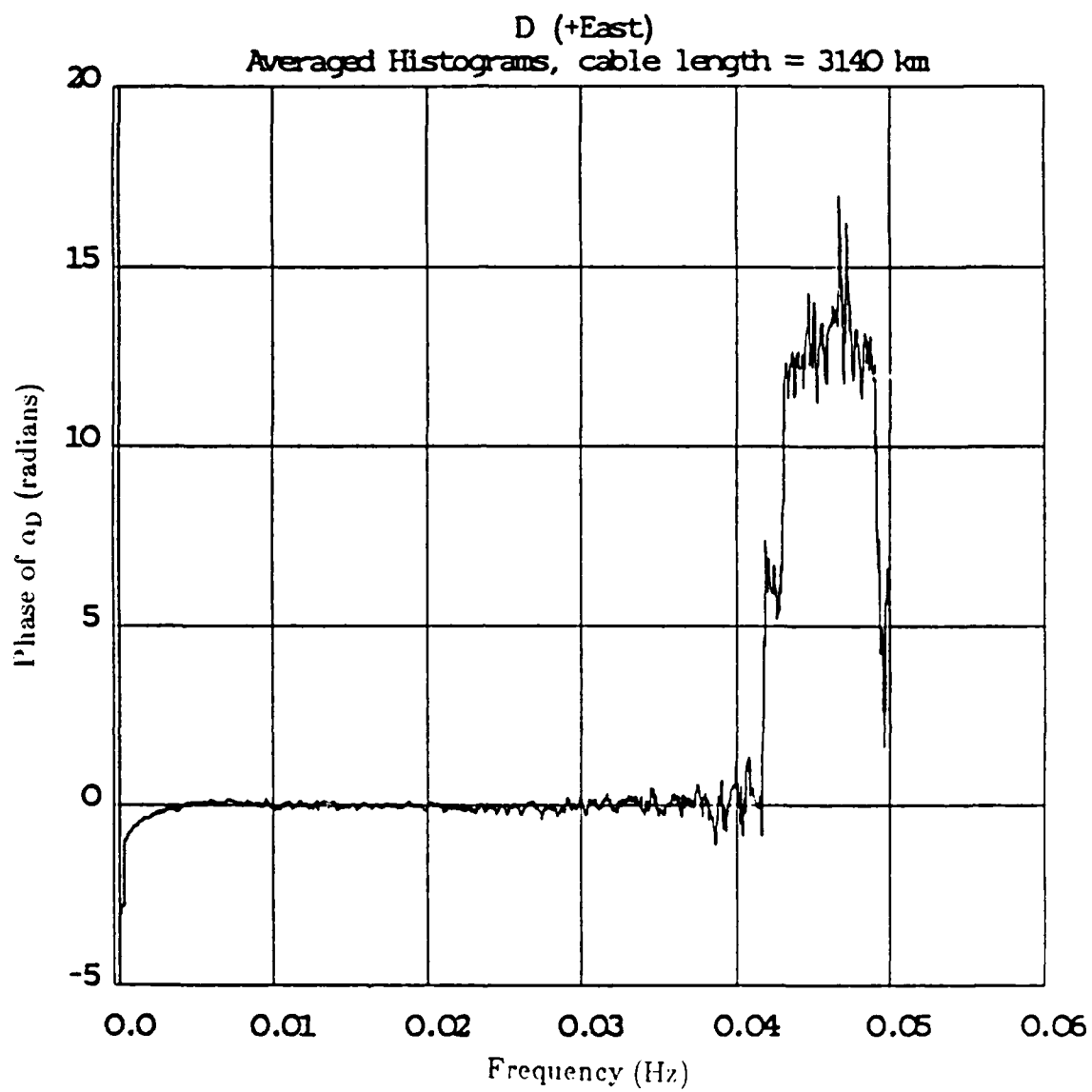


Fig. 3.19b. Phase of transfer function  $\alpha_D$  for TAT-6 at 3140 km. all data.

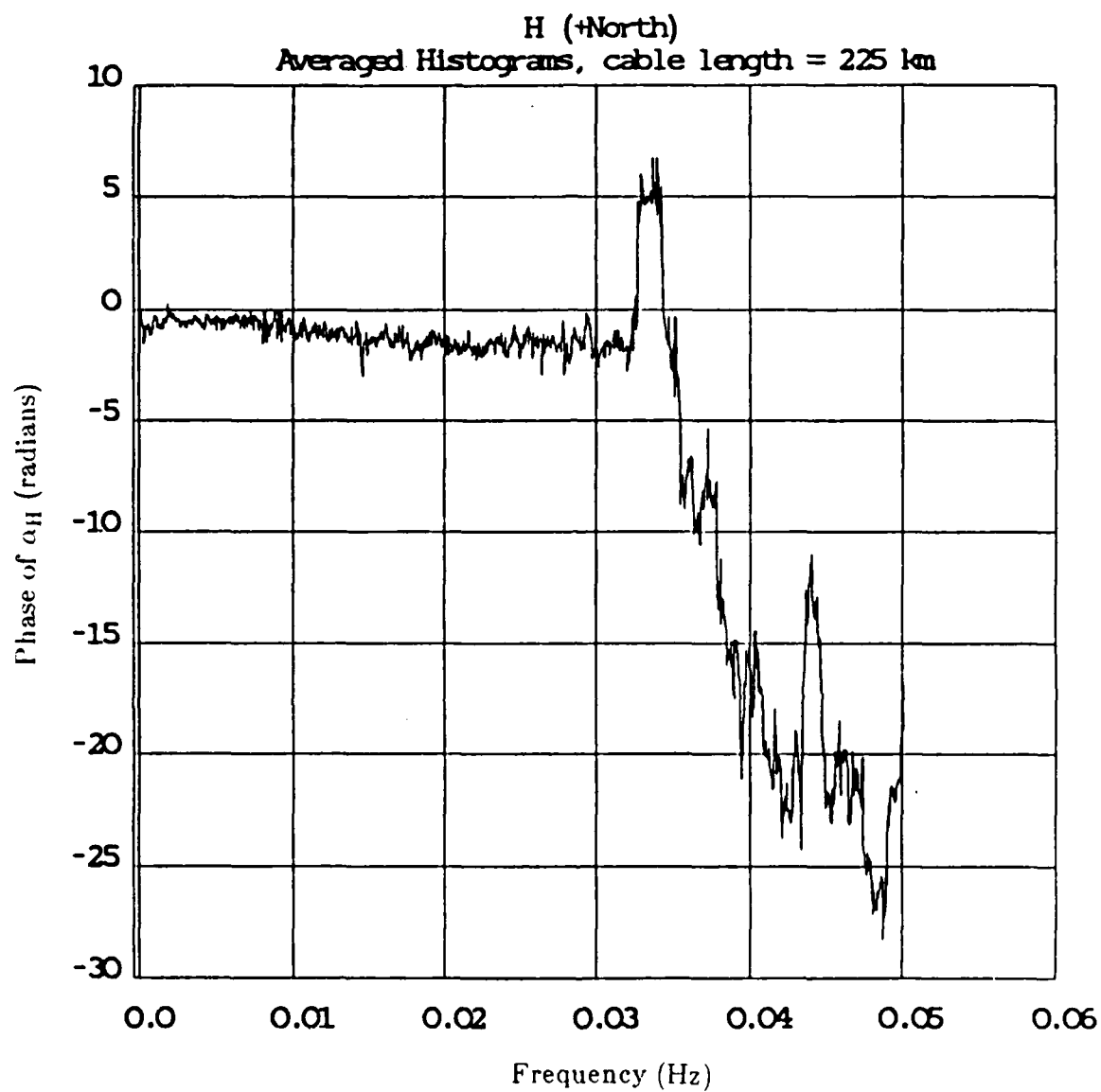


Fig. 3.20a. Phase of transfer function  $\alpha_H$  for TAT-6 at 225 km, all data.

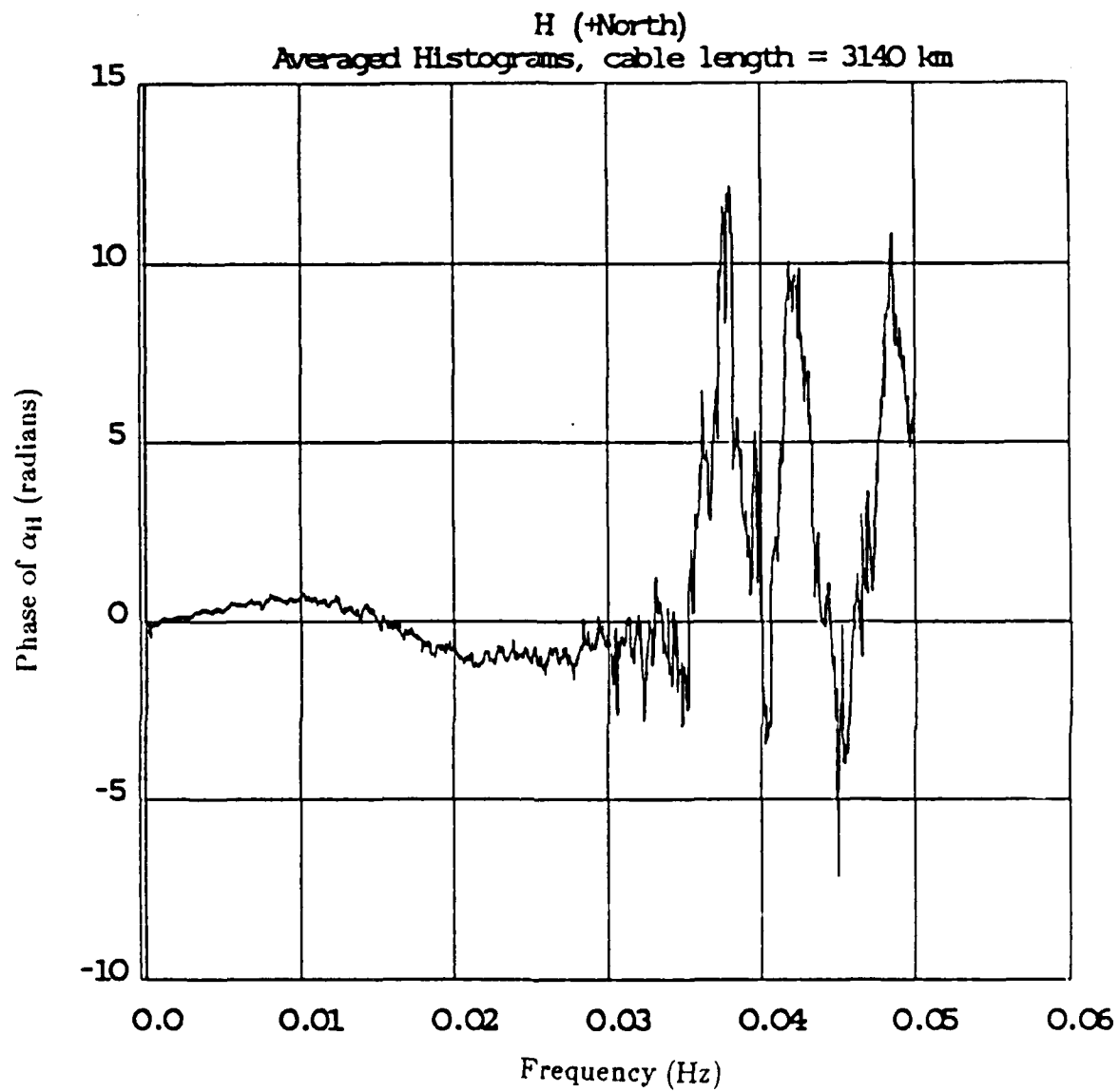


Fig. 3.20b. Phase of transfer function  $\alpha_H$  for TAT-6 at 3140 km, all data.

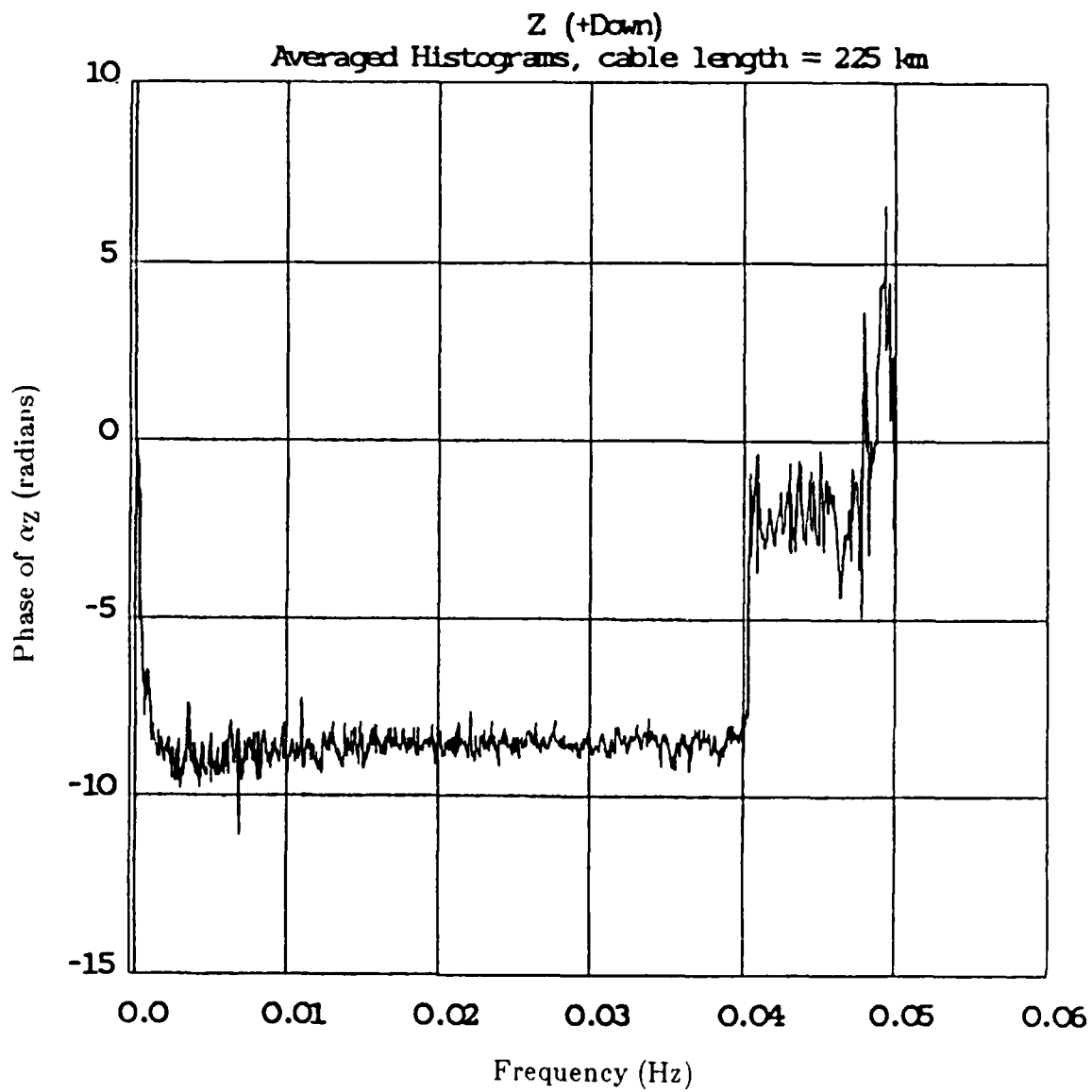


Fig. 3.21a. Phase of transfer function  $\alpha_z$  for TAT-6 at 225 km, all data.

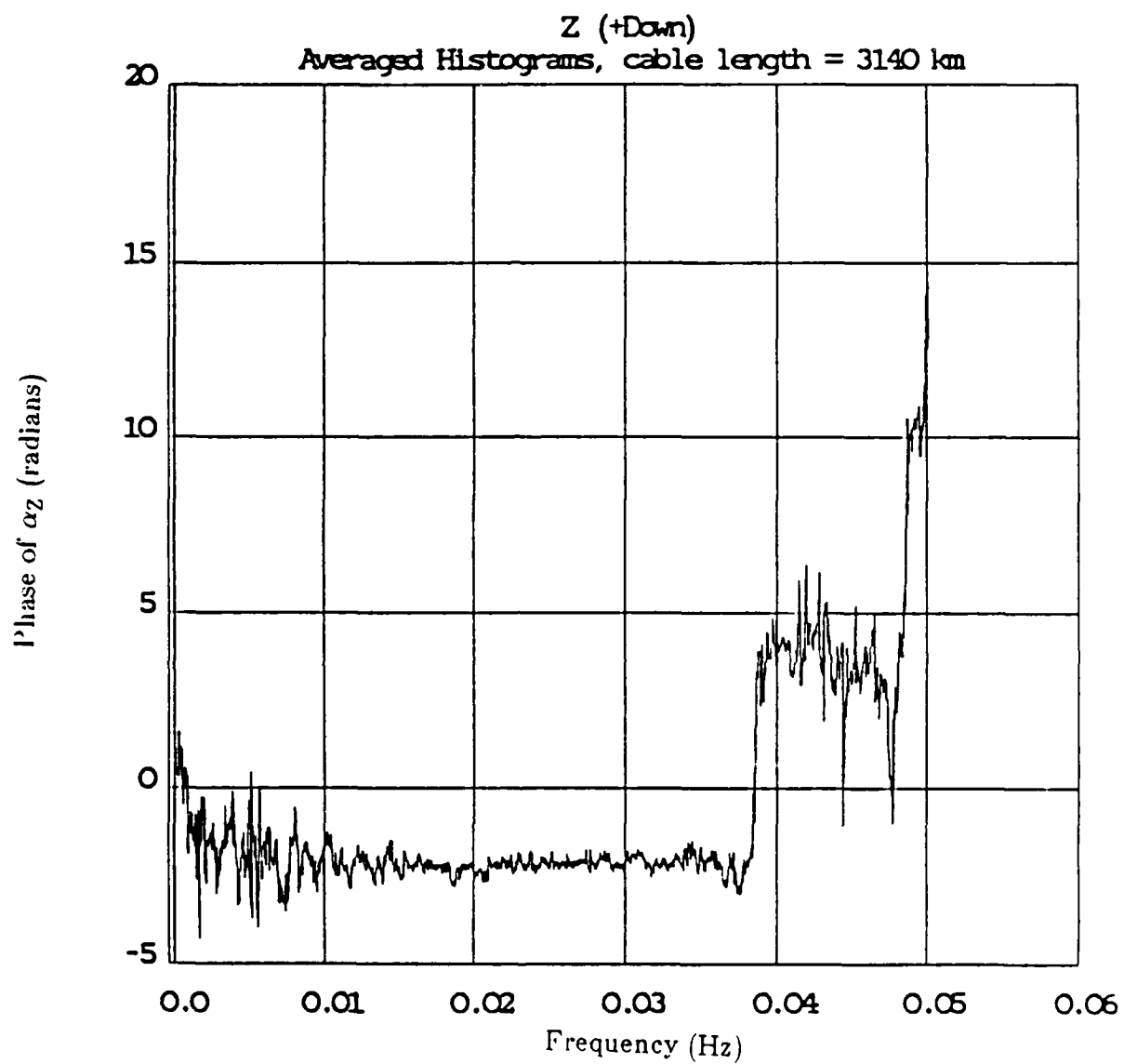


Fig. 3.21b. Phase of transfer function  $\alpha_z$  for TAT-6 at 3140 km, all data.

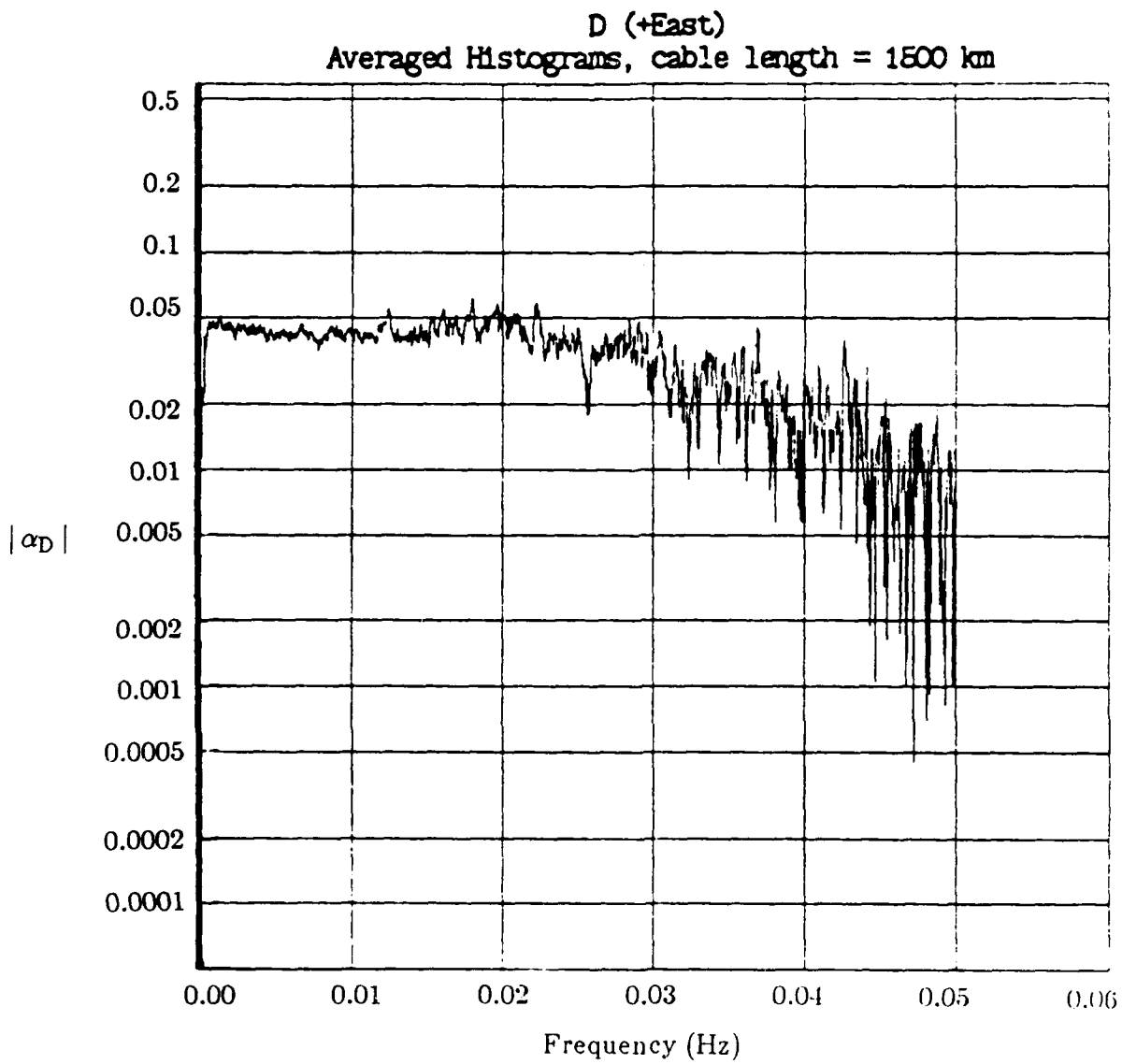


Fig. 3.22a. Magnitude of transfer function  $a_D$  for TAT-7 at 1500 km. all data.



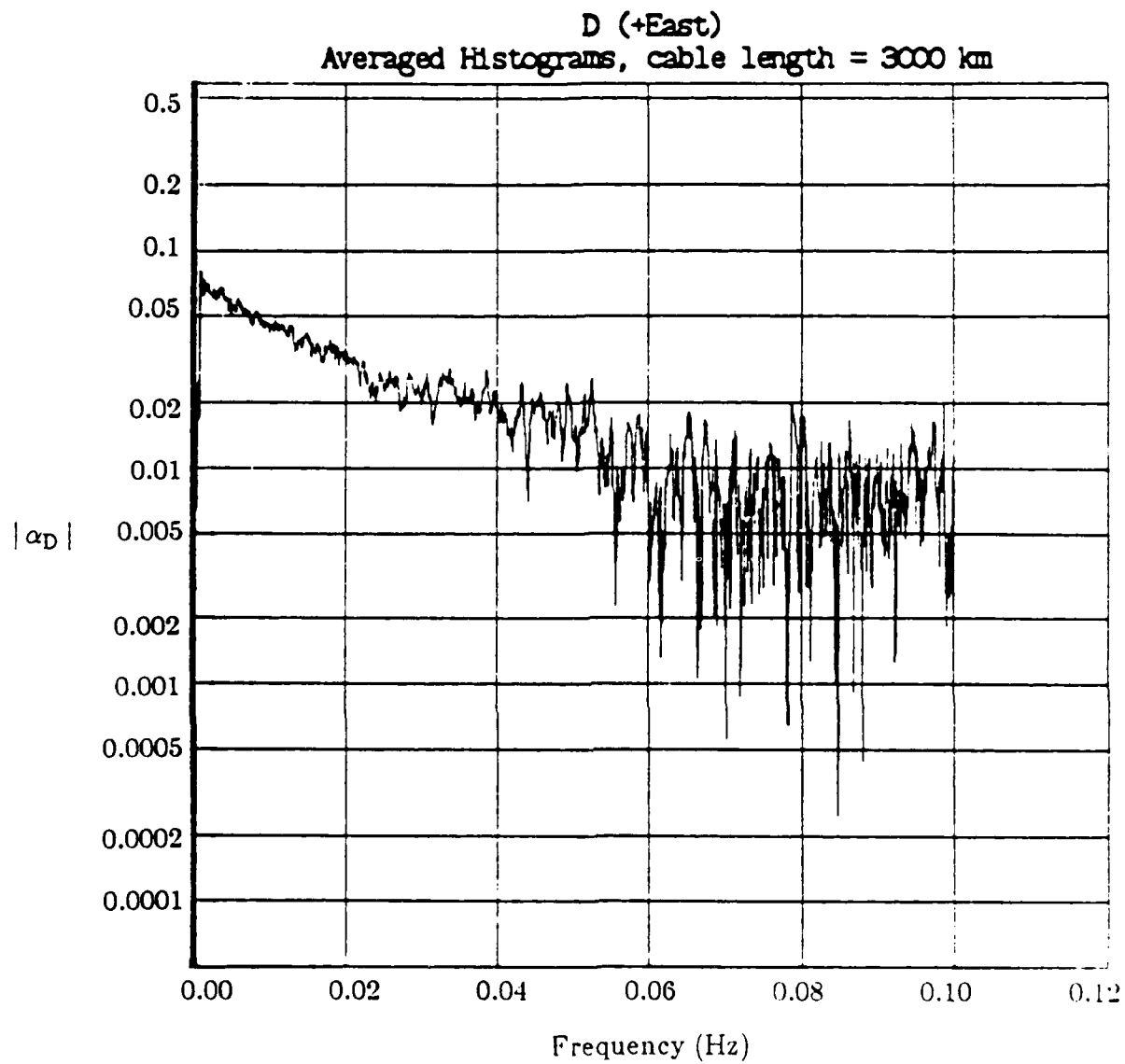


Fig. 3.22b. Magnitude of transfer function  $\alpha_D$  for TAT-7 at 3000 km, all data.

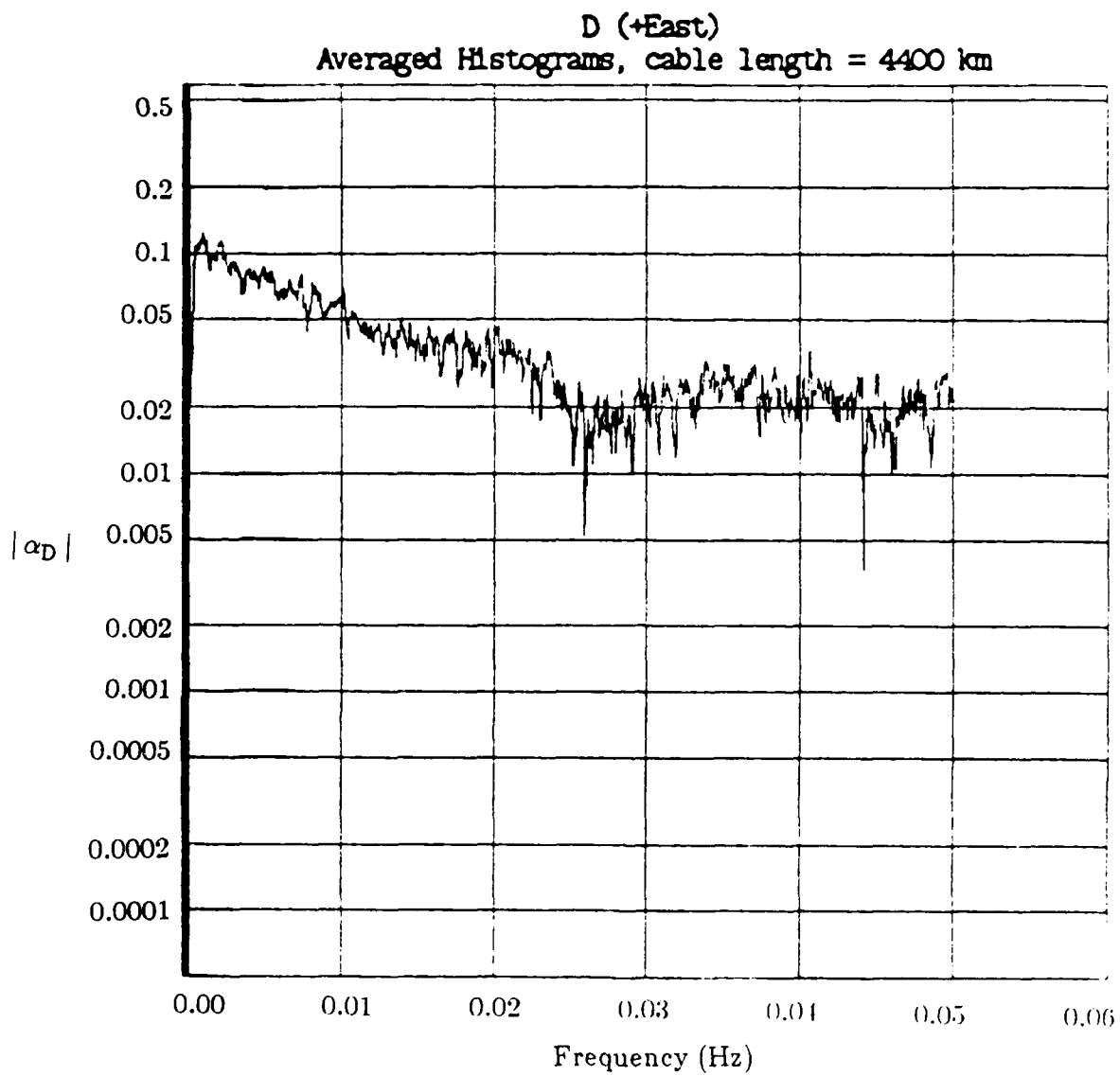


Fig. 3.22c. Magnitude of transfer function  $\alpha_D$  for TAT-7 at 4400 km, all data.

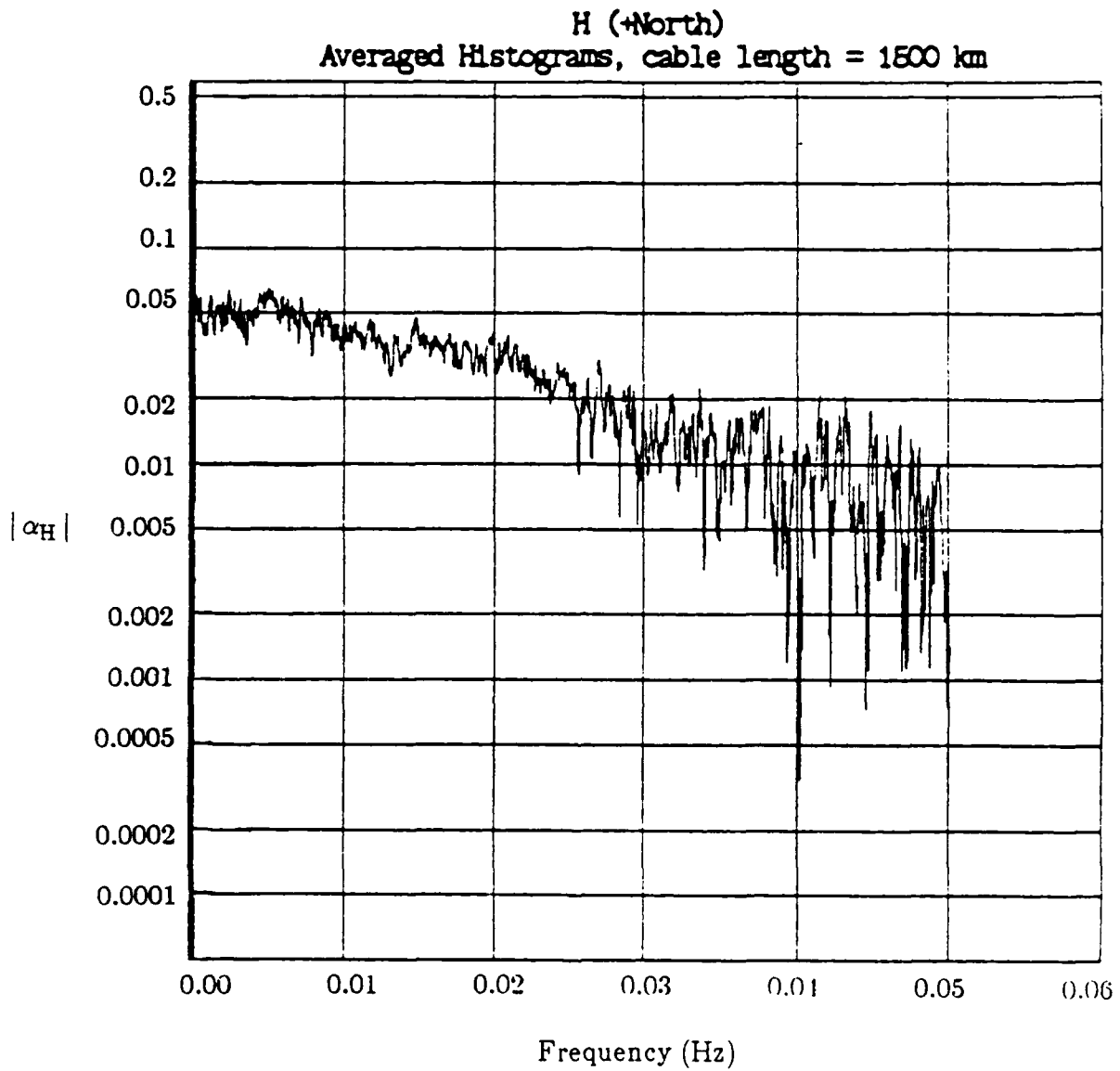


Fig. 3.23a. Magnitude of transfer function  $\alpha_H$  for TAT-7 at 1500 km, all data.

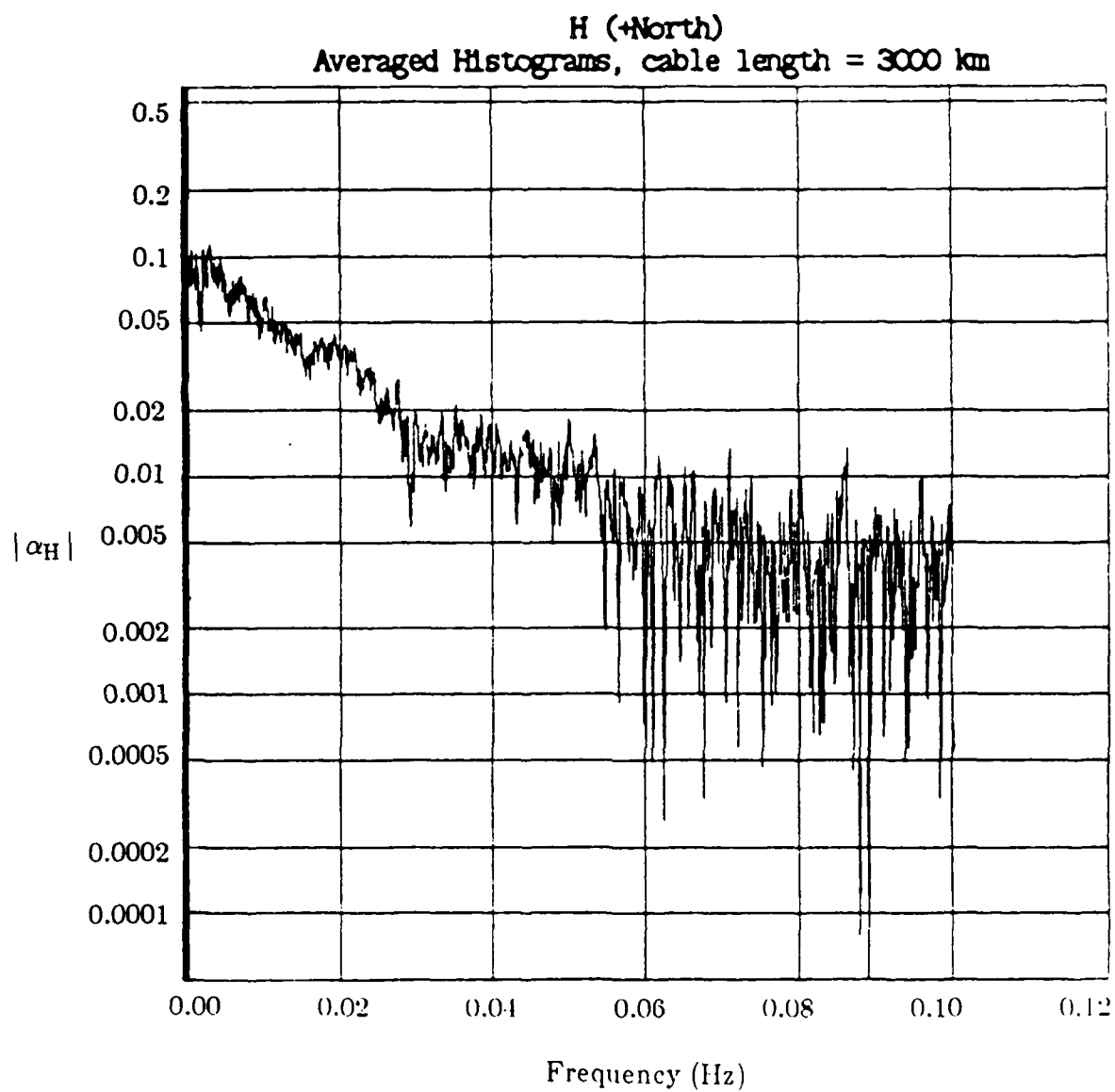


Fig. 3.23b. Magnitude of transfer function  $\alpha_H$  for TAT-7 at 3000 km, all data.

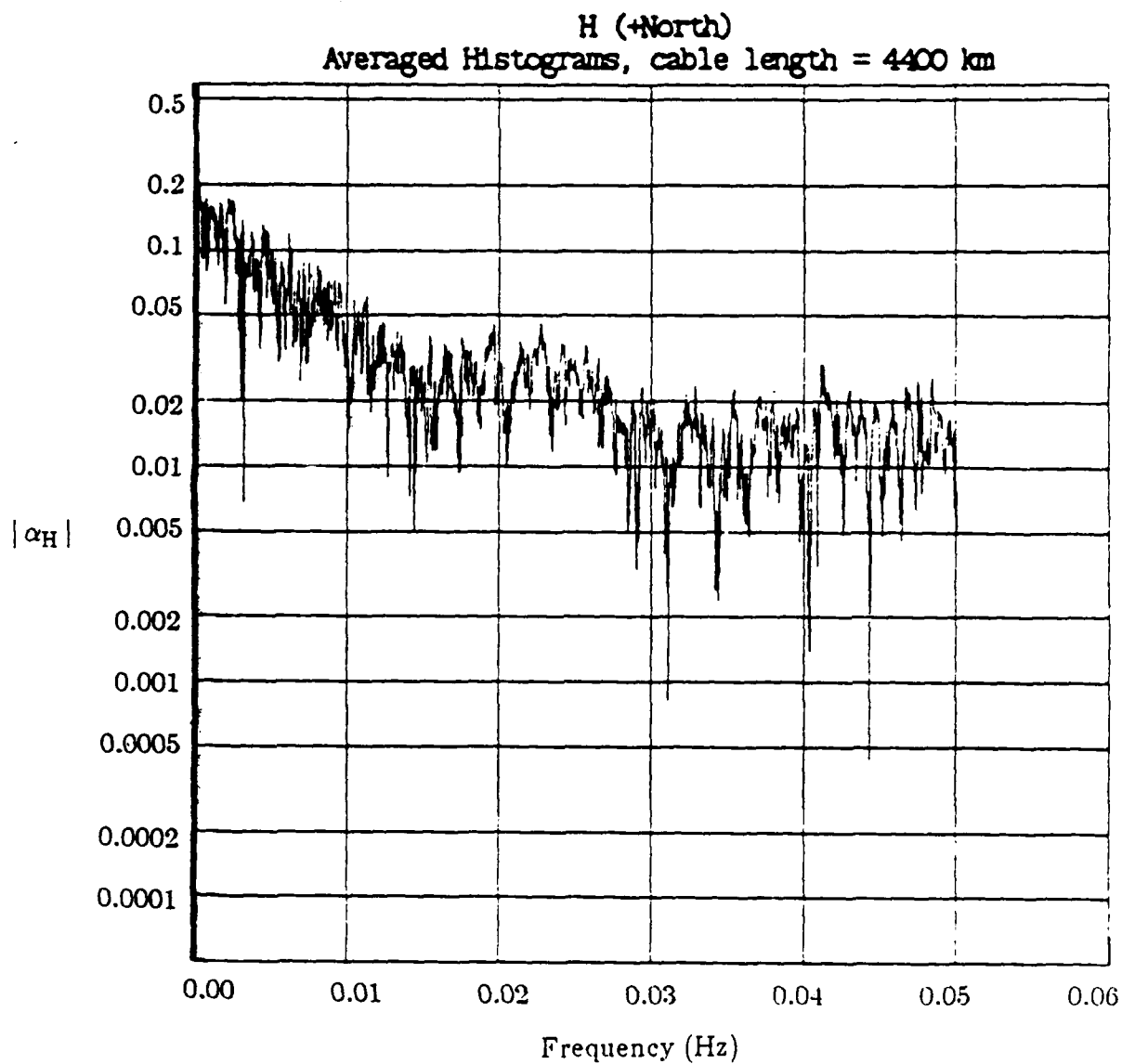


Fig. 3.23c. Magnitude of transfer function  $\alpha_H$  for TAT-7 at 4400 km. all data.

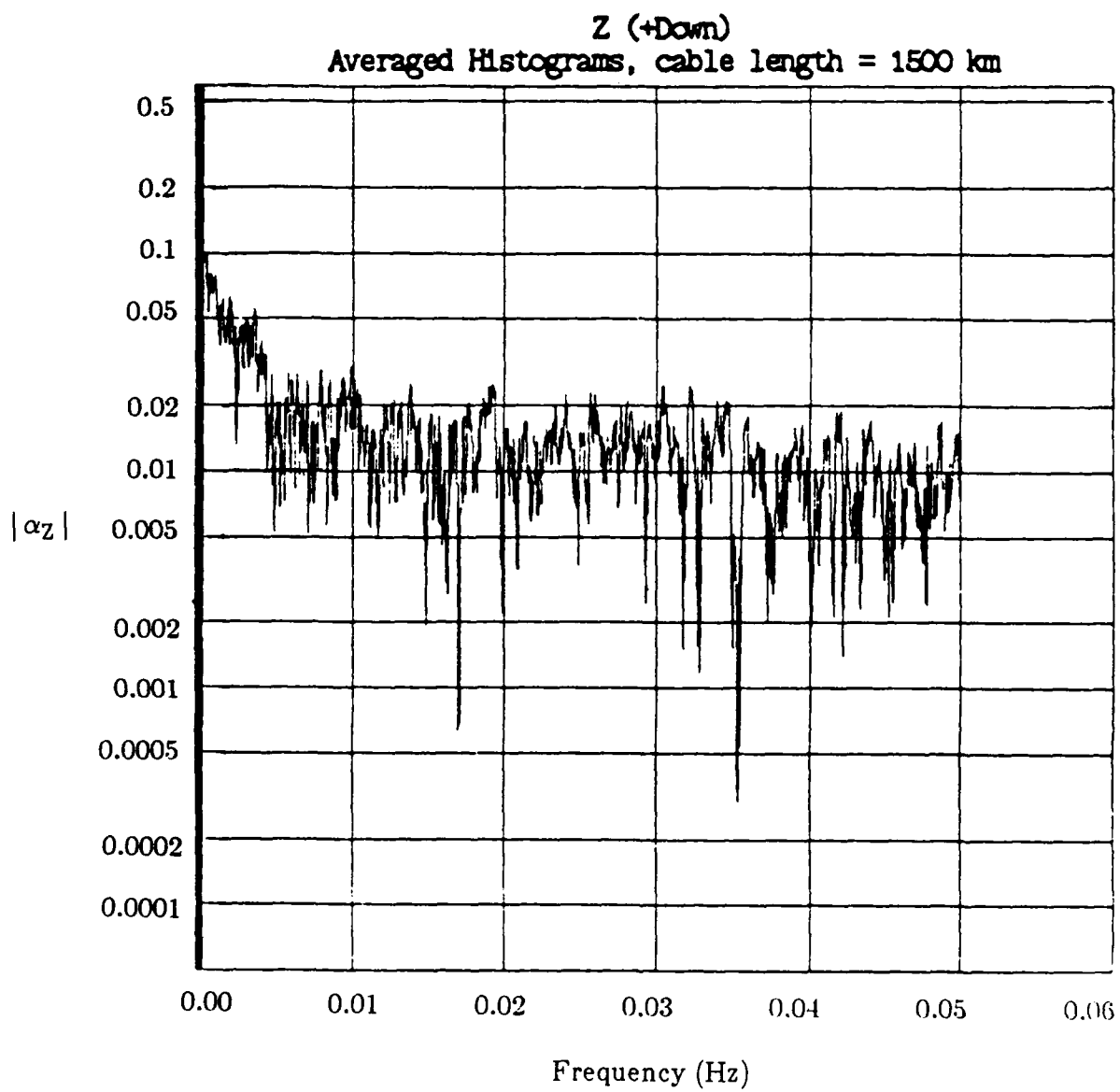


Fig. 3.24a. Magnitude of transfer function  $\alpha_z$  for TAT-7 at 1500 km, all data.

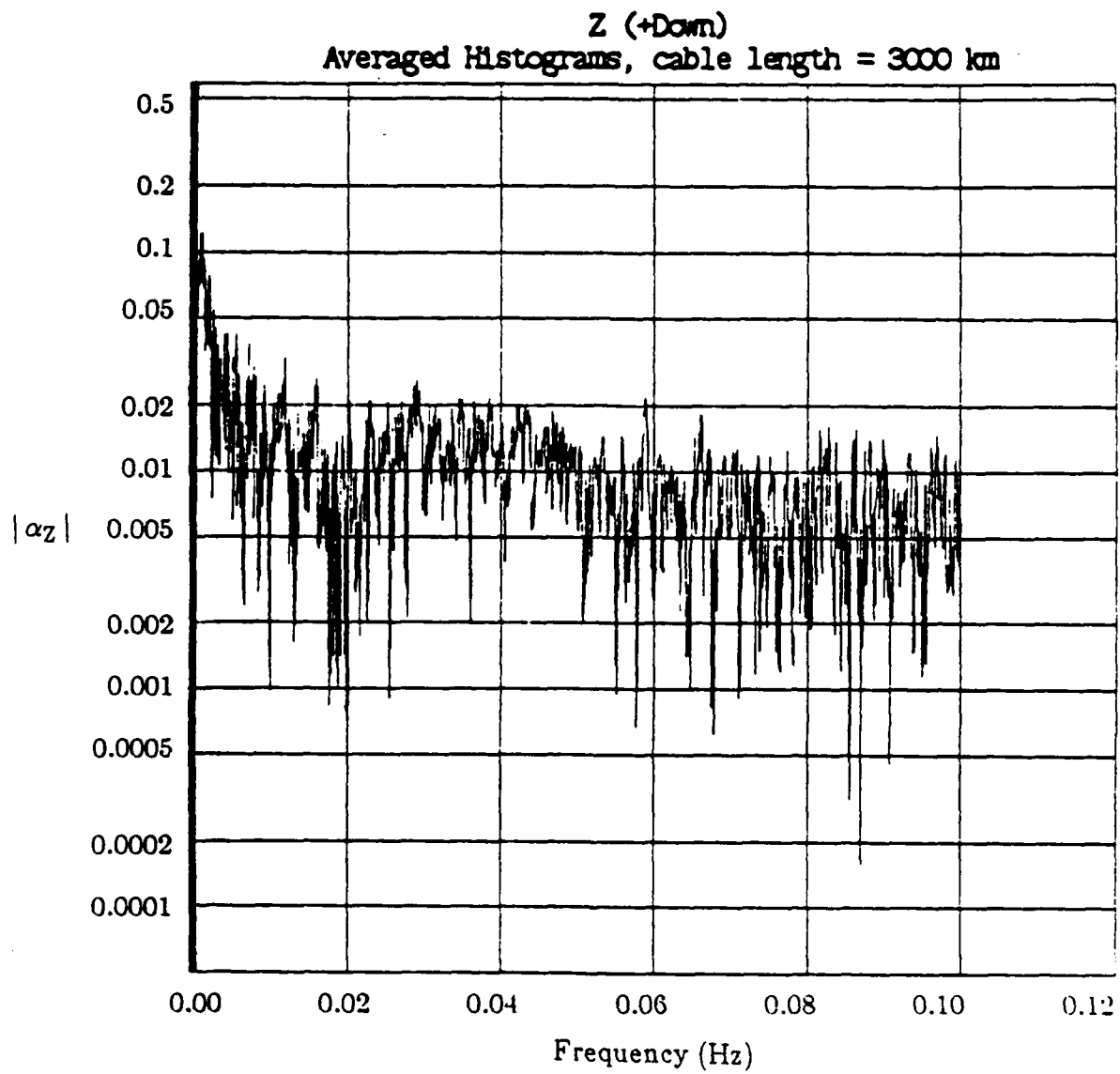


Fig. 3.24b. Magnitude of transfer function  $\alpha_z$  for TAT-7 at 3000 km. all data.

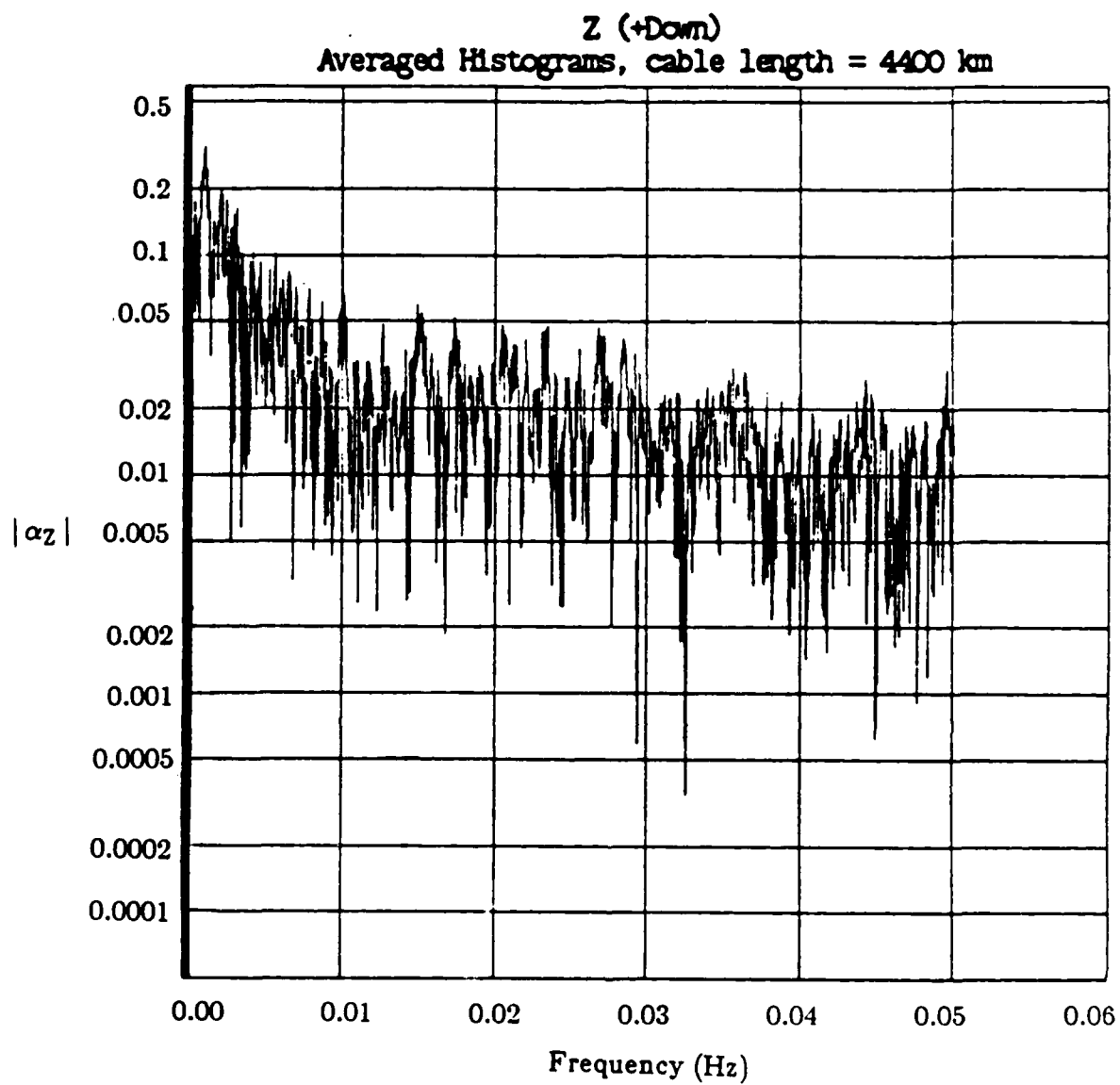


Fig. 3.24c. Magnitude of transfer function  $\alpha_z$  for TAT-7 at 4400 km, all data.



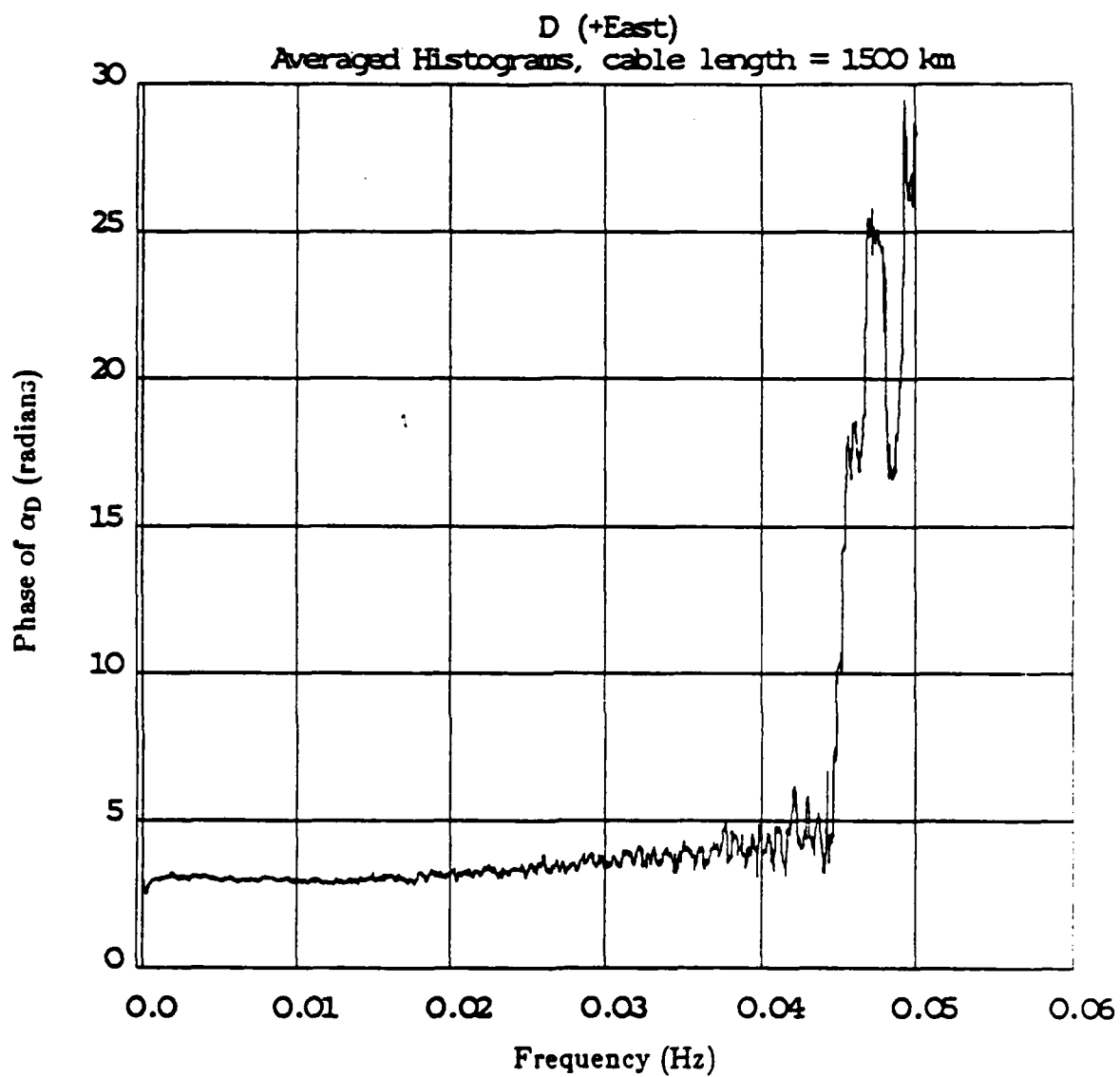


Fig. 3.25a. Phase of transfer function  $\alpha_D$  for TAT-7 at 1500 km, all data.

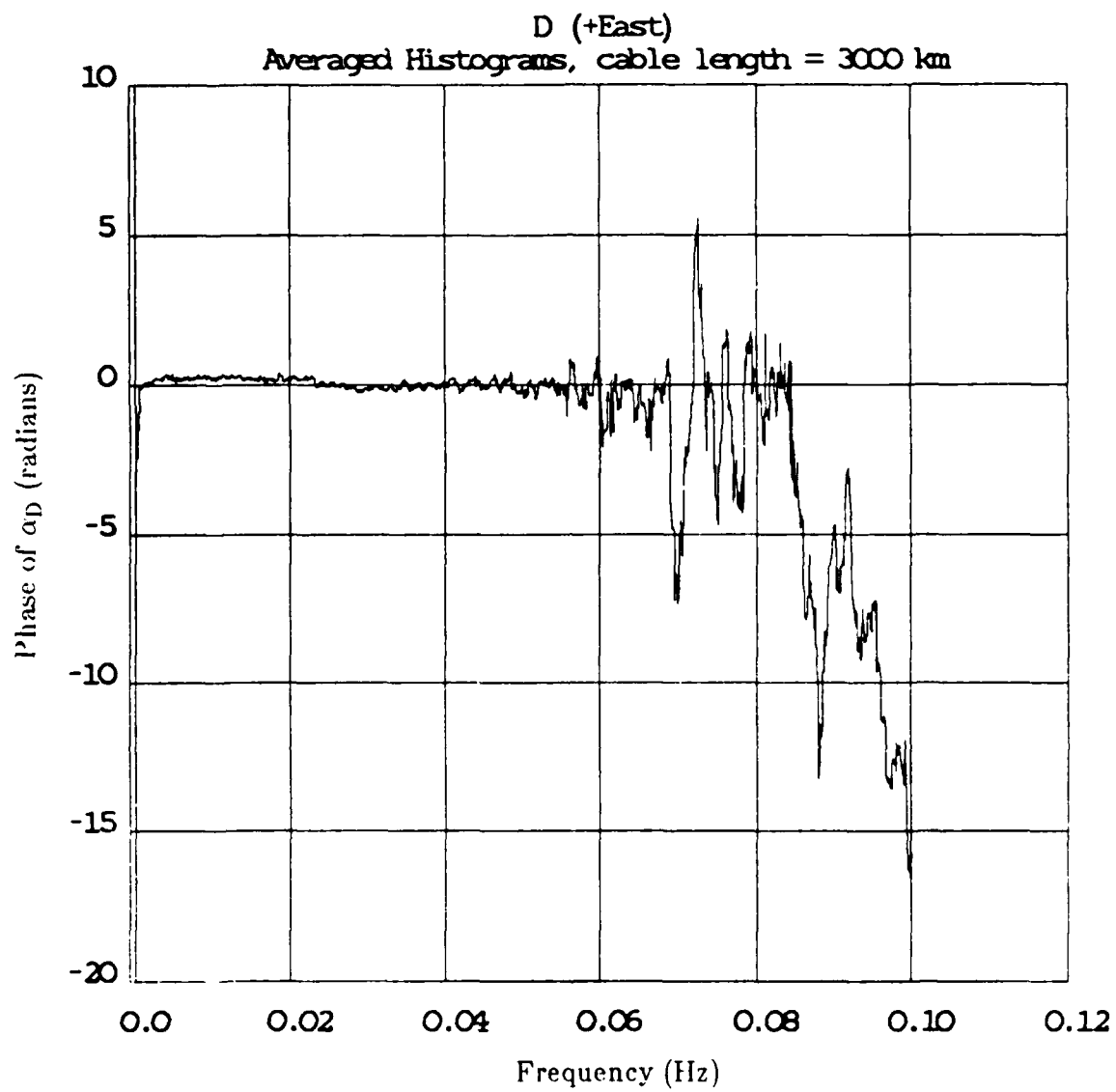


Fig. 3.25b. Phase of transfer function  $\alpha_D$  for TAT-7 at 3000 km, all data.

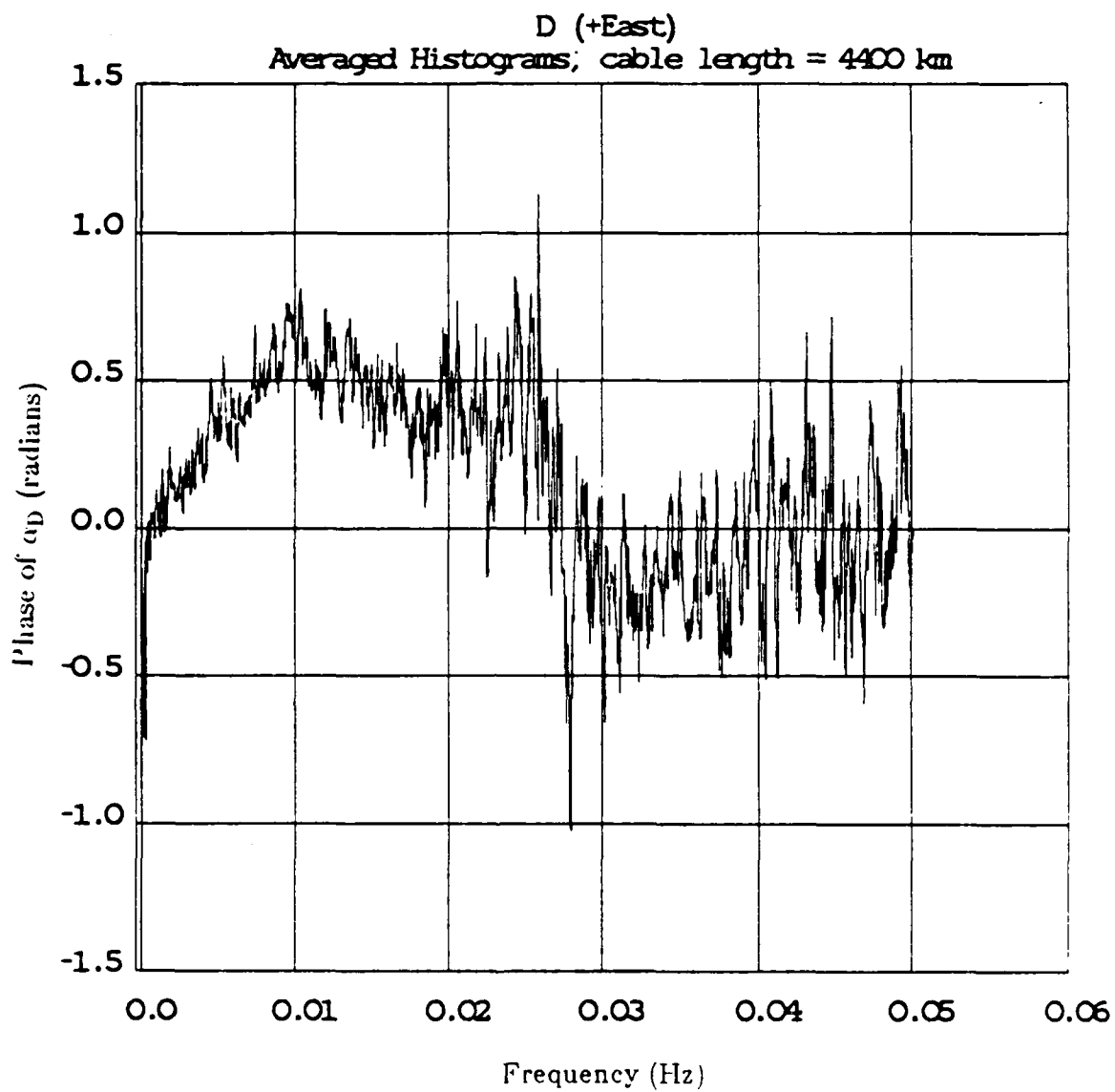


Fig. 3.25c. Phase of transfer function  $\alpha_D$  for TAT-7 at 4400 km. all data.

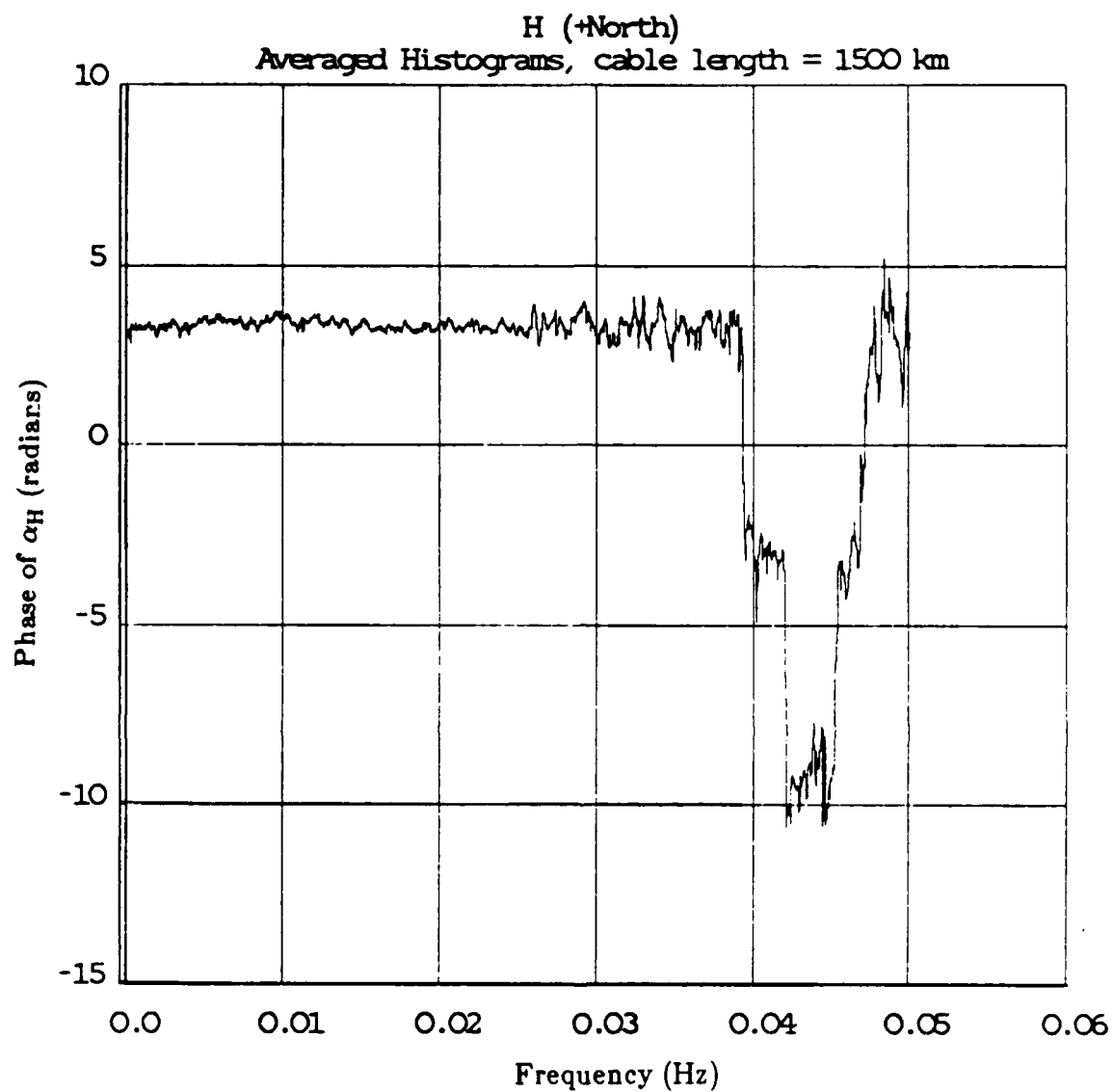


Fig. 3.26a. Phase of transfer function  $\alpha_H$  for TAT-7 at 1500 km, all data.

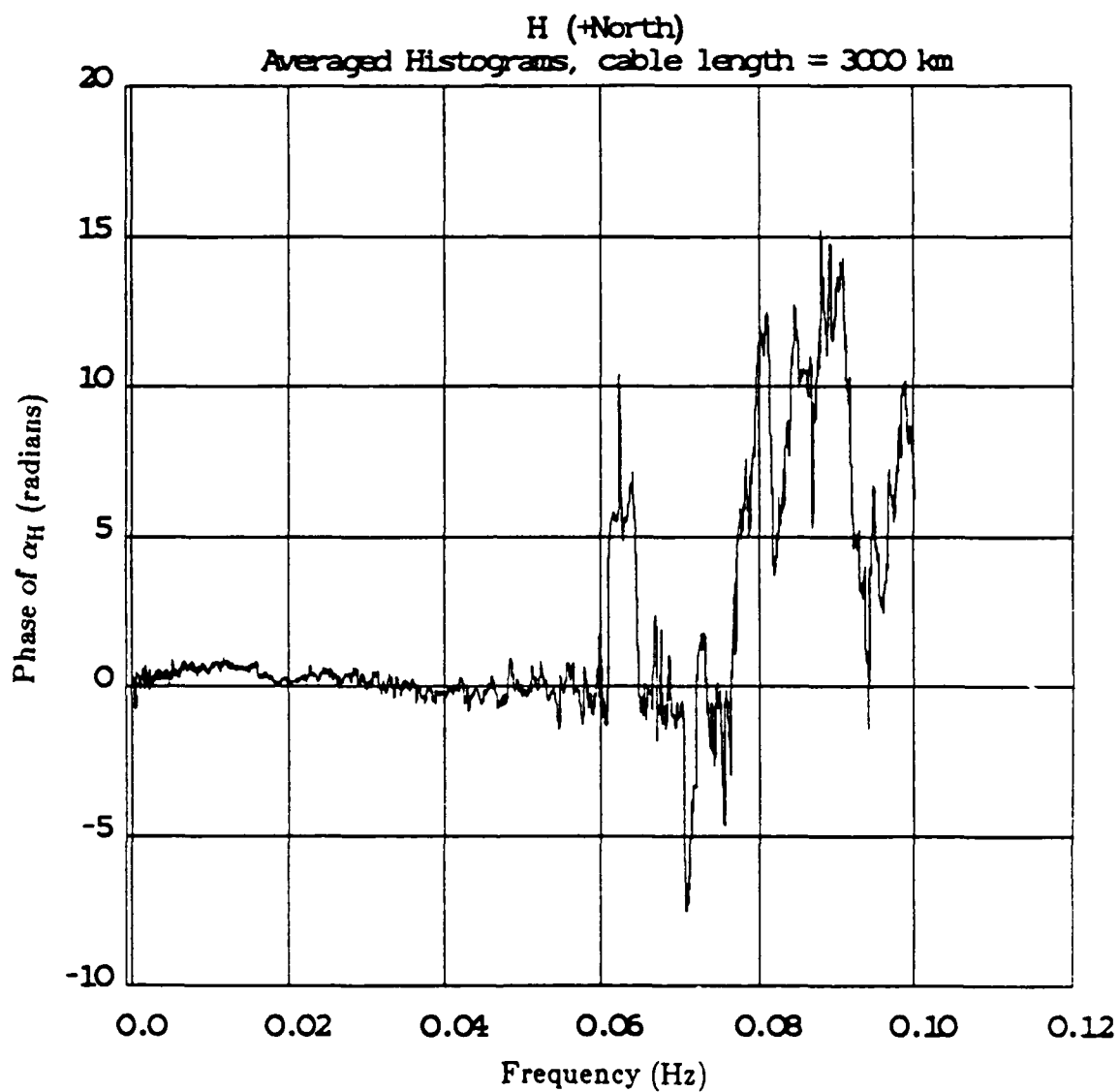


Fig. 3.26b. Phase of transfer function  $\alpha_H$  for TAT-7 at 3000 km, all data.

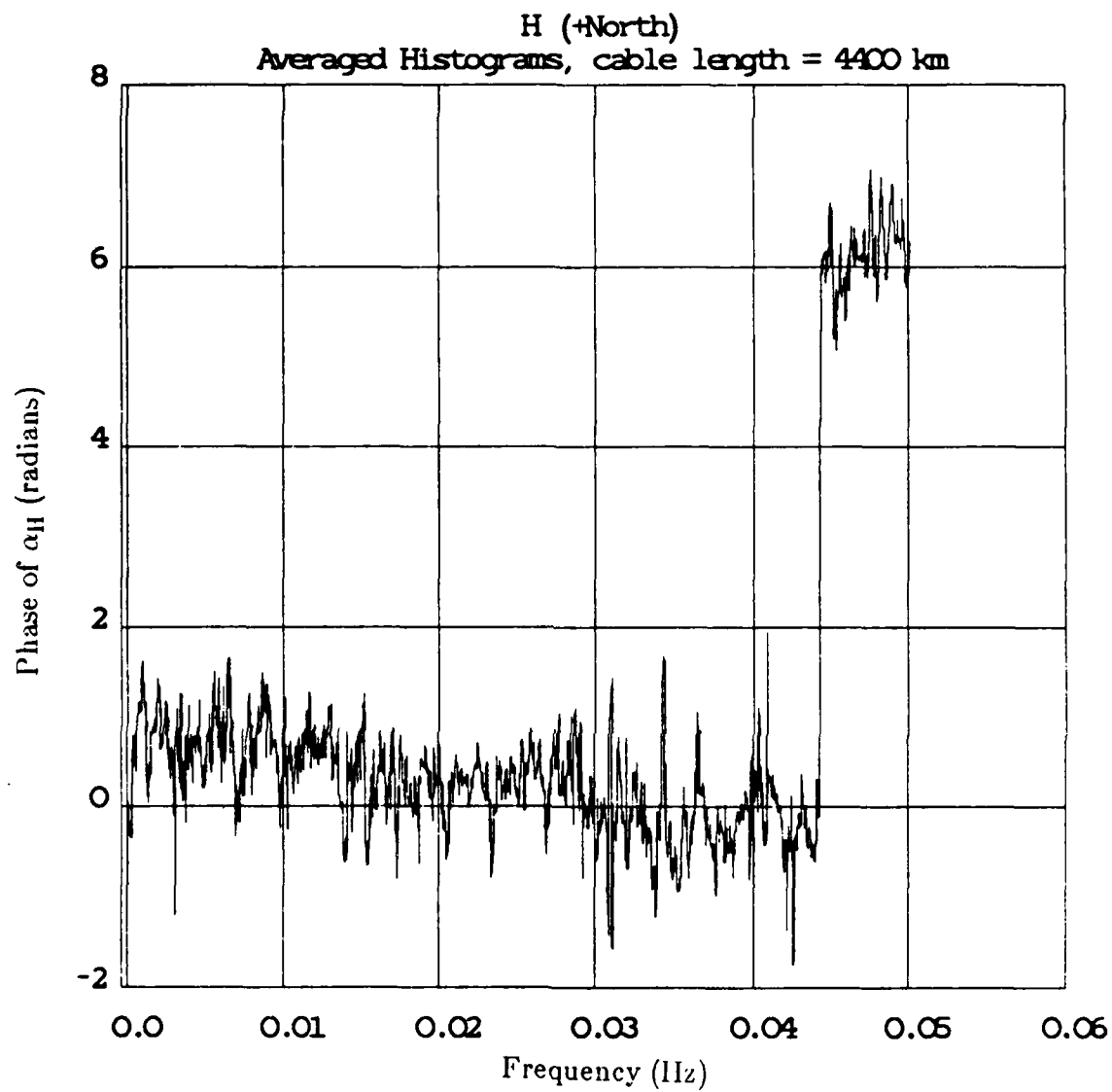


Fig. 3.26c. Phase of transfer function  $\alpha_H$  for TAT-7 at 4400 km, all data.

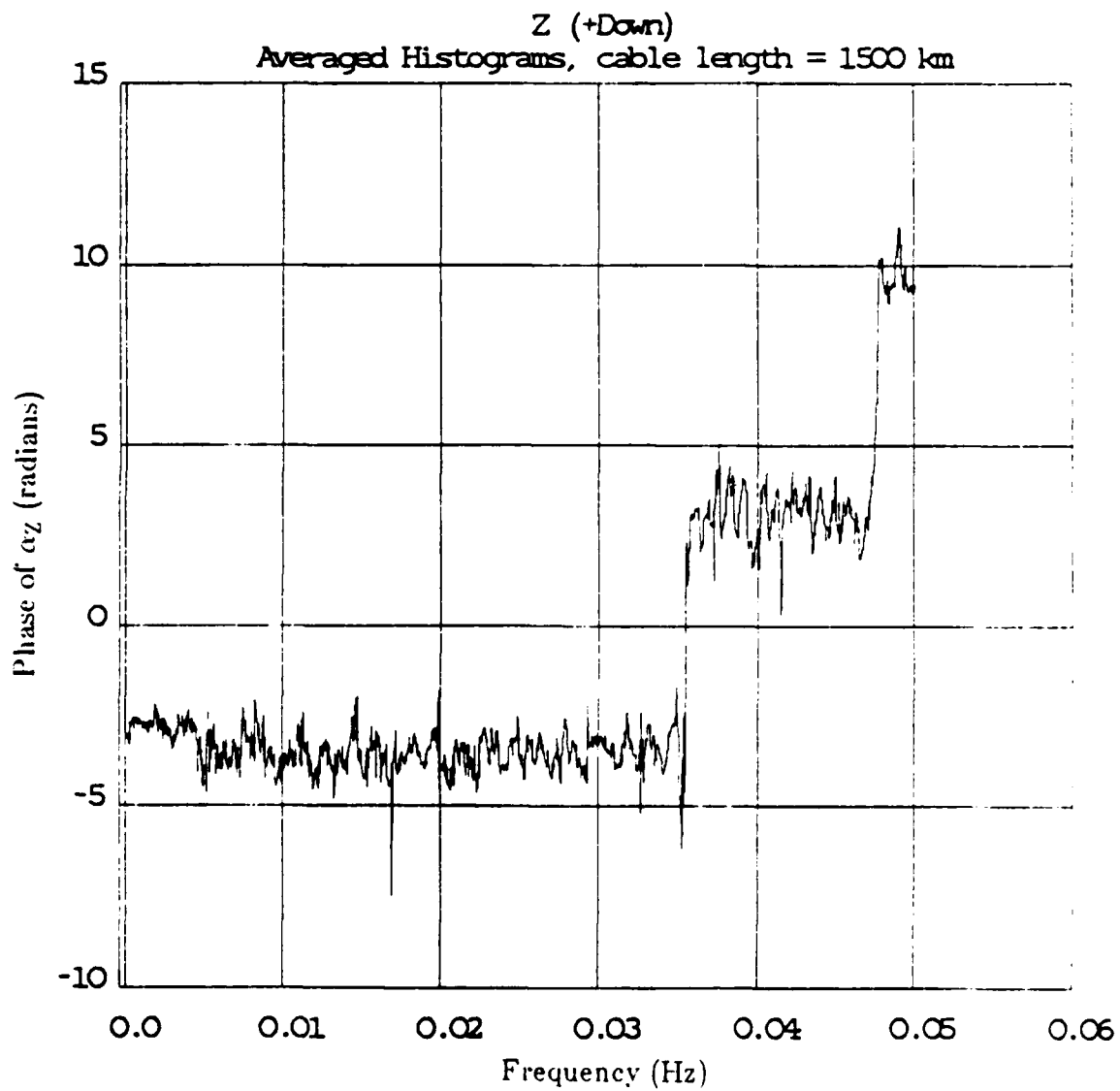


Fig. 3.27a. Phase of transfer function  $\alpha_z$  for TAT-7 at 1500 km. all data.

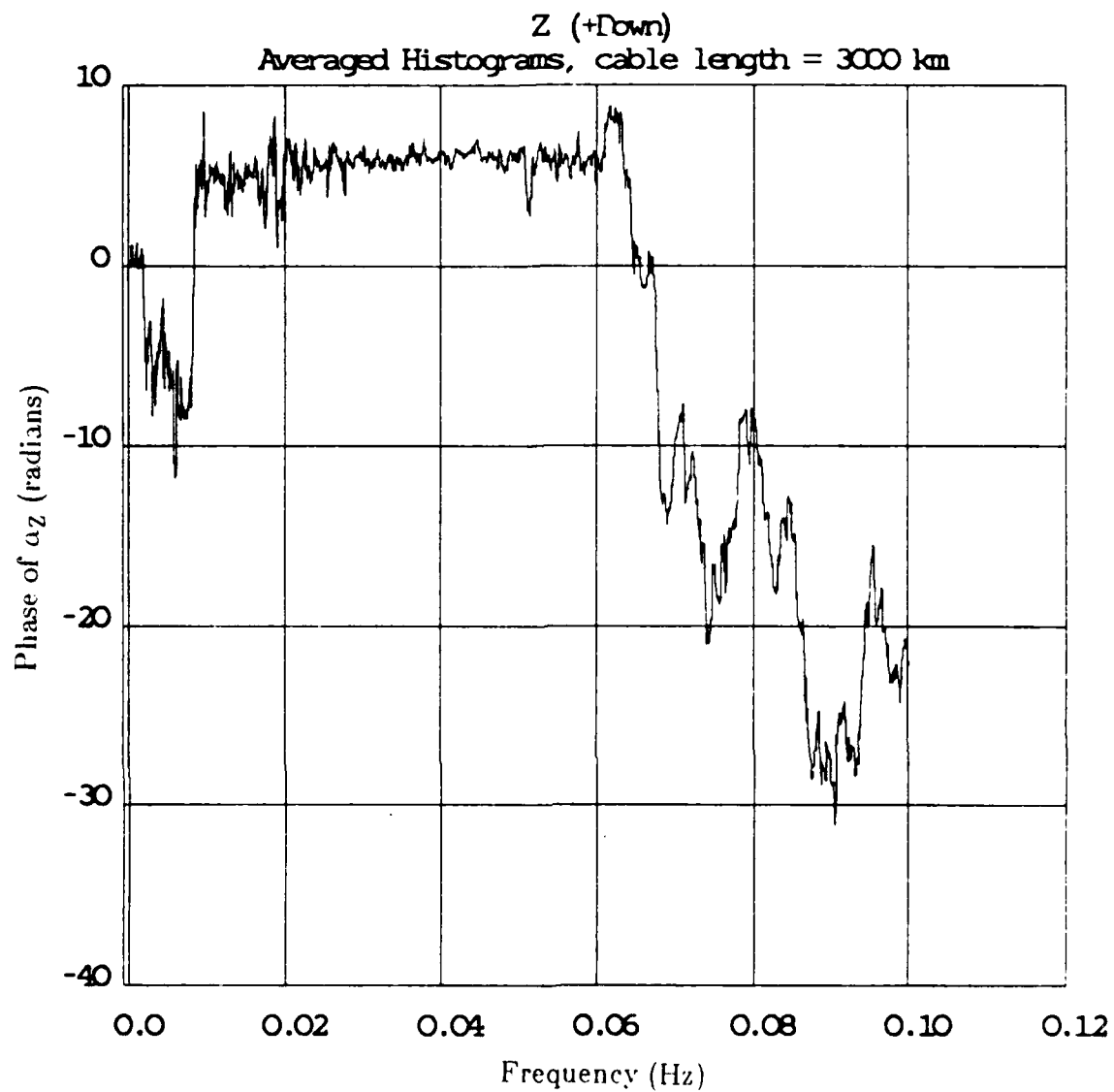


Fig. 3.27b. Phase of transfer function  $\alpha_z$  for TAT-7 at 3000 km, all data.



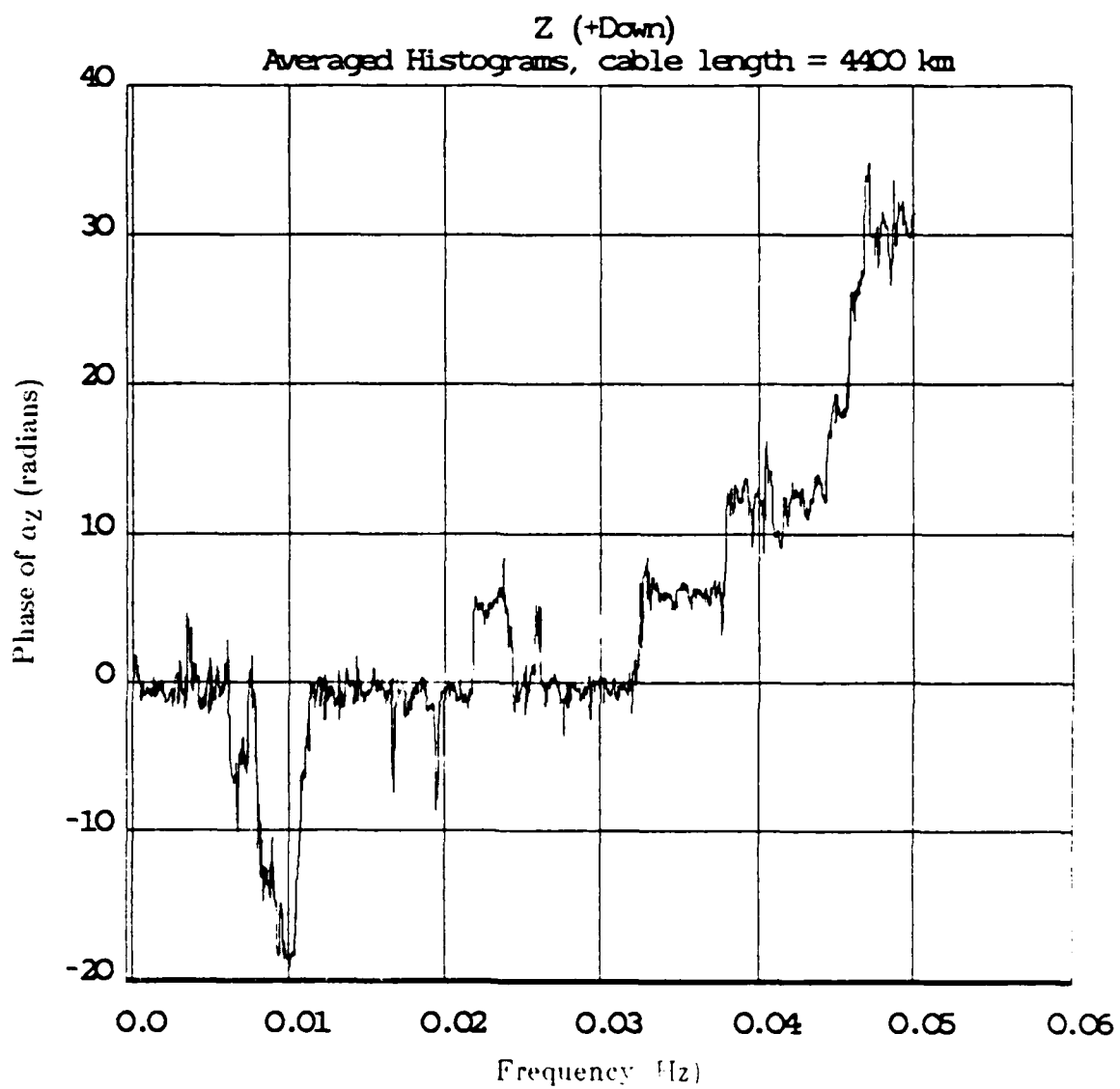


Fig. 3.27c. Phase of transfer function  $\alpha_z$  for TAT-7 at 4400 km, all data.

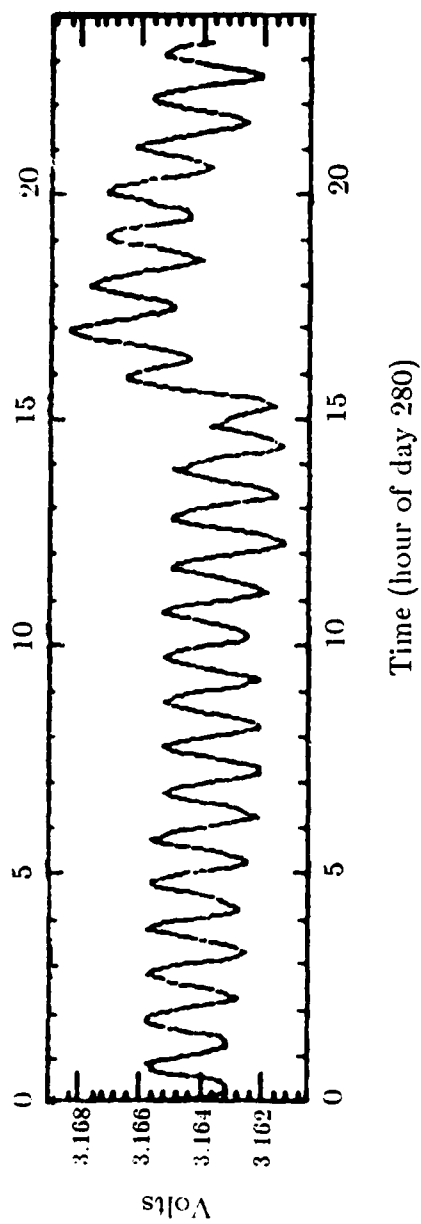


Fig. 3.28. Temperature fluctuations in the Tuckerton station exhibiting the air conditioning unit cycling related to the noise problems for the powered TAT-7 data taken in late 1986.

TAT-4 D (+East), 2sec, 86.279.3-5, 25km

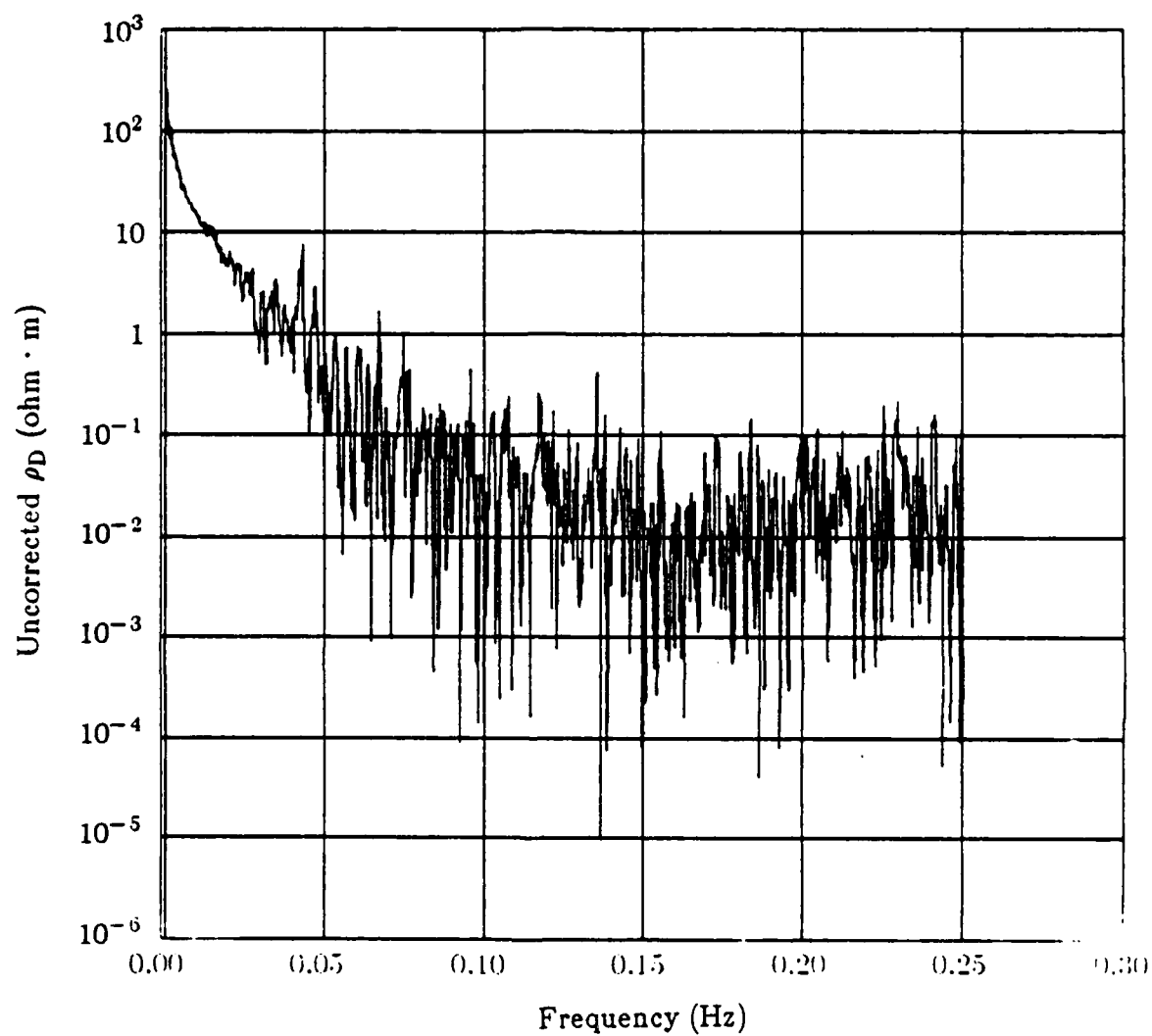


Fig. 3.29a. Effective resistivity  $\rho_D$  (2 hrs, TAT-4 at 25 km).

TAT-4 H (+North), 2sec, 86.279.3-5, 25km

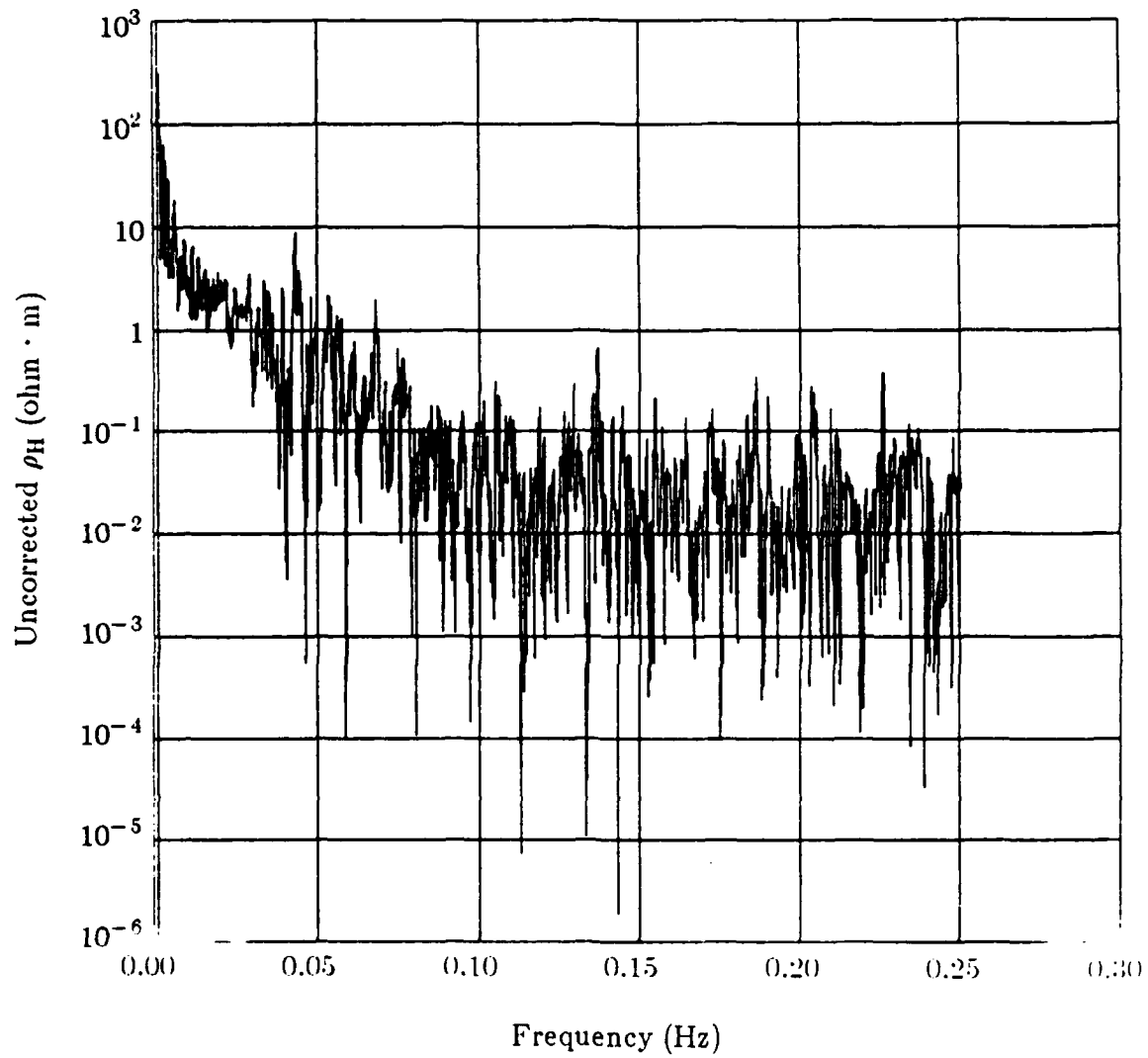


Fig. 3.29b. Effective resistivity  $\rho_H$  (2 hrs, TAT-4 at 25 km).

TAT-4 Z (+Down), 2sec, 86.279.3-5, 25km

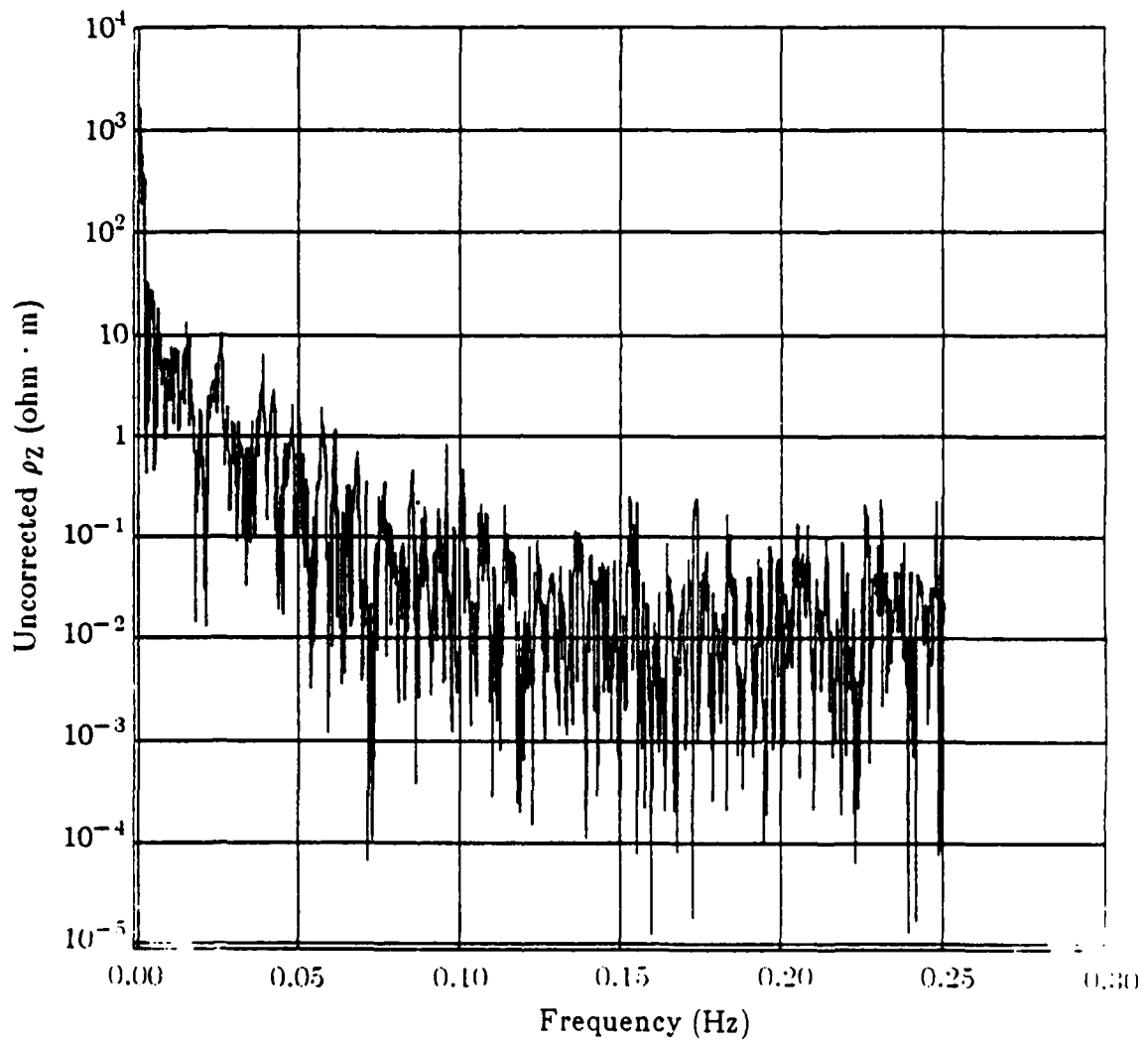


Fig. 3.29c. Effective resistivity  $\rho_z$  (2 hrs, TAT-4 at 25 km).

TAT-4 Induced Voltage and D (+East), 2 second, 86.279.3-5, 25 km

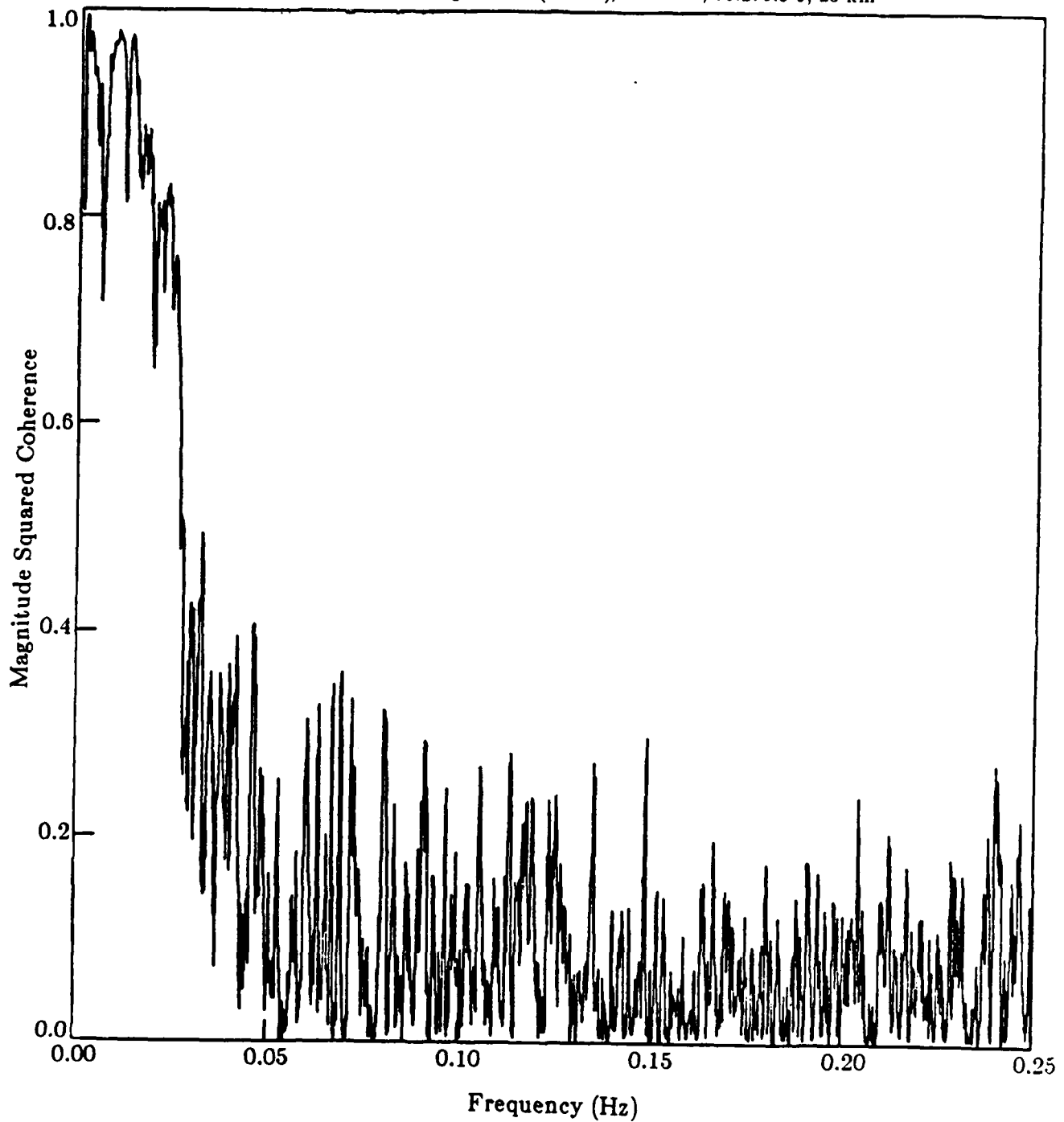


Fig. 3.30a. Magnitude squared coherence for V and D (2 hrs, TAT-4 at 25 km).

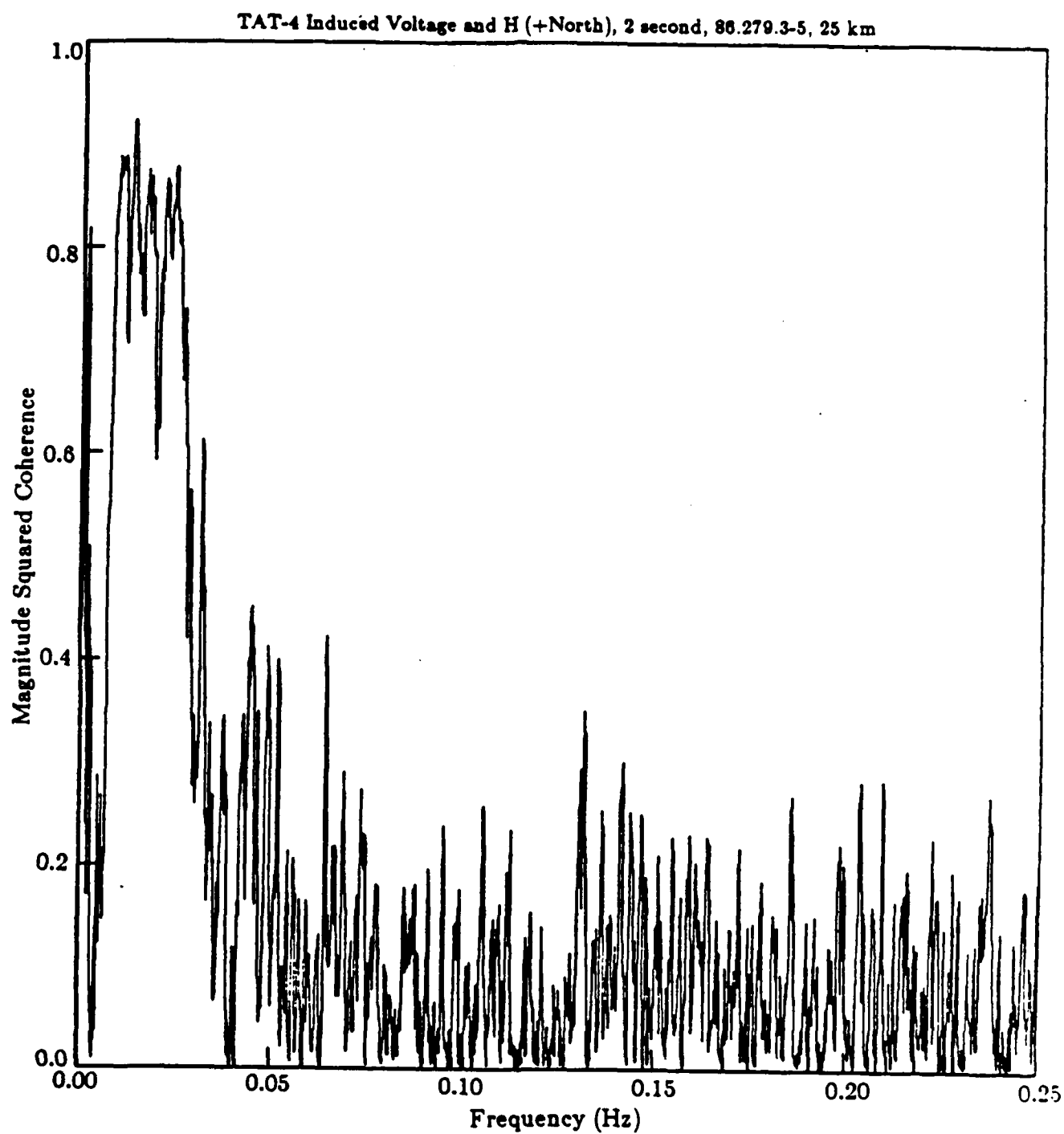


Fig. 3.30b. Magnitude squared coherence for V and H (2 hrs, TAT-4 at 25 km).

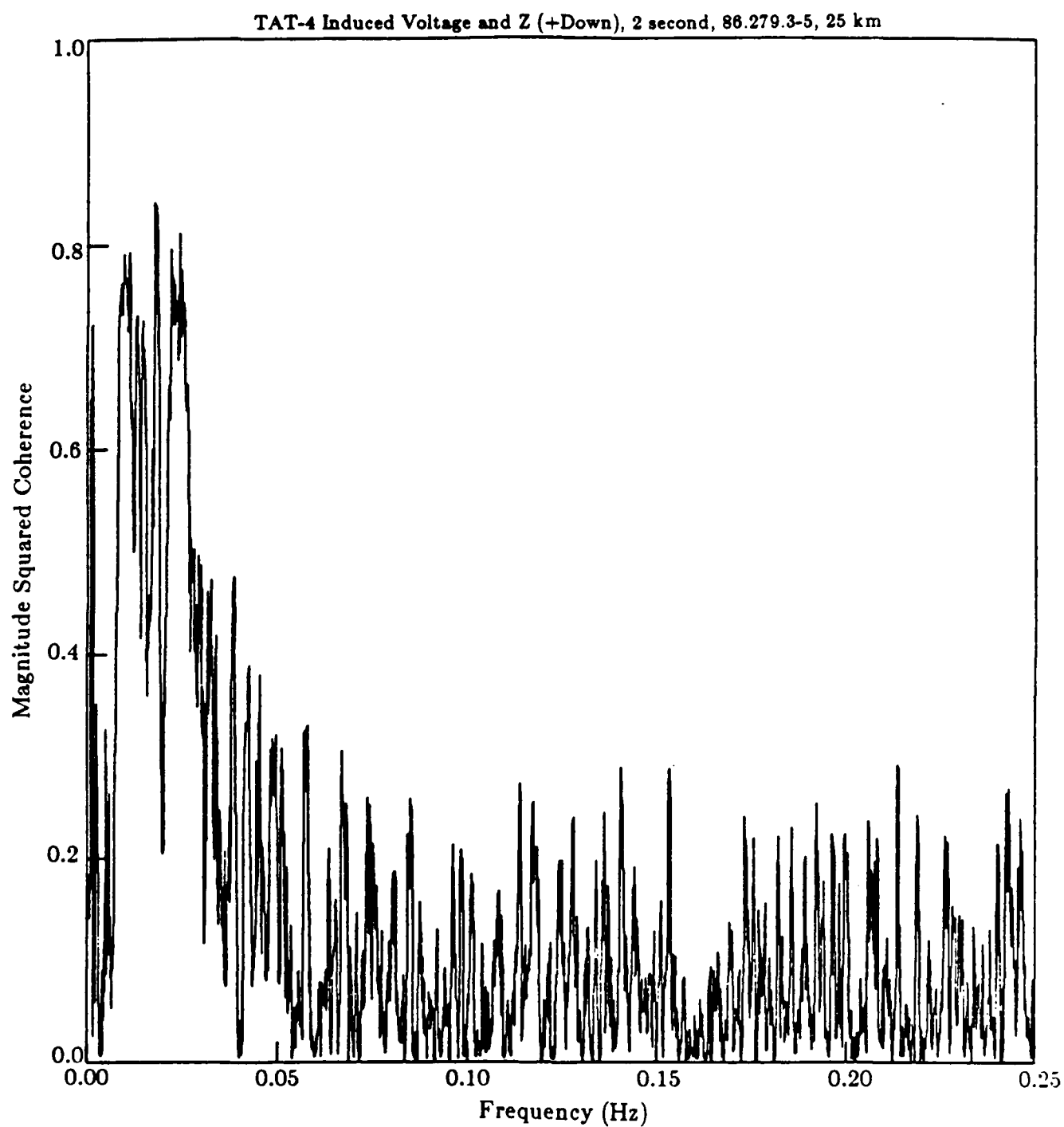
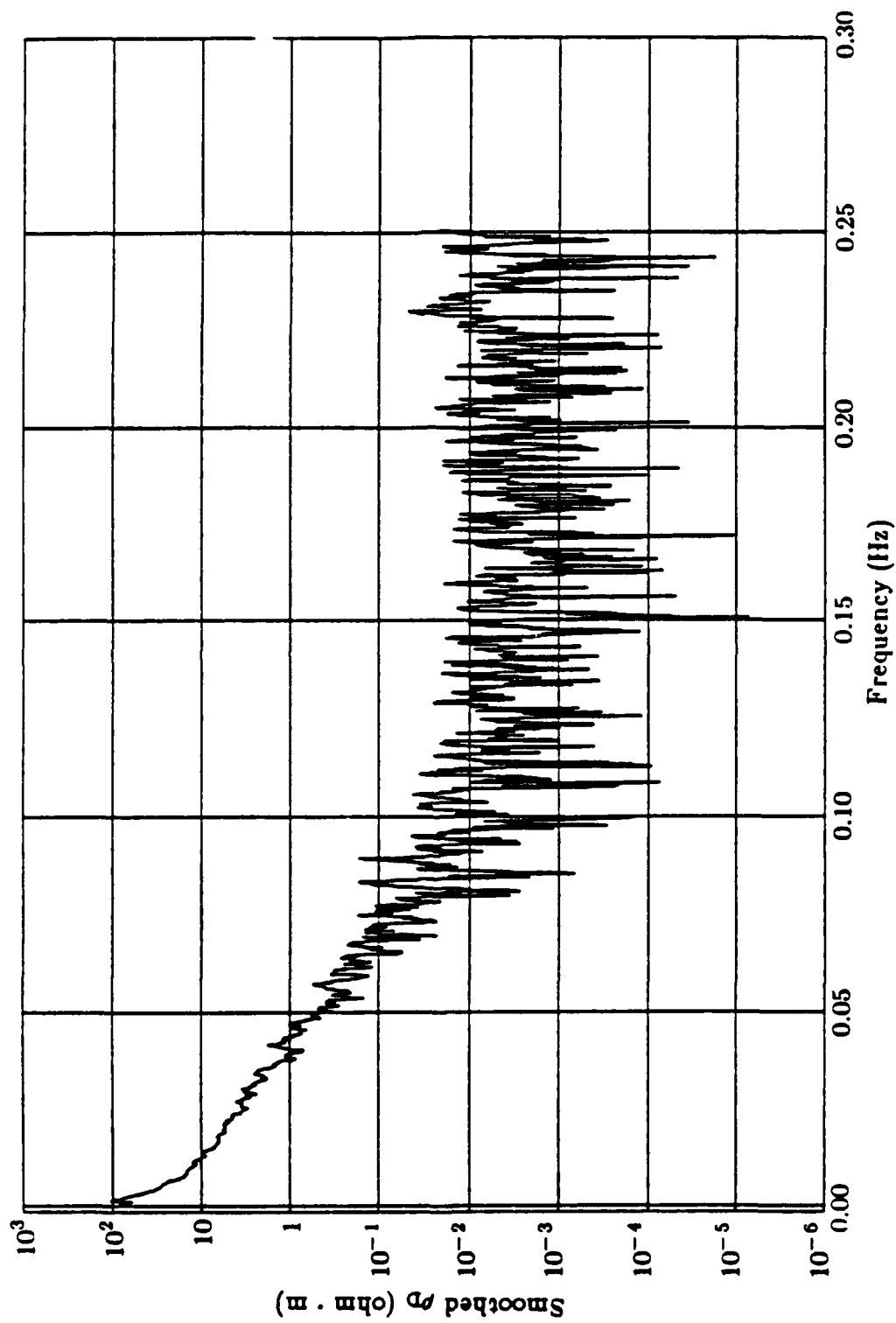


Fig. 3.30c. Magnitude squared coherence for V and Z (2 hrs, TAT-4 at 25 km).



**TAT4 Day 279 1986 Cable Effective Resistivity  
Calculated from Averaged Transfer Functions  
D (+East)**



**Fig. 3.31a. Smoothed effective resistivity  $\rho_p$  (day 270, TAT-4 at 25 km).**

TAT4 Day 279 1986 Cable Effective Resistivity  
 Calculated from Averaged Transfer Functions  
 H (+North)

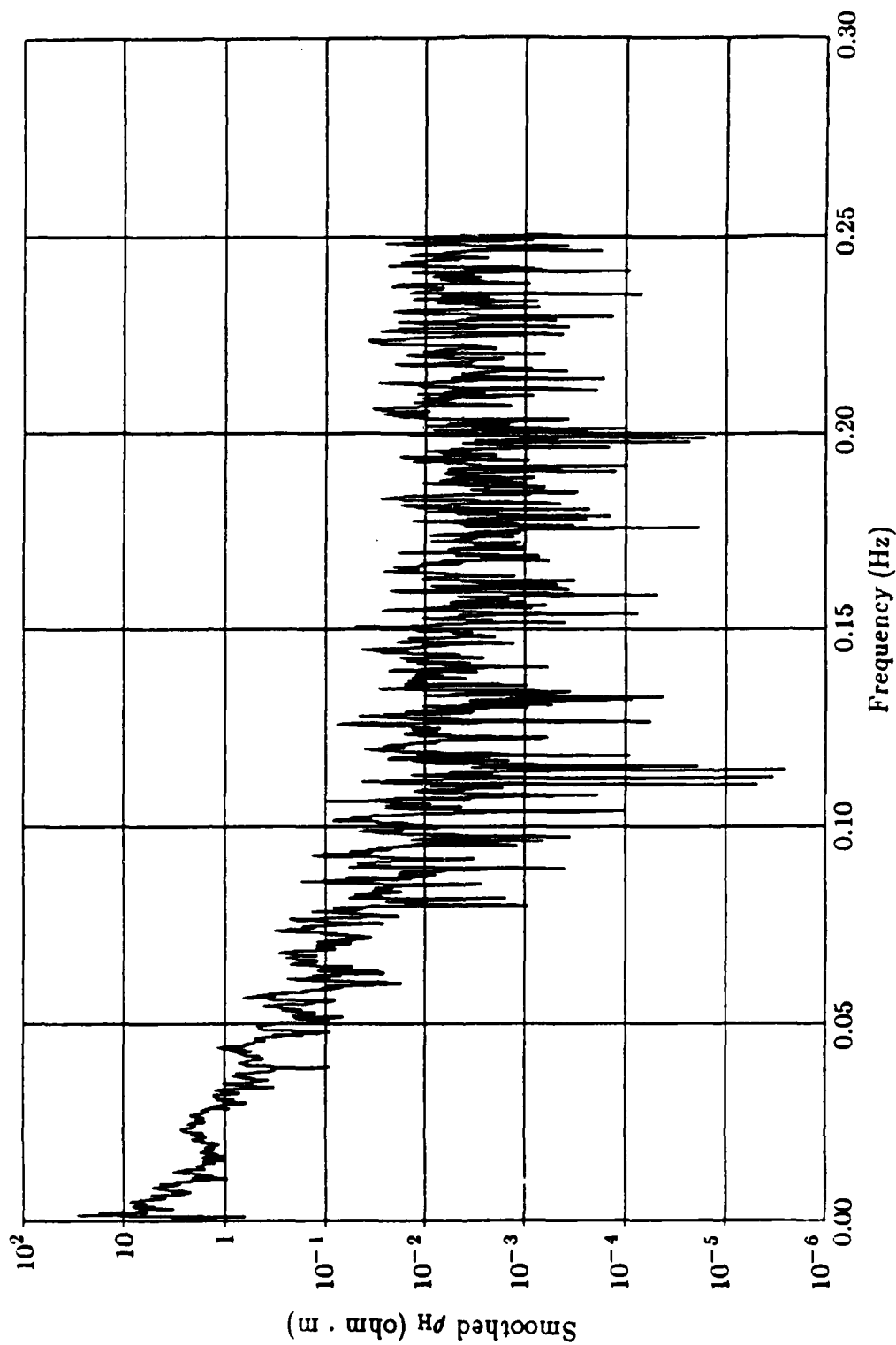


Fig. 3.31b. Smoothed effective resistivity  $\rho_H$  (day 279, TAT-4 at 25 km).

TAT4 Day 279 1986 Cable Effective Resistivity  
Calculated from Averaged Transfer Functions  
Z (+Down)

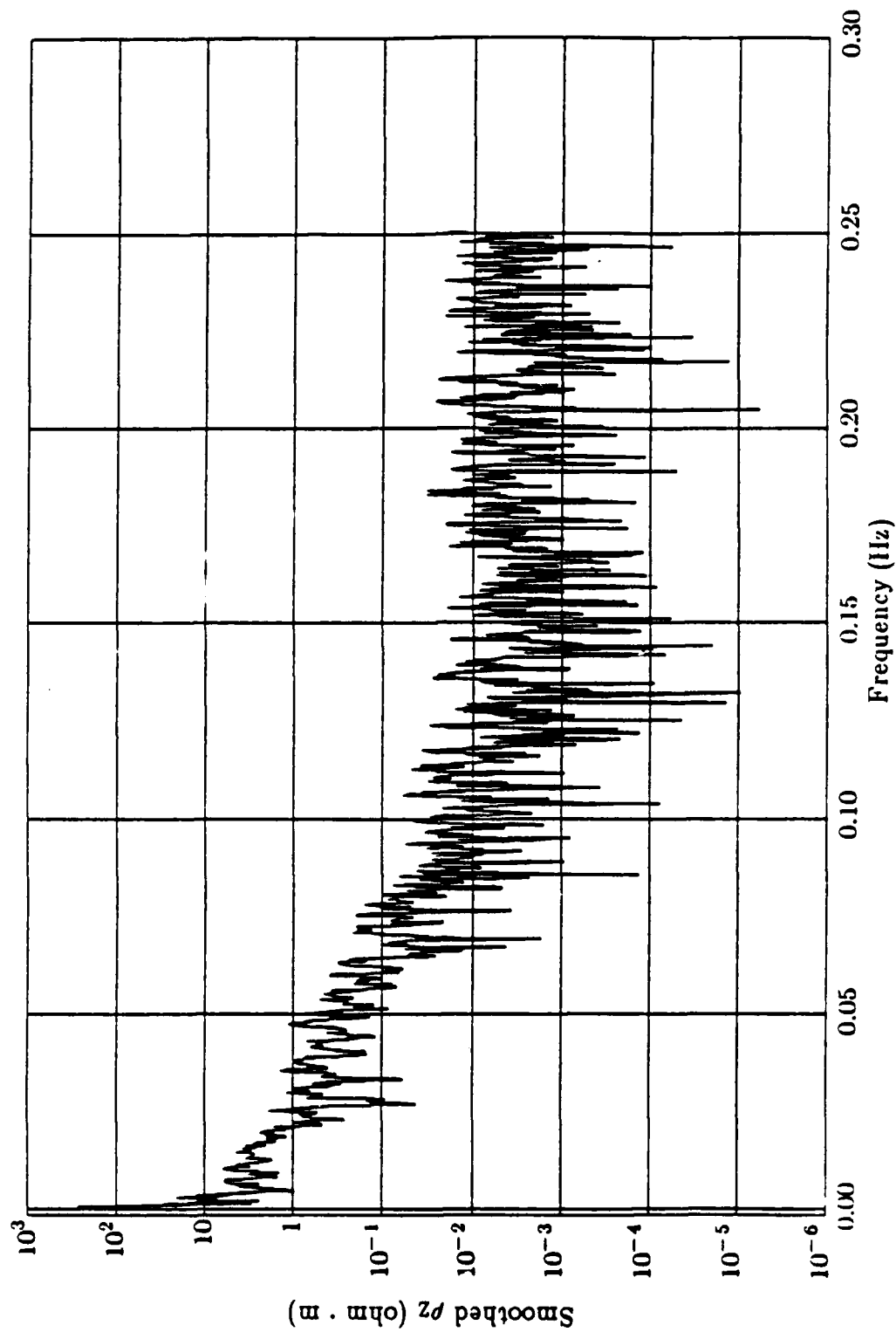


Fig. 3.31c. Smoothed effective resistivity  $\rho_z$  (day 279, TAT-4 at 25 km).

TAT4 Day 280 1986 Cable Effective Resistivity  
Calculated from Averaged Transfer Functions  
D (+East)

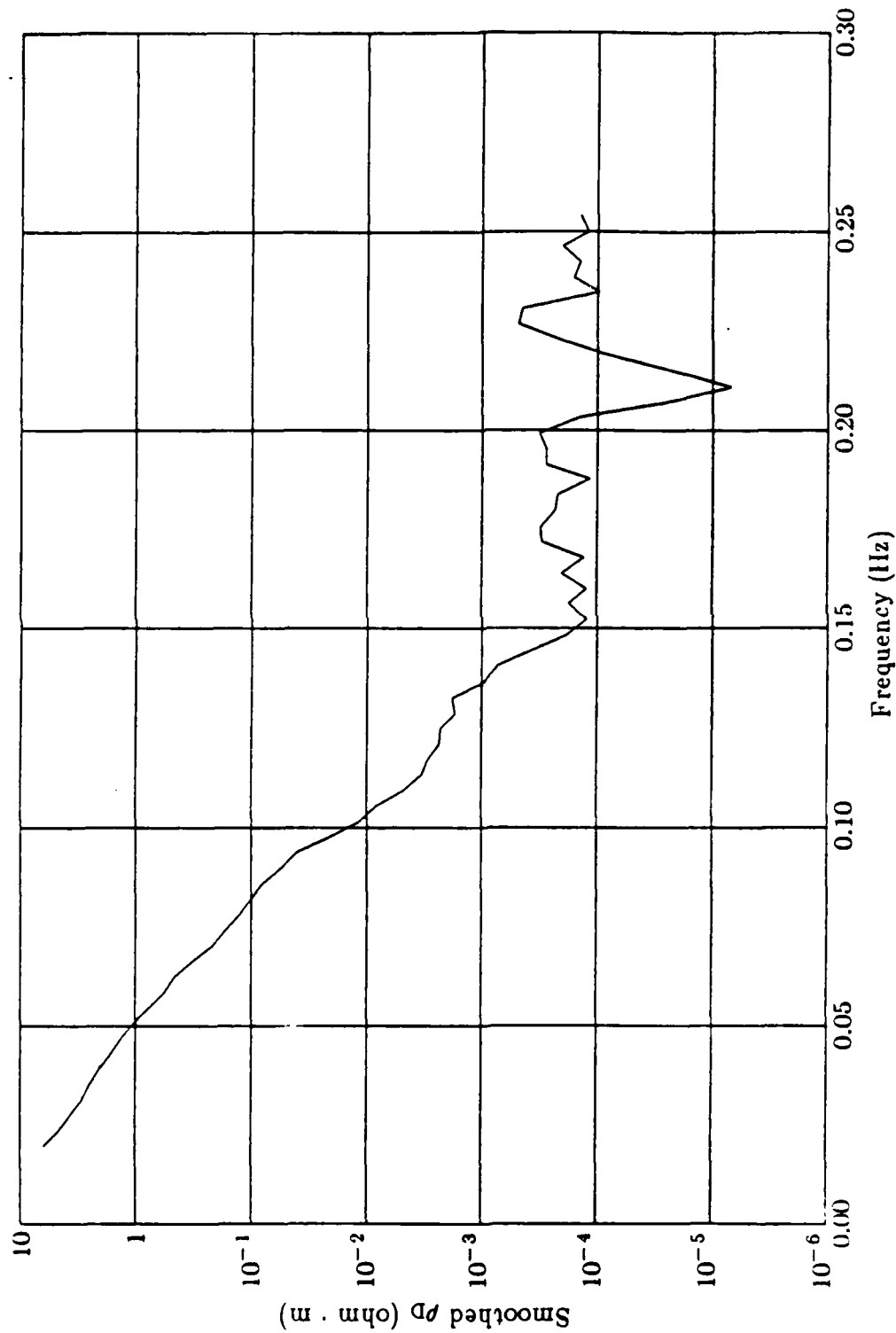


Fig. 3.32a. Smoothed effective resistivity  $\rho_D$  (day 280, TAT-4 at 25 km).

TAT4 Day 280 1986 Cable Effective Resistivity  
 Calculated from Averaged Transfer Functions  
 H (+North)

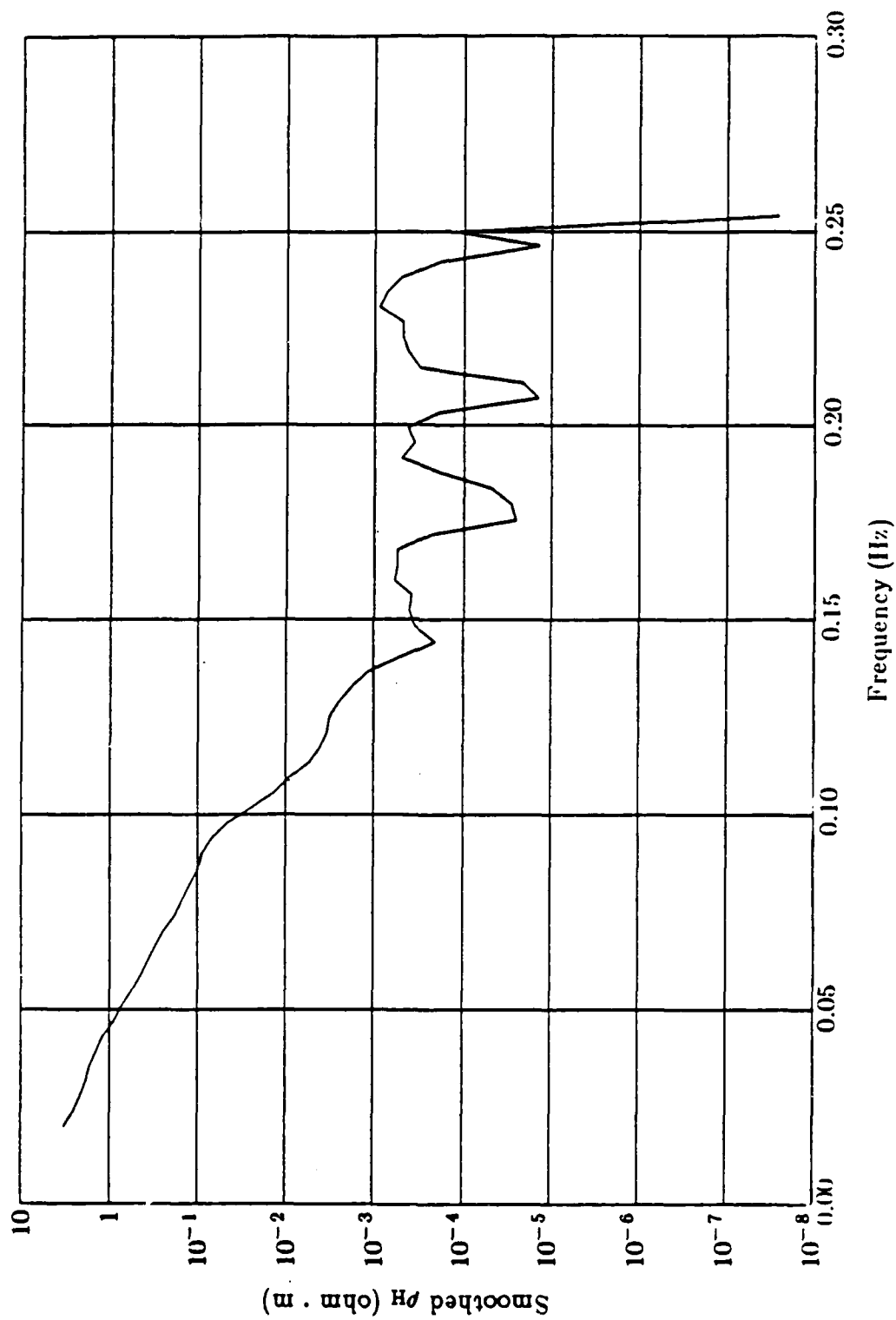


Fig. 3.32b. Smoothed effective resistivity  $\rho_H$  (day 280, TAT-4 at 25 km).

TAT4 Day 280 1986 Cable Effective Resistivity  
Calculated from Averaged Transfer Functions  
Z (+Down)

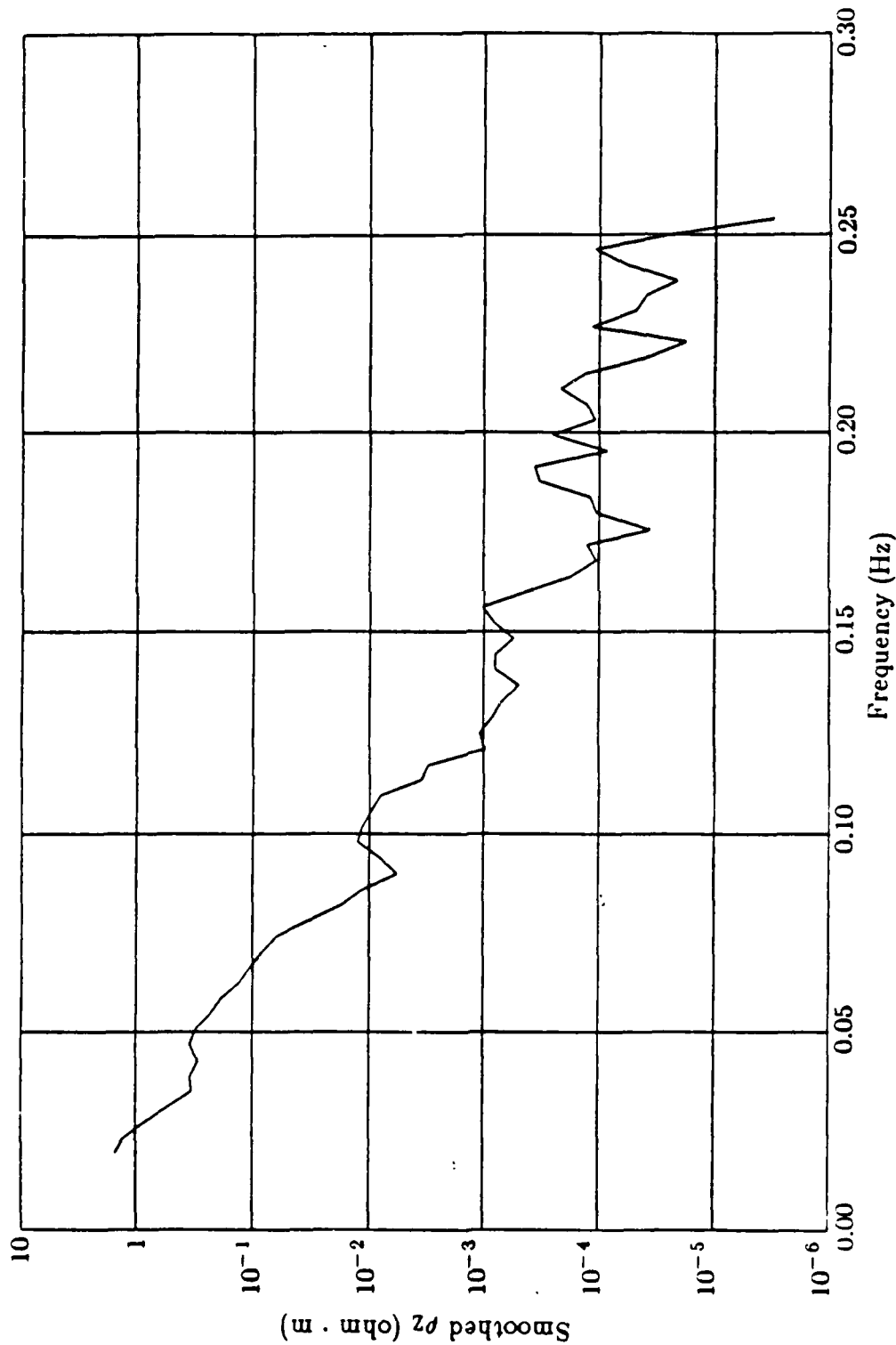


Fig. 3.32c. Smoothed effective resistivity  $\rho_z$  (day 280, TAT-4 at 25 km).

TAT-4 Induced Voltage and D (+East), 2 second, 86.280.3-5, 25 km

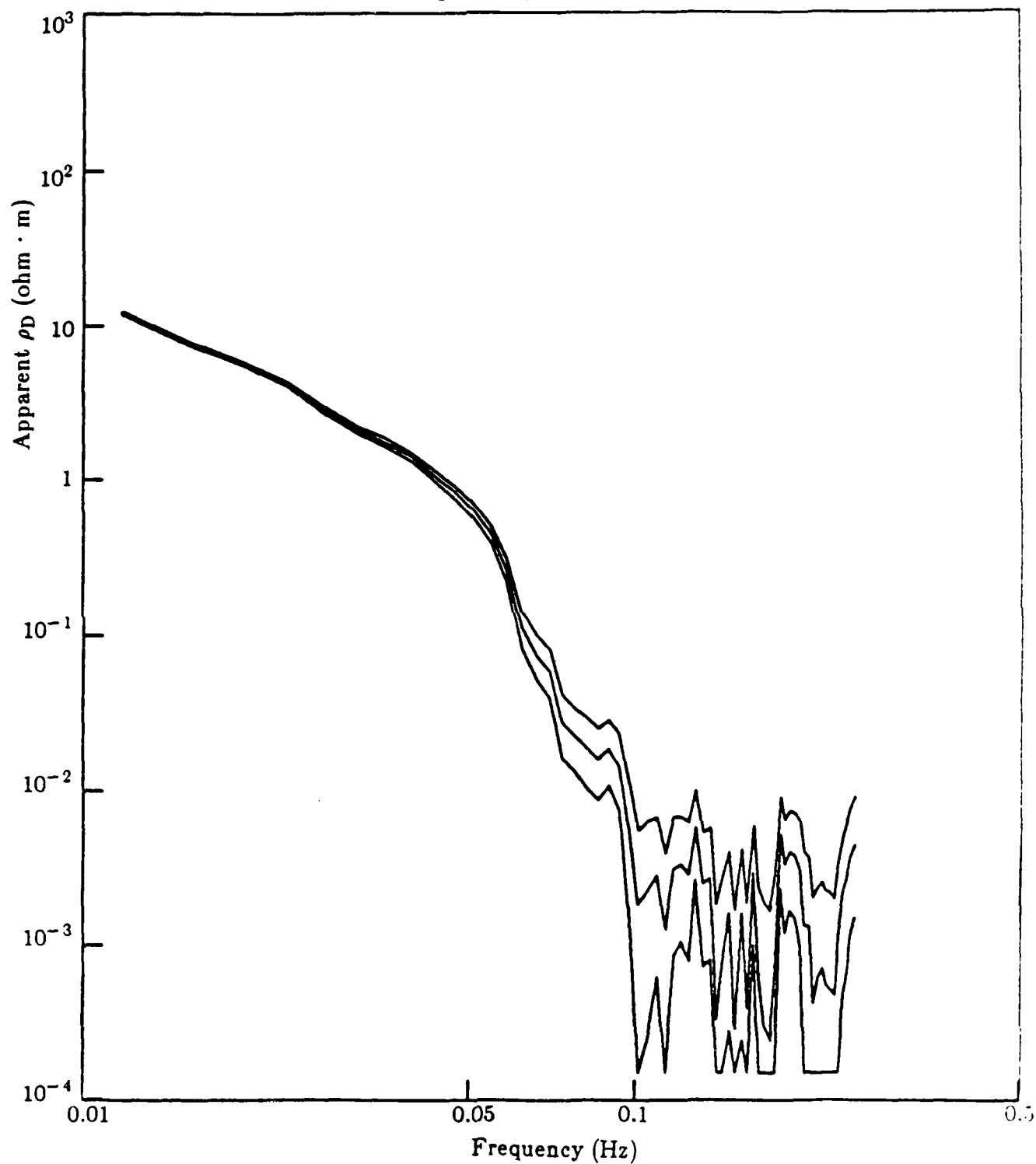


Fig. 3.33a. Smoothed effective resistivity  $\rho_D$  and  $\pm 1$  standard deviation lines (2 hrs. TAT-4 at 25 km - new program).

TAT-4 Induced Voltage and H (+North), 2 second, 86.280.3-5, 25 km

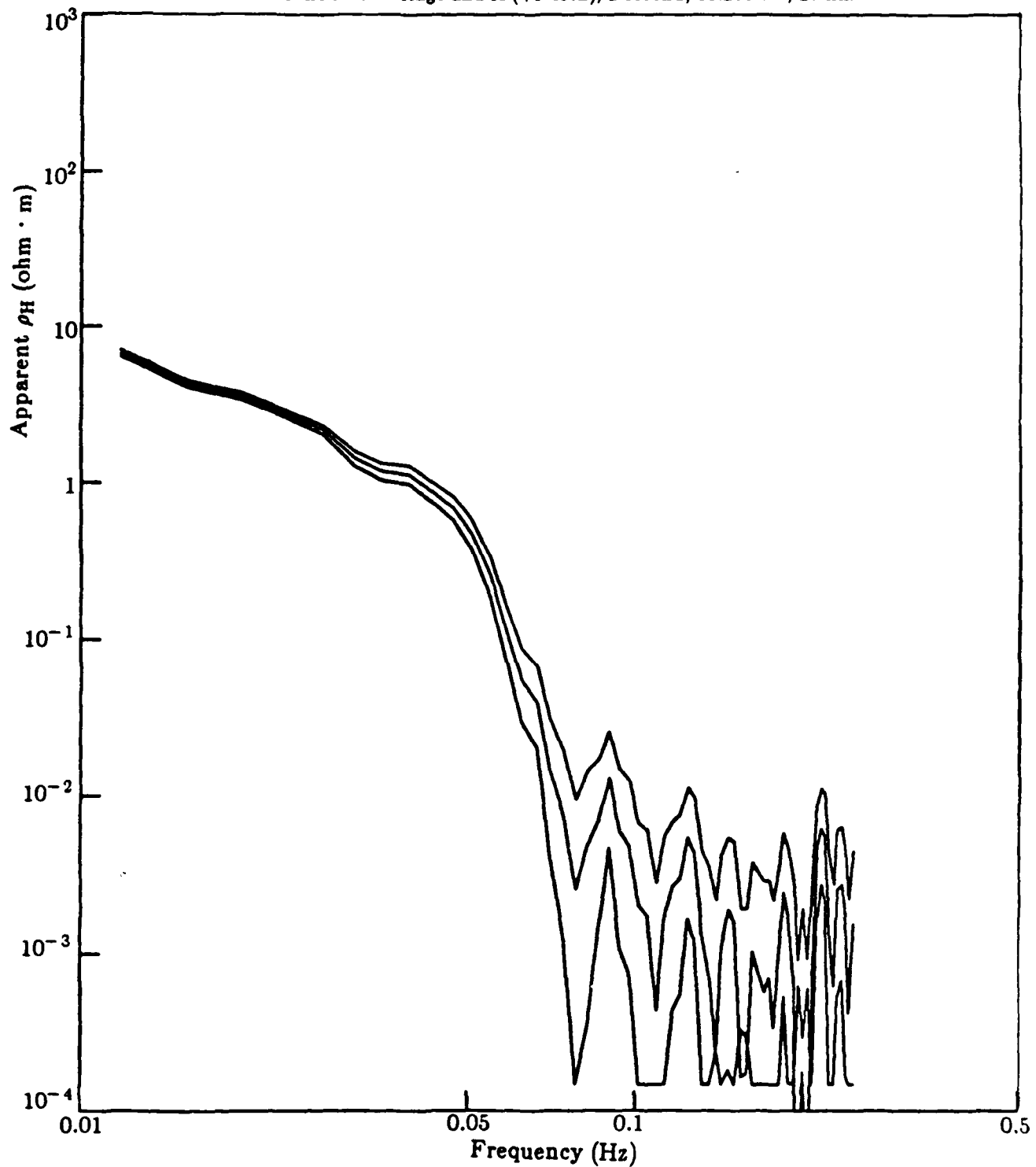


Fig. 3.33b. Smoothed effective resistivity  $\rho_H$  and  $\pm 1$  standard deviation lines (2 hrs. TAT-4 at 25 km - new program).



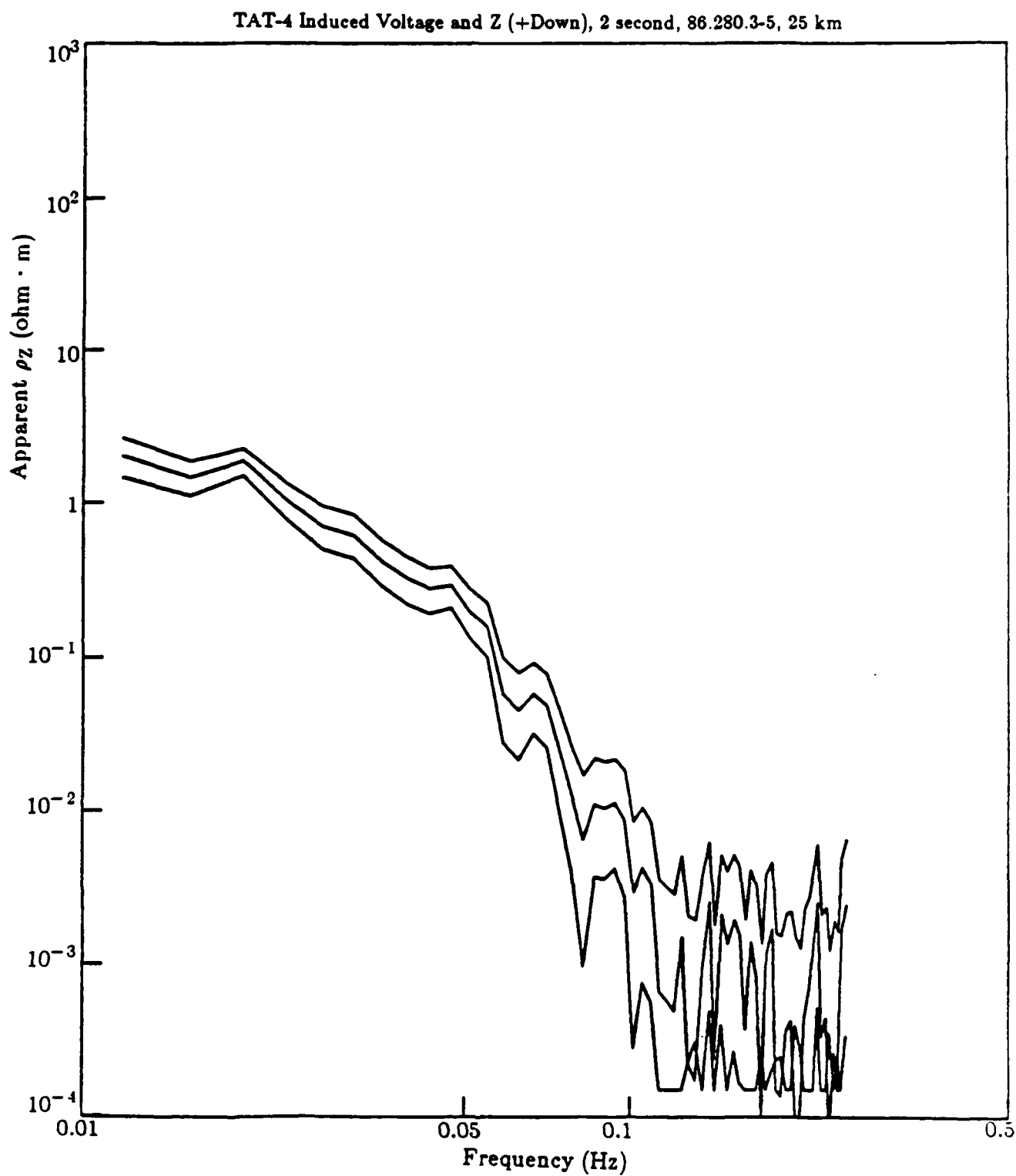


Fig. 3.33c. Smoothed effective resistivity  $\rho_z$  and  $\pm 1$  standard deviation lines (2 hrs. TAT-4 at 25 km - new program).

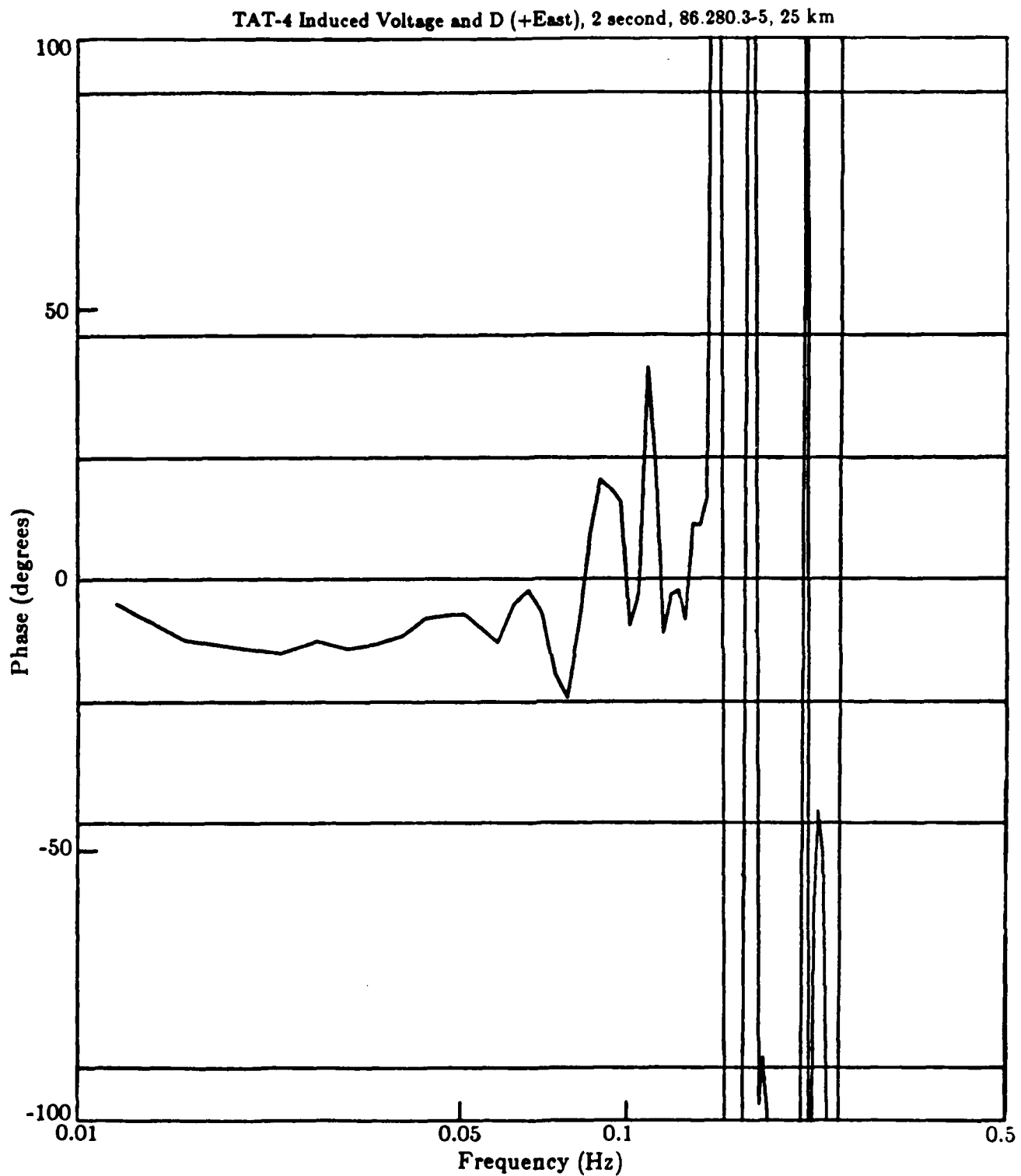


Fig. 3.34a. Phase of transfer function  $\alpha_D$  (2 hrs, TAT-4 at 25 km - new program).

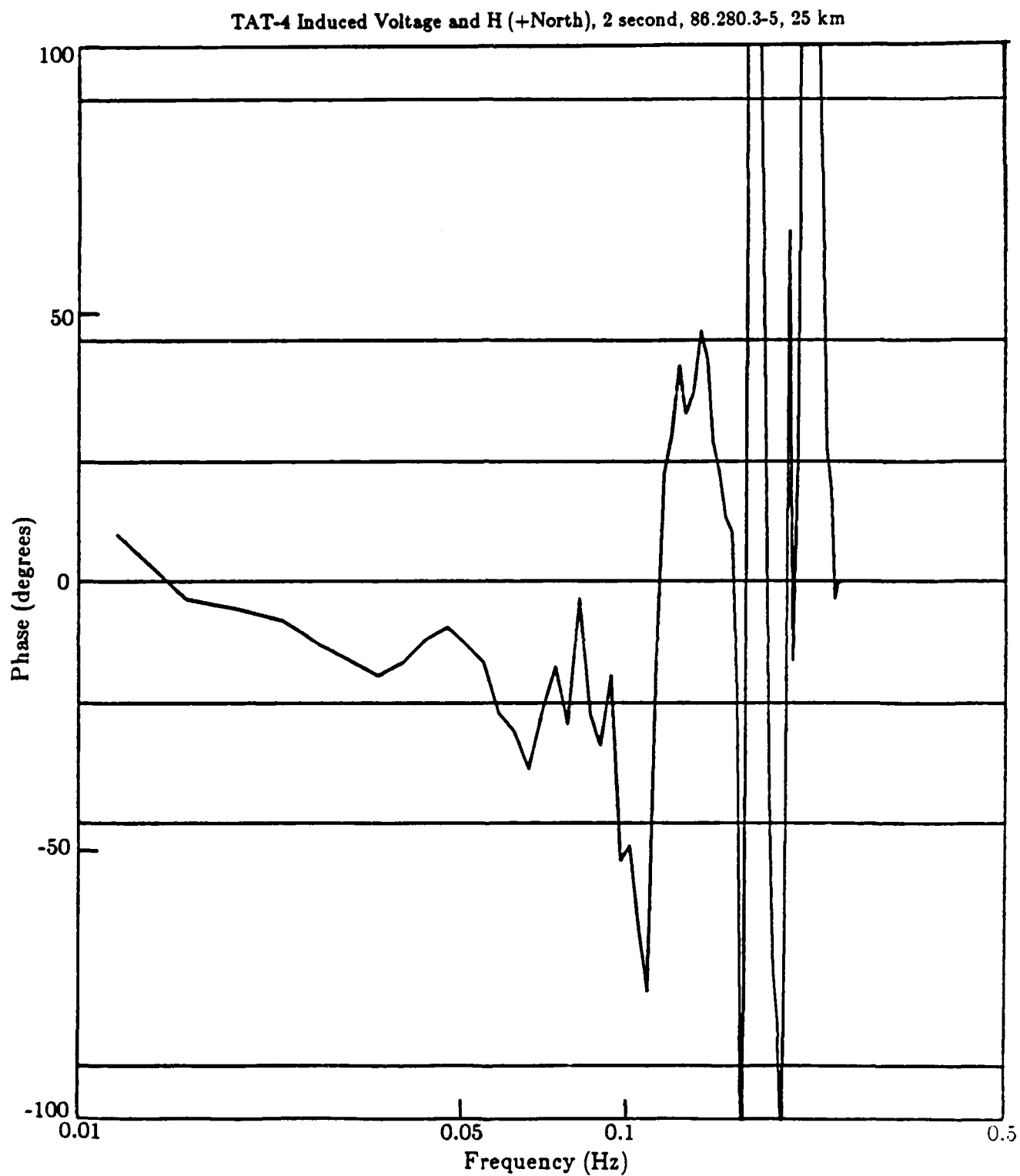


Fig. 3.34b. Phase of transfer function  $\alpha_H$  (2 hrs, TAT-4 at 25 km - new program).

TAT-4 Induced Voltage and Z (+Down), 2 second, 86.280.3-5, 25 km

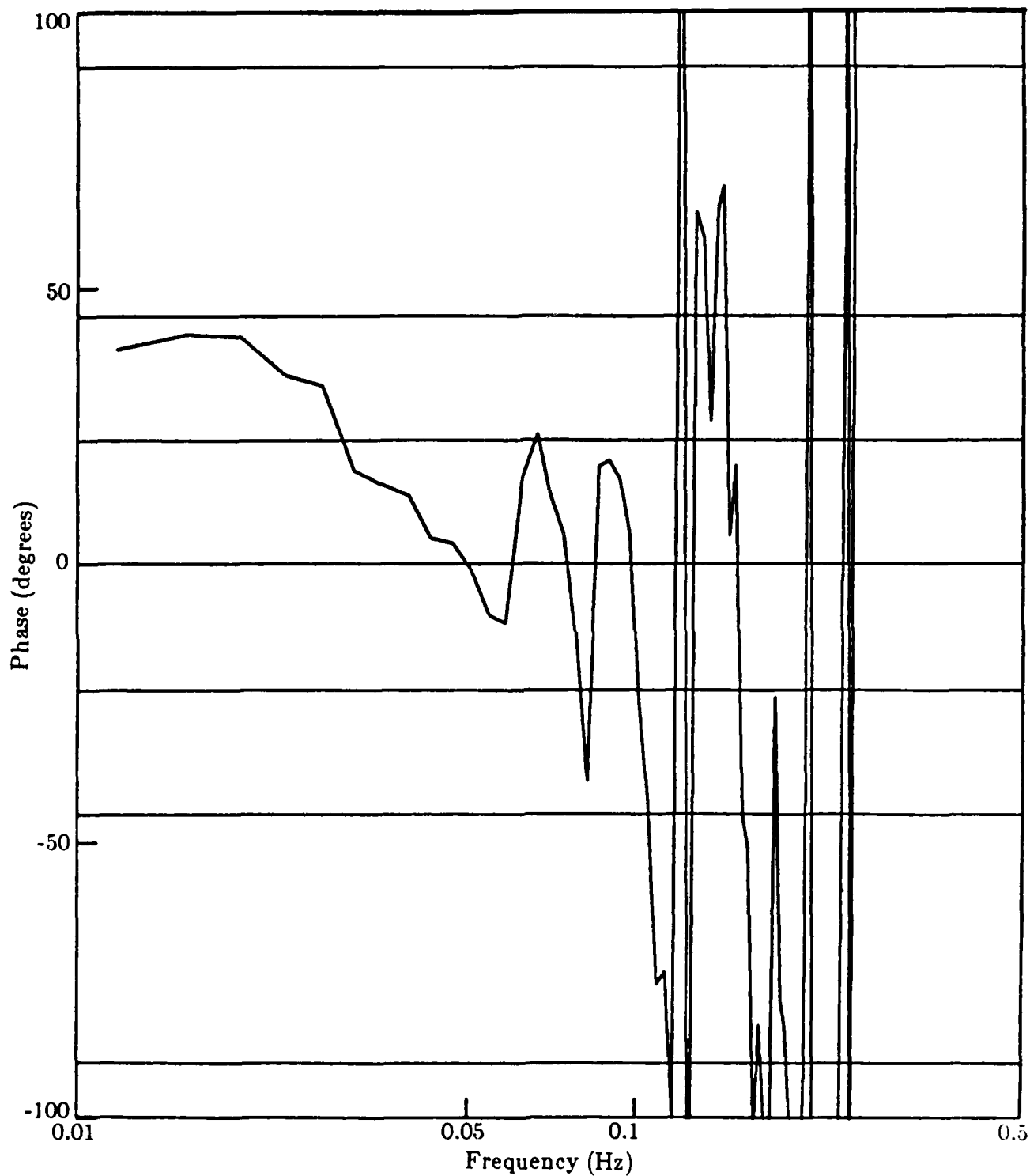


Fig. 3.34c. Phase of transfer function  $\alpha_z$  (2 hrs, TAT-4 at 25 km - new program).

## CHAPTER 4

### SUMMARY OF INTERPRETATION OF THE DATA

#### 4.1 - GENERAL SUMMARY

The most relevant (and most reliable) data are from the TAT-6 experiment. This report concentrates on these data, but the results from the TAT-7 and TAT-4 data are consistent with those of the TAT-6 data. As mentioned in Chapter 3, the measured transfer functions (ratio of the cable voltage fluctuations to sea-level magnetic field fluctuations ) from the 225 km length cable compared to the transfer functions at 3140 km exhibit very little length dependence for frequencies above around 0.01 Hz. This implies that most of the electric field coupling for frequencies above 0.01 Hz occurs on the continental shelf, since the transfer functions measured basically give the integrated electric field along the length of the cable. The very low frequency data (i.e. less than around 0.01 Hz) are length dependent, as one would expect if the field diffusion through the conducting ocean takes place according to the standard textbook skin-depth argument. Specifically, at 0.01 Hz the skin depth in seawater is 2.6 km, comparable to the depth at the ocean bottom (5 km). so for frequencies at or below 0.01 Hz, appreciable field penetration to the ocean bottom does occur. On the other hand, at 0.05 Hz the skin depth in sea water is 1.15 km. This implies that at 0.05 Hz, fields cannot penetrate appreciably to the ocean bottom, but on the other hand these fields are not attenuated appreciably at the shallow depth (0.2 km) of the continental shelf.

The correlations between the cable voltage fluctuations and the D (east-west) and H (north-south) magnetic field fluctuations are consistent with this interpretation. For the 225 km cable length, high correlations with D are

obtained, consistent with the simple perpendicular electric/magnetic field configuration. This is because the TAT-6 cable starts off from Rhode Island mainly in the North-South direction, as shown in Fig. 2.1. At the longer length of 3140 km, a high correlation with the very low frequency H field is seen, indicating low frequency field penetration through the ocean and correlation of the mostly East-West oriented cable with the North-South magnetic field, again as expected.

One noticeable feature of the oceanic geology is the so-called East-Coast magnetic anomaly, or ECMA. This feature, long known as a static phenomenon [1], has recently been observed in the TAT-7 data [2]. The anomaly is that instead of the basically east-west cable voltage fluctuations being highly correlated with the perpendicular magnetic field H component, it is highly correlated with the D component instead. For the TAT-6 experiment, there is already a high correlation of the cable voltage with the D component due to the initial north-south run over the continental shelf as mentioned above. Therefore the East-Coast magnetic anomaly seen in the TAT-7 data is disguised in the TAT-6 case, since it would simply show up as an anomalous extra correlation of the voltage with the D component. Because this correlation happens to be high in the TAT-6 case anyway, as noted above, the anomaly is harder to isolate than in the TAT-7 case.

For the TAT-4 cable which runs south-east, reasonably high correlations were obtained for the voltage with both the D and H components, as could be expected.

The values for the effective resistivity obtained from the transfer functions satisfy a sanity check, being roughly between the values for seawater

and typical land values at least over the low frequency range.

However, substantial structure is seen in the frequency dependence of the transfer functions and in the effective resistivity above 0.01 Hz, and is different from the situation in the L4/L5 case (cf. Ref. [1] and Fig. 7.1). The most pronounced effect here is a drop in the effective resistivity by several orders of magnitude between 0.01 Hz and 0.05 Hz (the maximum frequency available in the TAT-6 experiment). Part of this drop is due to the factor  $1/f$  ( $f$  = frequency) in the definition of the effective resistivity and part is due to a falloff of the transfer functions in frequency. However, it is not the case that this falloff can be attributed to the simple skin-depth argument (i.e., that the skin depth decreases with frequency). This is because, as noted above, most coupling to the TAT-6 cable occurs on the continental shelf. The continental shelf, on average, is only about 200 meters below the ocean surface, and at the frequencies being discussed there is little attenuation (attenuation factors are less than 2 for the continental shelf). Thus, the simple situation which occurred in the L4/L5 case where the effective resistivity appeared to be roughly frequency independent in the range up to 0.1 Hz is not seen here. As discussed in the next chapter, more complex arguments must be invoked in order to understand this behavior.

#### 4.2 - MEASUREMENTS AT HIGHER FREQUENCY

The faster sampling rate used in the measurements of the cut TAT-4 cable in principle allow information at higher frequencies than 0.05 Hz. Here the apparent behavior of the effective resistivities flattens out with frequency, with no further drop-off in evidence. This, however, does not necessarily mean that the effective resistivities have ceased to fall off with frequency- or indeed that

they might not exhibit some other behavior with frequency, even including a rise with frequency. The reason is that both the voltage and magnetic field measurements are susceptible to large relative noise contamination. The voltage is contaminated by electrochemical stochastic noise introduced by the seawater-coaxial conductor coupling at the cable end. This noise is magnified in relative importance here because the overall magnetic-field-induced voltage fluctuations are less due to the short cut TAT-4 cable length. Also, the magnetometer has a sensitivity limit for signals, below which noise is introduced. Hence at high frequencies the effective resistivities may merely be measuring the ratio of the noise spectra for the voltage and the magnetic field component measurements, thus masking the true behavior of the system. The smoothing procedure seems to have rendered the data usable out to, say 0.1 Hz, but noise problems still seem to plague the data past this point. Hence, it would seem that, unfortunately, no really reliable information can be drawn for the effective resistivities out to the 0.25 Hz Nyquist limit for these measurements. On the other hand, these data seem compatible with data from the other cables out to 0.1 Hz, including the length dependence. Some of the TAT-7 data at 3000 km taken with a sampling rate of 5 sec/measurement also seem to have effective resistivities which level off near 0.1 Hz (cf. Figs. 3.12b, 3.13b).

#### 4.3 - HIGH FREQUENCY OSCILLATIONS

As indicated several times in this report, an apparent noisy behavior sets in at "high" frequencies (above frequencies around 0.05-0.1 Hz). While some sources for noise exist, as have already been mentioned, it is possible that other physical effects involving, for example, ionospheric resonances also contribute to these oscillations. Some preliminary work in this area is contained in Ref. [3].



The nature of the high frequency oscillations in these experiments thus is probably some mixture of noise which is irrelevant to threat considerations and physical effects that would occur under threat conditions. An understanding of this separation, while very difficult, would also be required in the absence of experimental information up to 1 Hz in order to perform an extrapolation which agreed with the physically caused oscillations and ignored the irrelevant noise.

Fig. 4.1 exhibits a study made of the high frequency oscillations in the TAT-4 data in the following way. Spectral plots were made of the transfer functions for windows of data with central position moving in time. Thus, data with a window around a certain time of day were processed, then data with a window around that time plus a small increment were processed, and so forth. Fig. 4.1 shows that the high frequency fluctuations are not very reproducible from one window to the next. Such fluctuations are characteristic of a large stochastic component, compatible with the observations made above.

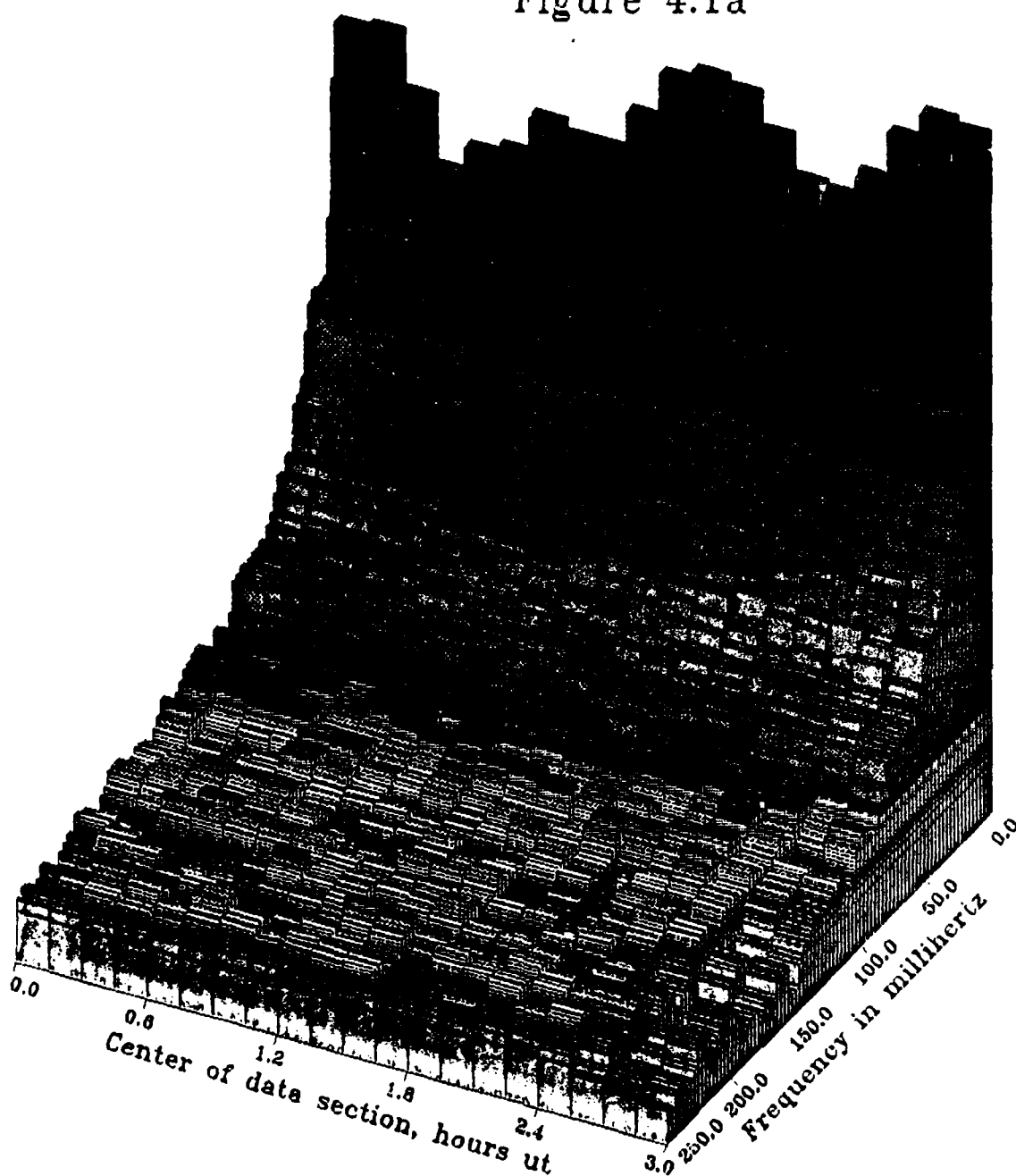
As we describe in following chapters, this whole problem is finessed in the following way. The extrapolation up to the 1 Hz region will be done with model results that, in the region of the oscillations observed here, overestimate the experimental results, including the experimentally observed oscillations. Therefore, the exact nature of the oscillations becomes a moot issue, because only an upper bound above these oscillations is being used.

#### REFERENCES (Chapter 4)

1. See, e.g., C. L. Drake, J. Heirtzler, and J. Hirshman, "Magnetic Anomalies off Eastern North America", J. Geoph. Res., Vol 68, pp 5259-5275 (1963); L. E. Alsop and M. Talwani, "The East Coast Magnetic Anomaly", Science Vol. 226, pp 1189-1191 (1984) and references therein.
2. L. J. Lanzerotti, D. J. Thomson, and L. V. Medford, private communication.
3. A. D. Chave, D. J. Thomson, and M. E. Anders, in press, J. Geoph. Res..

Fig. 4.1. Study of the high-frequency oscillations. The three-dimensional plots exhibit (a) the spectra of the TAT-4 induced voltage and (b) the D-component of the magnetic field, plotted against a window center position in time.

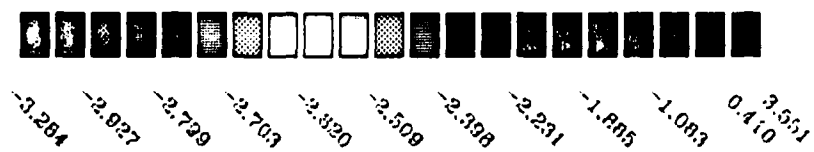
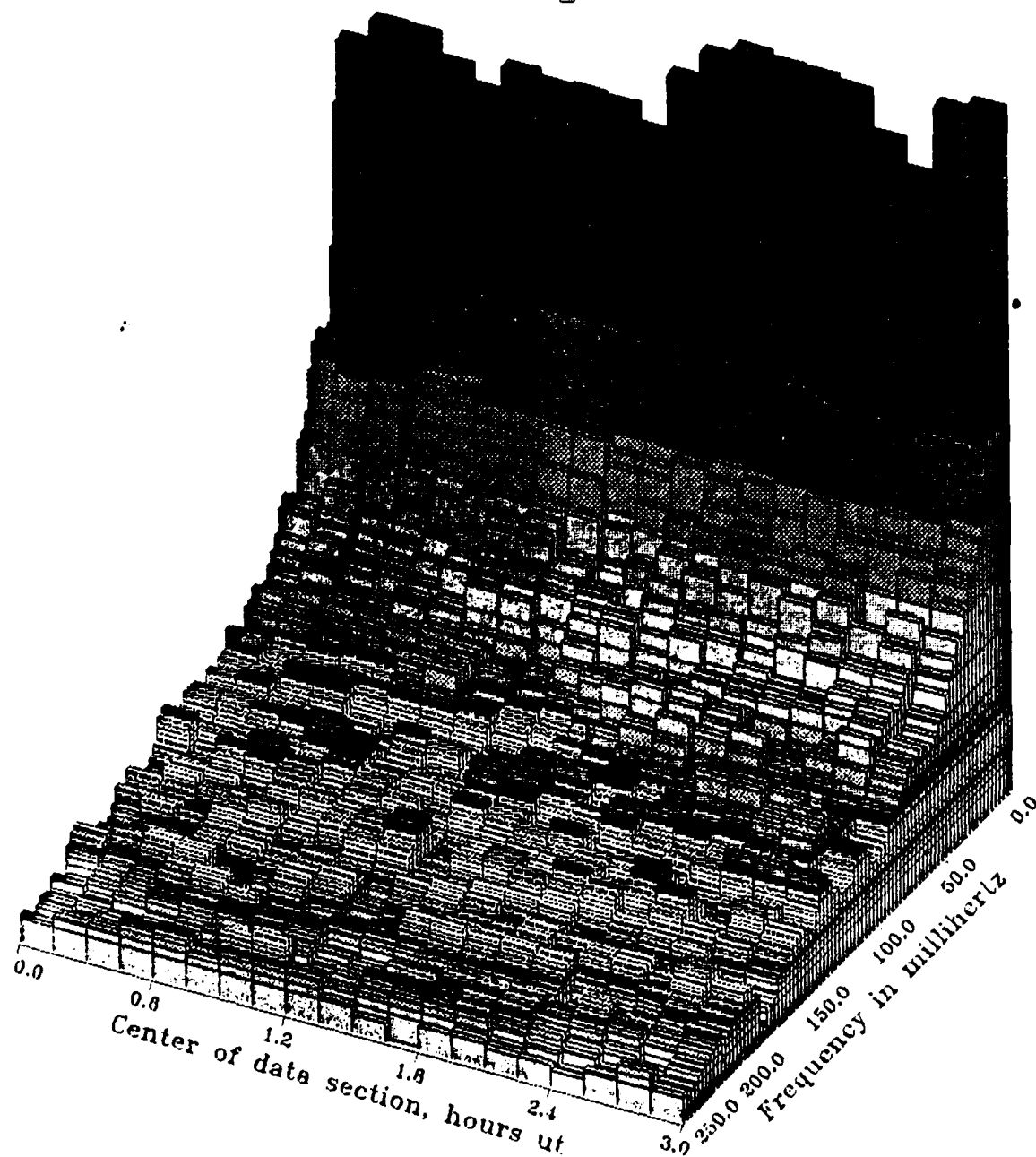
Figure 4.1a



-7.001 -6.949 -6.894 -6.835 -6.771 -6.701 -6.624 -6.548 -6.468 -6.388 -6.308 -6.228 -6.148 -6.068 -5.988 -5.908

Log spectrum

Figure 4.1b



Log spectrum

## CHAPTER 5

### MODELING SUMMARY

In this chapter the modeling designed to effectuate the frequency extrapolation of the effective resistivity necessary to obtain the MHD threat at frequencies up to 1 Hz is described. Chapter 6, along with Appendices A and B, contains the details.

The modeling effort is composed of several steps. First, a quasi-analytic approach was used. The basic idea is to divide up the complicated land-ocean environment into regions. Solutions to the Maxwell equations are written in each region. The boundary conditions are then imposed approximately by a least-squares procedure [1]. The fields thus obtained can be used to calculate the voltage fluctuations in a submarine cable and the transfer functions. The model can then be used to extrapolate the transfer functions to the 1 Hz frequency range of interest. Of special interest here are the potential leakage fields. Such fields are considered absent by definition in the simple layer models common in geophysics [2]. Extensions to include an ocean generally assume that its conductivity is infinite and its depth is zero [3]. This, however, yields zero horizontal electric field at the ocean bottom and hence zero coupling to cables. Hence these models are therefore not of sufficient sophistication for us. A proposal to include a realistic land/ocean geometry was studied [4]. As mentioned above, we conjecture that these fields could be a cause of the falloff in frequency of the effective resistivity.

This quasi-analytic approach was first developed in Ref. 5, where the problem involved incident electromagnetic fields on an island in an ocean. The results for this island problem geometry were encouraging. Qualitatively correct

shapes were obtained for all fields compared to experiments, and magnitudes were obtained that were generally correct within a factor of two.

The results for the ocean/land environment that have been obtained are summarized as follows. The least-squares procedure works to give the textbook answers for layered geometry problems (i.e., no vertical boundaries). Results for a more complex and realistic geometry with a vertical boundary have been achieved. The geometry had a "barrier" substance below the ocean on the continental shelf, whose conductivity was varied as a parameter in the model. The model results exhibit a falloff of the the effective resistivity with frequency, through not as fast as the measured data over the available frequency range. Nonetheless, the falloff does allow the possibility of a reasonable model-dependent extrapolation to the frequency region of up to 1 Hz.

The results for the semi-analytic least squares method are summarized in Figs. 5.1-5.2. Fig. 5.1a shows the effective resistivity plotted against the data for  $\rho_D$  for TAT-6, 225 km. Two different curves for barrier conductivities  $\sigma_{\text{barrier}} = 0.01$  and 0.1 are shown. Fig. 5.1b shows the same two curves, this time plotted against the data for  $\rho_{II}$  for TAT-7, 3000 km. It is seen that the curves have the behavior mentioned above. Fig. 5.2 shows the effective resistivity from this approach extrapolated out to 1 Hz.

A more direct, though less analytic, approach is a numerical solution of Maxwell's equations through a code. The finite element method as described in Appendix B was used. The results are similar to those obtained using the semi-analytic method. Fig. 5.3 exhibits the effective resistivity from this approach.

## REFERENCES (Chapter 5)

1. F. James and M. Roos, "Minuit- A System for Function Minimization and Analysis of the Parameter Errors and Correlations". Computer Physics Communications 10, 343 (1975).
2. I. I. Rokityansky, "Goelectromagnetic Investigation of the Earth's Crust and Mantle", Springer-Verlag, Berlin (1982). See page 57.
3. See, e.g., G. Fischer, "Electromagnetic Induction Effects at an Ocean Coast", Proceedings of the IEEE, Vol. 67, No. 7, pp. 1050-1060 (1979) and references therein.
4. J. W. Dash, private communication.
5. A. Beilis, J. W. Dash, and A. Farrow, "Analytic " $\alpha$  - Pole" Approach to an Electromagnetic Scattering Problem", IEEE Transactions EMC. Vol. 29 , No. 2, pp. 175-185 (1987).



Comparison of Effective Resistivity using Fitted  
Layered Solutions with Different Barrier Conductivities  
to Empirical Data: Rho-D Tat6 225 Km Cable

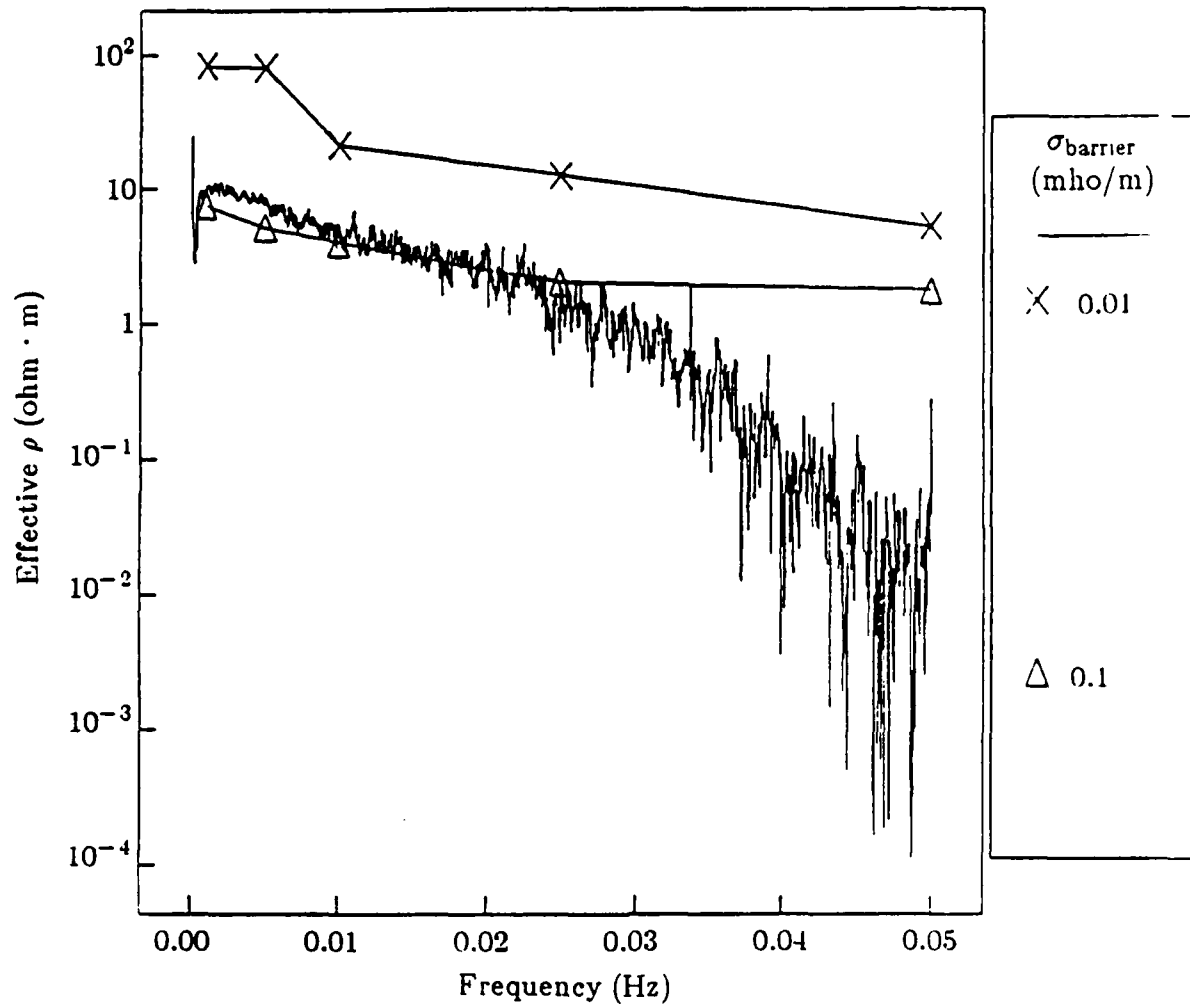


Fig. 5.1a. Results for the effective resistivity for the semi-analytic fitted solution as a function of frequency for two barrier conductivities ( $\sigma_{\text{barrier}} = 0.01, 0.1$  mho/m). Also shown are the data for  $\rho_D$  for TAT-6 at 225 km.

Comparison of Effective Resistivity using Fitted  
Layered Solutions with Different Barrier Conductivities  
to Empirical Data: Rho-H Tat7 3000 Km Cable

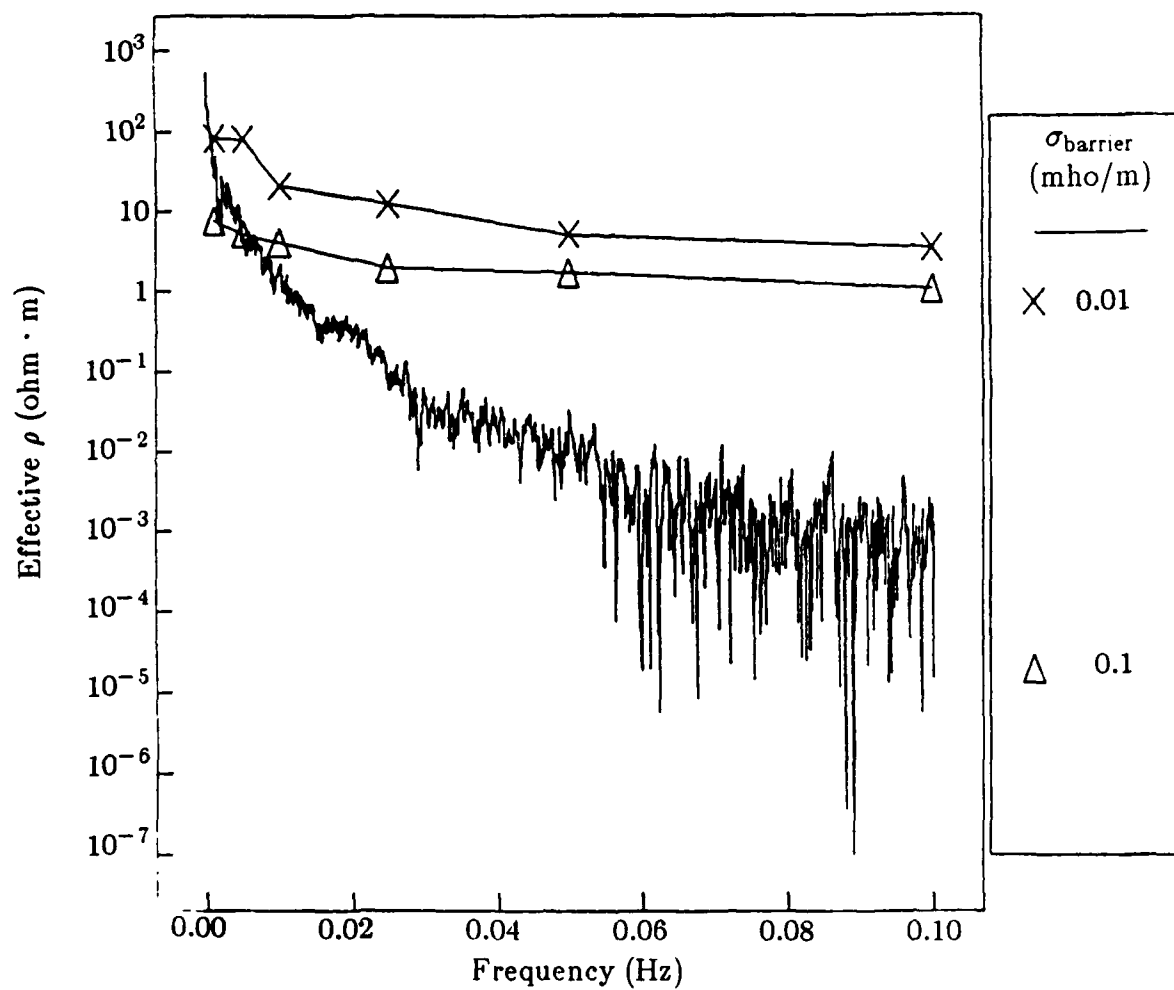


Fig. 5.1b. Same as Fig. 5.1a plotted with the data for  $\rho_H$  for TAT-7 at 3000 km.

Effective Resistivity using Fitted  
Layered Solutions with Different Barrier Conductivities

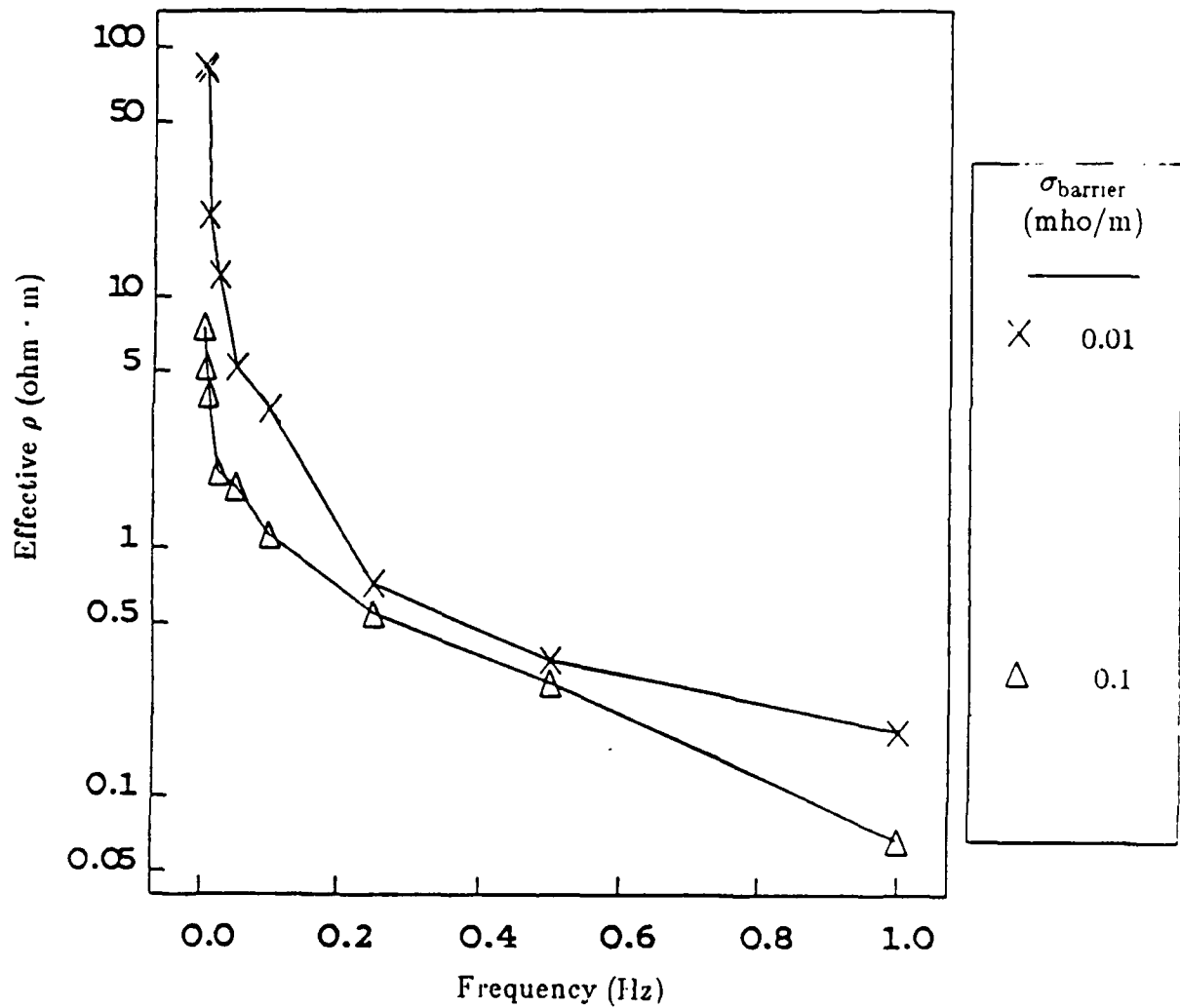


Fig. 5.2. The effective resistivity for the semi-analytic fitted solution as a function of frequency out to 1 Hz for two barrier conductivities ( $\sigma_{\text{barrier}} = 0.1, 0.01$  mho/m).

Effective Resistivity Using Finite Element  
Solution With Different Barrier Conductivities  
For Only The Long Cable Segment

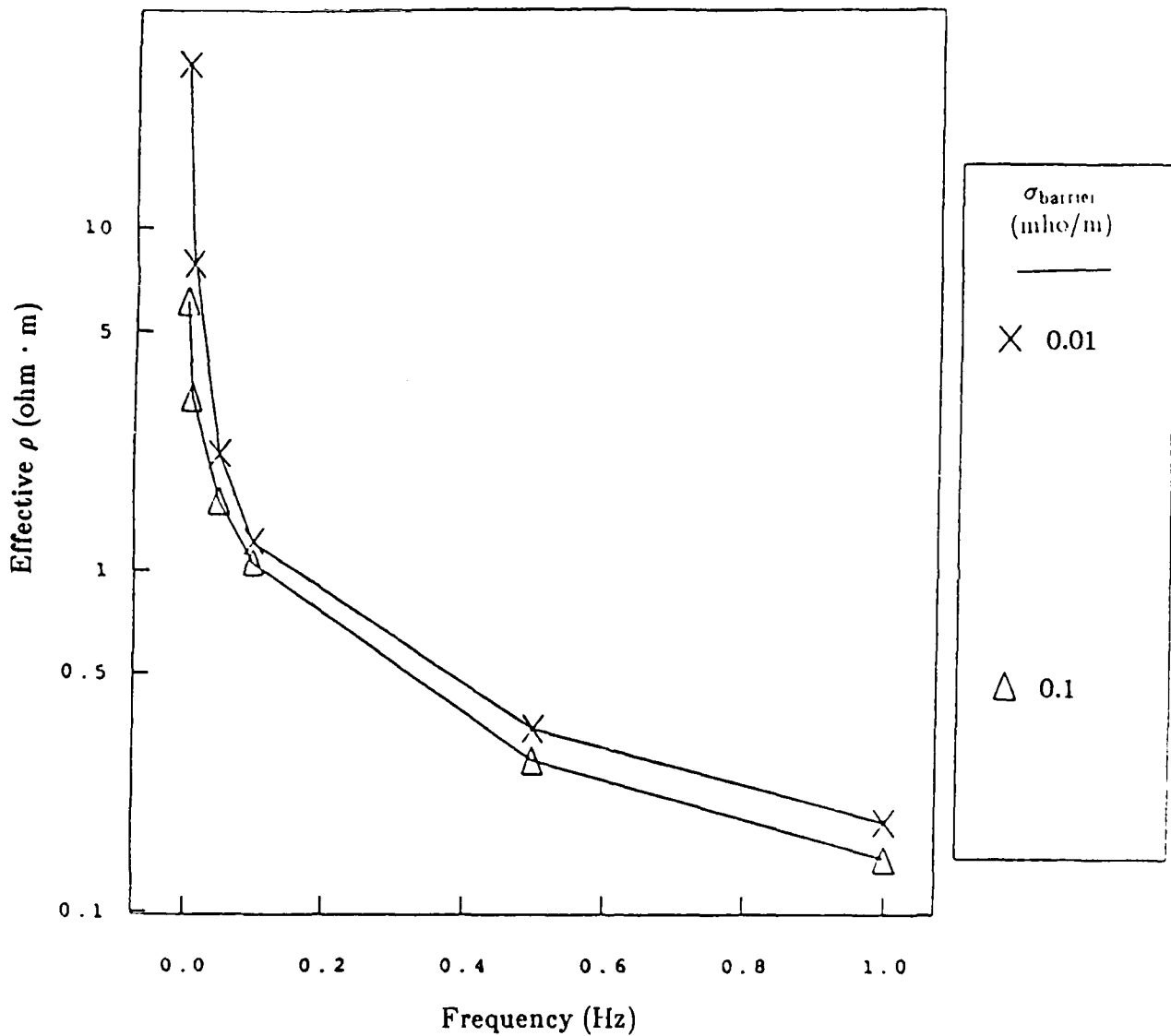


Fig. 5.3. The effective resistivity from the finite element code solution as a function of frequency out to 1 Hz for two barrier conductivities ( $\sigma_{\text{barrier}} = 0.1, 0.01$  mho/m).

## CHAPTER 6

### NUMERICAL MODELING RESULTS

#### 6.1 - THE SEMI-ANALYTIC LAND/OCEAN MODEL

The semi-analytic land/ocean model, described in detail in Appendix A, originated in Ref. [1]. The basic idea is to write down exact solutions to Maxwell's equations in each region. Some of these solutions are textbook "trivial" solutions, corresponding to an asymptotic condition far from vertical interfaces, where a purely horizontally layered geometry is relevant. Other solutions which are more general and these have parameters which are not determined a-priori. Then the boundary conditions between regions are approximately incorporated by varying the parameters of the solutions in each region using the least-squares program Minuit [2]. A "barrier" was introduced under the ocean on the continental shelf, potentially distinct from the "land", as explained in Appendix A. The results constitute the semi-analytic approach to the modeling effort [3].

The first step was to perform some sanity checks with the exact textbook "trivial" solutions (see Appendix A). This was used as a benchmark for the application of the method to the problem at hand. Results were obtained by fitting parameters first with two and then with three layers. Fig. 6.1 shows the 3-layer geometry representing air/ocean/barrier (in this test the barrier conductivity was set equal to that of land, and  $f = 0.1$  Hz). The fields are actually dependent only on the vertical  $z$  co-ordinate in this simple case, since the geometry is translation invariant in the horizontal co-ordinates  $x$  and  $y$ . For the more general case with vertical boundaries considered in Appendix A,

independence of  $x$  is maintained, but the fields in general now depend on  $y$  and  $z$ . None of this should obscure the fact that the fields themselves are vectors and point in certain directions. In the simple horizontally-layered case the magnetic and electric field vectors in fact point in the  $x$  and  $y$  directions, respectively.

It is important to remember that this semi-analytic approach allows analytic formulae for the electric field. Thus, no numerical differentiation problems are encountered for obtaining the electric field from the magnetic field.

For the transition of fields from the air into the ocean, there is almost total reflection, producing a doubling of the  $H_x$  field and almost total cancellation of the  $E_y$  field, involving delicate cancellations between relatively large numbers. Fig. 6.2a exhibits  $H_x$  for a normally incident downward propagating plane wave with magnitude one with the three-layer geometry. The depth of the ocean is taken as 0.2 km, appropriate to the depth of the water above the continental shelf, and the frequency is 0.1 Hz. The exact result is the solid line while the fit is the dotted line. Fig. 6.2b is the same for  $E_y$ . The other field components are zero, as they should be. The surface current  $J_y$  is shown in Figs. 6.2c. Finally, Figs. 6.3a-c exhibit the same quantities, with the depth of the ocean taken as 4 km this time, appropriate to the ocean abyss.

The geometry of Fig. 6.4 was used to model the land-ocean environment. This is a simplified version of the geometry shown in Fig. A1. In fact, only the continental shelf was considered, since the data analysis showed that very small coupling to submarine cables occurred on the ocean abyss past the continental shelf. The simplification of the problem was moreover required due to the

restricted complexity from the point of view of the least-squares fitting program.

Thus, the barrier under the continental shelf was modeled by a uniform homogeneous conducting material with a conductivity that was treated as a parameter, called the "barrier conductivity"  $\sigma_{\text{barrier}}$  in this report.  $\sigma_{\text{barrier}}$  was fixed for each fit in advance. Values of 0.001 (a typical value for surface land), 0.01, and 0.1 mho/m were used.

The following procedure was adopted in the fitting procedure. A "first approximation 2 layer/3 layer trivial" model was first defined. In this model, the fields to the left of the vertical boundary are defined as the solution to the trivial 2 layer problem, and the fields to the right of the vertical boundary are defined as the solution to the trivial 3 layer problem. This should provide a valid approximation far from the vertical boundary, basically since the boundary should be invisible at large distances from it. Supplementing this first approximation, additional terms were introduced with variable parameters fitted by the program. Up to 15 real parameters can be varied at once by Minuit. This unfortunately only allows several terms to be varied at once, since each term contains 4 real parameters (a complex normalization and a complex exponent parameter). Moreover, it is easy to see analytically that the continuity requirements cannot be satisfied exactly with only one additional term per region. Indeed, it is probable that many terms would be required for quantitative accuracy. On the other hand, the introduction of many terms implies prohibitive complexity for the Minuit program. Hence a compromise had to be reached. Basically, most fits were done with only one additional term in the land, the ocean, and the barrier, and no additional terms in the air. For the fit described in detail below, extra terms were included.

The results for the effective resistivity  $\rho_{\text{model}}$  for the semi-analytic model as a function of frequency for two different barrier conductivities ( $\sigma_{\text{barrier}} = 0.01, 0.1$  mho/m) are shown in Fig. 6.5a. Also shown are the data for  $\rho_D$  for the TAT-6, 225-km length cable. Here  $\rho_{\text{model}}$  is defined as

$$\rho_{\text{model}} = \left| \frac{V_{\text{cable}}}{H_x} \right|^2 \frac{1}{\mu_0 \omega L_{\text{eff}}^2} \quad (6.1)$$

The model magnetic field  $H_x$  at a model station position 2 km inland was used for the normalization, although the results are not sensitive to this convention.

Here, following the discussion in Appendix C,

$$V_{\text{cable}} = - \int_C \vec{E} \cdot d\vec{l} \quad (6.2)$$

with  $C$  being the contour along the cable position. Also,  $\omega = 2\pi f$  is the radian frequency and  $L_{\text{eff}}$  is the effective length, taken here as 200 km. Further,  $\mu_0 = 4\pi \times 10^{-7}$  ohm-sec/meter was taken as the permeability of all substances. The displacement current was very small in the conducting bodies, as measured by the dielectric constants  $\epsilon = 2\epsilon_0, 5\epsilon_0$ , and  $5\epsilon_0$  in the water, land, and barrier respectively. Here  $\epsilon_0 = 1/[\mu_0 c^2] = 1/[36\pi] \times 10^{-9}$  mho-sec/meter (with  $c$  being the speed of light) is the dielectric constant in free space or air.

Actually, only the part of the cable at the ocean/barrier interface was used for the contour  $C$  in practice. The segments corresponding to the vertical rise of the cable from the ocean bottom to land as well as the land segment from



the shore to the station were not incorporated, since the fitting routine did not allow such complexity without excessive effort. However, it would be expected that due to the short lengths of these segments the contributions to  $V_{\text{cable}}$  would be small. Some examination of this point was done in the fit described below and in the finite element method described below and the general validity of this point was established. In particular, it turns out that at frequencies below 0.1 Hz, the shore-station contribution was less than around 10 % to  $\rho_{\text{eff}}$ . At 1 Hz, the shore-station contribution was comparable to the ocean bottom contribution, but both were quite small. The contribution of the vertical segment was very small (less than 5 % even at 1 Hz), and could be ignored.

Fig. 6.5b shows the model  $\rho_{\text{eff}}$  plotted this time along with  $\rho_H$  from TAT-7, 3000 km. Figs. 6.6a,b exhibit the results from the first approximation (the trivial 2 layer/3 layer model) plotted against these same data. It is seen that in all cases, a falloff of the model  $\rho_{\text{eff}}$  does occur with frequency, though not as fast as in the data over this frequency range. At  $\sigma_{\text{barrier}} = 0.1 \text{ mho/m}$  the fitted semi-analytic results are mostly close to the first approximation model. This curve seems to provide the best approximation to the data at low frequencies for the parameters we considered. It lies somewhat above the data at the maximum experimental frequency.

Figs. 6.7a,b exhibit the extrapolations of the fitted results and the first approximation out to 1 Hz. It is seen that the extrapolated model effective resistivities are all substantially below the value 1 ohm-m, and for the case  $\sigma_{\text{barrier}} = 0.1 \text{ mho/m}$  the extrapolated model effective resistivity is about 0.1 ohm-m.

Figs 6.9-6.14 exhibit the electric and magnetic fields, as well as the total currents along various cuts in the geometry which are shown in Fig. 6.8. These figures exhibit to what extent the fitting program was able to satisfy the requirements of continuous tangential electric field, normal total current, and magnetic field. Extra terms were added to the fit for these figures, but the results are representative. The boundary conditions at the land/air and ocean/air interfaces were exceptionally difficult to treat due to the large impedance mismatches between the air and these conducting materials. Also, the least-squares program as described in Appendix A.4 turned out to be somewhat insensitive to the phases of the fields due to the definition of the chi-square function, though as the exact results are approached, the phases would be correctly given by the least-squares results.

Figs. 6.9-6.14 indicate that the conjecture of the vertical boundary modifying the fields only locally is basically correct. Physically, surface charges on the vertical boundary generate an extra piece of the  $E_y$  component of the electric field. This piece dies off at distances greater than some scale, here less than about 1-2 km, from the vertical boundary. Past this point, the trivial layered solutions are again obtained.

## 6.2 - THE FINITE ELEMENT CODE [4]

In order to check the finite element code technique described in Appendix B, the same tests described above for the trivial 2-layer problem and 3-layer problem were performed. The boundary conditions were specified as the appropriate analytic solution around the computer generated boundary, as described in Appendix B. It should be noted that since  $H_x$  is determined only numerically, a numerical differentiation procedure was needed to obtain the

electric field. This lead to some spikes near interfaces for the electric field which are artificial and smoothed out by hand. The same problems experienced in the semi-analytic approach for the air/land and air/water interfaces due to the large impedance mismatch were also found in the finite element approach.

The results for the fields in the three layer problem are shown in Figs 6.15. The results agree well with the three-layer analytic solution.

The finite element results for  $\rho_{\text{eff}}$  for the full problem with the vertical boundary for frequencies out to 1 Hz are exhibited in Fig. 6.16. For comparison with the semi-analytic fit method, only the contribution to  $\rho_{\text{eff}}$  from the continental-shelf ocean bottom has been plotted, but as mentioned above, the other contributions are small except near 1 Hz, where the whole  $\rho_{\text{eff}}$  is small anyway. Compared to the semi-analytic method, Fig. 6.7, the results seem quite similar. Figs. 6.17 - 6.22 show the details of the fields obtained at  $c_{\text{barrier}} = 0.1 \text{ mho/m}$  with  $f = 0.1 \text{ Hz}$ .

### 6.3 - CONCLUSIONS FOR THE MODELING EFFORT

The fact that the finite element code and the semi-analytic solution approach give rather similar results lends confidence to the overall modeling effort to obtain the extrapolation to the 1 Hz region needed for the MHD threat evaluation on submarine cables. One plausible source of the difference between the results of the two modeling approaches and the measured data arises from the simplistic modeling of the barrier region under the ocean on the continental shelf. The geology of this region would be expected to exhibit a complex structure.

Based on the modeling, the effective resistivity would appear to be at or below  $\rho_{\text{eff}} = 1 \text{ ohm-m}$  at 0.1 - 1 Hz for the land/ocean environment.

## REFERENCES (Chapter 6)

1. A. Beilis, J. W. Dash, and A. Farrow, "Analytic "  $\alpha$ -pole" Approach to an Electromagnetic Scattering Problem", IEEE Transactions EMC Vol. 29, No. 2, pp. 175-185 (1987).
2. F. James and M. Roos, "Minuit- A System for Function Minimization and Analysis of the Parameter Errors and Correlations", Computer Physics Communications 10, 343 (1975).
3. The results of this section were obtained by J. W. Dash and D. R. Macauley, AT&T Bell Laboratories.
4. The results of this section were obtained by J. W. Dash and M. Driscoll, AT&T Bell Laboratories.

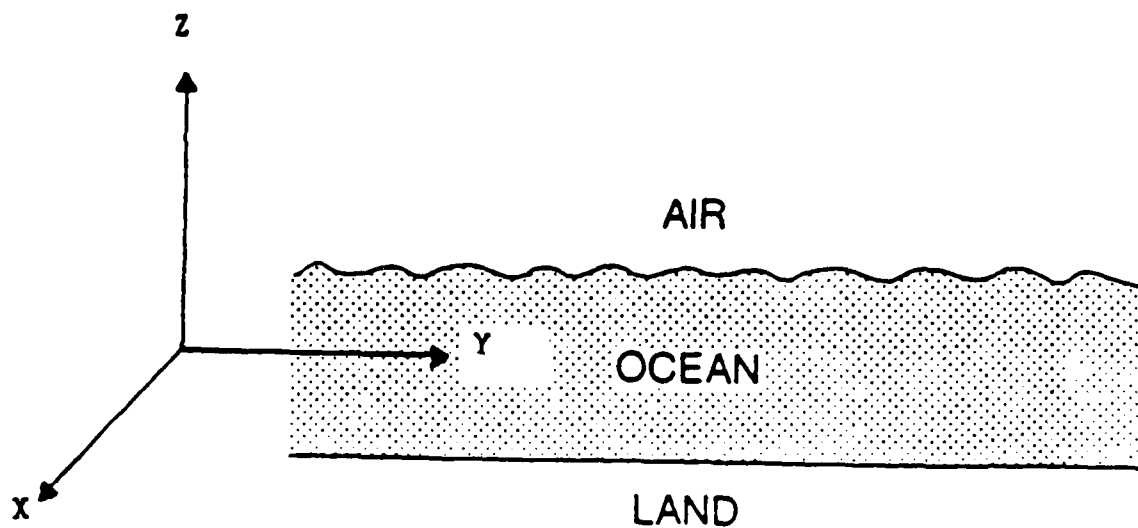


Fig. 6.1. The simple three-layer geometry air/ocean/barrier. The fields depend only on the  $z$ -coordinate.

Three layer: air / ocean / continental shelf  
 z-dependence (frequency = 0.1 Hz)

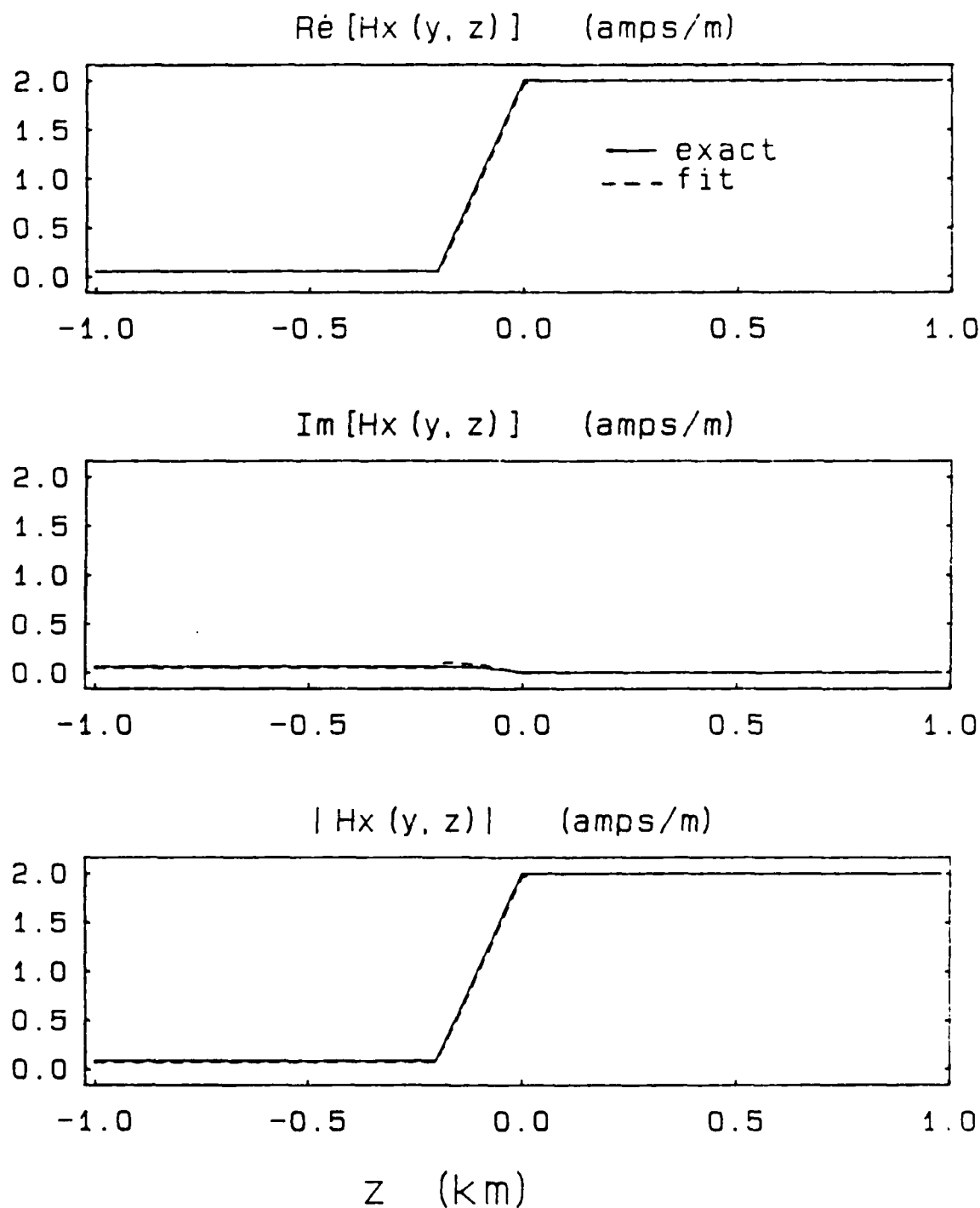


Fig. 6.2a.  $H_x$  for the air/ocean/barrier layered geometry (ocean depth = 0.2 km). The dashed (solid) line is the least-squares fit (exact result).

Three layer: air / ocean / continental shelf  
 z-dependence (frequency = 0.1 Hz)

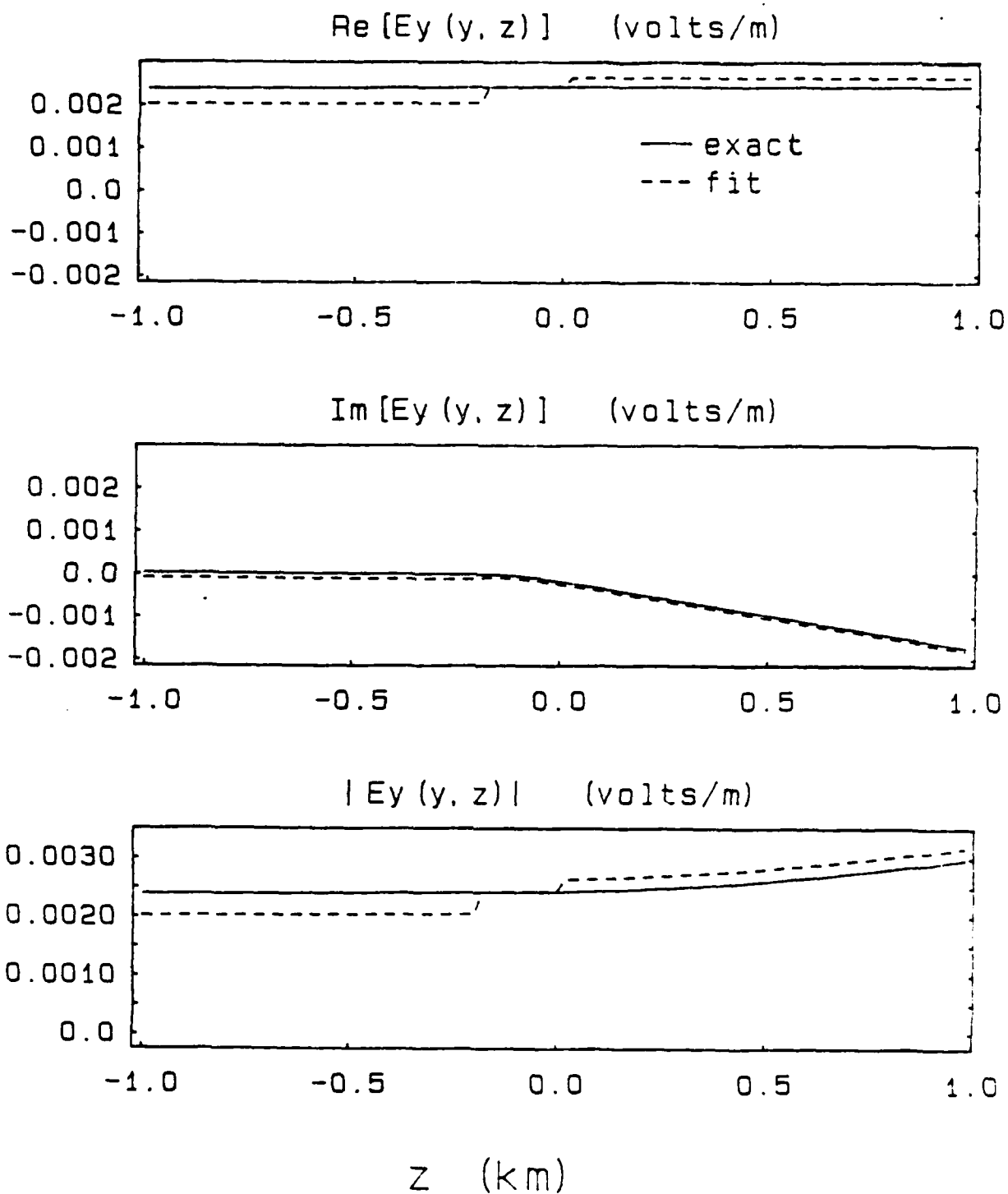


Fig. 6.2b.  $E_y$  for the air/ocean/barrier layered geometry (ocean depth = 0.2 km). The dashed (solid) line is the least-squares fit (exact result).



Three layer: air / ocean / continental shelf  
 z-dependence (frequency = 0.1 Hz)

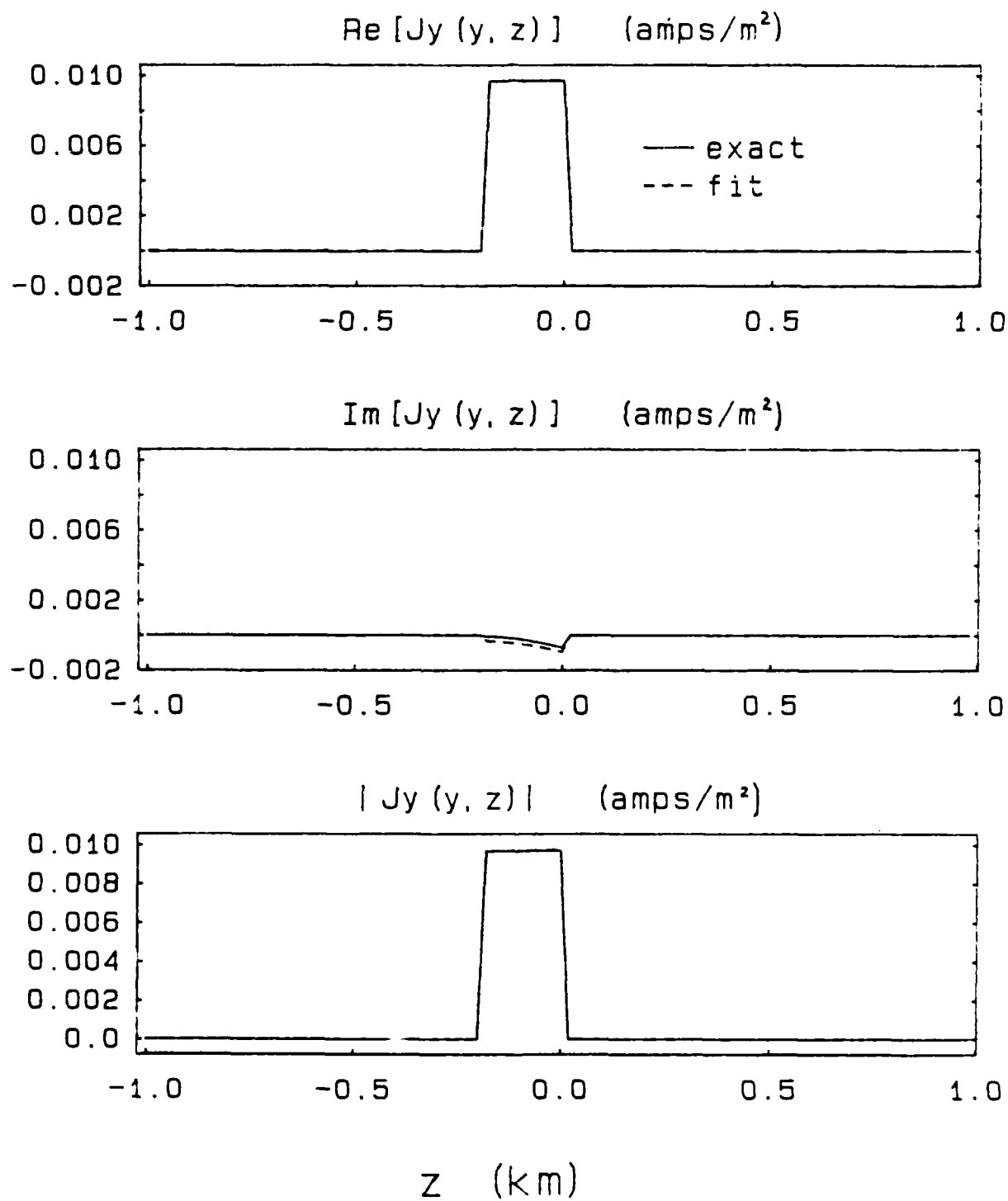


Fig. 6.2c.  $J_y$  for the air/ocean/barrier layered geometry (ocean depth = 0.2 km). The dashed (solid) line is the least-squares fit (exact result). The two solutions are almost identical.

Three layer: air / ocean (4 km) / land  
 z-dependence (frequency = 0.1 Hz)

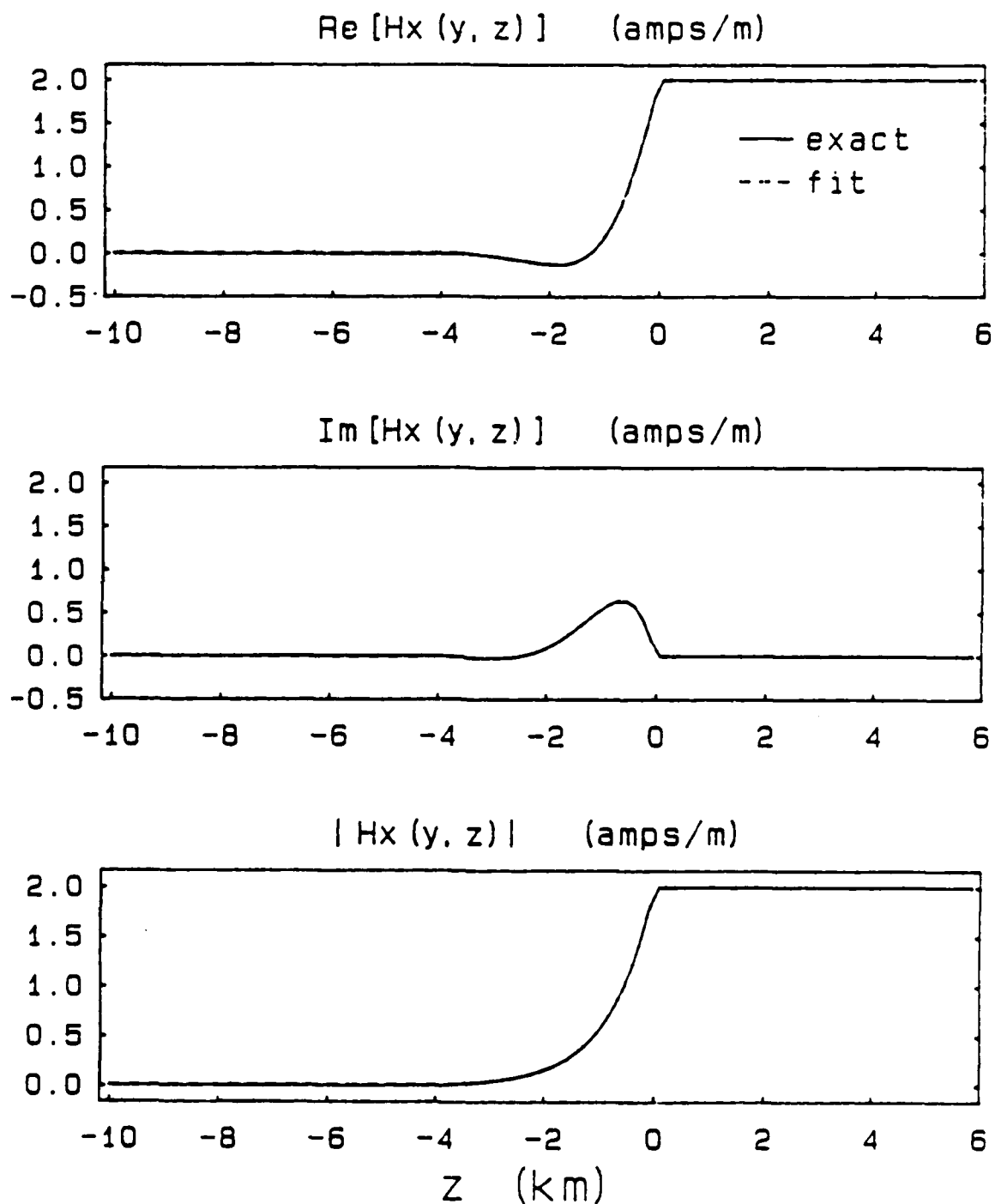


Fig. 6.3a.  $H_x$  for the air/ocean/barrier layered geometry (ocean depth = 4.0 km). The dashed (solid) line is the least-squares fit (exact result). The two solutions are essentially identical.

Three layer: air / ocean (4 km) / land  
 z-dependence (frequency = 0.1 Hz)

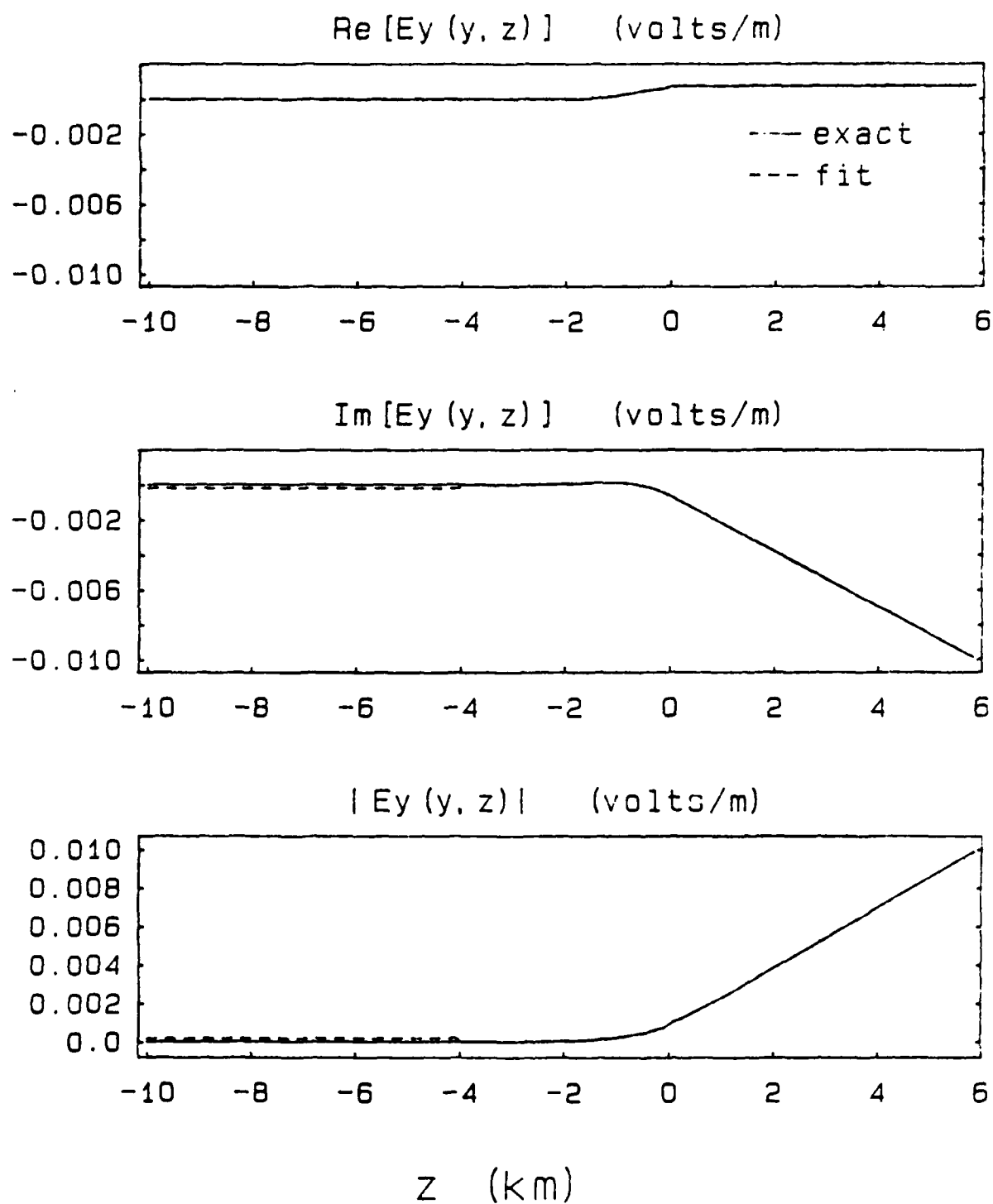


Fig. 6.3b.  $E_y$  for the air/ocean/barrier layered geometry (ocean depth = 4.0 km). The dashed (solid) line is the least-squares fit (exact result). The solutions are almost identical.

Three layer: air / ocean (4 km) / land  
 z-dependence (frequency = 0.1 Hz)

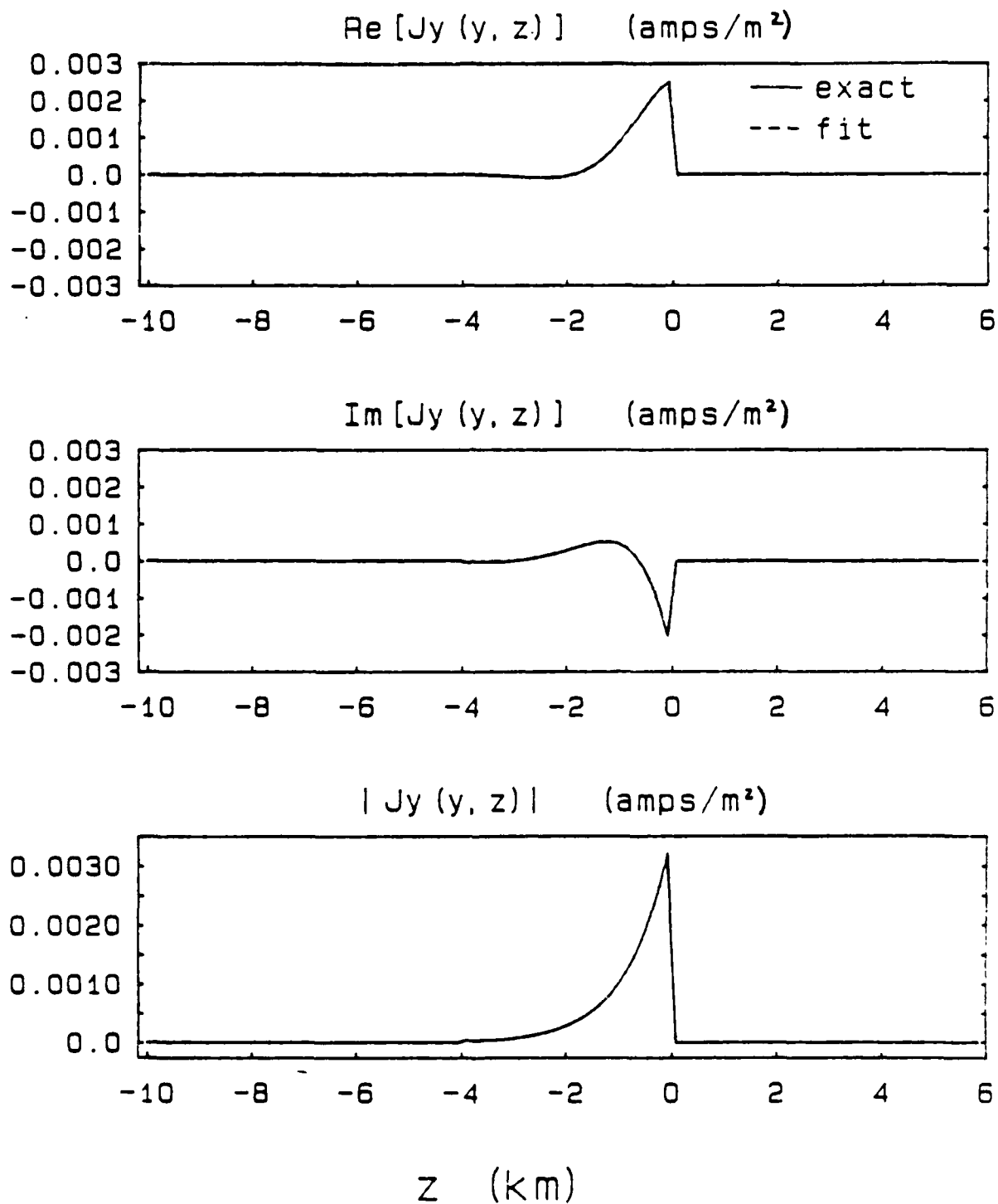


Fig. 6.3c.  $J_y$  for the air/ocean/barrier layered geometry (ocean depth = 4.0 km). The dashed (solid) line is the least-squares fit (exact result). The solutions are essentially identical.

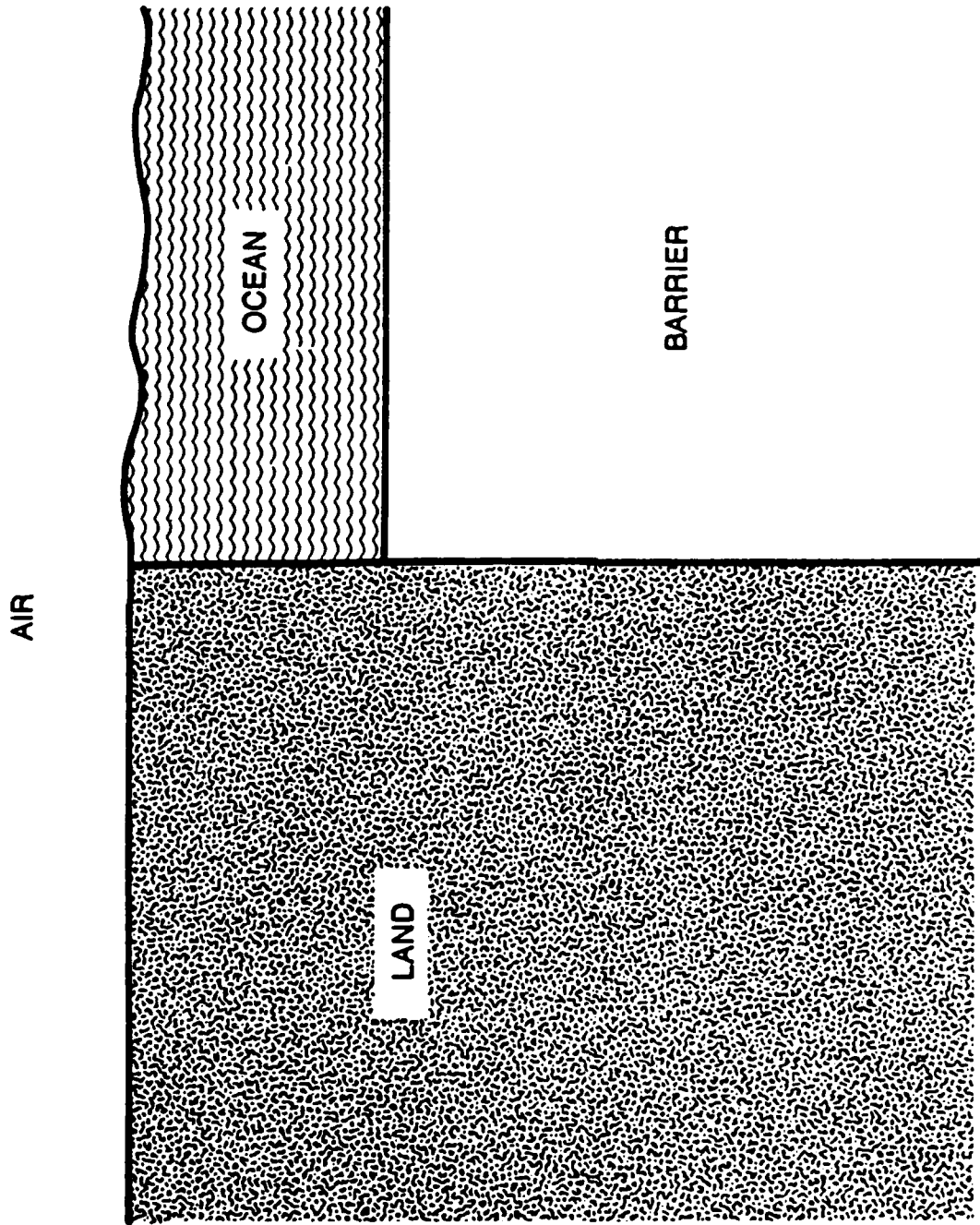


Fig. 6.4. Geometry used for modeling the land/ocean environment.

Comparison of Effective Resistivity using Fitted  
Layered Solutions with Different Barrier Conductivities  
to Empirical Data: Rho-D Tat6 225 Km Cable

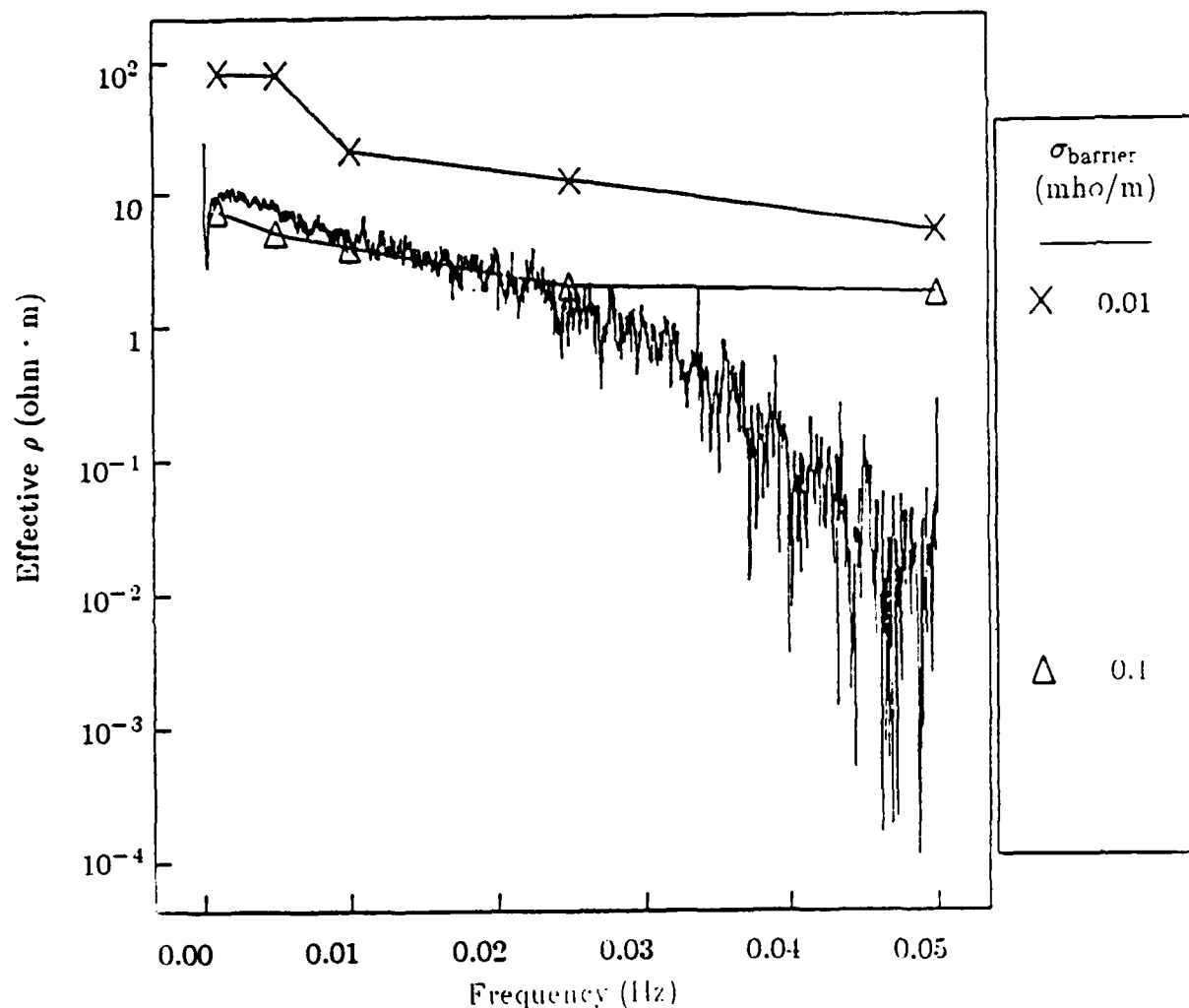


Fig. 6.5a. The effective resistivity for the semi-analytic solution as a function of frequency for two different barrier conductivities ( $\sigma_{\text{barrier}} = 0.01, 0.1$  mho/m). Also shown are the data for  $\rho_D$  for TAT-6 at 225 km.

Comparison of Effective Resistivity using Fitted  
Layered Solutions with Different Barrier Conductivities  
to Empirical Data: Rho-H Tat7 3000 Km Cable

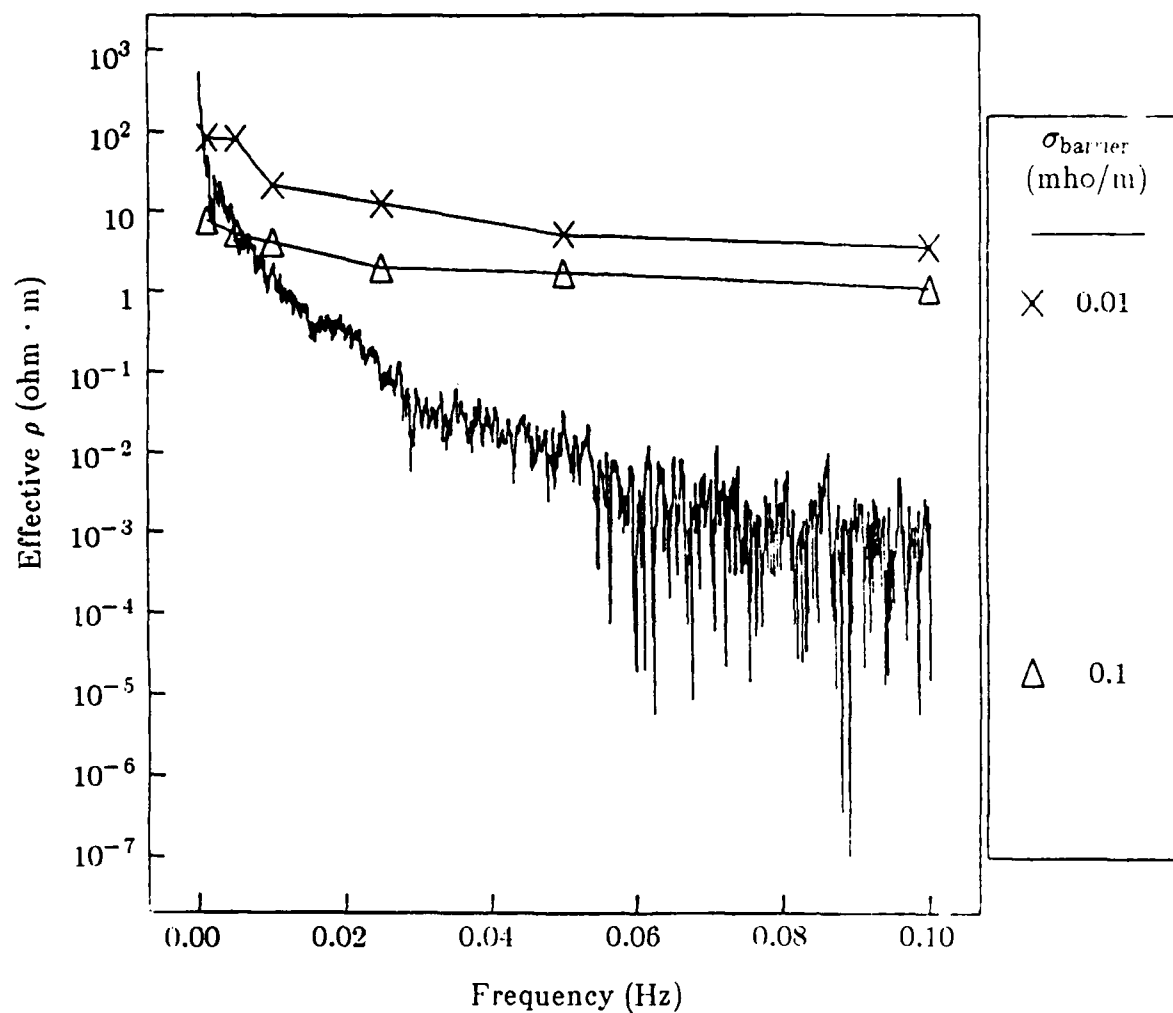


Fig. 6.5b. Same as Fig. 6.5a plotted with the data for  $\rho_H$  for TAT-7 at 3000 km.

Comparison of Effective Resistivity using Trivial  
Layered Solutions with Different Barrier Conductivities  
to Empirical Data: Rho-D Tat6 225 Km Cable

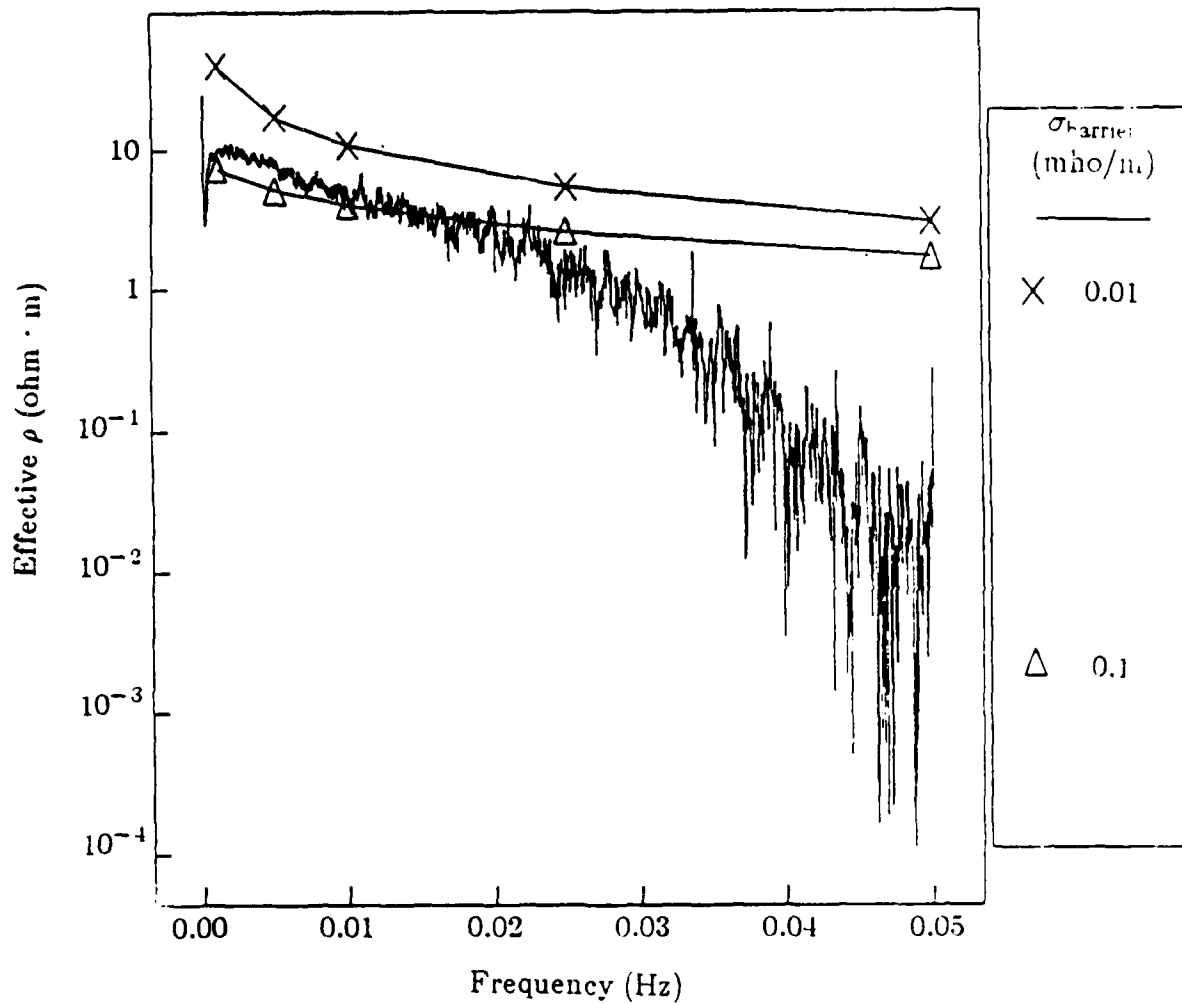


Fig. 6.6a. Same as Fig. 6.5a except the "trivial" 2-layer/3-layer model results are shown.



Comparison of Effective Resistivity using Trivial  
Layered Solutions with Different Barrier Conductivities  
to Empirical Data: Rho-H Tat7 3000 Km Cable

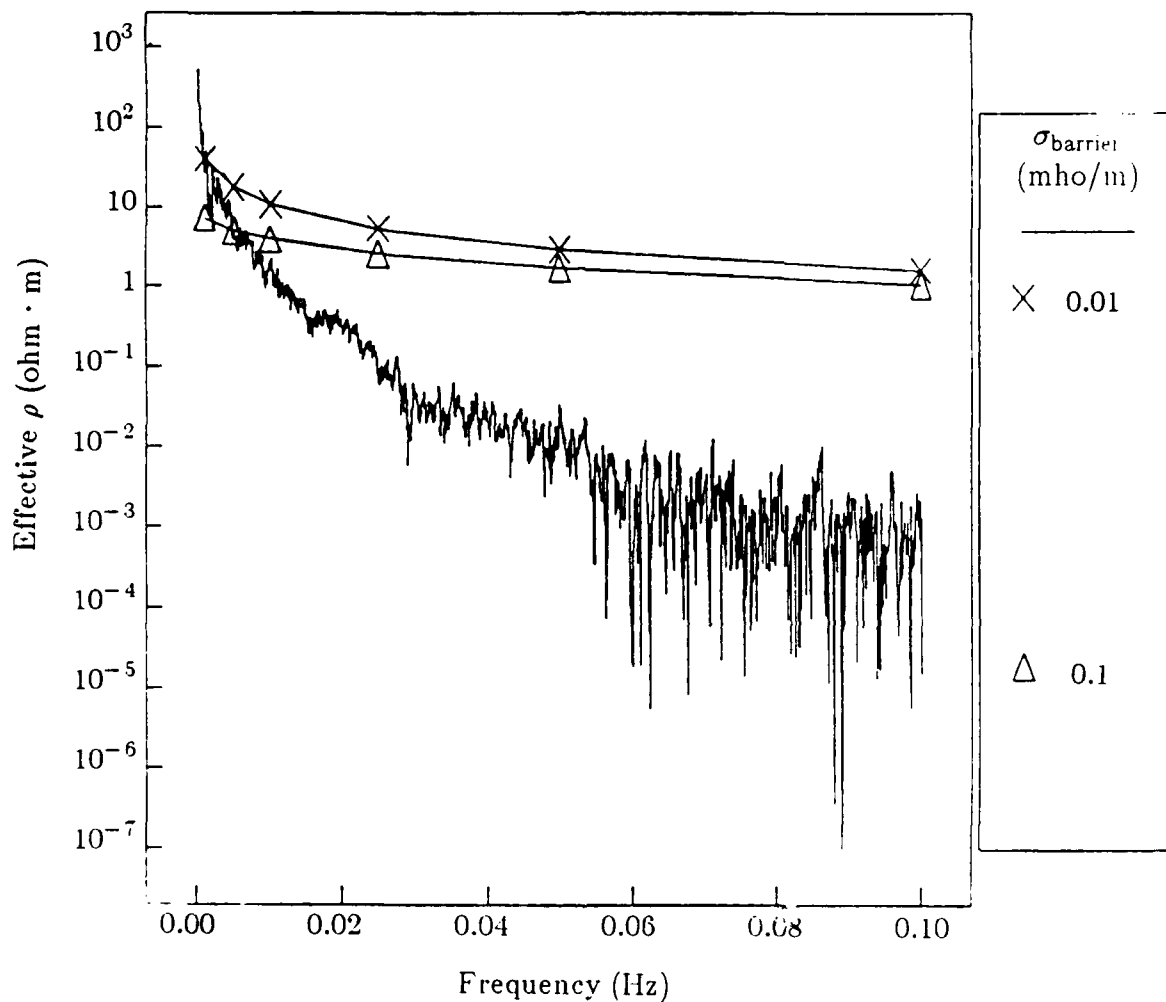


Fig. 6.6b. Same as Fig. 6.5b except the "trivial" 2-layer/3-layer model results are shown.

Effective Resistivity using Fitted  
Layered Solutions with Different Barrier Conductivities

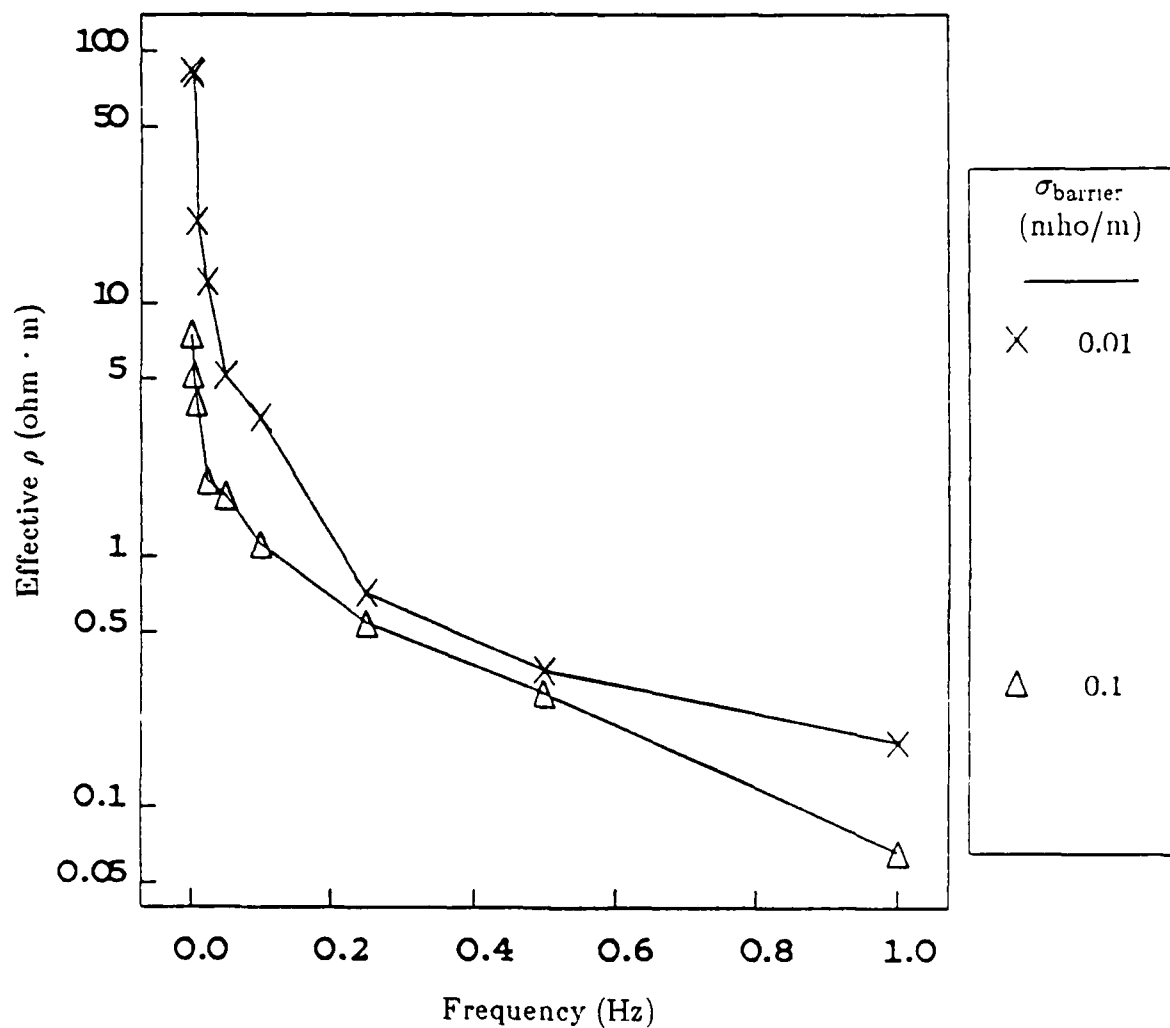


Fig. 6.7a. The effective resistivity for the semi-analytic solution as a function of frequency out to 1 Hz.

# Effective Resistivity using Trivial Layered Solutions with Different Barrier Conductivities

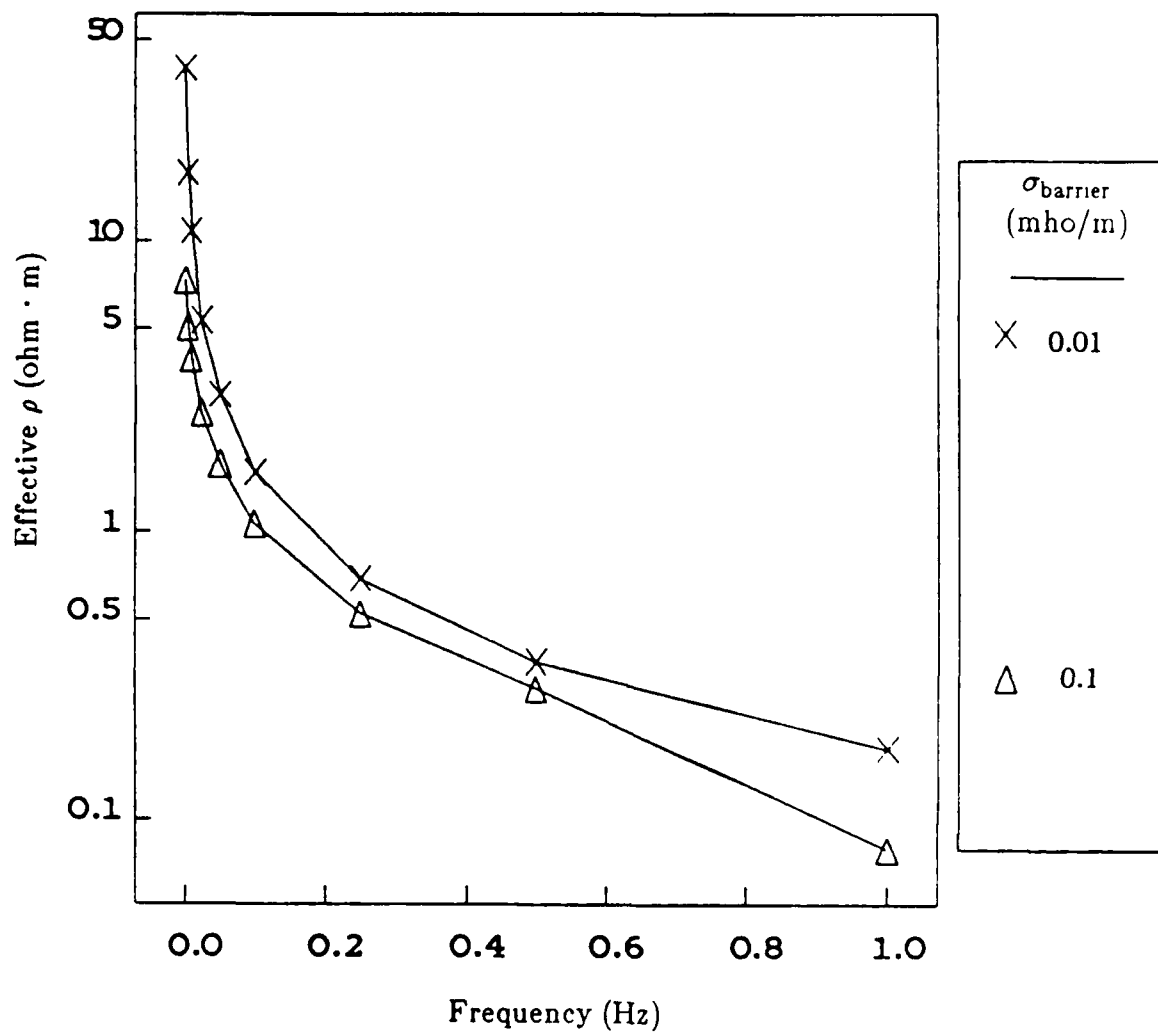


Fig. 6.7b. The effective resistivity for the "trivial" 2-layer/3-layer solution as a function of frequency out to 1 Hz.

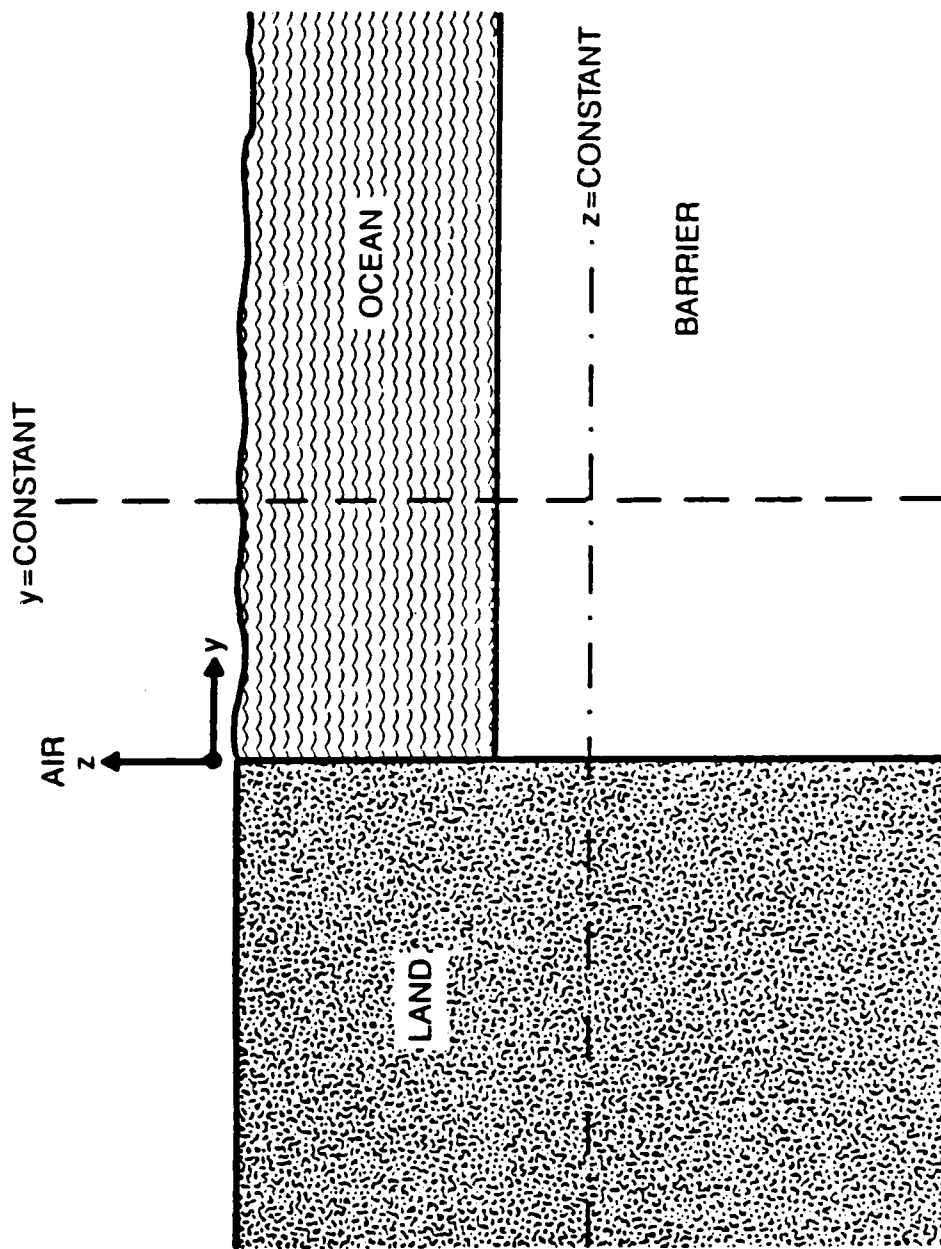


Fig. 6.8. The geometry for the plots 6.9 - 6.14 showing the cuts along which the various fields are plotted. Figs. 6.9 - 6.14 all have  $\sigma = 0.1 \text{ mho/m}$  for the barrier conductivity and are evaluated at a frequency of  $0.1 \text{ Hz}$ . The continuity conditions are that  $H_x$ ,  $E_y$ , and  $J_z$  are supposed to be continuous across horizontal boundaries, while  $H_x$ ,  $J_y$ , and  $E_z$  are supposed to be continuous across vertical boundaries.

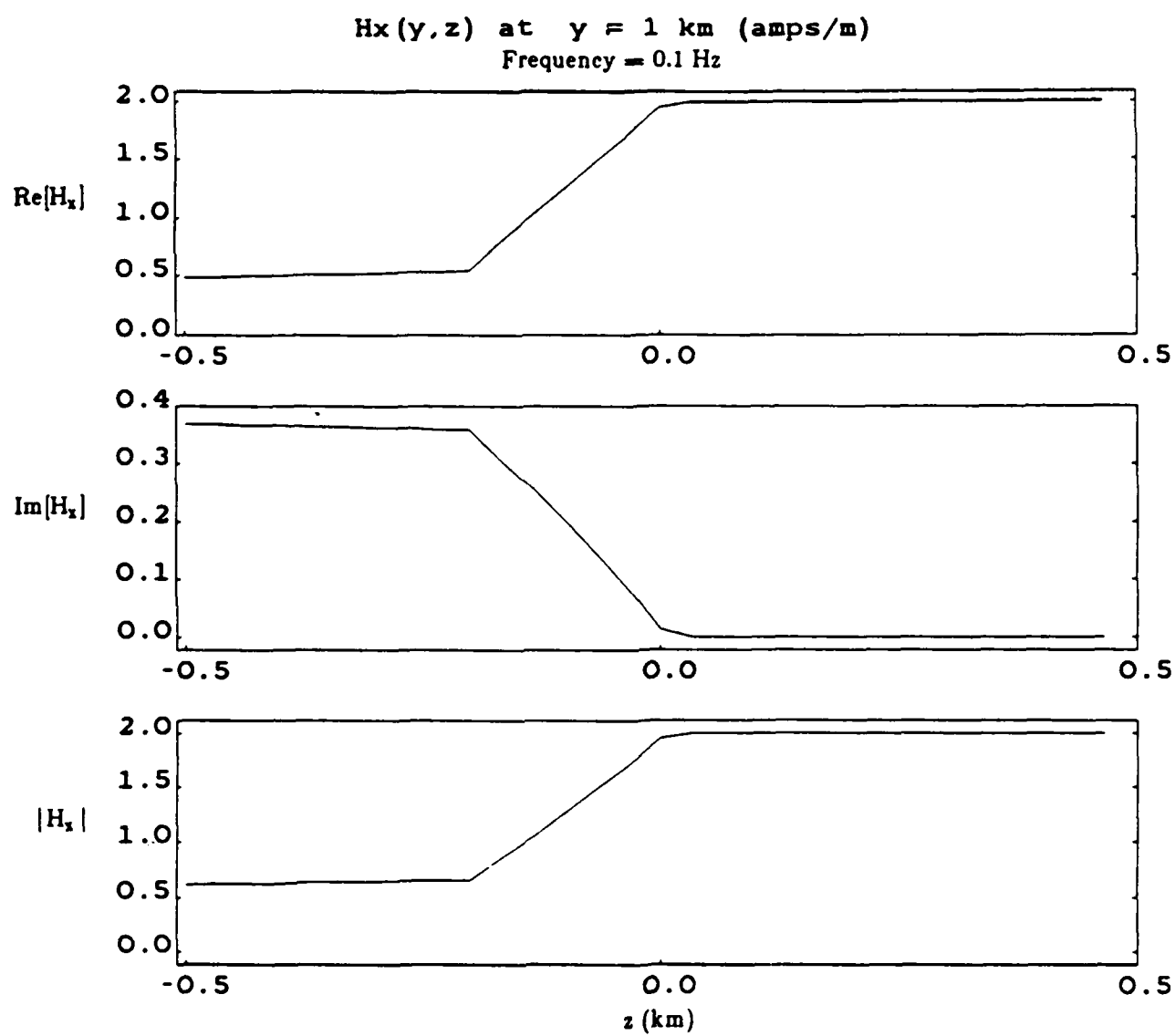


Fig. 6.9a. The magnetic field  $H_x$  from the fitted semi-analytic solution at  $y = 1$  km.

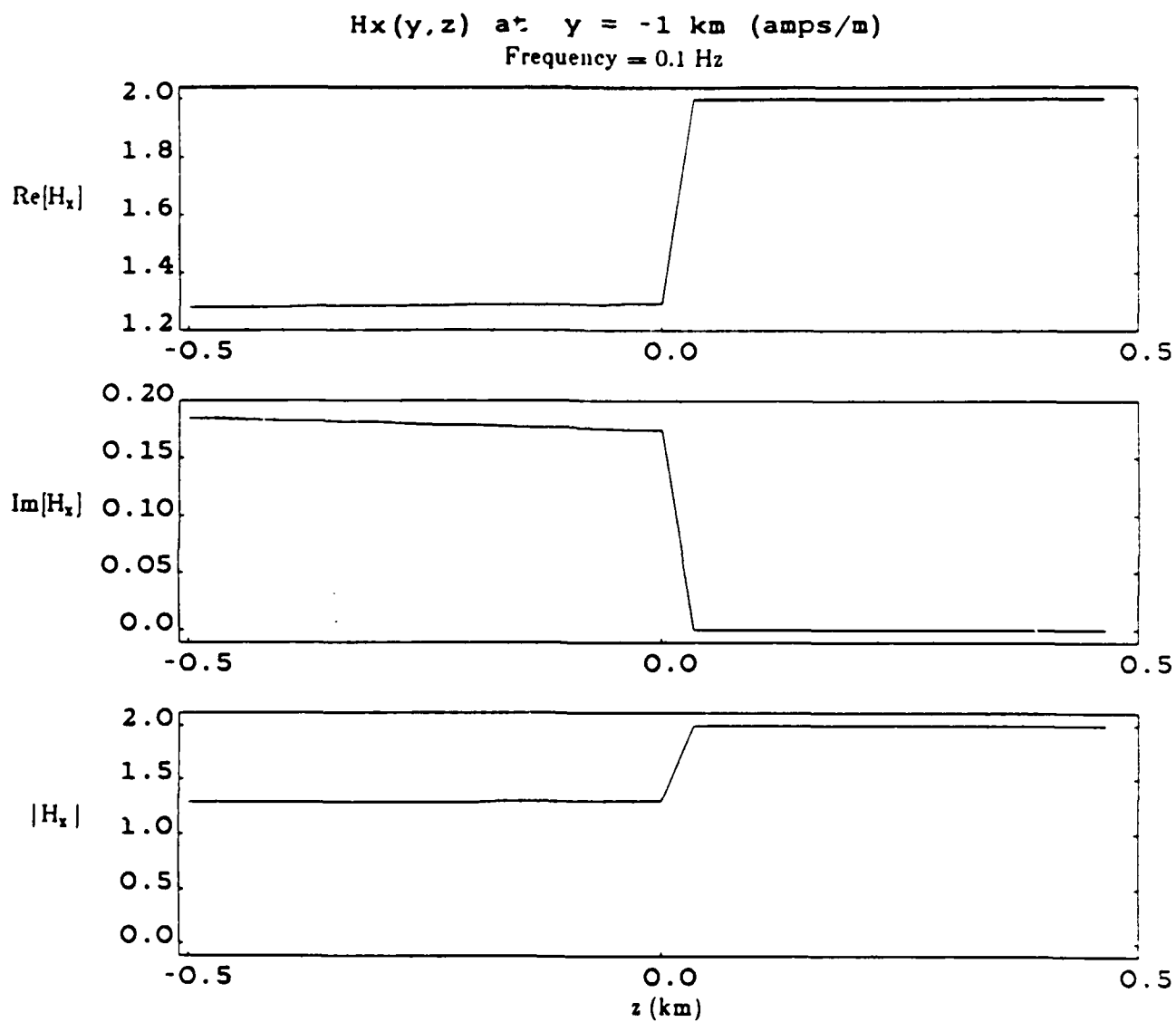


Fig. 8.9b. The magnetic field  $H_x$  from the semi-analytic solution at  $y = -1$  km.

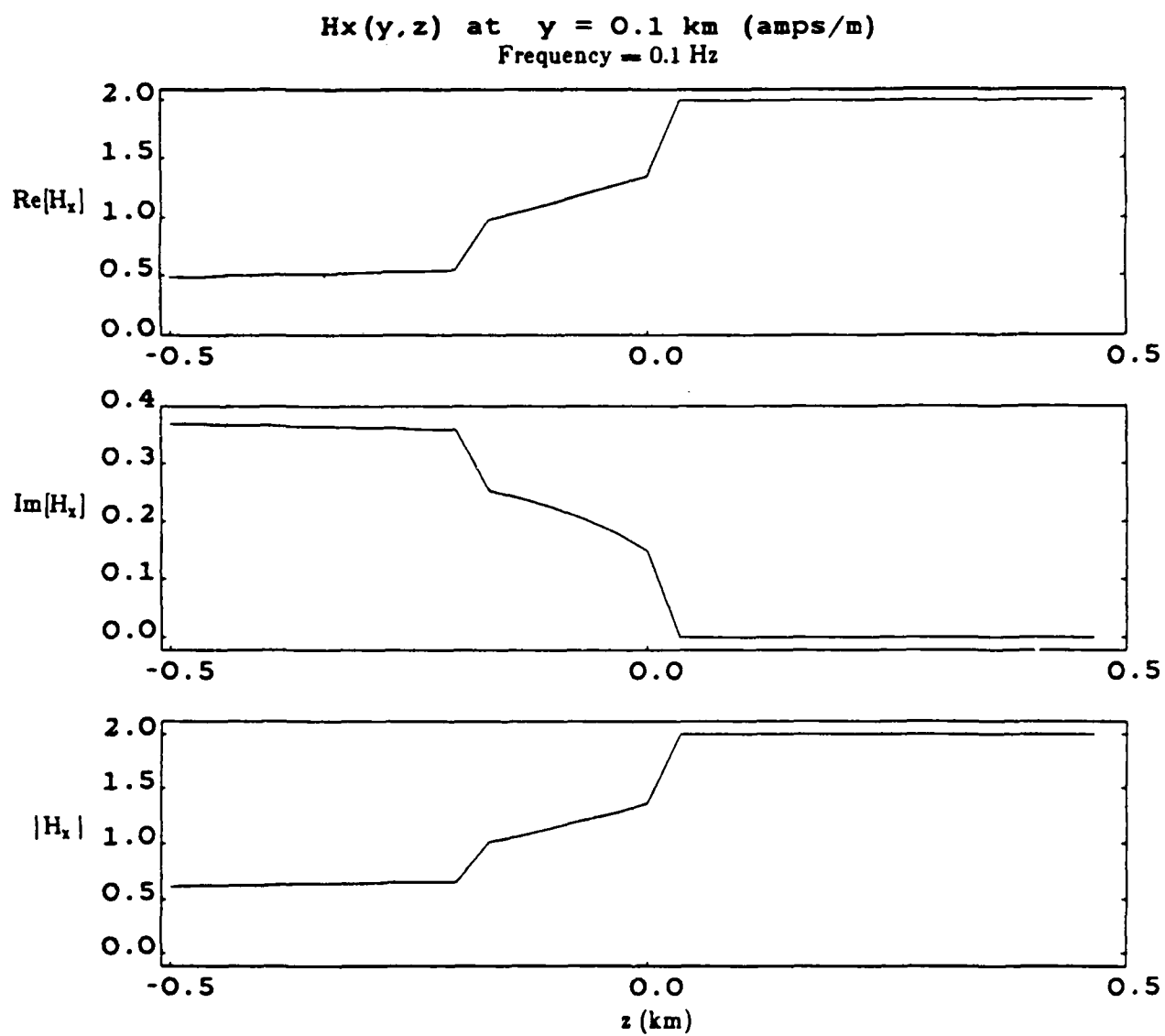


Fig. 6.9c. The magnetic field  $H_x$  from the semi-analytic solution at  $y = 0.1$  km.

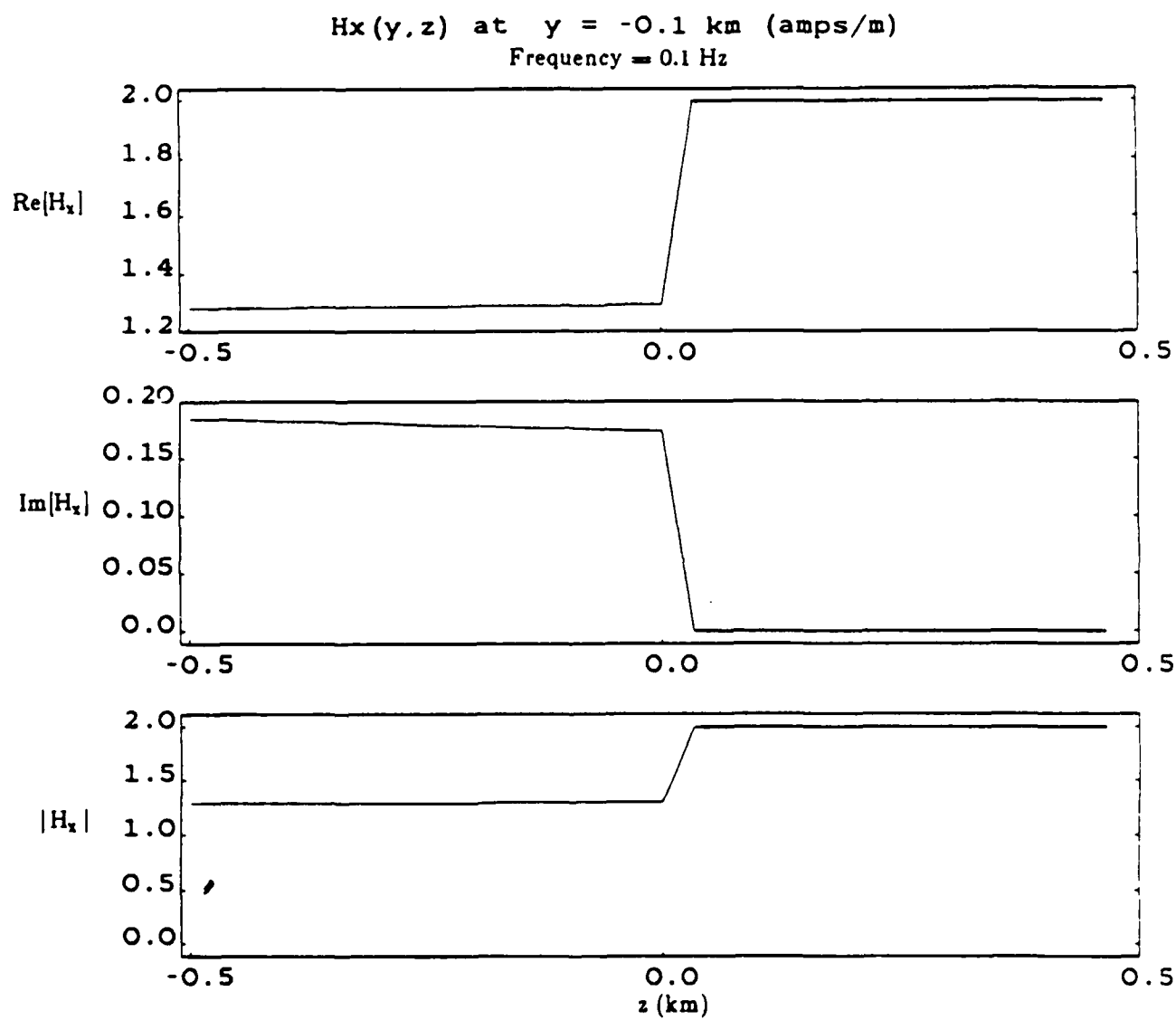


Fig. 6.9d. The magnetic field  $H_x$  from the semi-analytic solution at  $y = -0.1$  km.



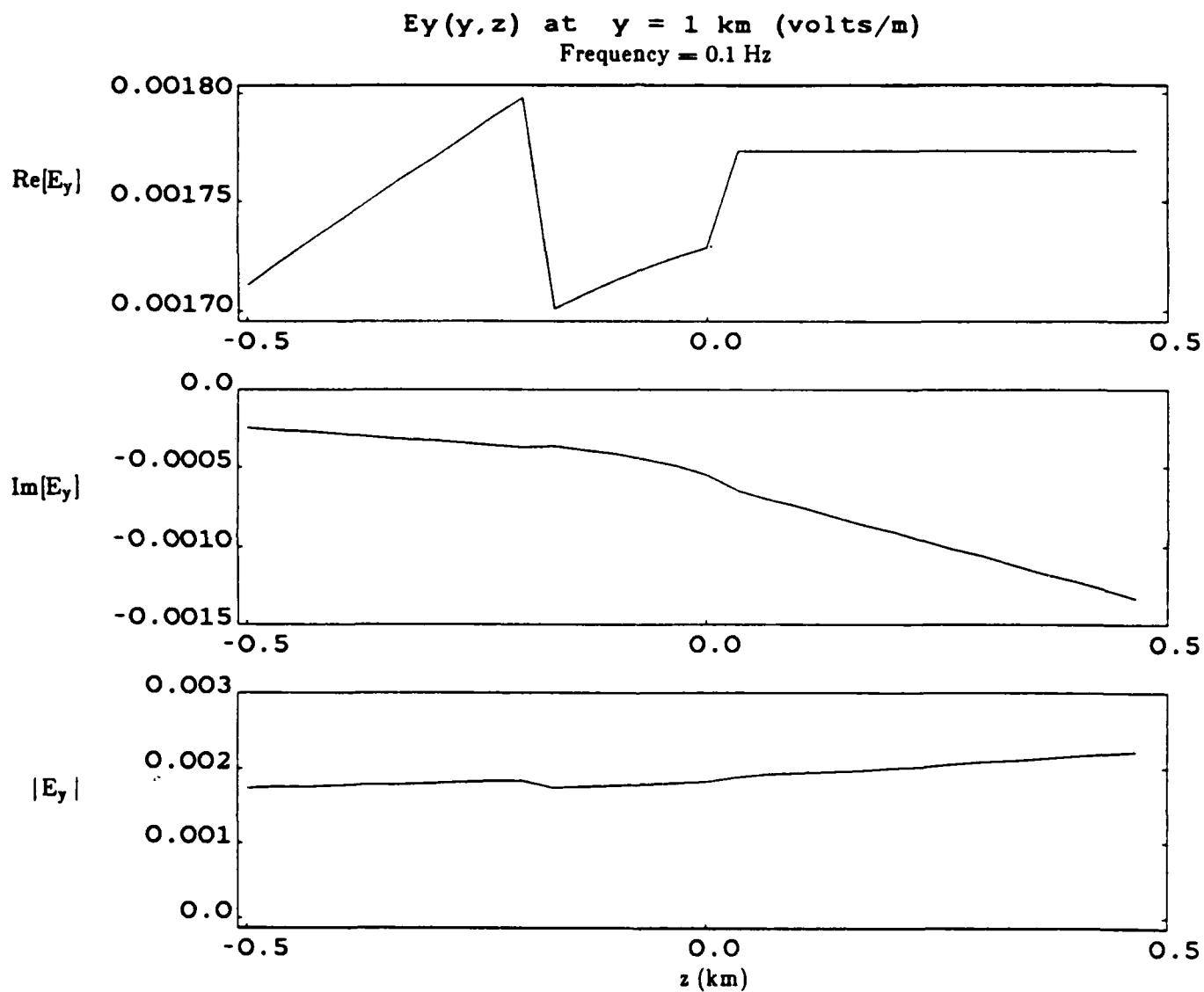


Fig. 6.10a. The electric field  $E_y$  from the semi-analytic solution at  $y = 1$  km.

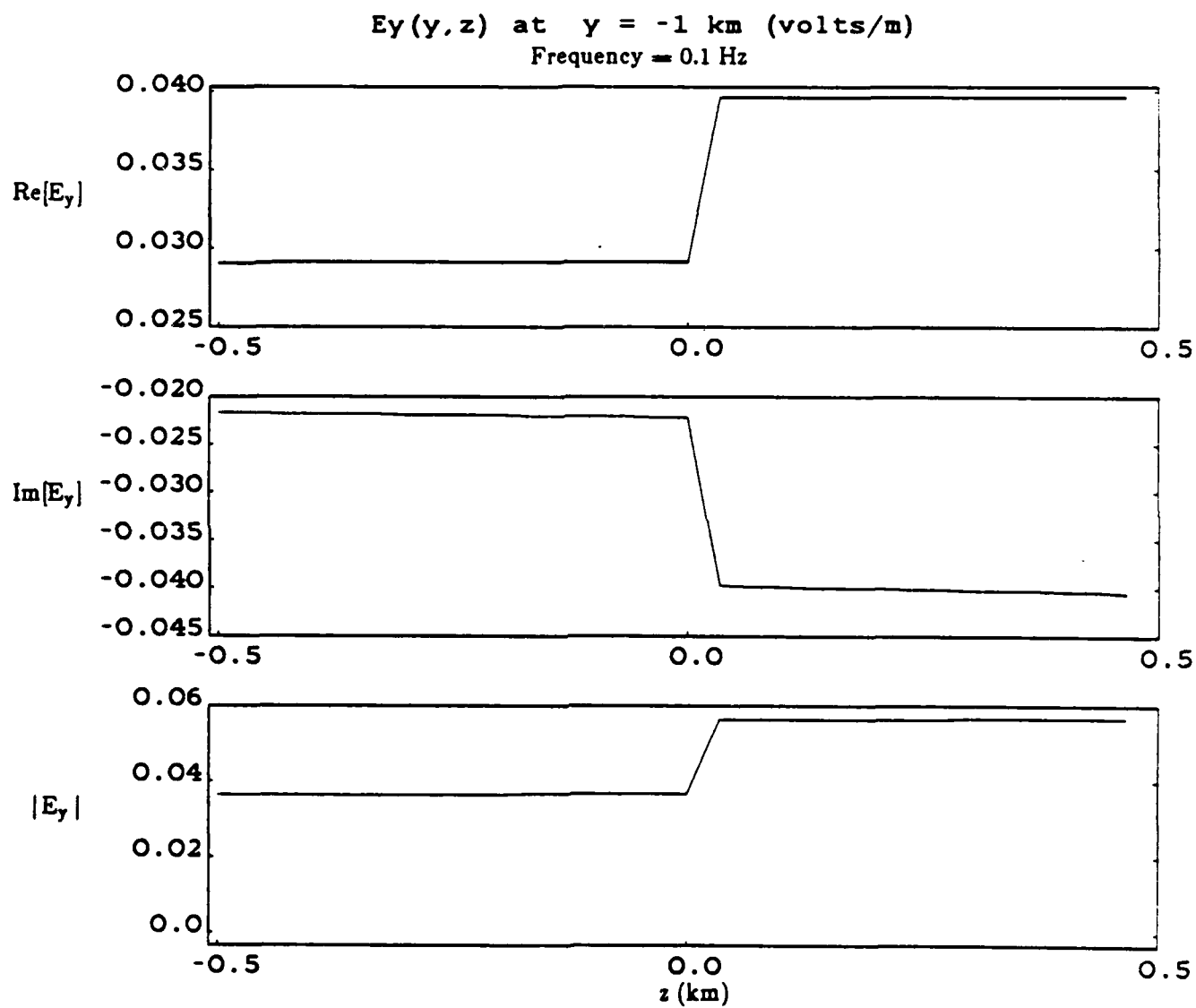


Fig. 6.10b. The electric field  $E_y$  from the semi-analytic solution at  $y = -1$  km.

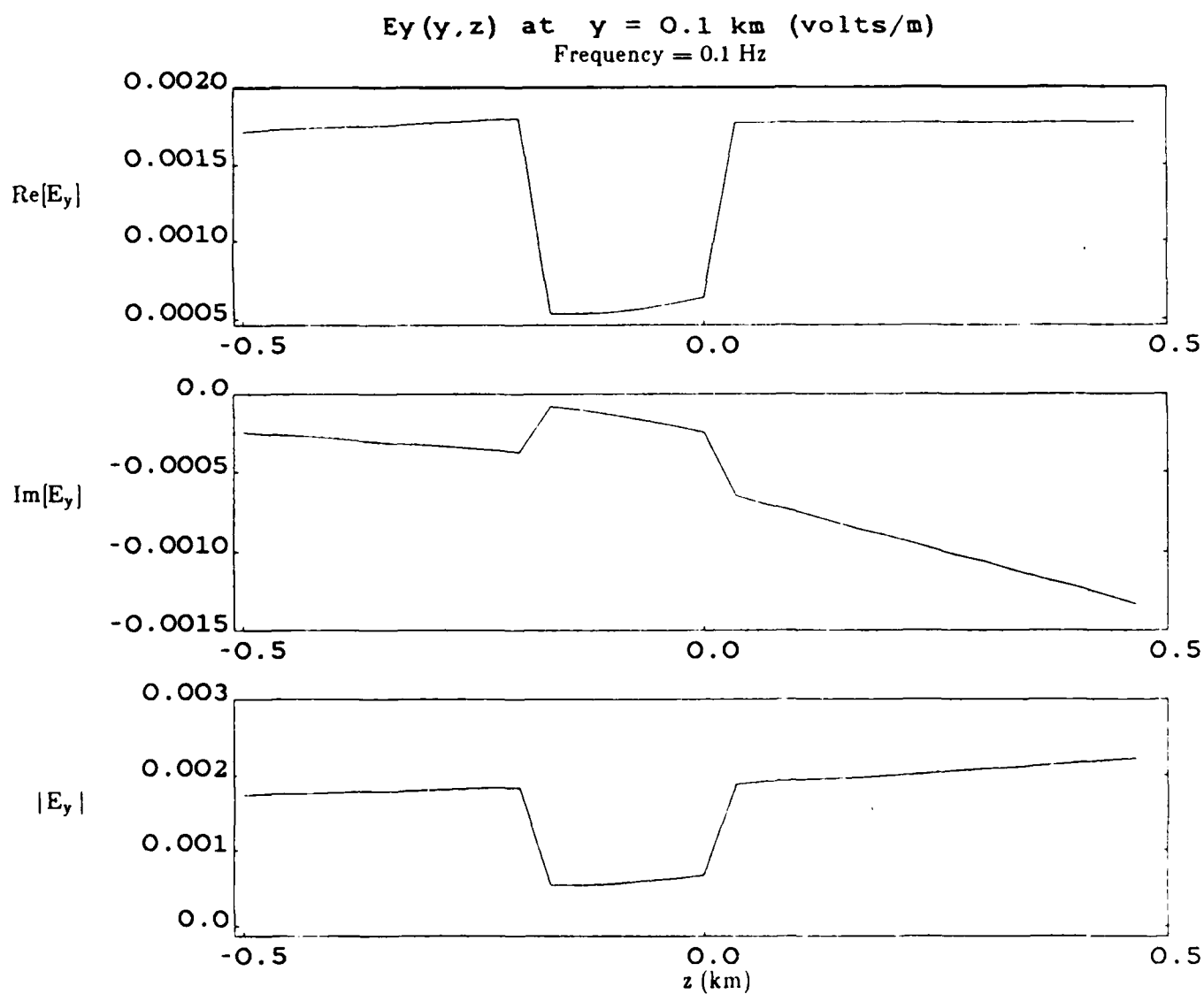


Fig. 6.10c. The electric field  $E_y$  from the semi-analytic solution at  $y = 0.1$  km.

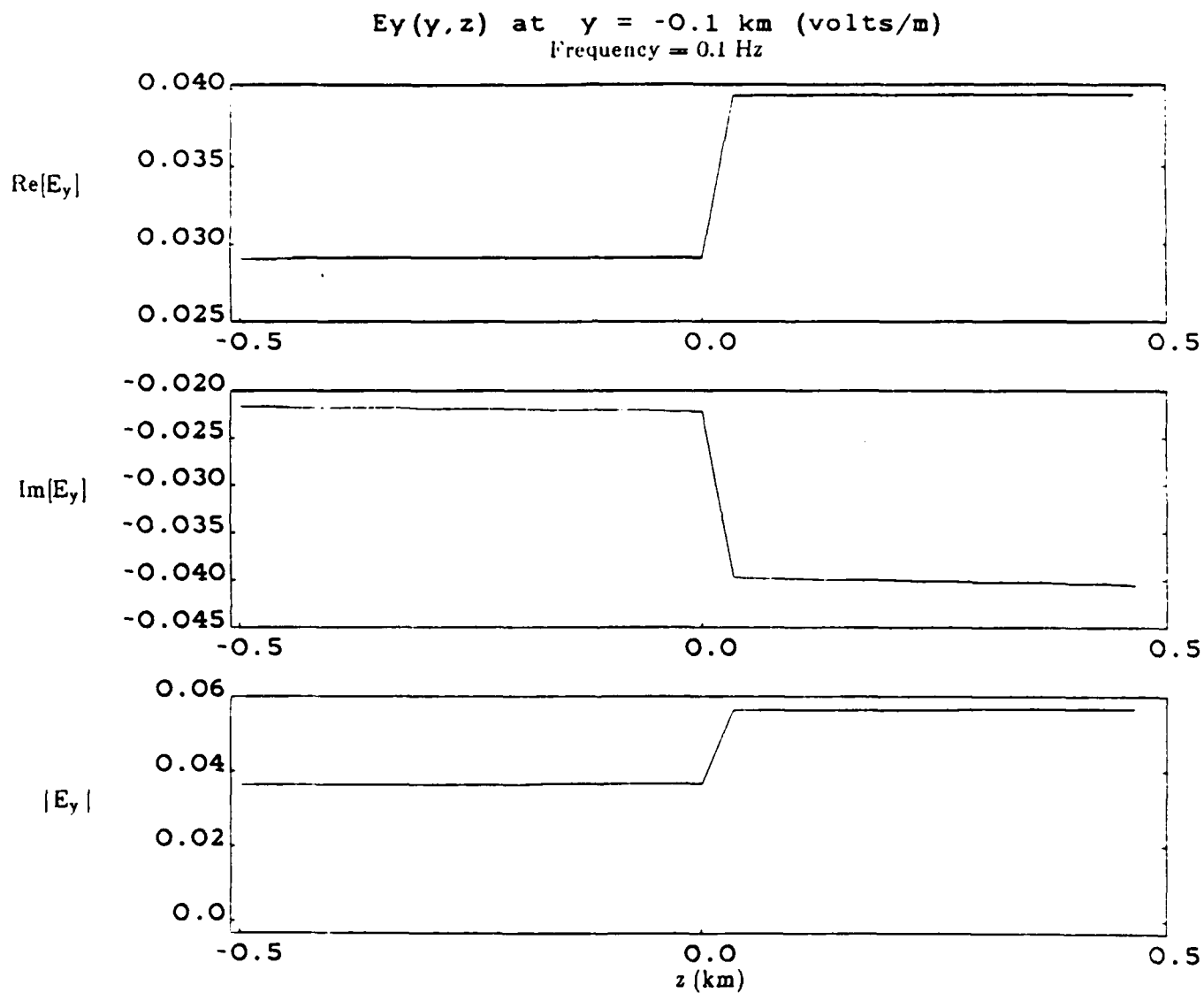


Fig. 6.10d. The electric field  $E_y$  from the semi-analytic solution at  $y = -0.1$  km.

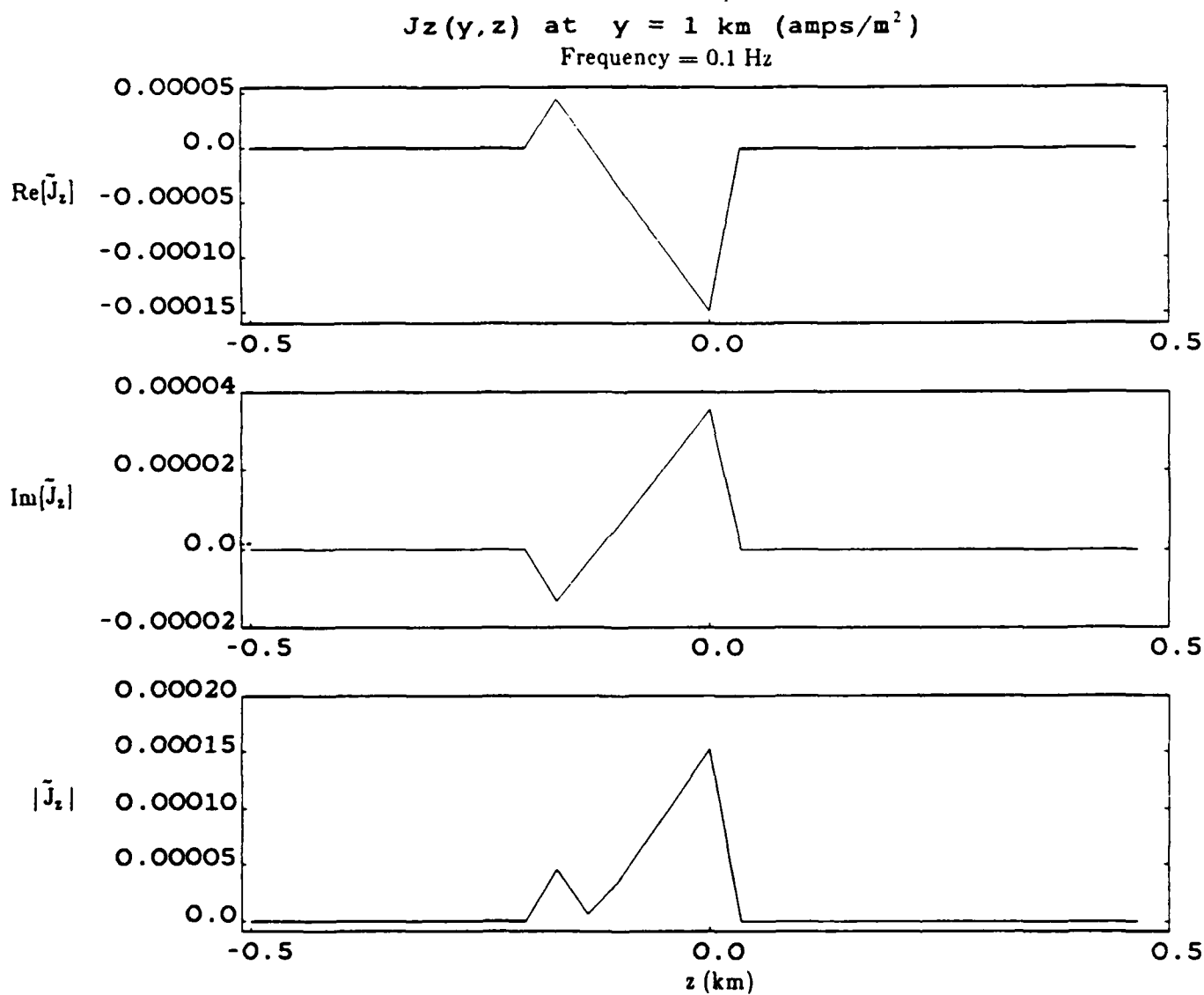


Fig. 6.11a. The total current  $\tilde{J}_z$  from the semi-analytic solution at  $y = 1$  km.

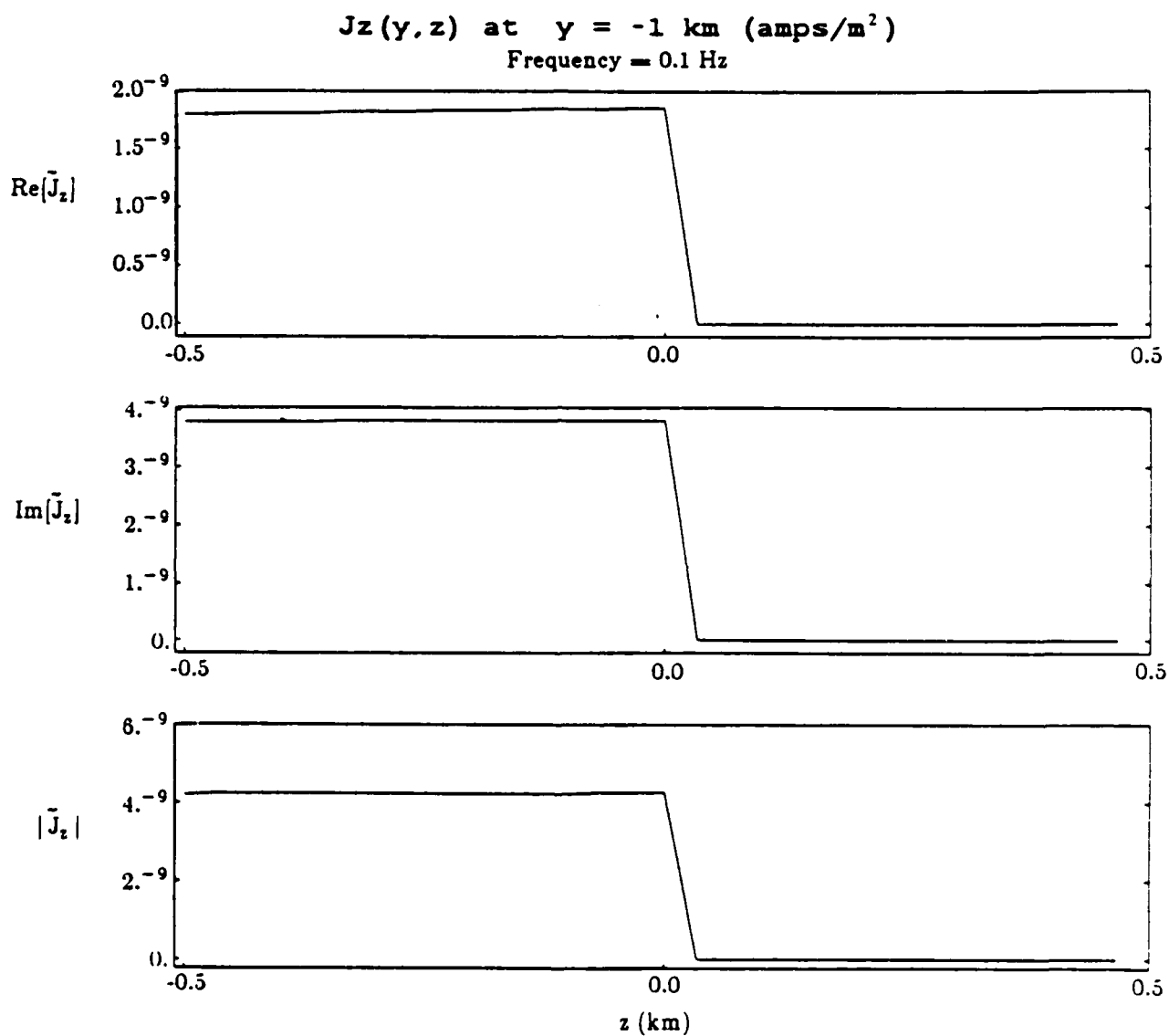


Fig. 6.11b. The total current  $\tilde{J}_z$  from the semi-analytic solution at  $y = -1$  km. (Ordinate label of  $n^{-m}$  means current of  $n \times 10^{-m}$  amps/m<sup>2</sup>.)

NO-R136 749

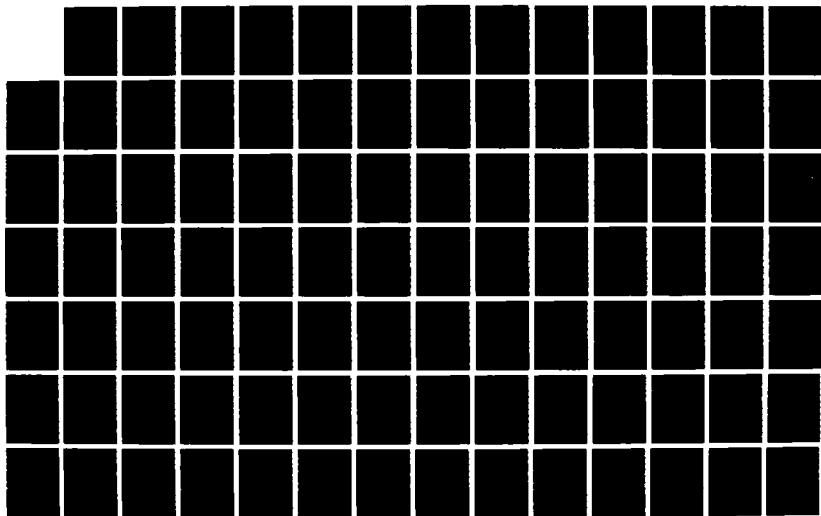
MAGNETOHYDRODYNAMIC (MHD) NUCLEAR WEAPONS EFFECTS ON  
SUBMARINE CABLE SYST. (U) AT AND T BELL LABS HOLMDEL NJ  
JUN 87 NCS-TID-87-14-VOL-1 DCR100-85-C-0060

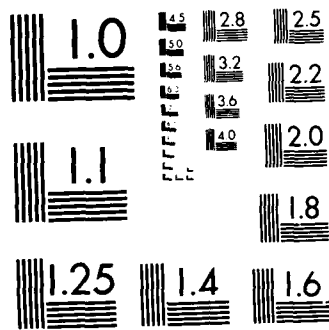
374

UNCLASSIFIED

F/G 28/14

ML







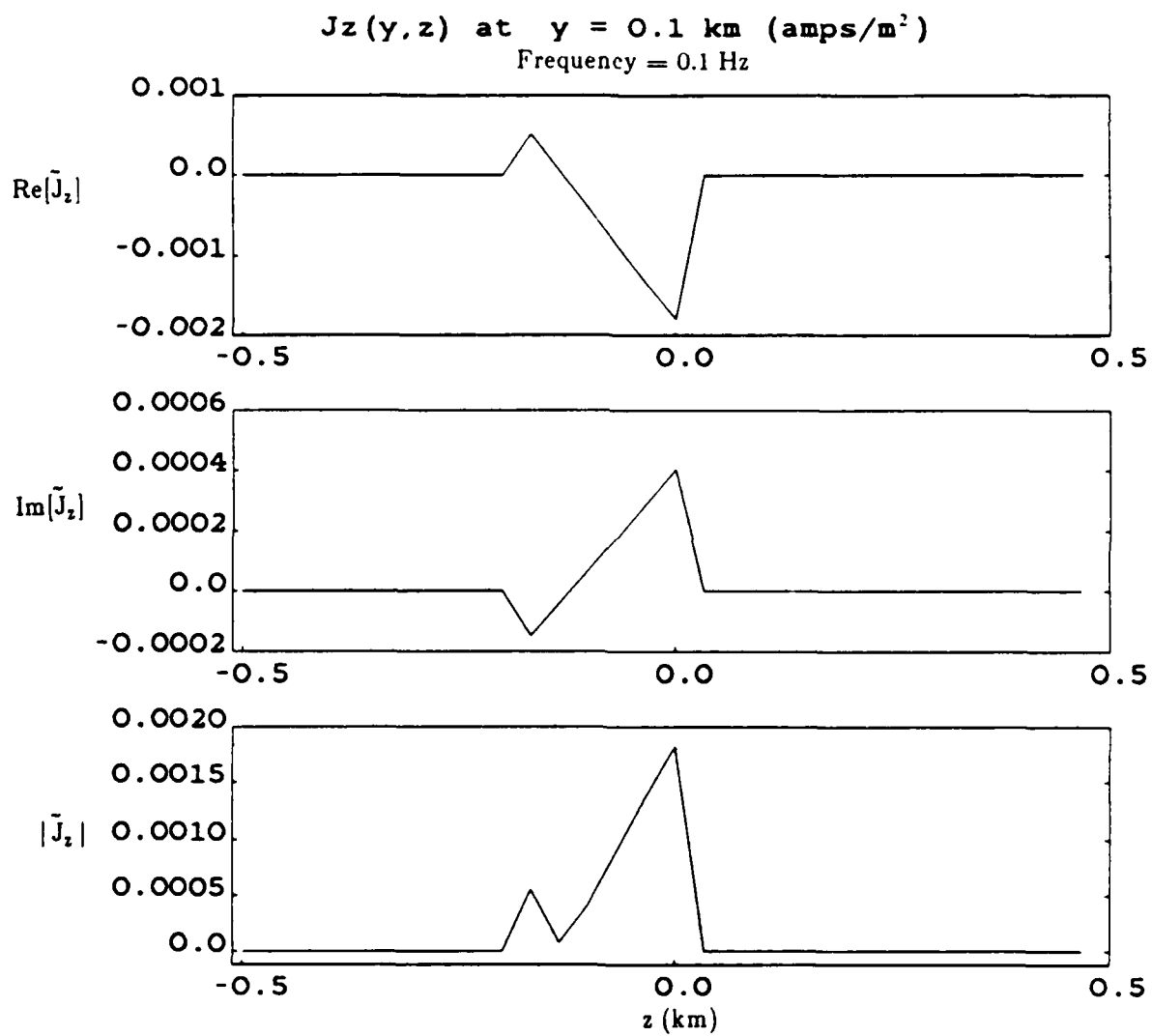


Fig. 6.11c. The total current  $\tilde{J}_z$  from the semi-analytic solution at  $y = 0.1 \text{ km}$ .

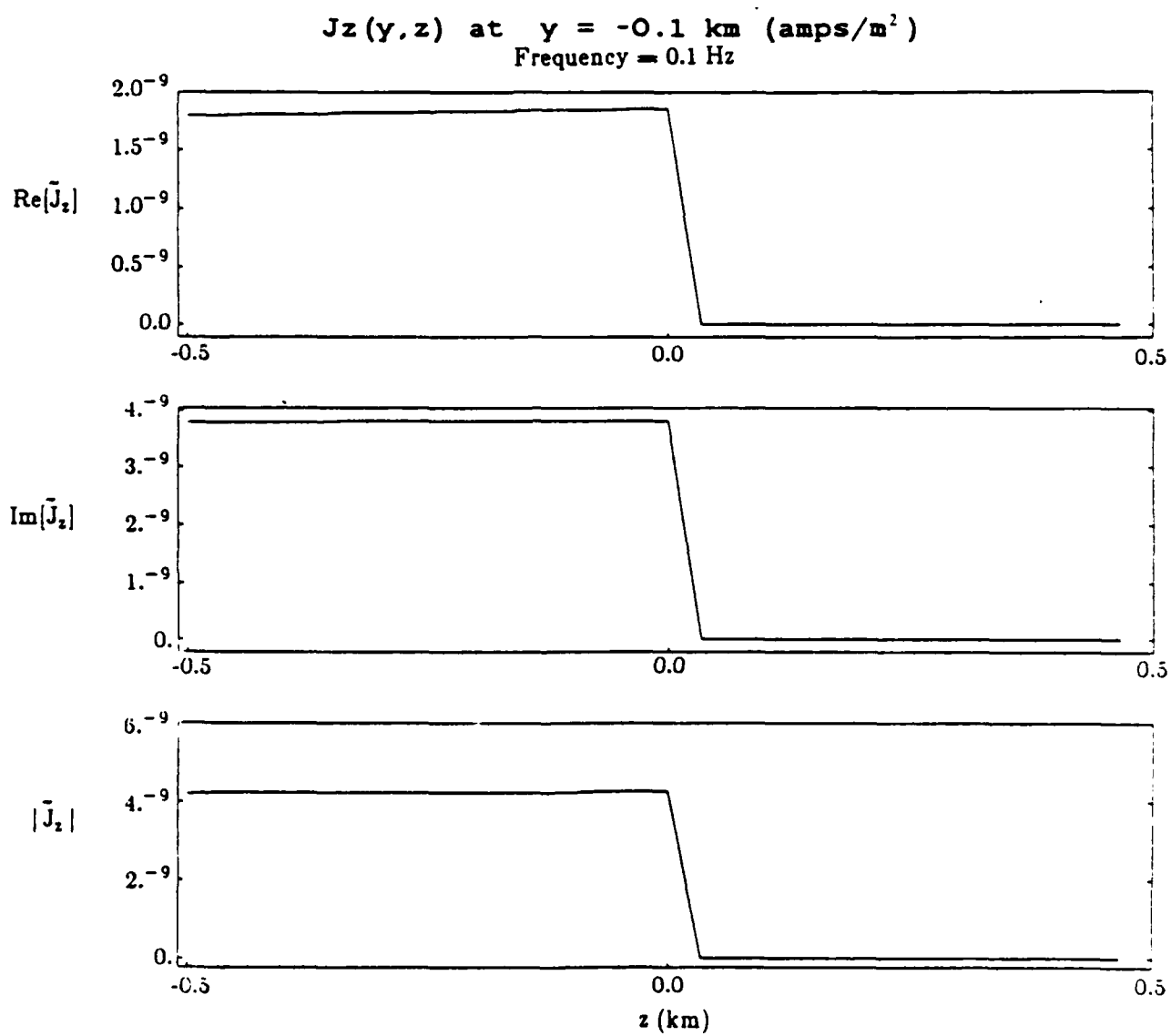


Fig. 8.11d. The total current  $\tilde{J}_z$  from the semi-analytic solution at  $y = -0.1 \text{ km}$ .

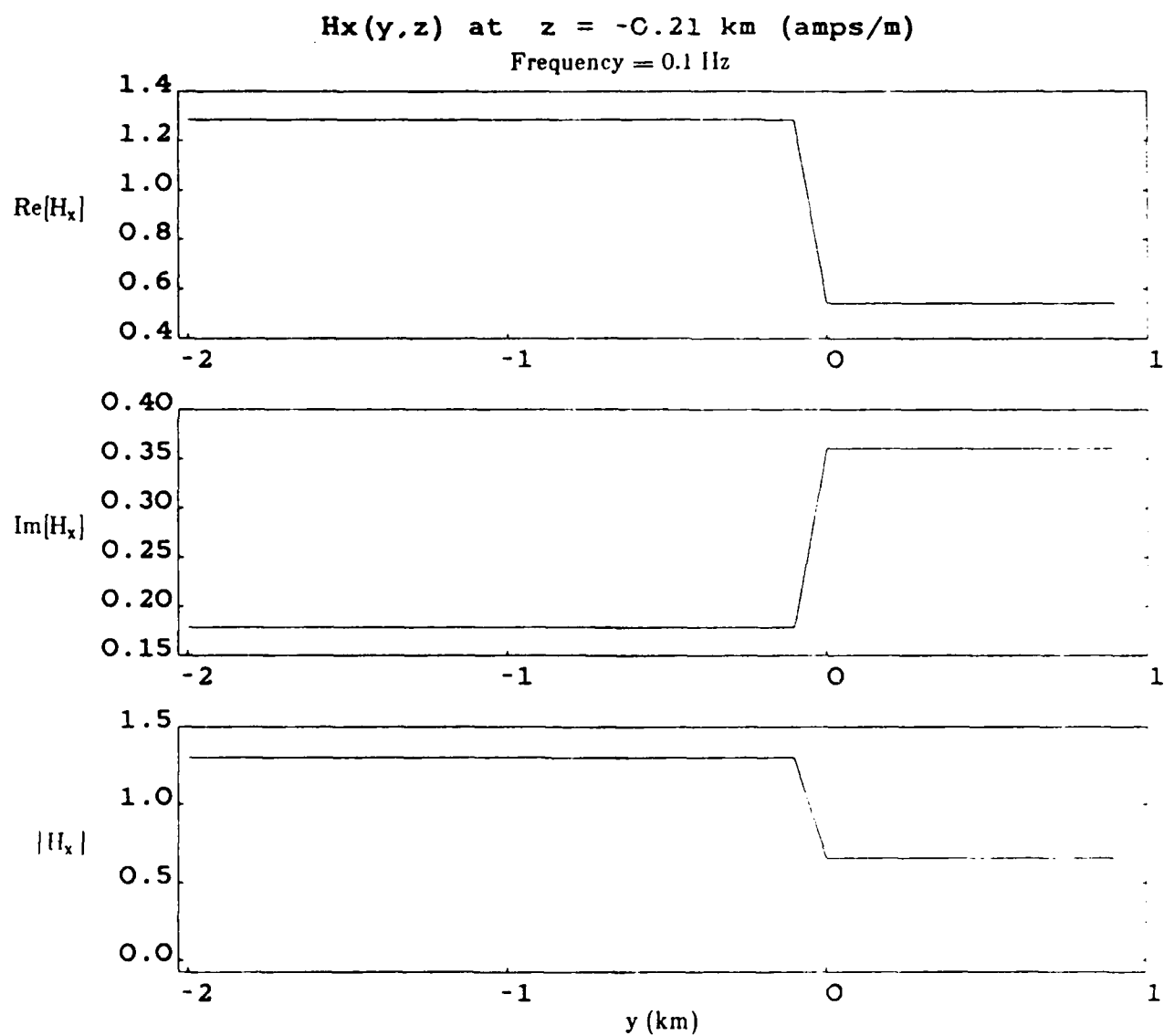


Fig. 6.12a. The magnetic field  $H_x$  from the semi-analytic solution at  $z = -0.21$  km.

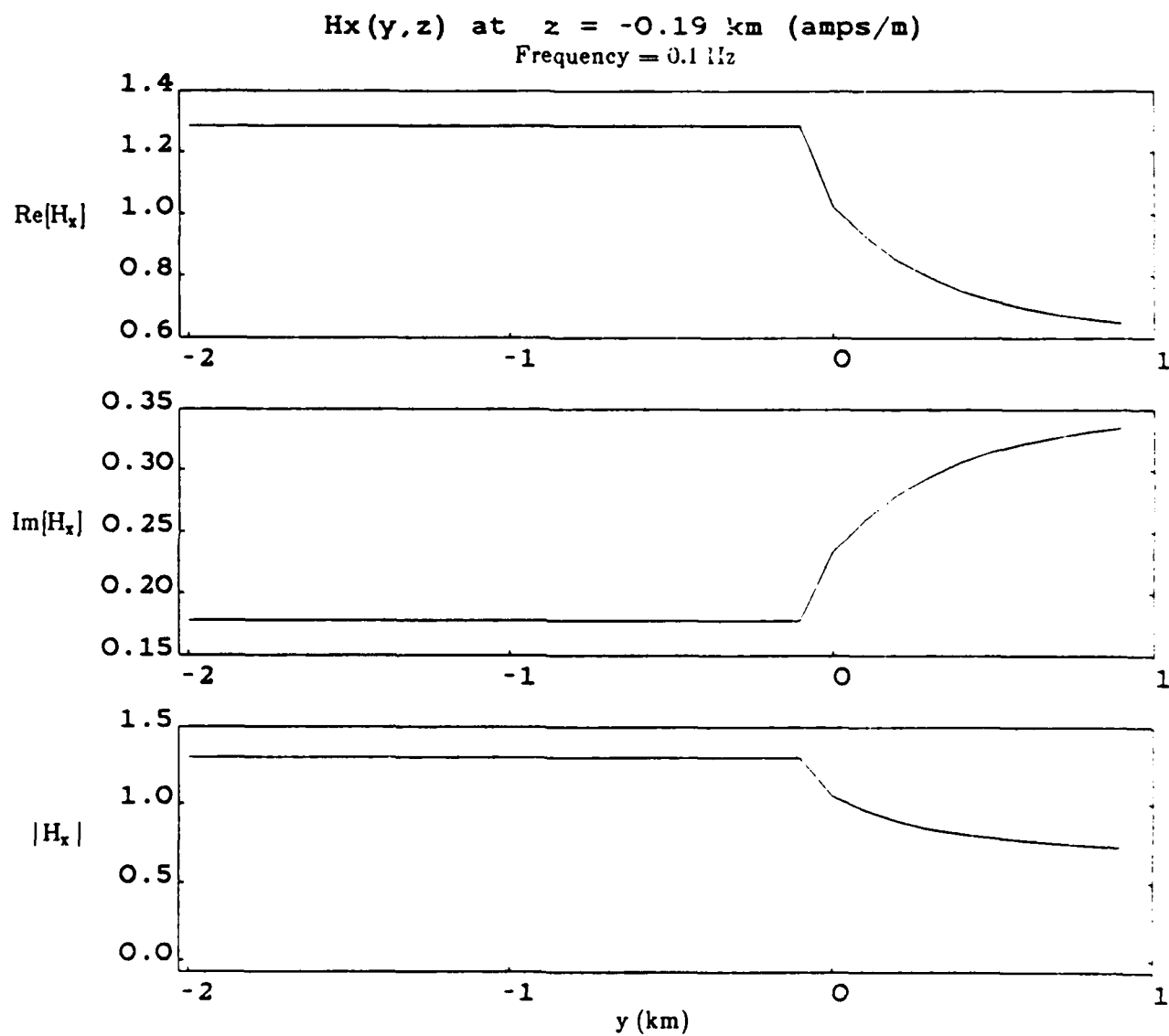


Fig. 6.12b. The magnetic field  $H_x$  from the semi-analytic solution at  $z = -0.19$  km.

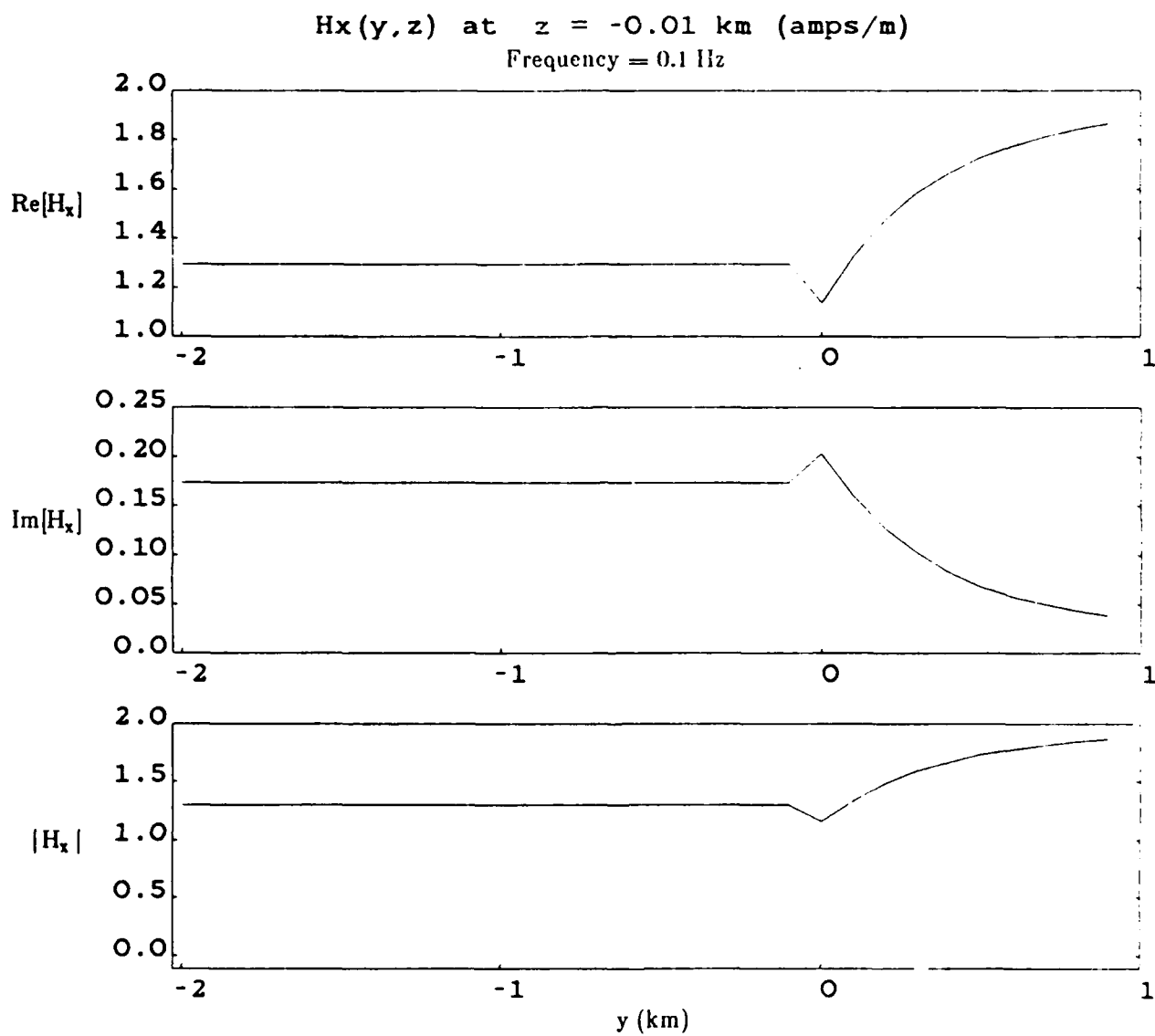


Fig. 6.12c. The magnetic field  $H_x$  from the semi-analytic solution at  $z = -0.01$  km.

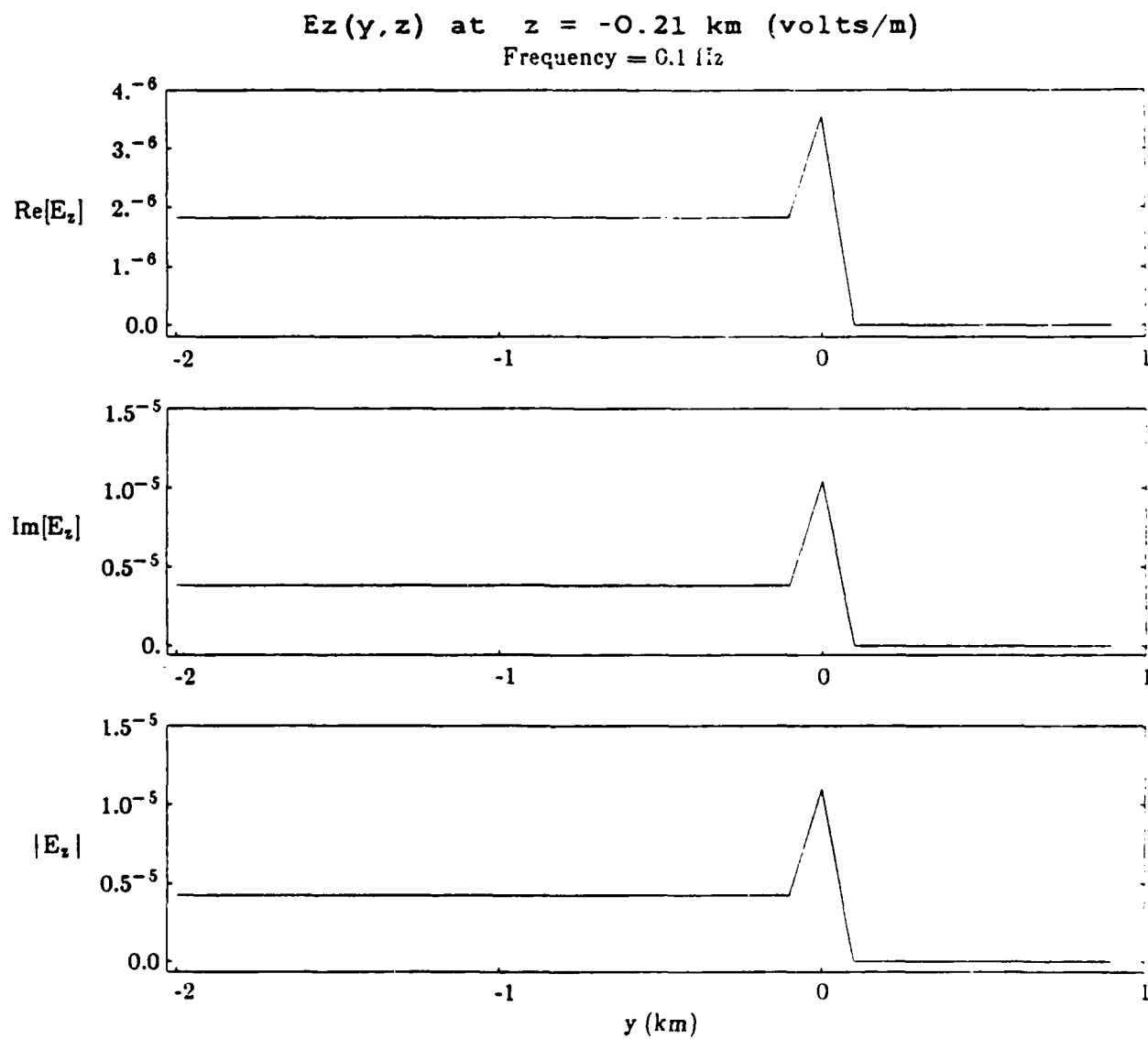


Fig. 6.13a. The electric field  $E_z$  from the semi-analytic solution at  $z = -0.21$  km.

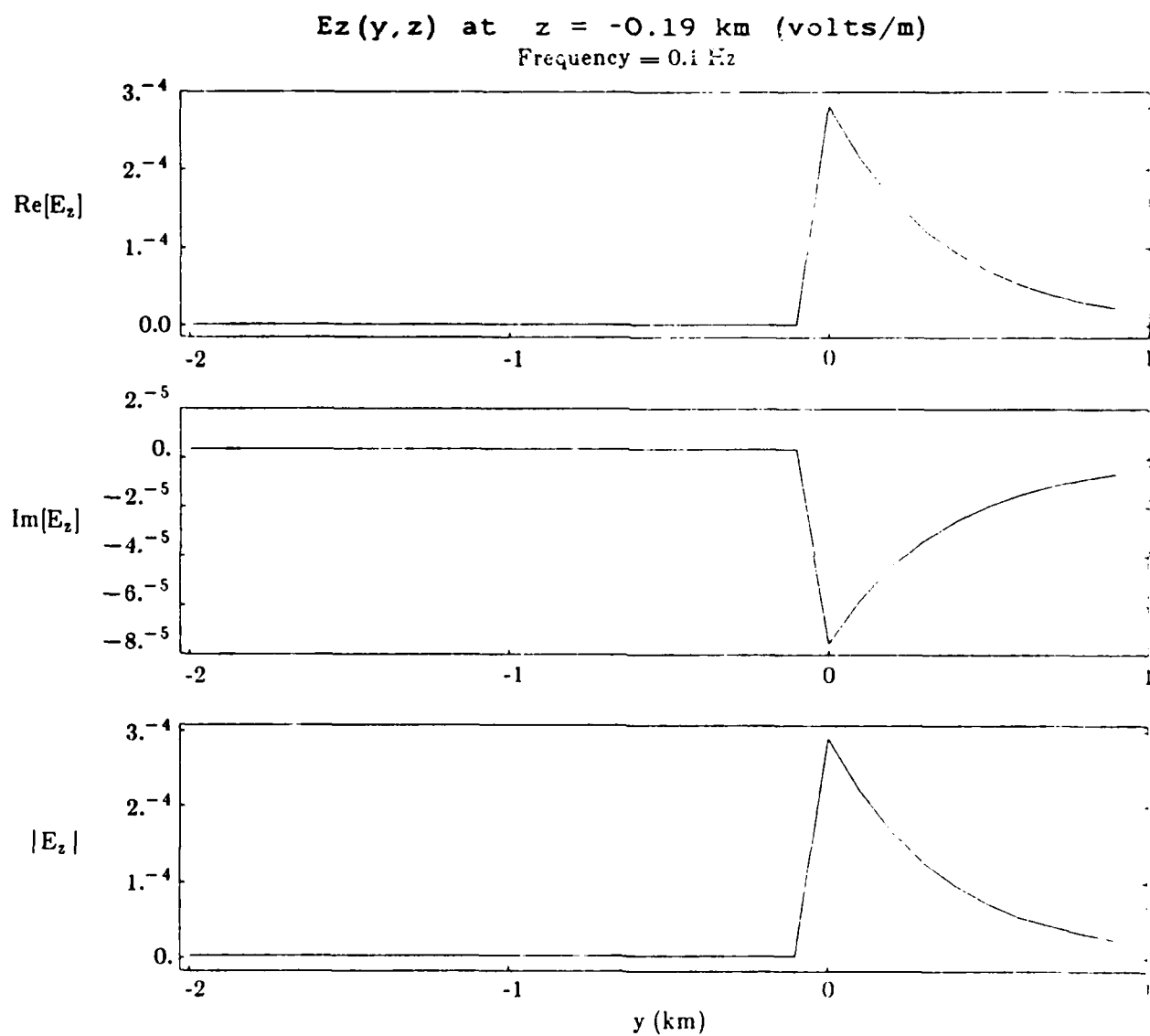


Fig. 8.13b. The electric field  $E_z$  from the semi-analytic solution at  $z = -0.19$  km.

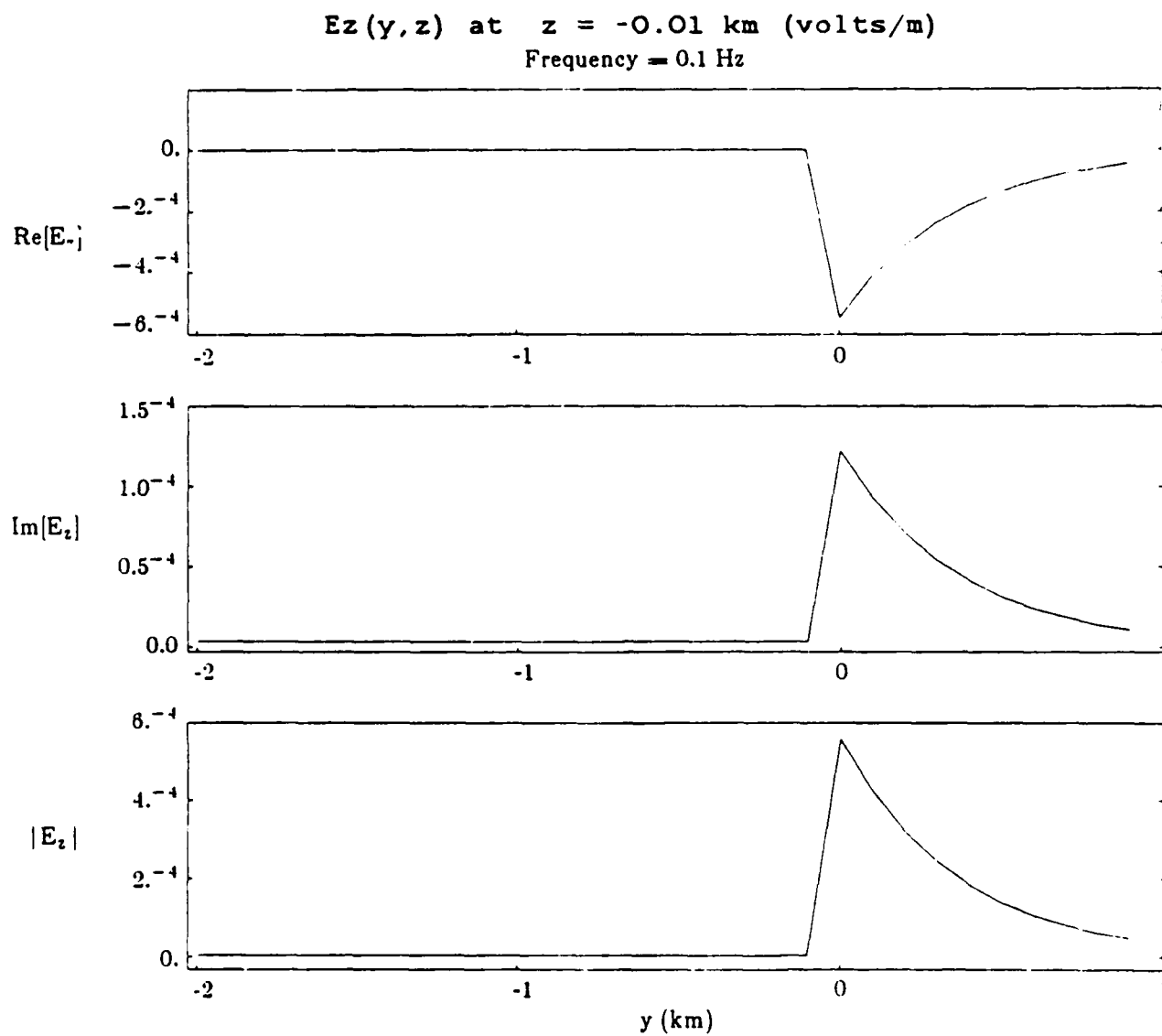


Fig. 6.13c. The electric field  $E_z$  from the semi-analytic solution at  $z = -0.01$  km.



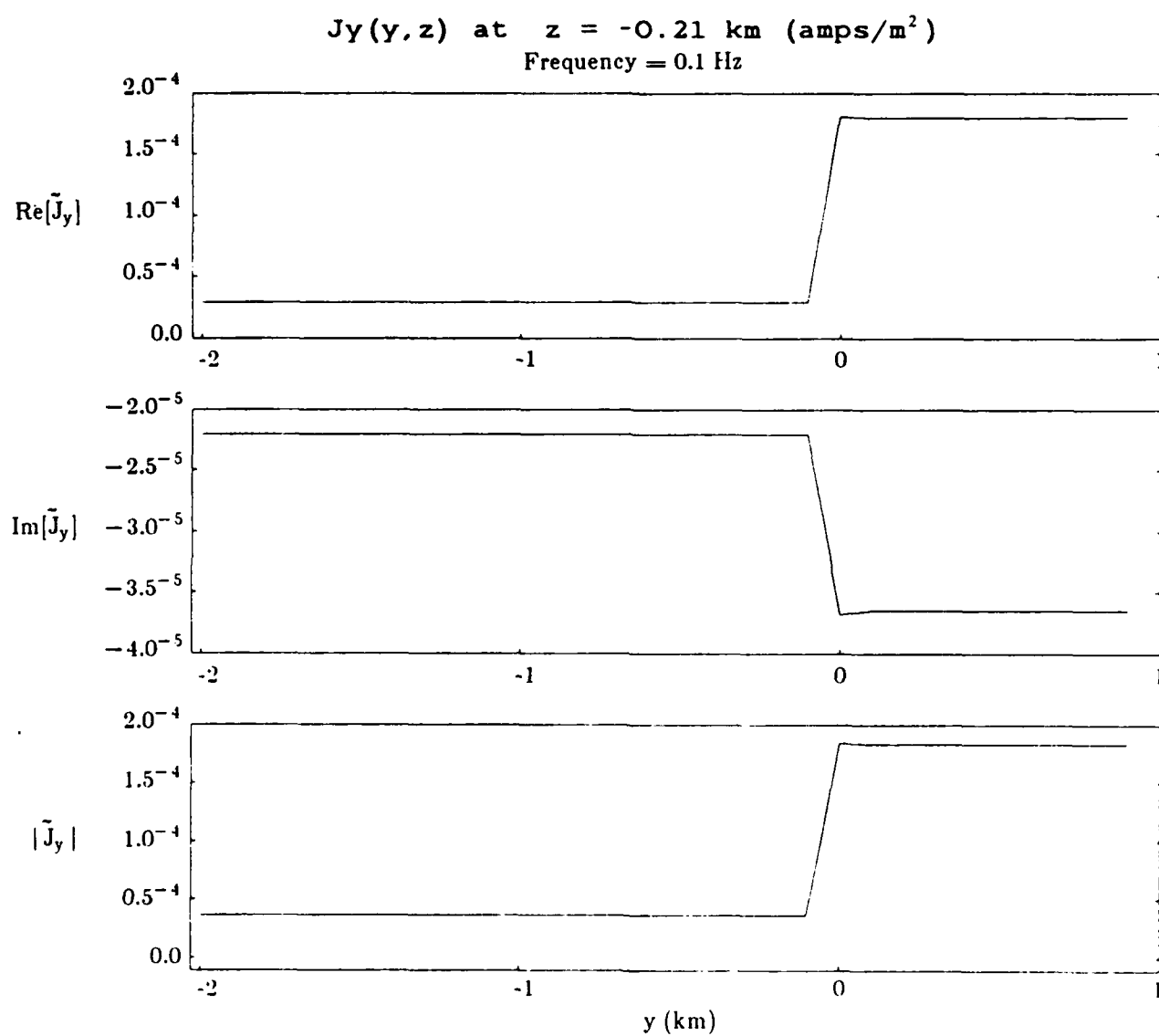


Fig. 6.14a. The total current  $\tilde{J}_y$  from the semi-analytic solution at  $z = -0.21$  km.

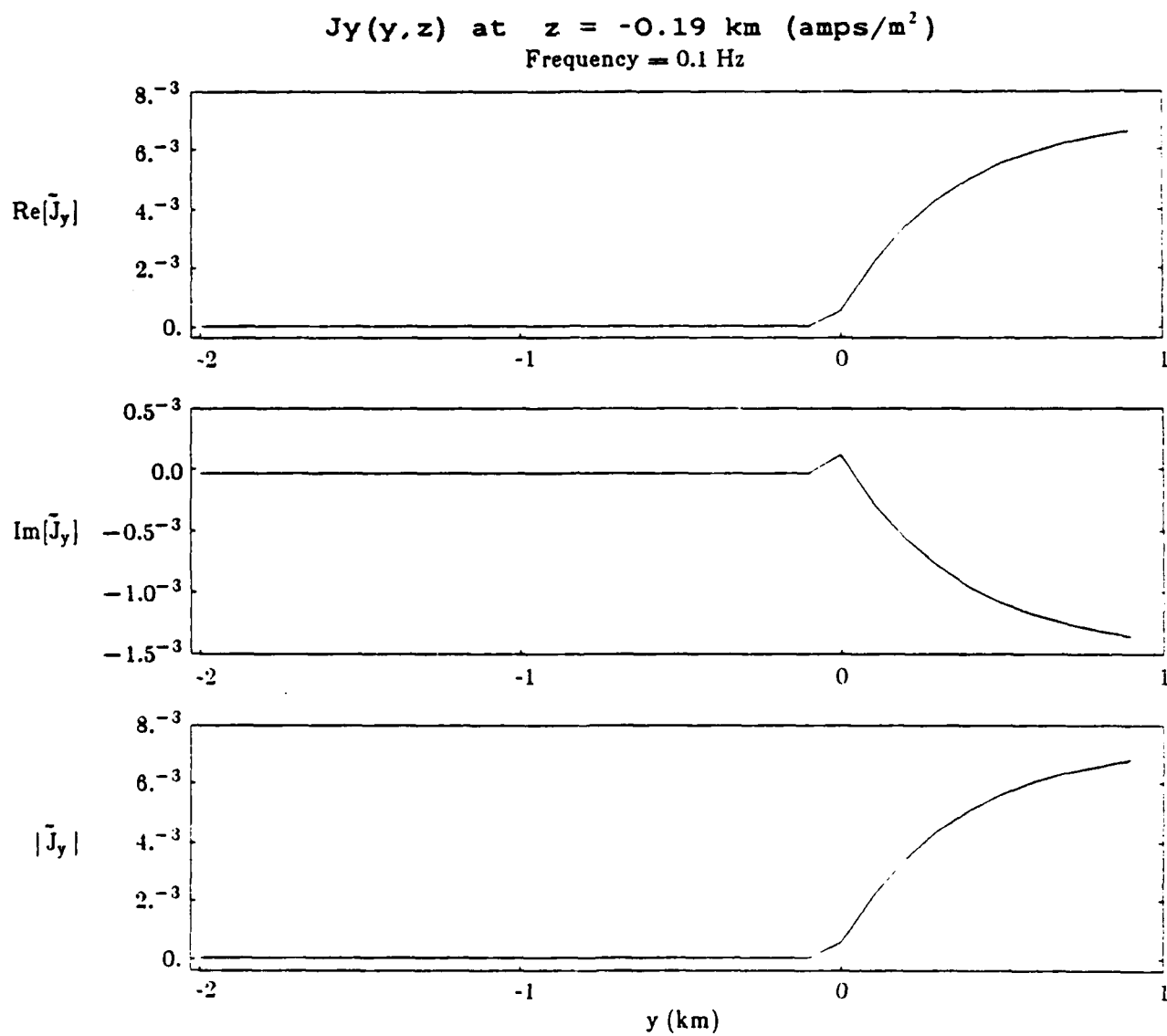


Fig. 6.14b. The total current  $\tilde{J}_y$  from the semi-analytic solution at  $z = -0.19$  km.

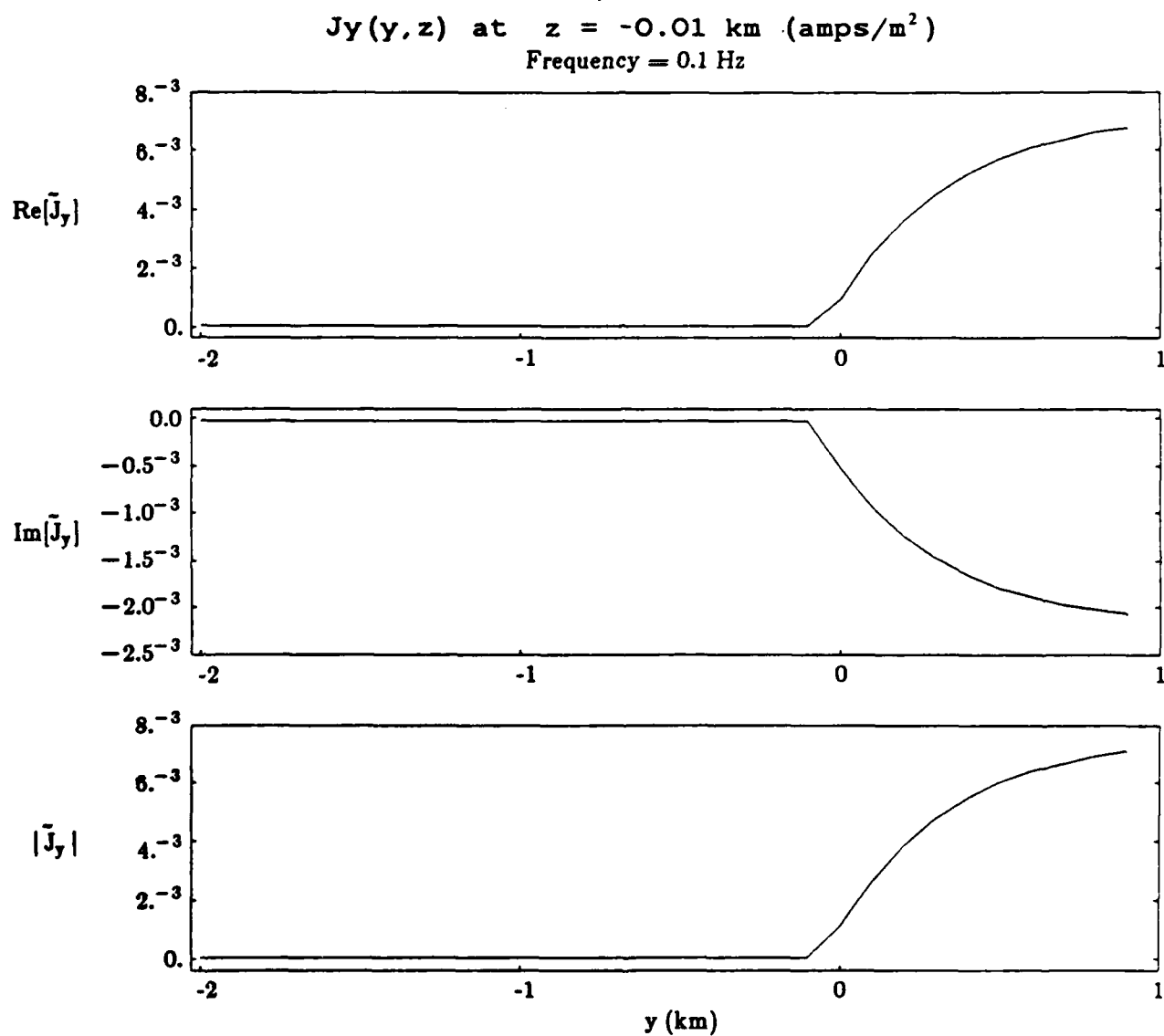


Fig. 6.14c. The total current  $\tilde{J}_y$  from the semi-analytic solution at  $z = -0.01$  km.

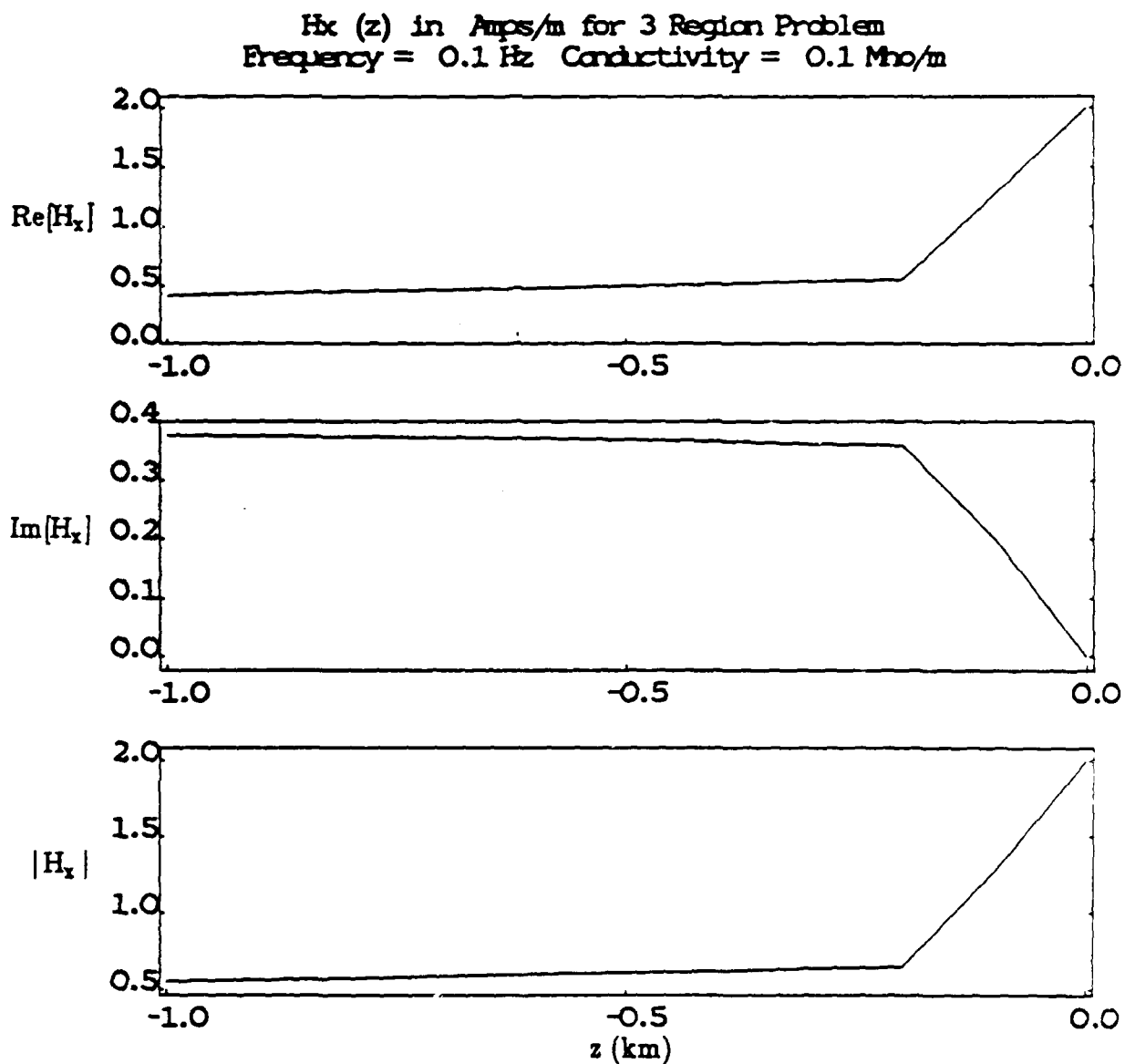


Fig. 8.15a.  $H_x$  for the air/ocean/barrier layered geometry; ocean depth = 0.2 km. The dashed (solid) line is the finite element code (exact) result. The frequency is 0.1 Hz and  $\sigma_{\text{barrier}} = 0.1$  mho/m.

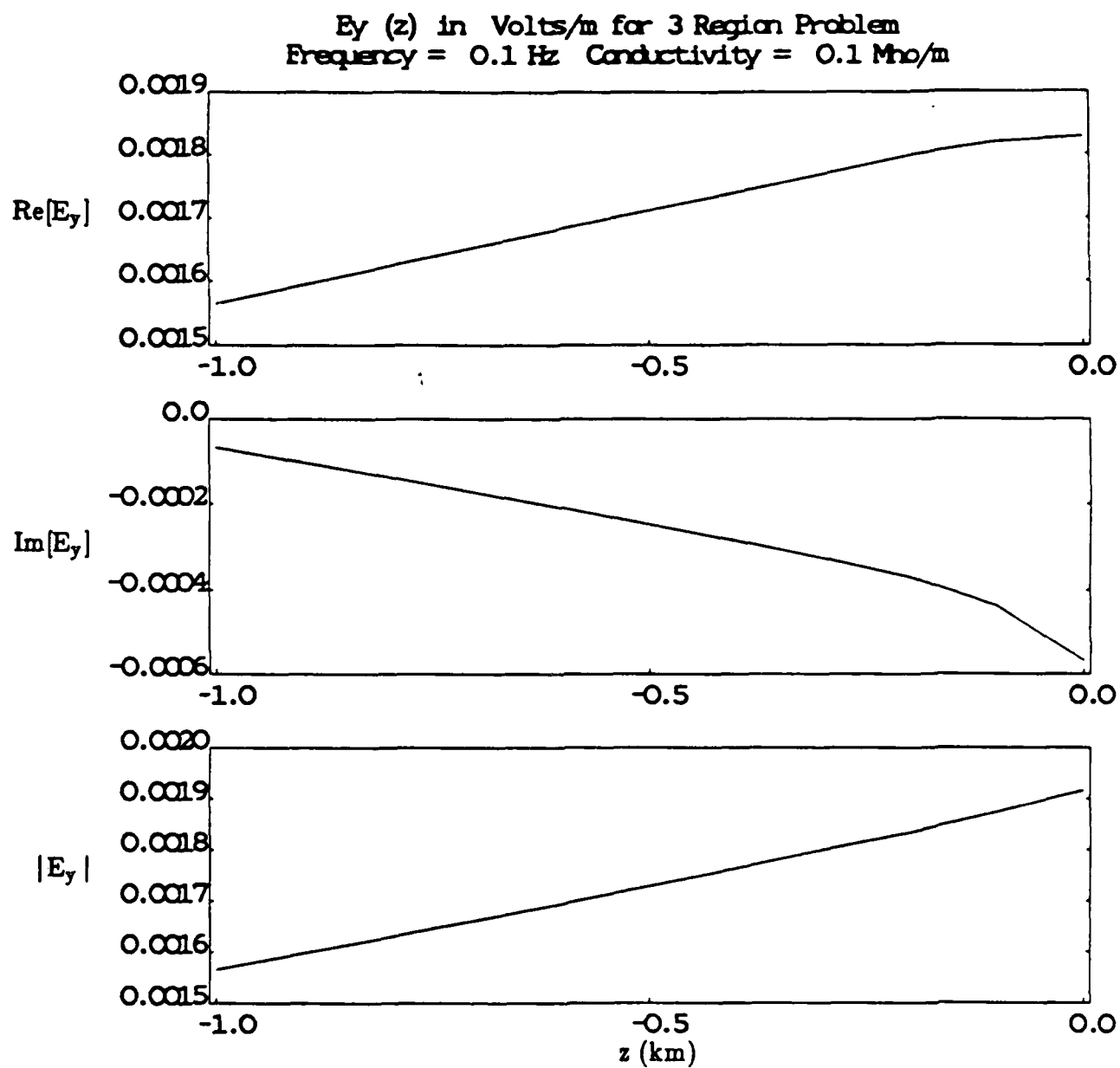


Fig. 6.15b.  $E_y$  for the air/ocean/barrier layered geometry; ocean depth = 0.2 km. The dashed (solid) line is the finite element code (exact) result.

Effective Resistivity Using Finite Element  
Solution With Different Barrier Conductivities  
For Only The Long Cable Segment

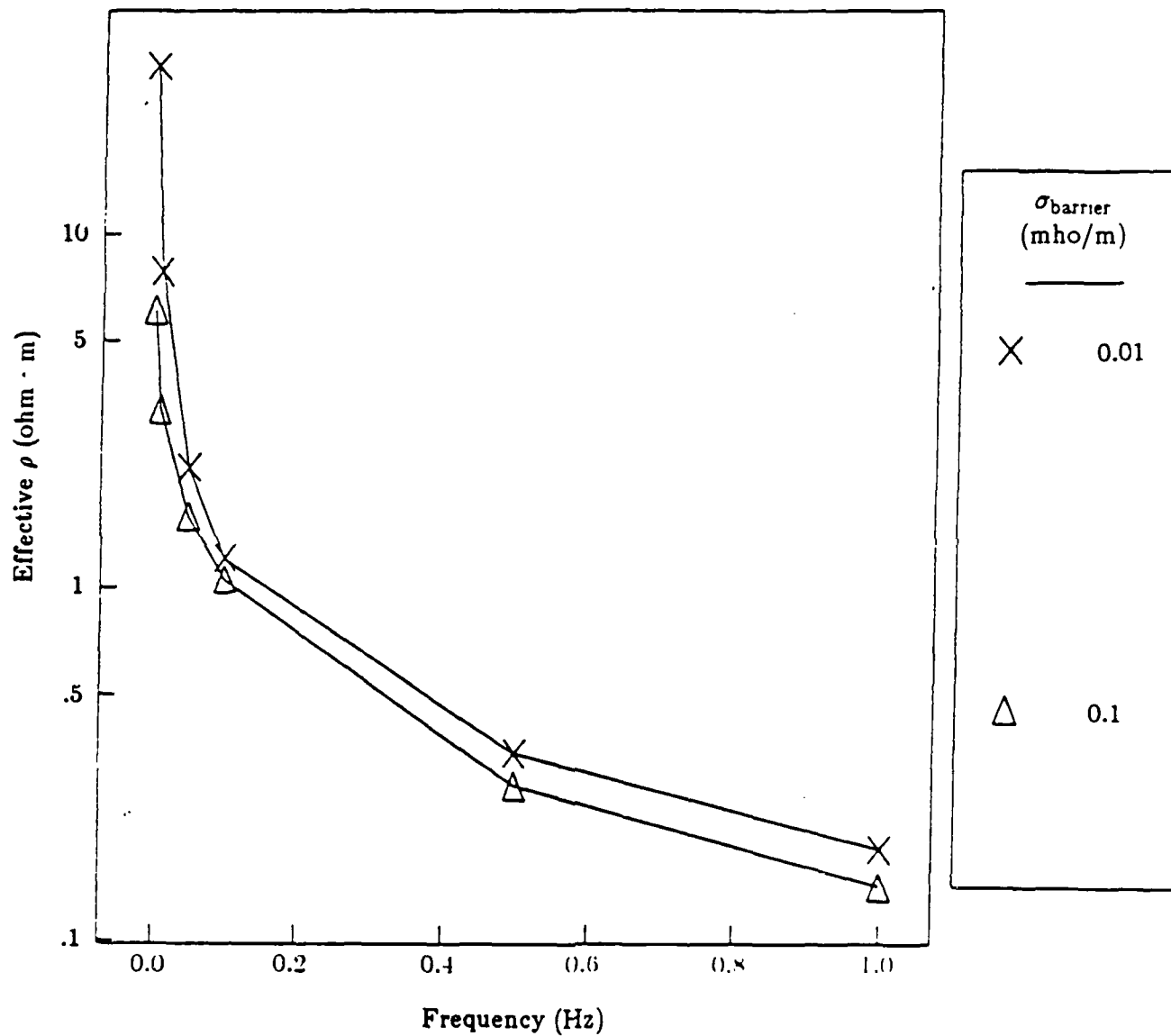


Fig. 6.16. The effective resistivity from the finite element code as a function of frequency out to 1 Hz for two barrier conductivities ( $\sigma_{\text{barrier}} = 0.1, 0.01$  mho/m).

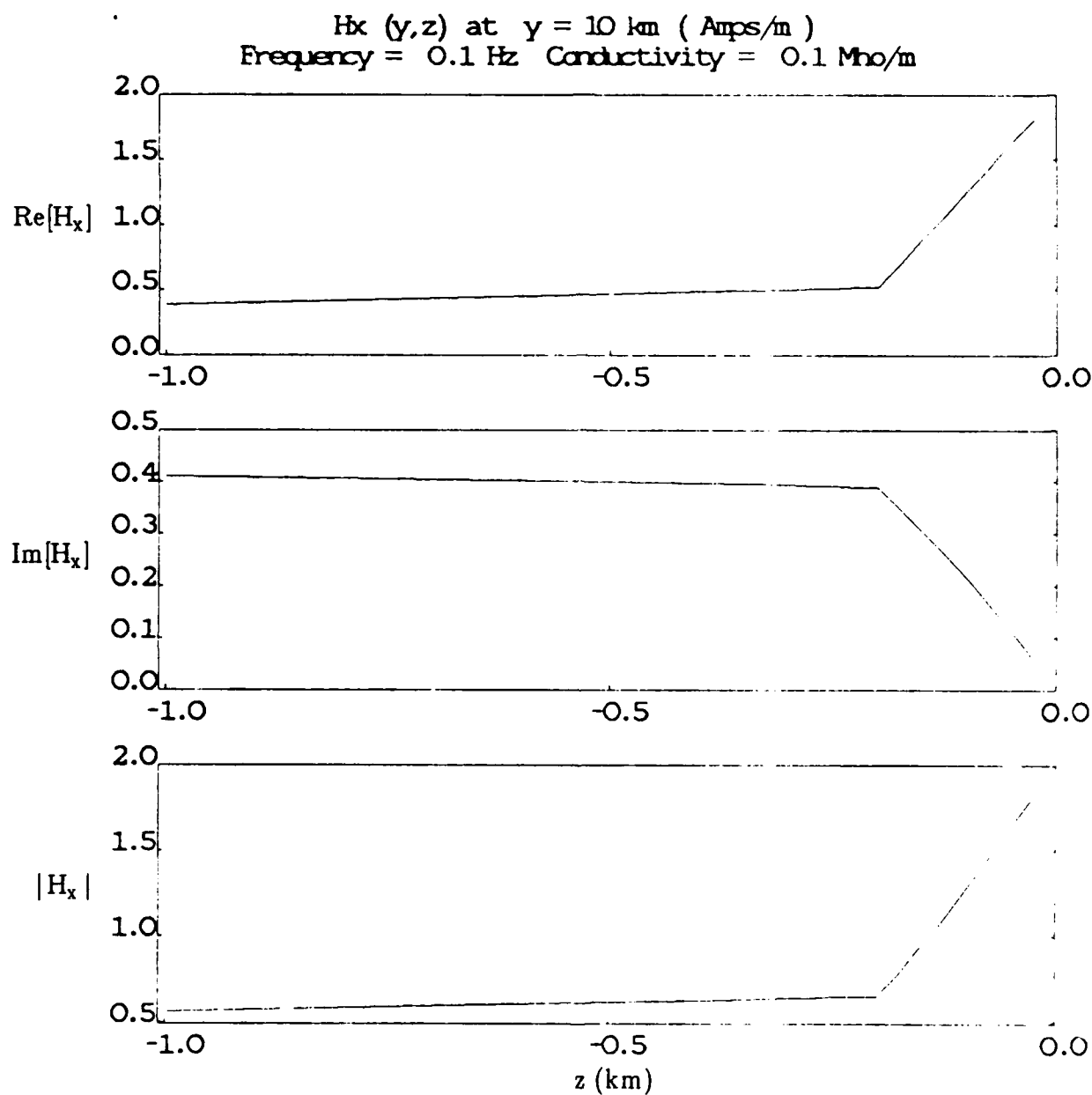


Fig. 6.17a. The magnetic field  $H_x$  solution from the finite element code at  $y = 10$  km. [Figs. 6.17- 6.22 all have  $\sigma = 0.1$  mho/m for the barrier conductivity and are evaluated at a frequency of 0.1 Hz. The continuity conditions are that  $H_x$ ,  $E_y$ , and  $\tilde{J}_z$  are supposed to be continuous across horizontal boundaries, while  $H_x$ ,  $J_y$ , and  $E_z$  are supposed to be continuous across vertical boundaries.]

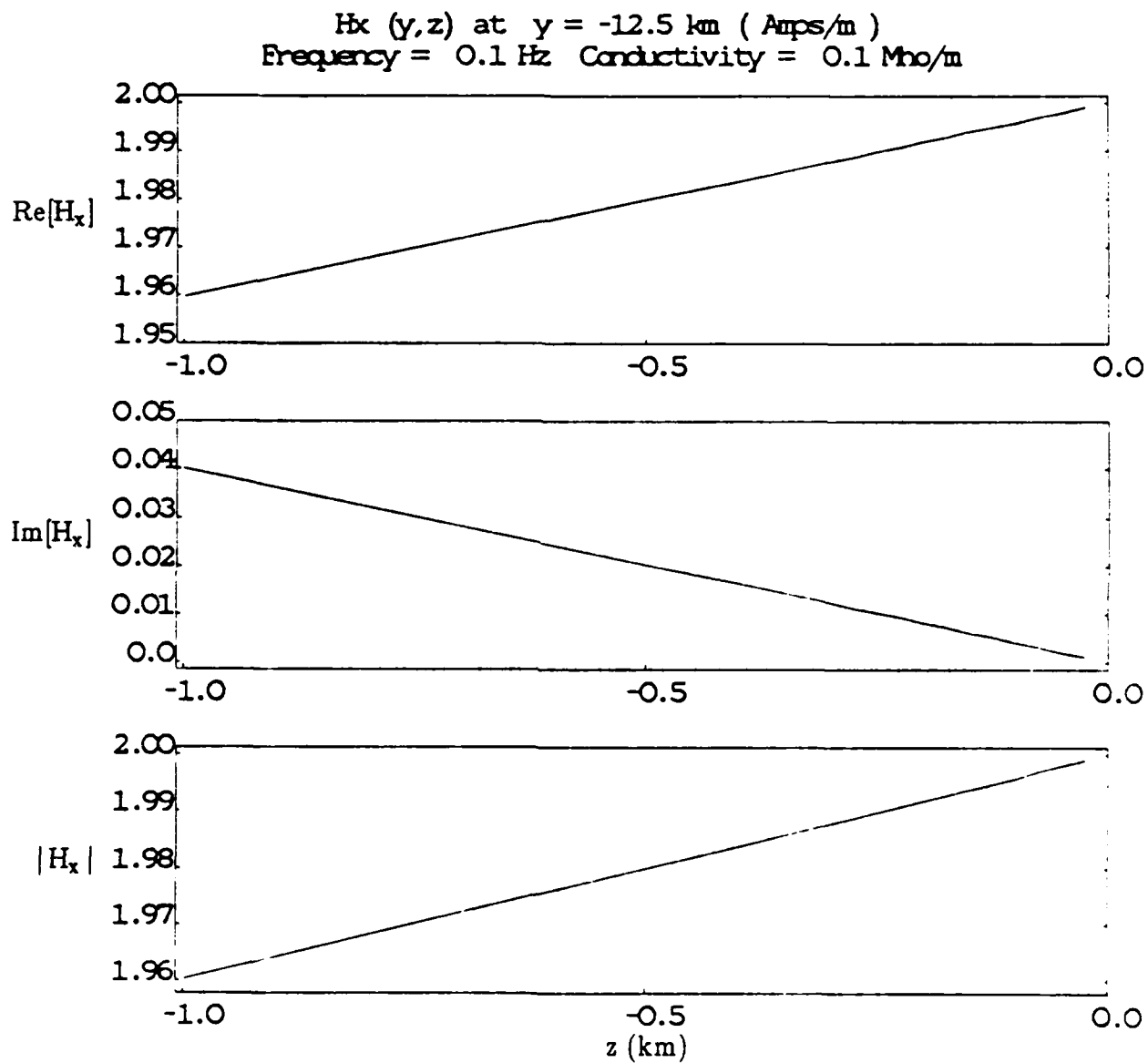


Fig. 6.17b. The magnetic field  $H_x$  from the finite element code at  $y = -12.5$  km.



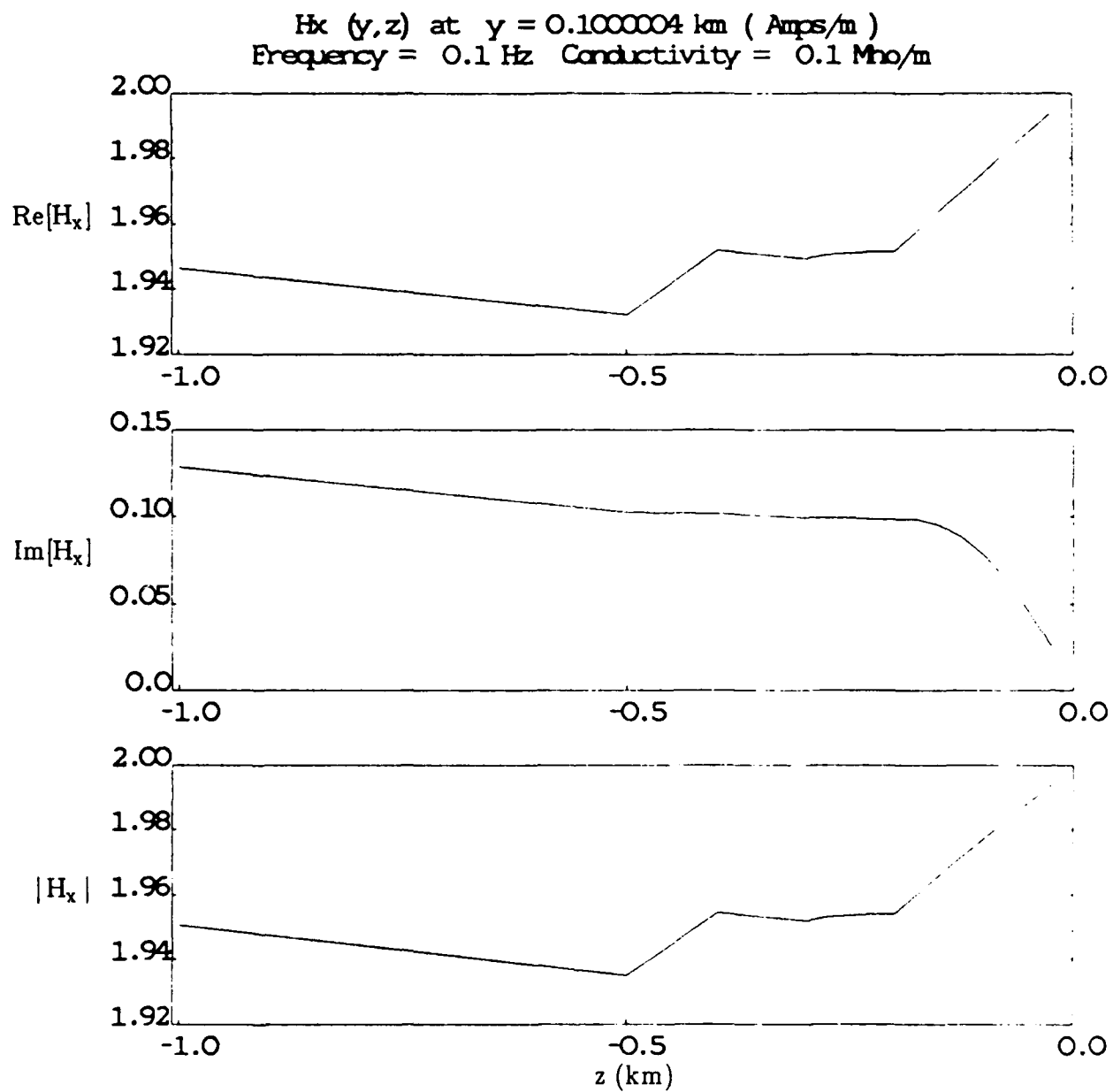


Fig. 6.17c. The magnetic field  $H_x$  from the finite element code at  $y = 0.1$  km.

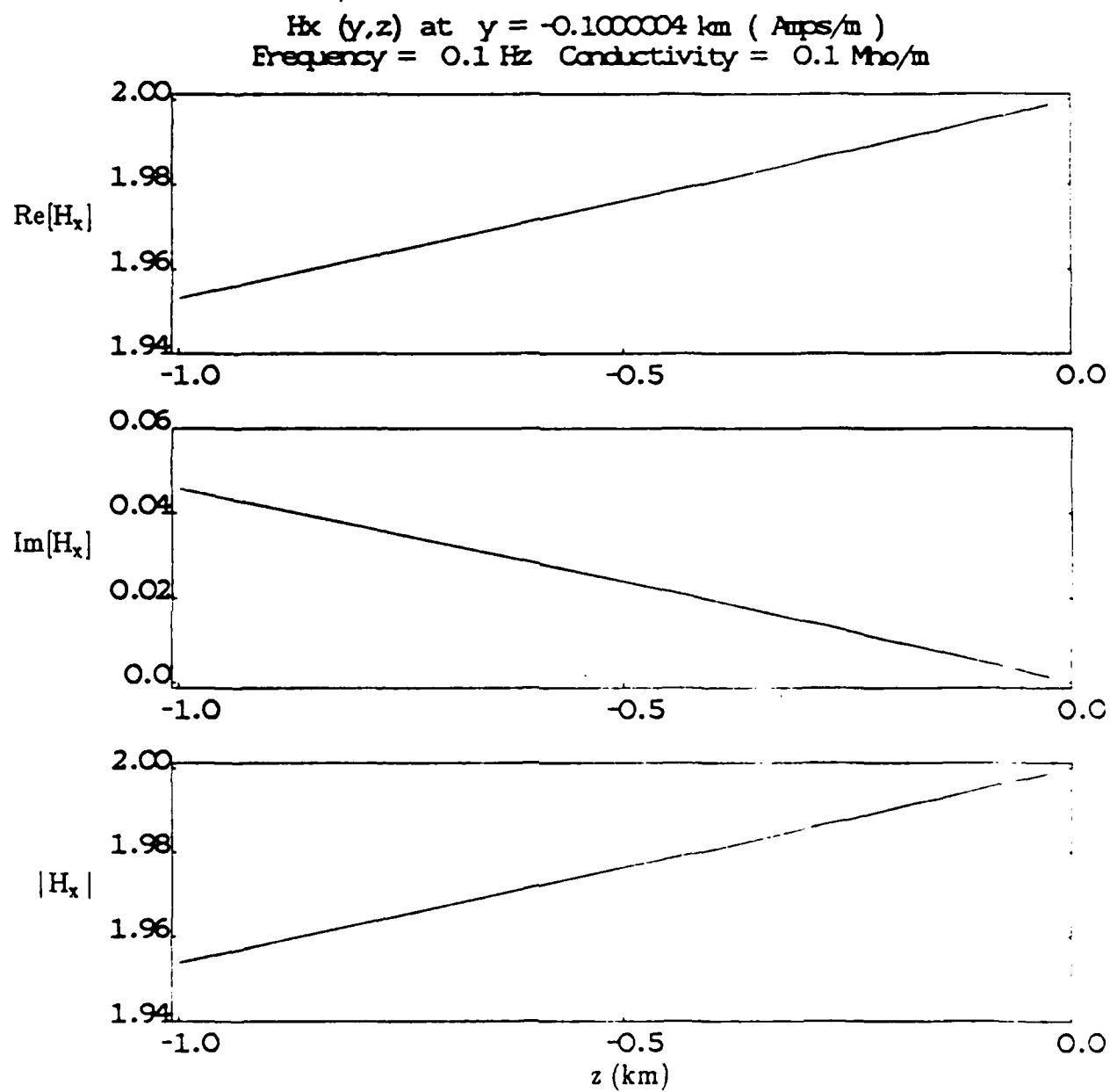


Fig. 6.17d. The magnetic field  $H_x$  from the finite element code at  $y = -0.1$  km.

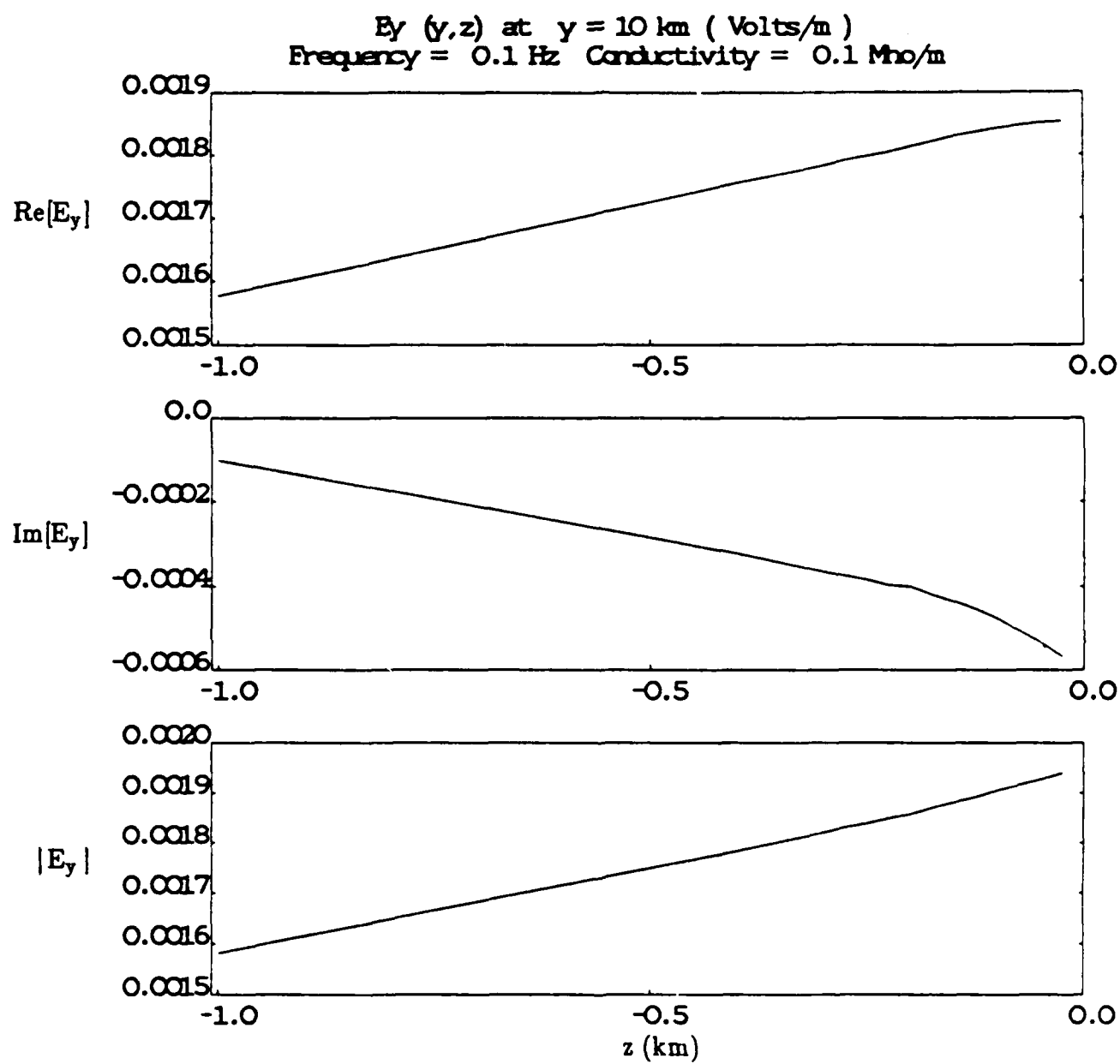


Fig. 6.18a. The electric field  $E_y$  from the finite element code at  $y = 10$  km.

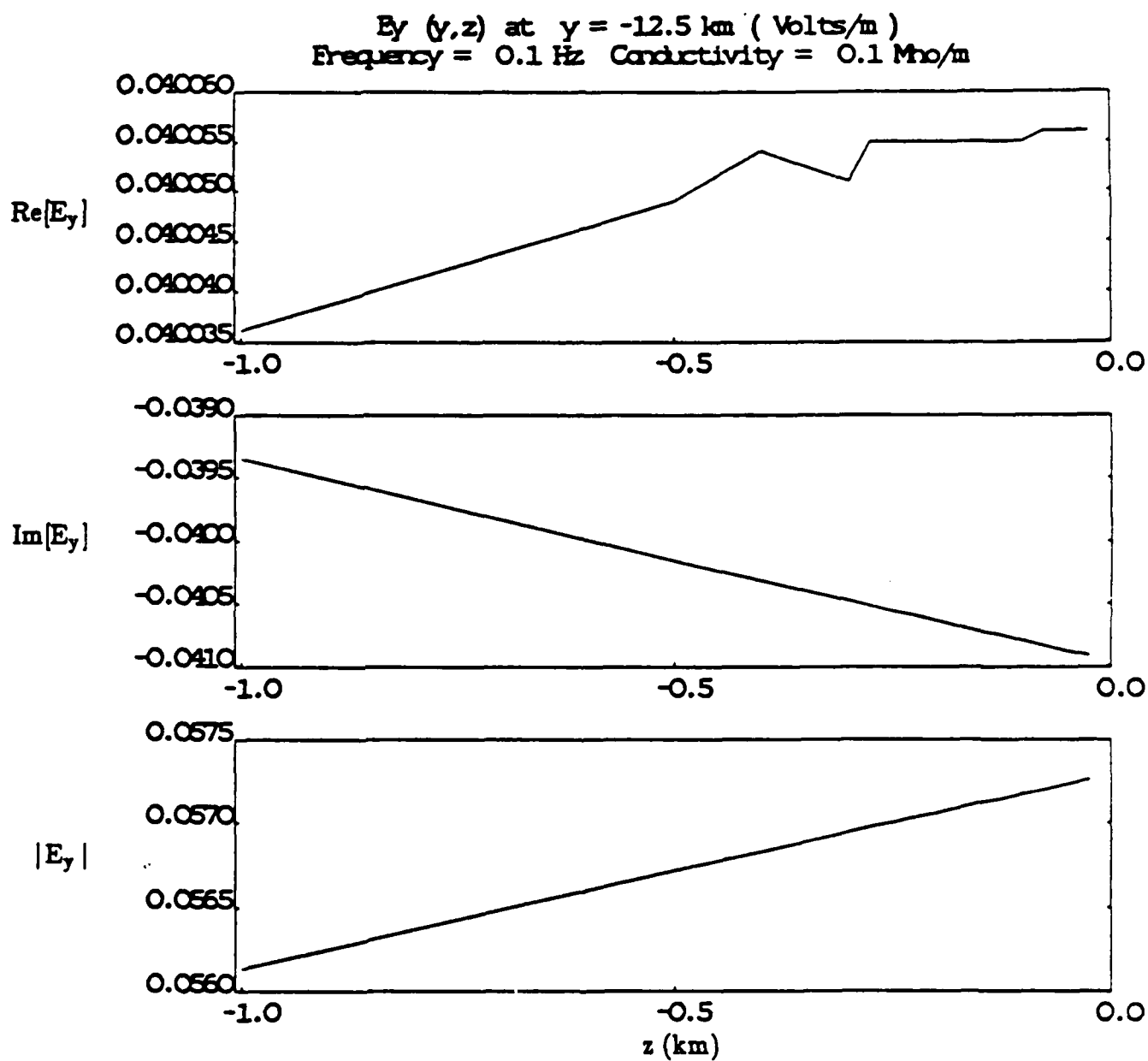


Fig. 6.18b. The electric field  $E_y$  from the finite element code at  $y = -12.5$  km.

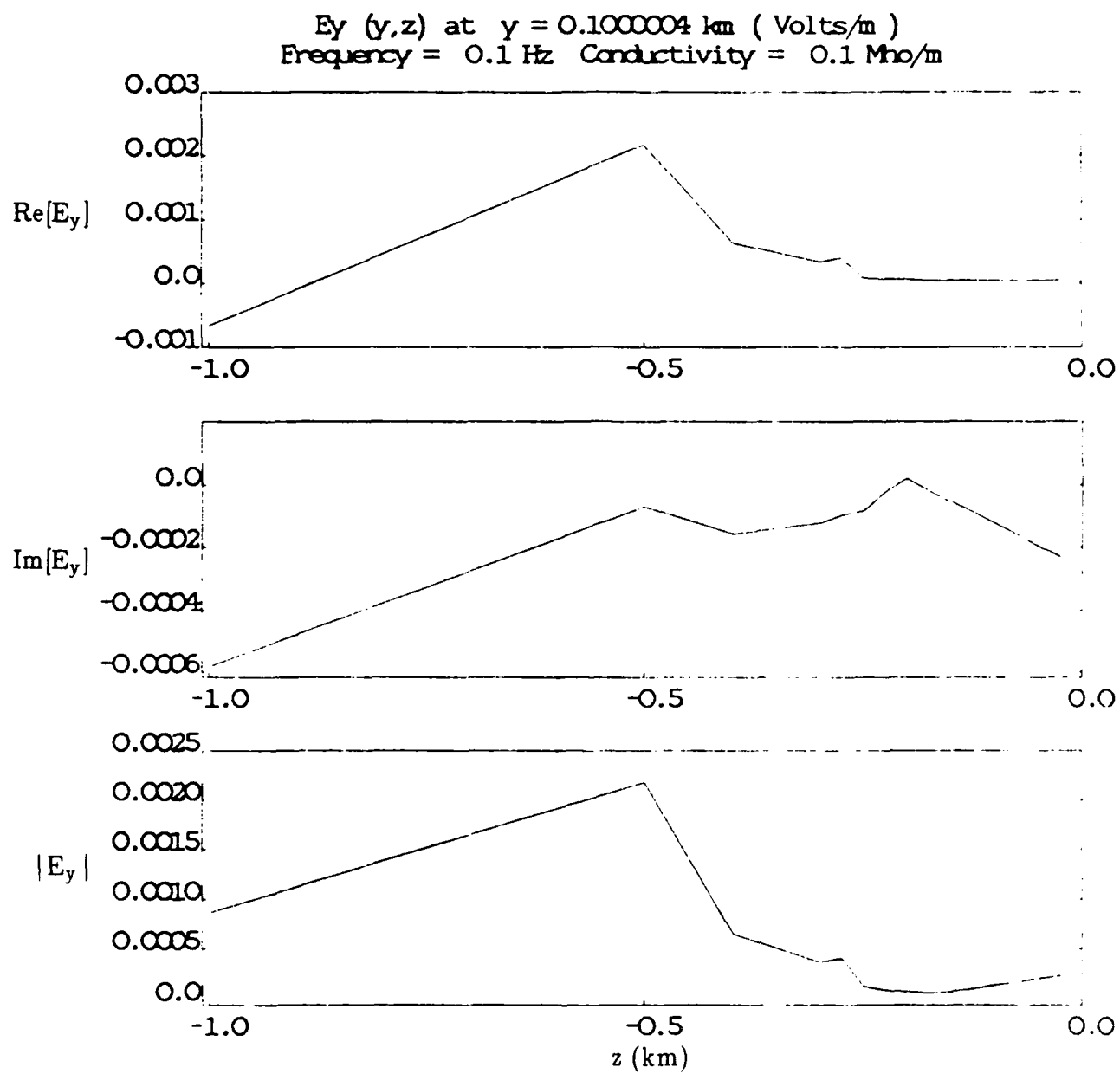


Fig. 6.18c: The electric field  $E_y$  from the finite element code at  $y = 0.1$  km.

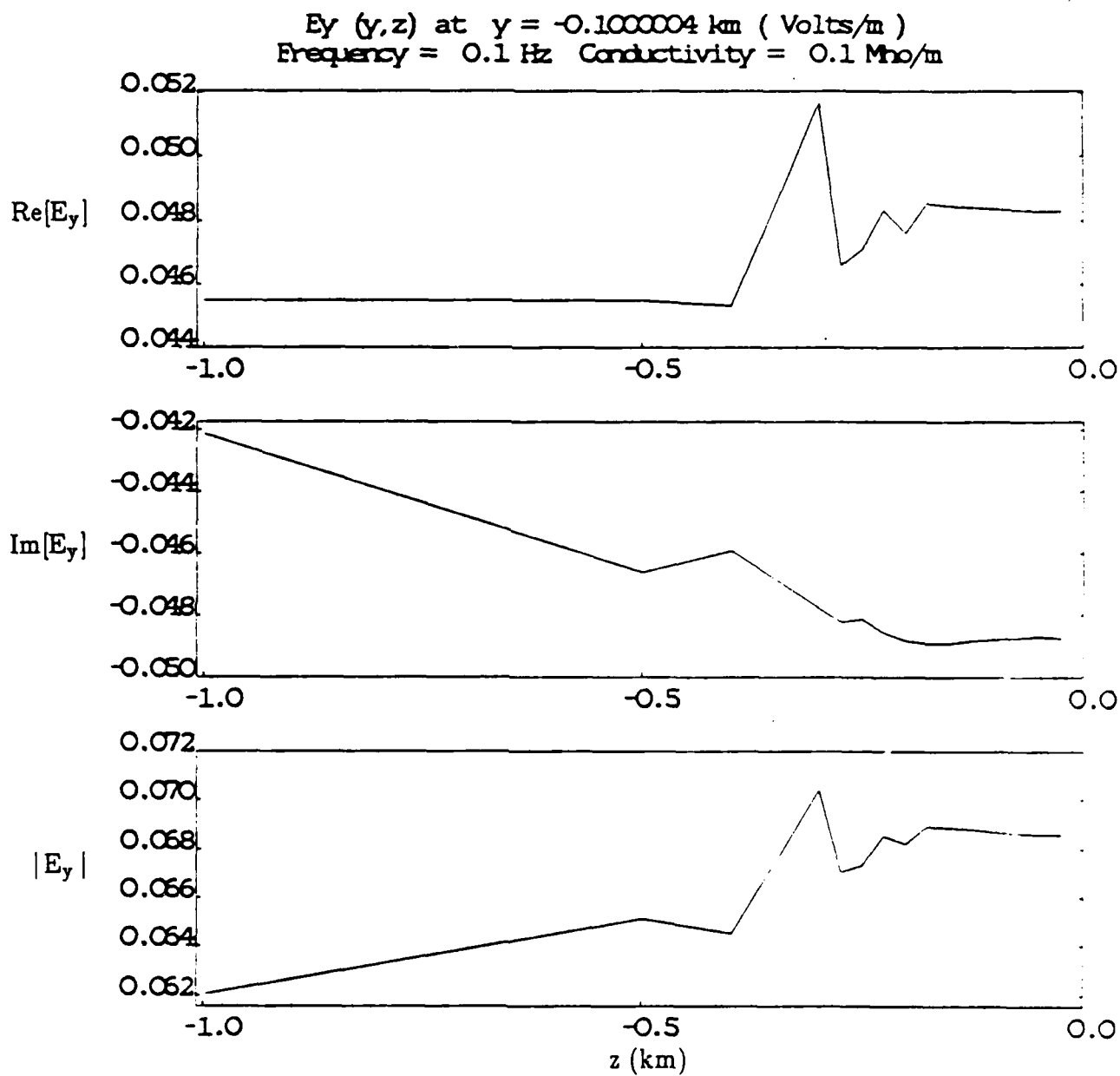


Fig. 6.18d. The electric field  $E_y$  from the finite element code at  $y = -0.1$  km.

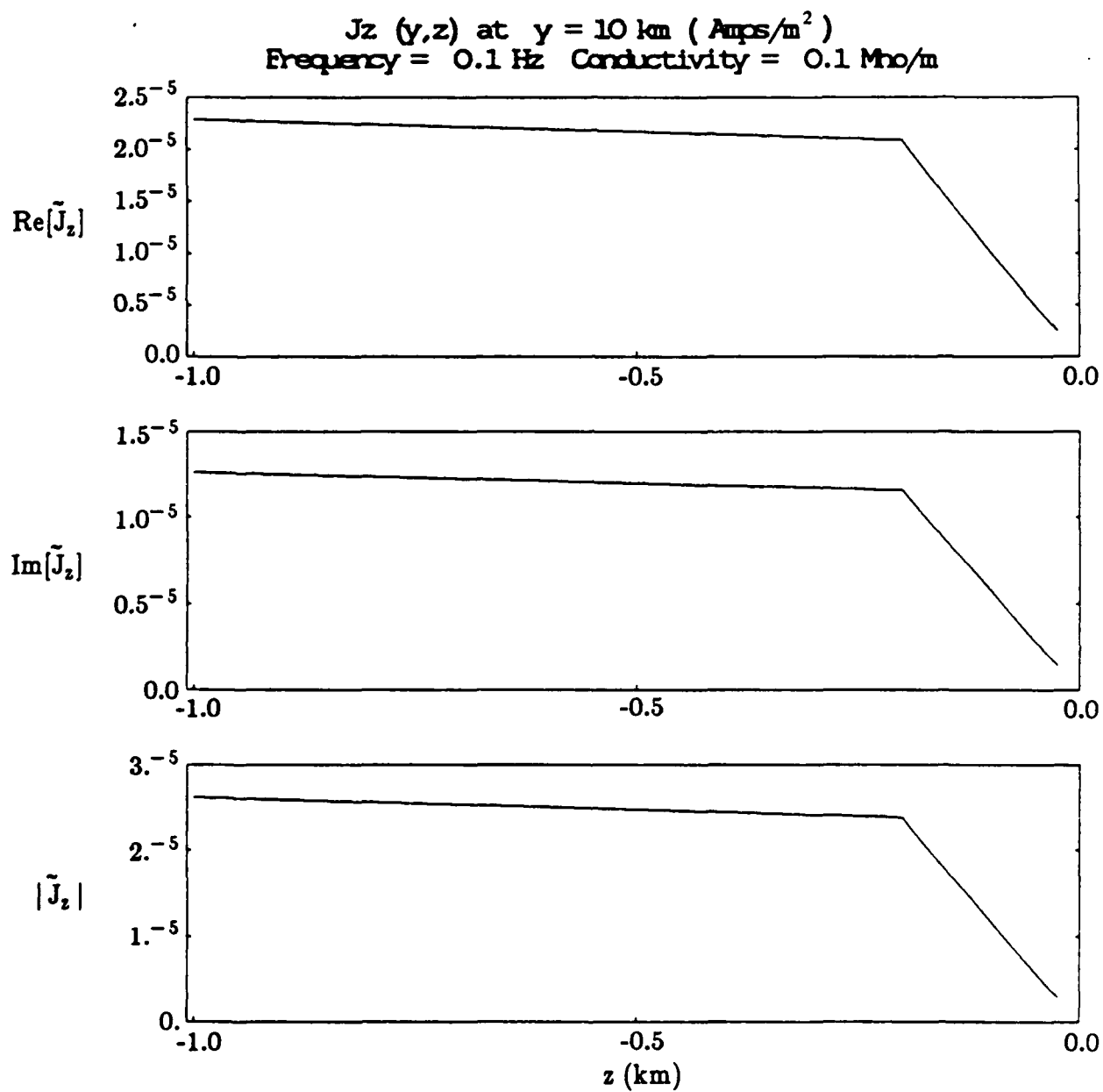


Fig. 6.19a. The total current  $\tilde{J}_z$  from the finite element code at  $y = 10 \text{ km}$ .

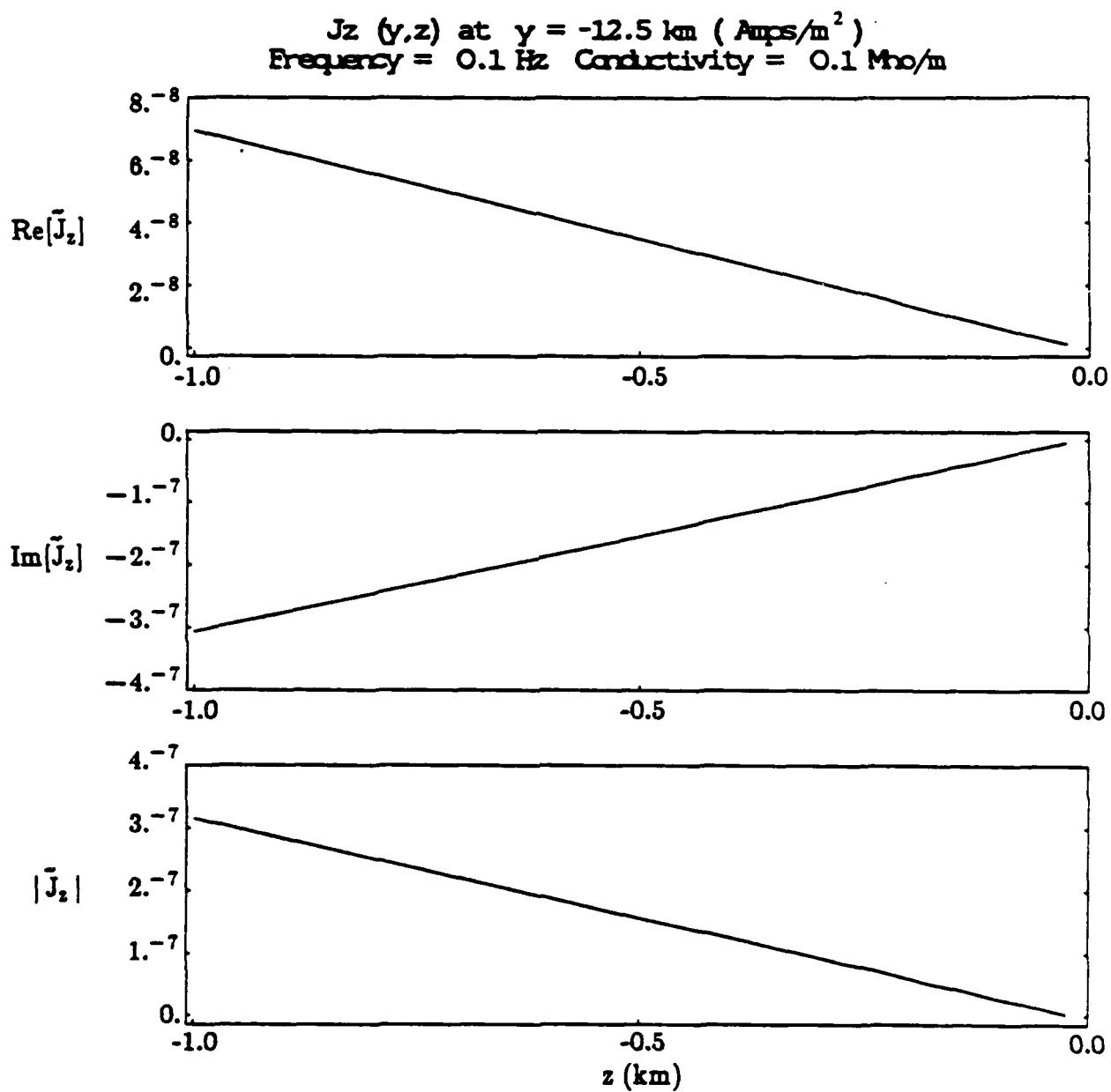


Fig. 6.19b. The total current  $\tilde{J}_z$  from the finite element code at  $y = -12.5 \text{ km}$ .



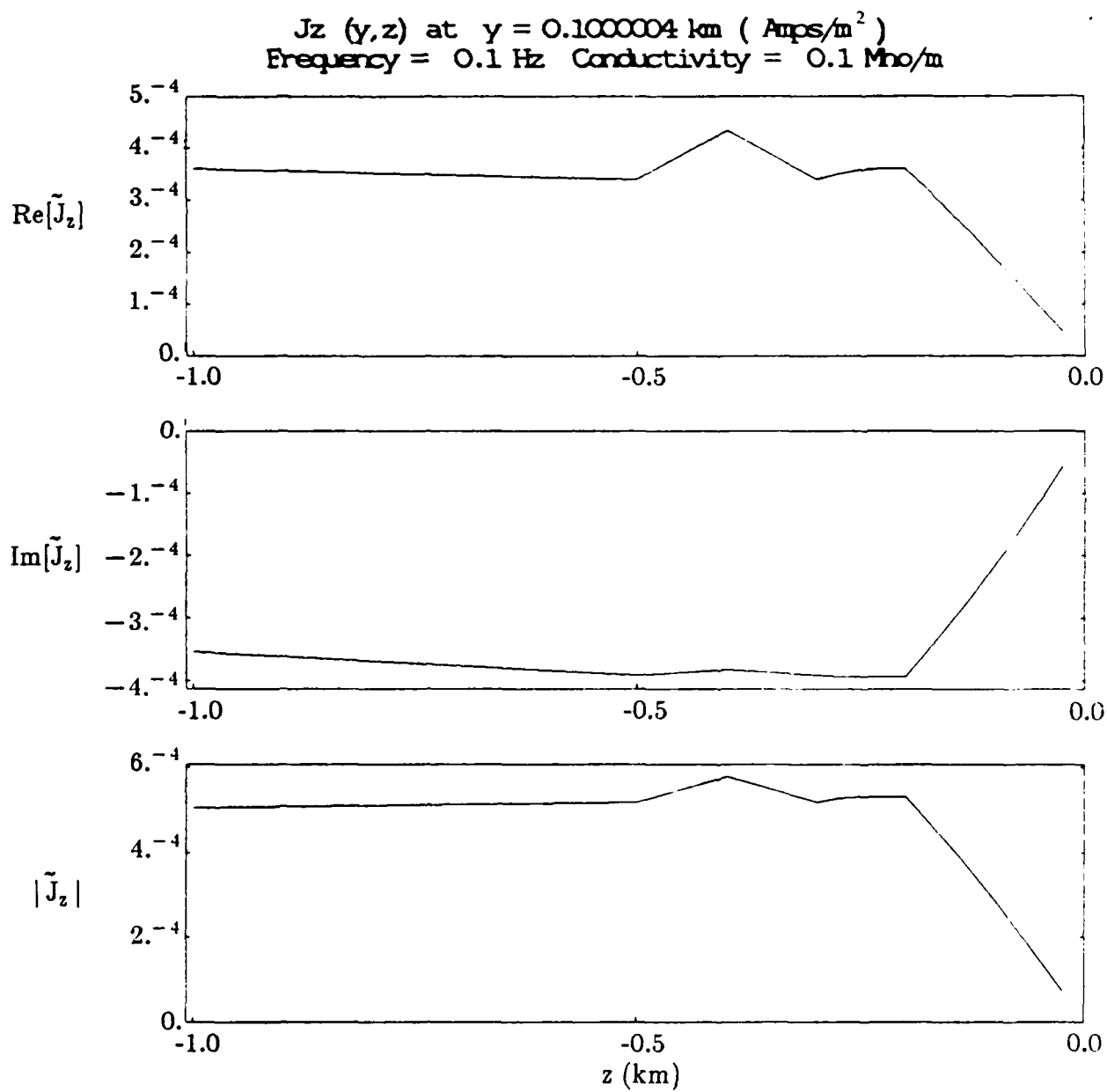


Fig. 6.19c. The total current  $\tilde{J}_z$  from the finite element code at  $y = 0.1$  km.

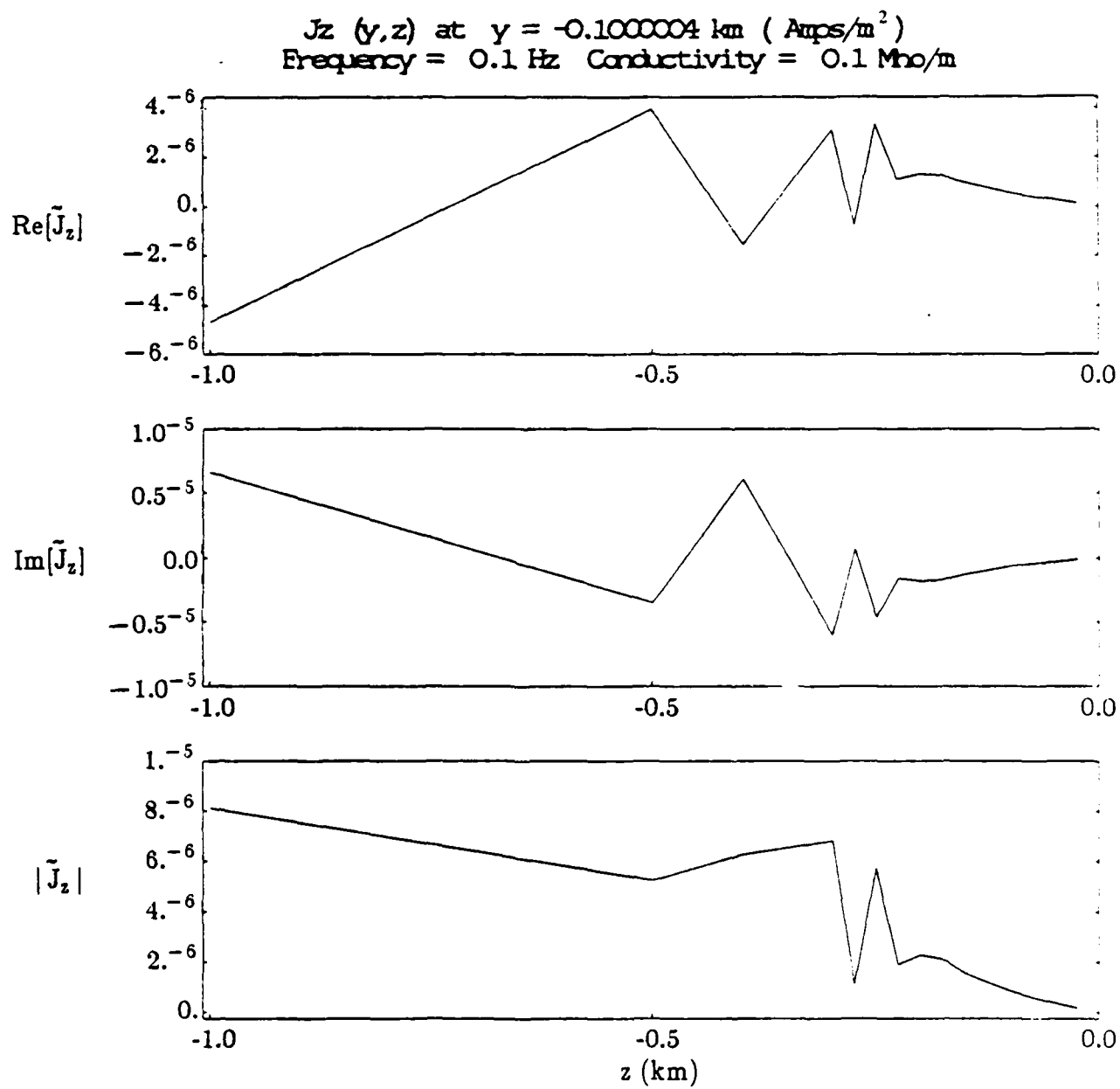


Fig. 8.19d. The total current  $J_z$  from the finite element code at  $y = -0.1$  km.

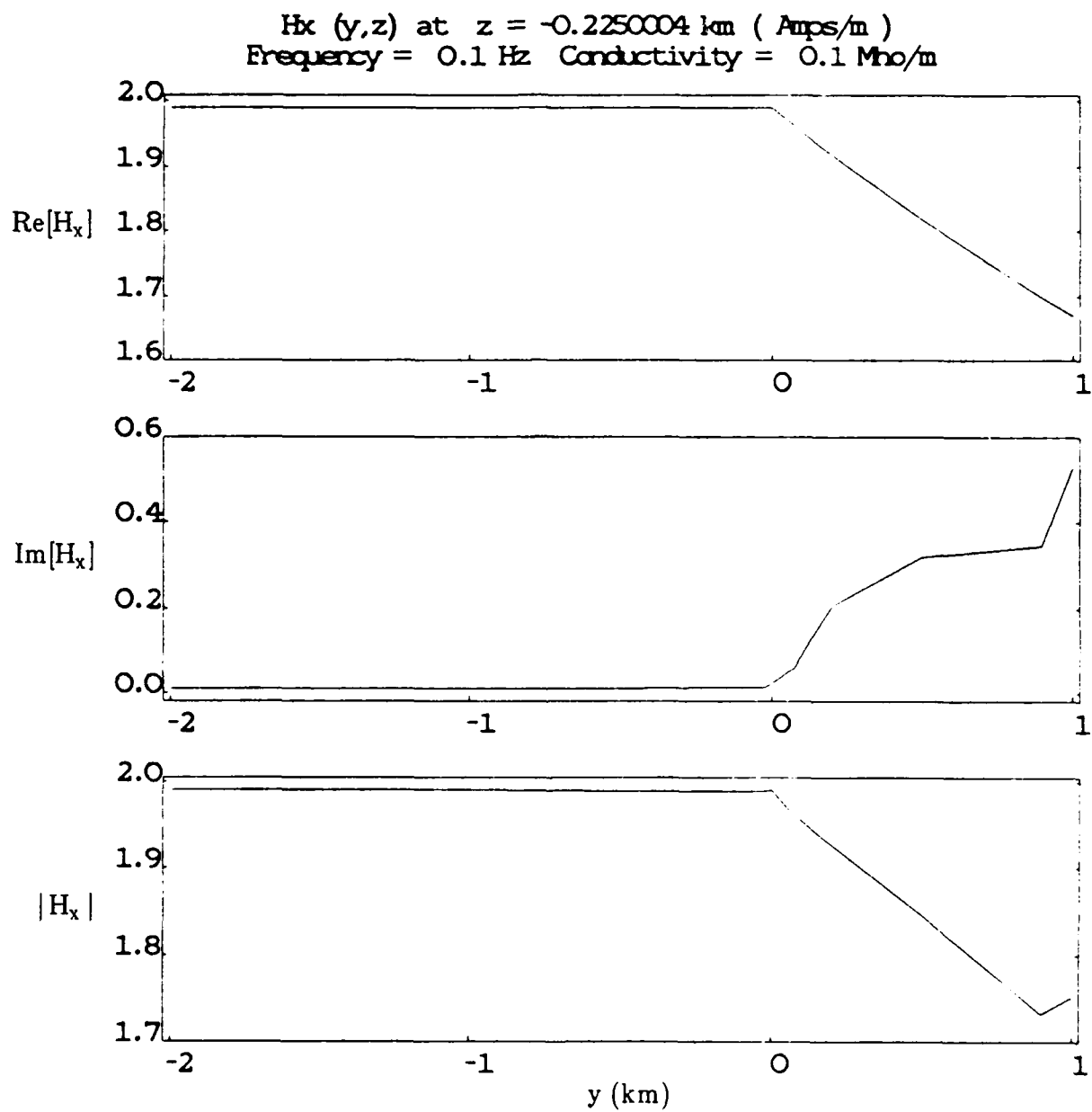


Fig. 6.20a. The magnetic field  $H_x$  from the finite element code at  $z = -0.225$  km.

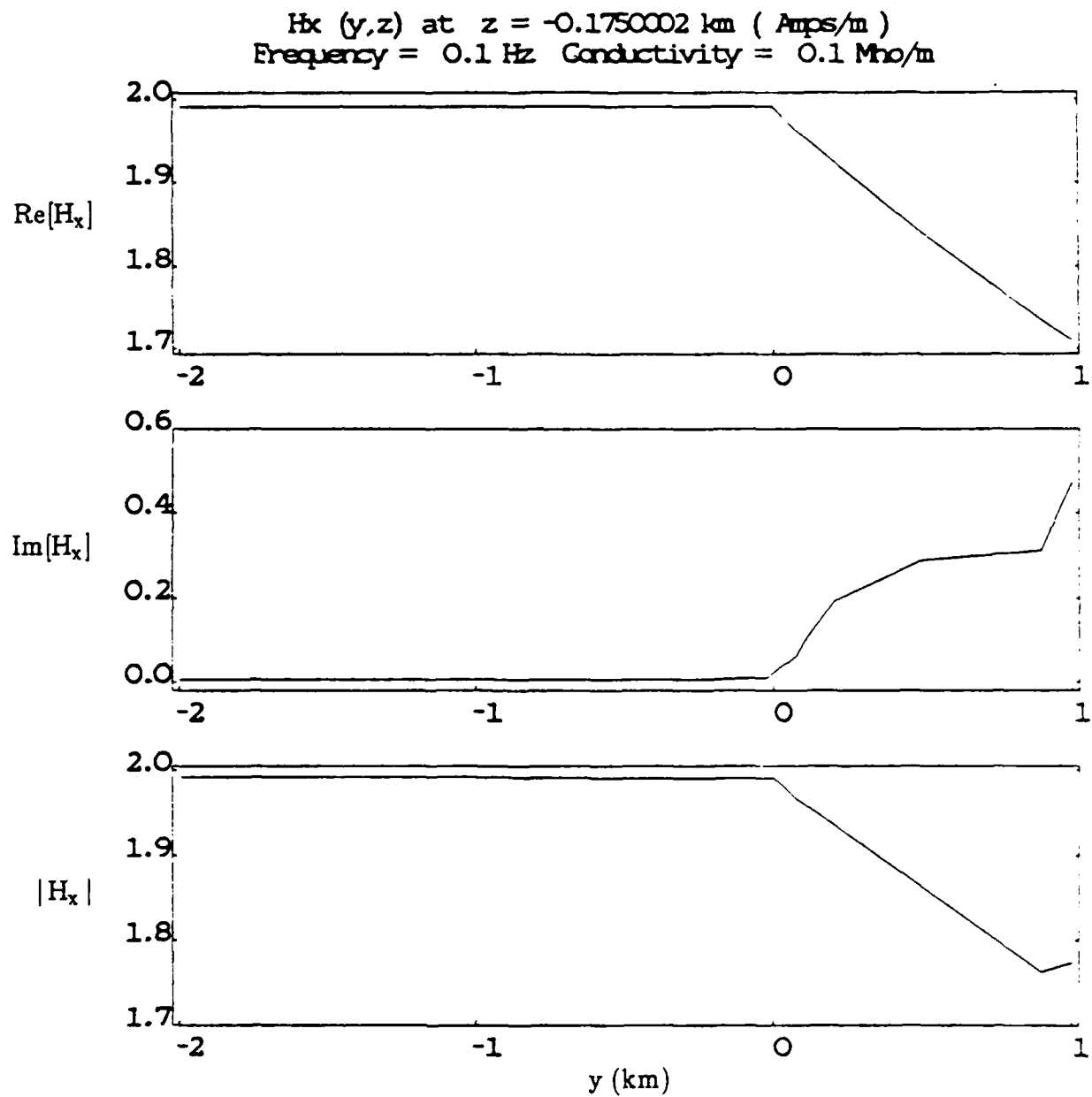


Fig. 6.20b. The magnetic field  $H_x$  from the finite element code at  $z = -0.175$  km.

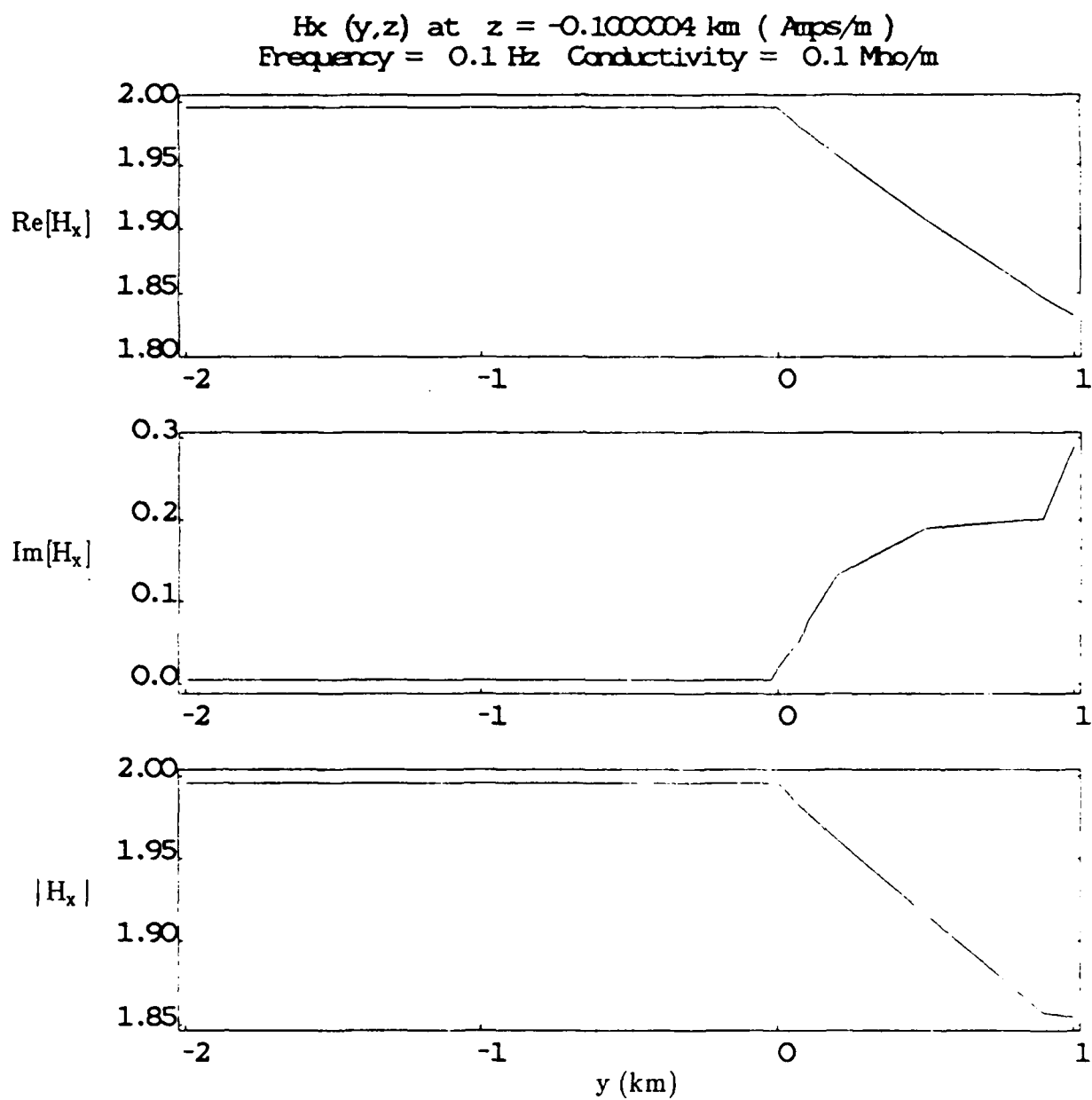


Fig. 6.20c. The magnetic field  $H_x$  from the finite element code at  $z = -0.1$  km.

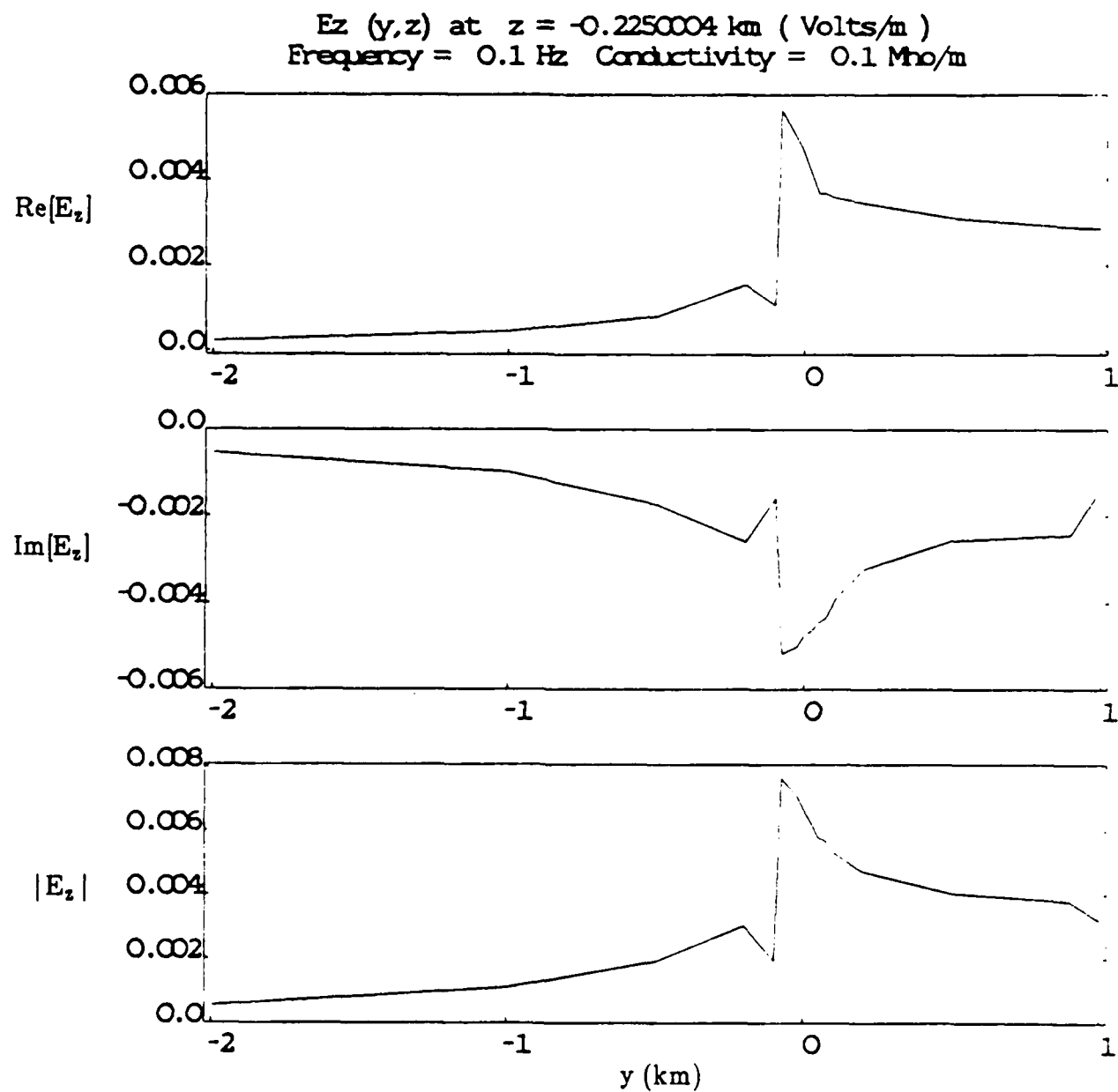


Fig. 8.21a. The electric field  $E_z$  from the finite element code at  $z = -0.225$  km.

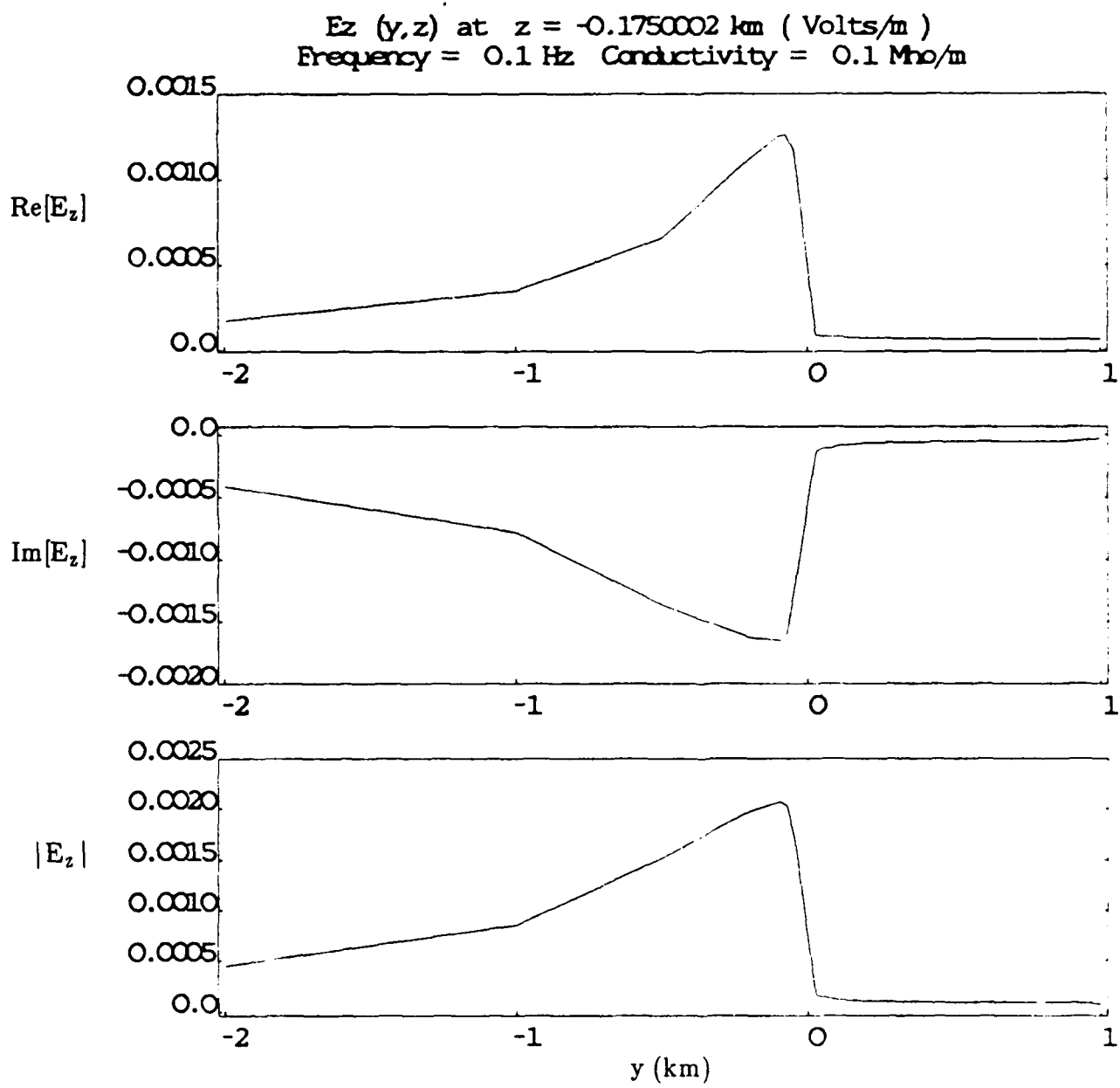


Fig. 6.21b. The electric field  $E_z$  from the finite element code at  $z = -0.175$  km.

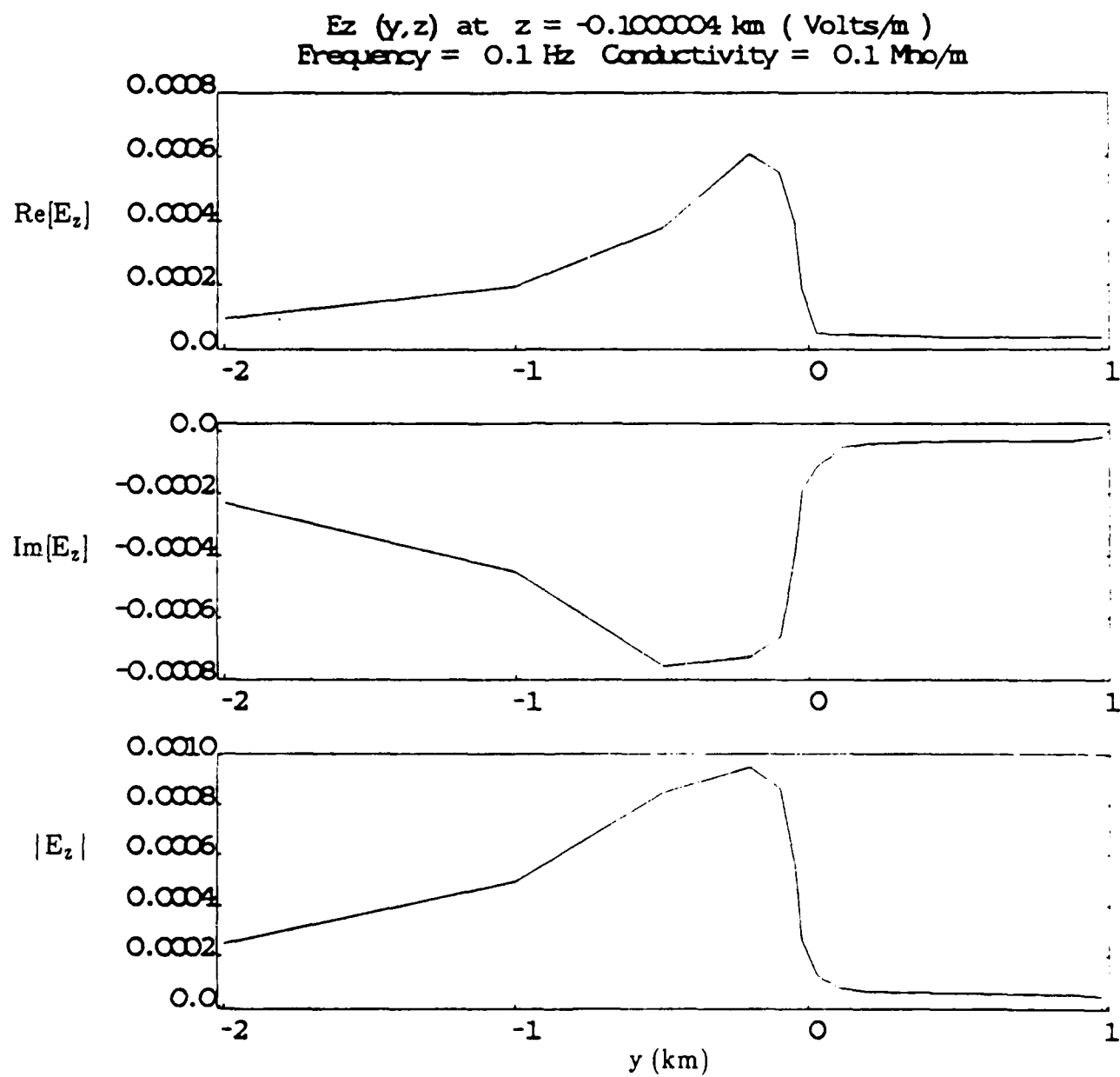


Fig. 6.21c. The electric field  $E_z$  from the finite element code at  $z = -0.1$  km.



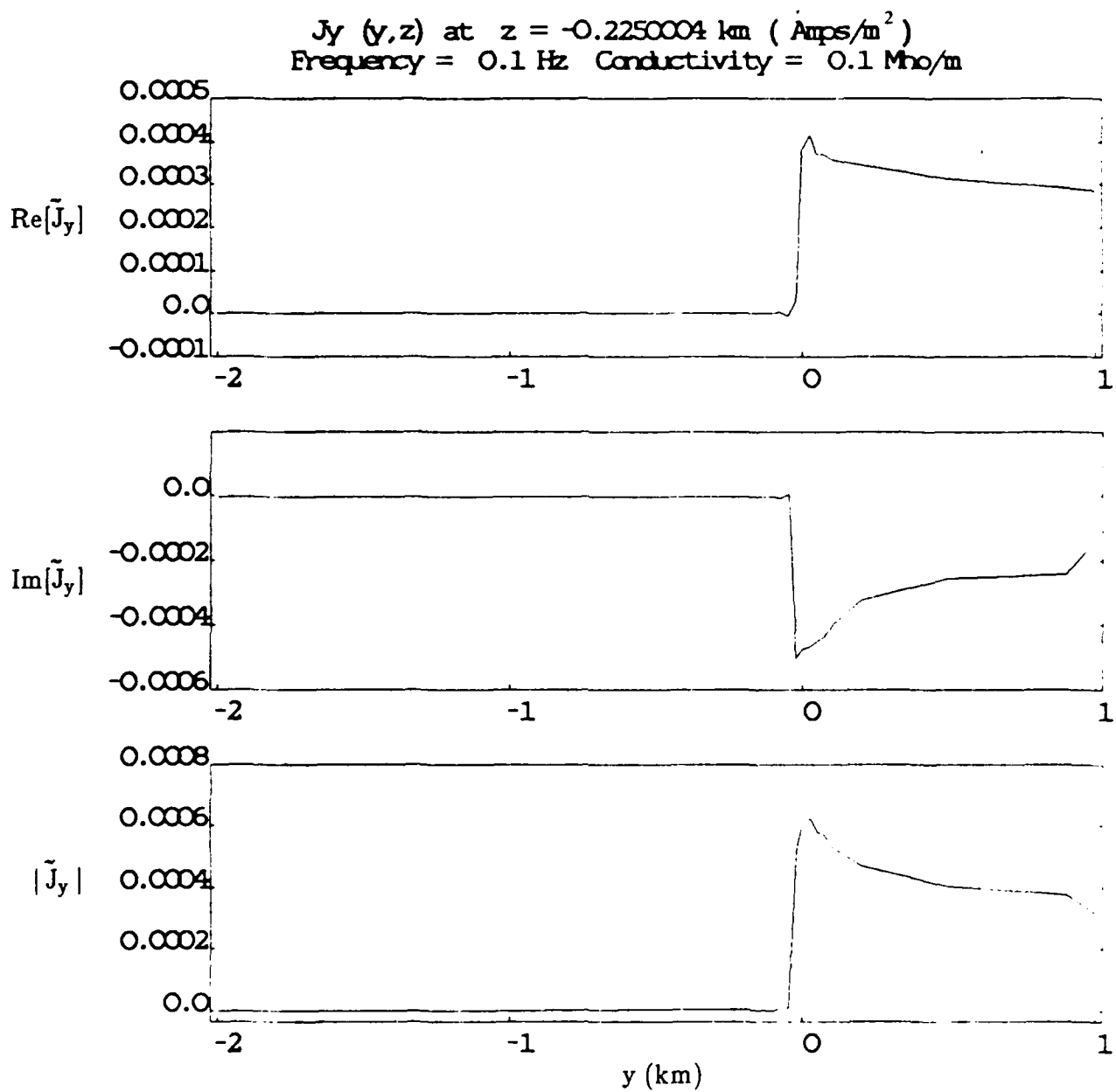


Fig. 6.22a. The total current  $\tilde{J}_y$  from the finite element code at  $z = -0.225 \text{ km}$ .

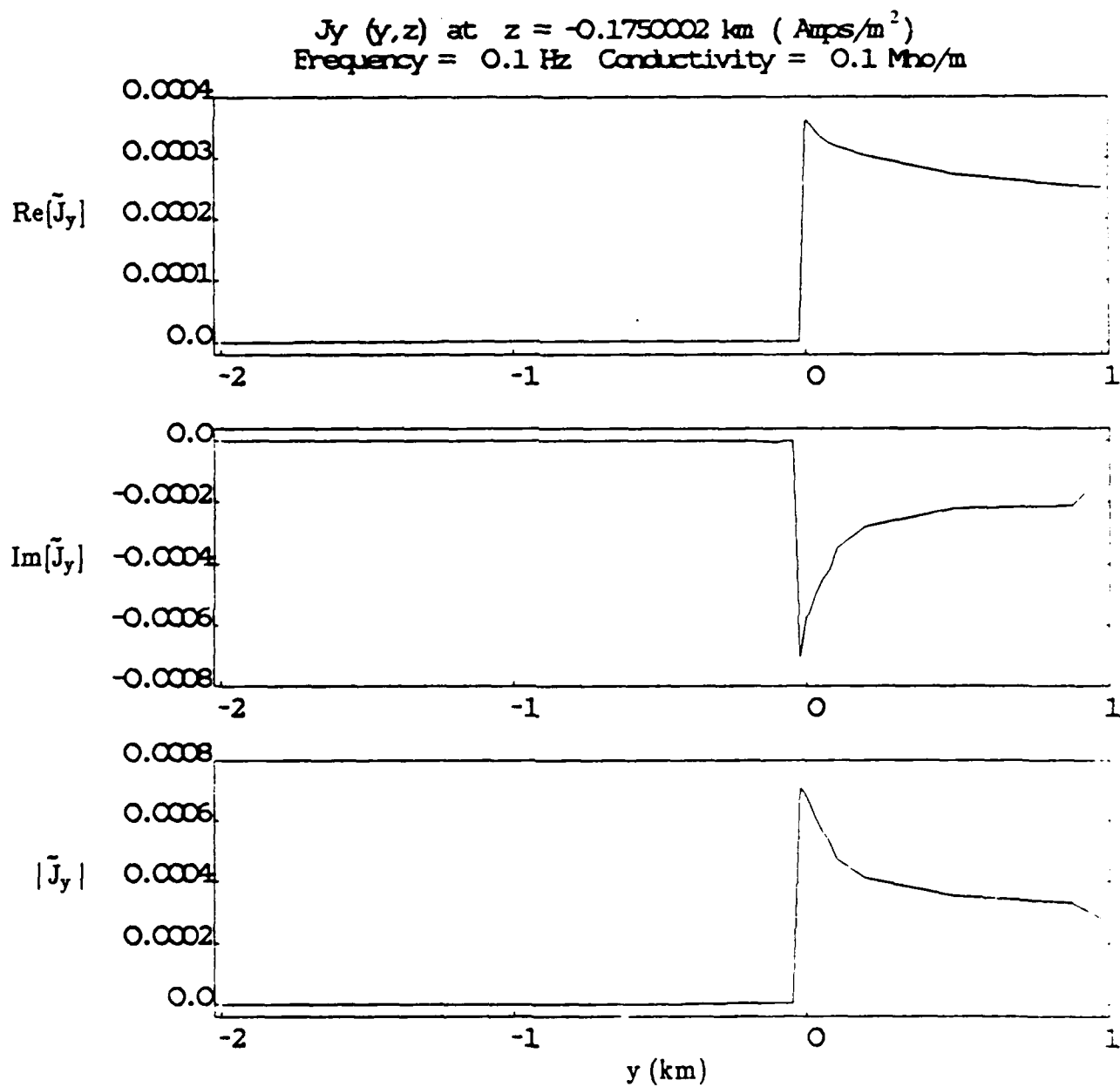


Fig. 6.22b. The total current  $\tilde{J}_y$  from the finite element code at  $z = -0.175 \text{ km}$ .

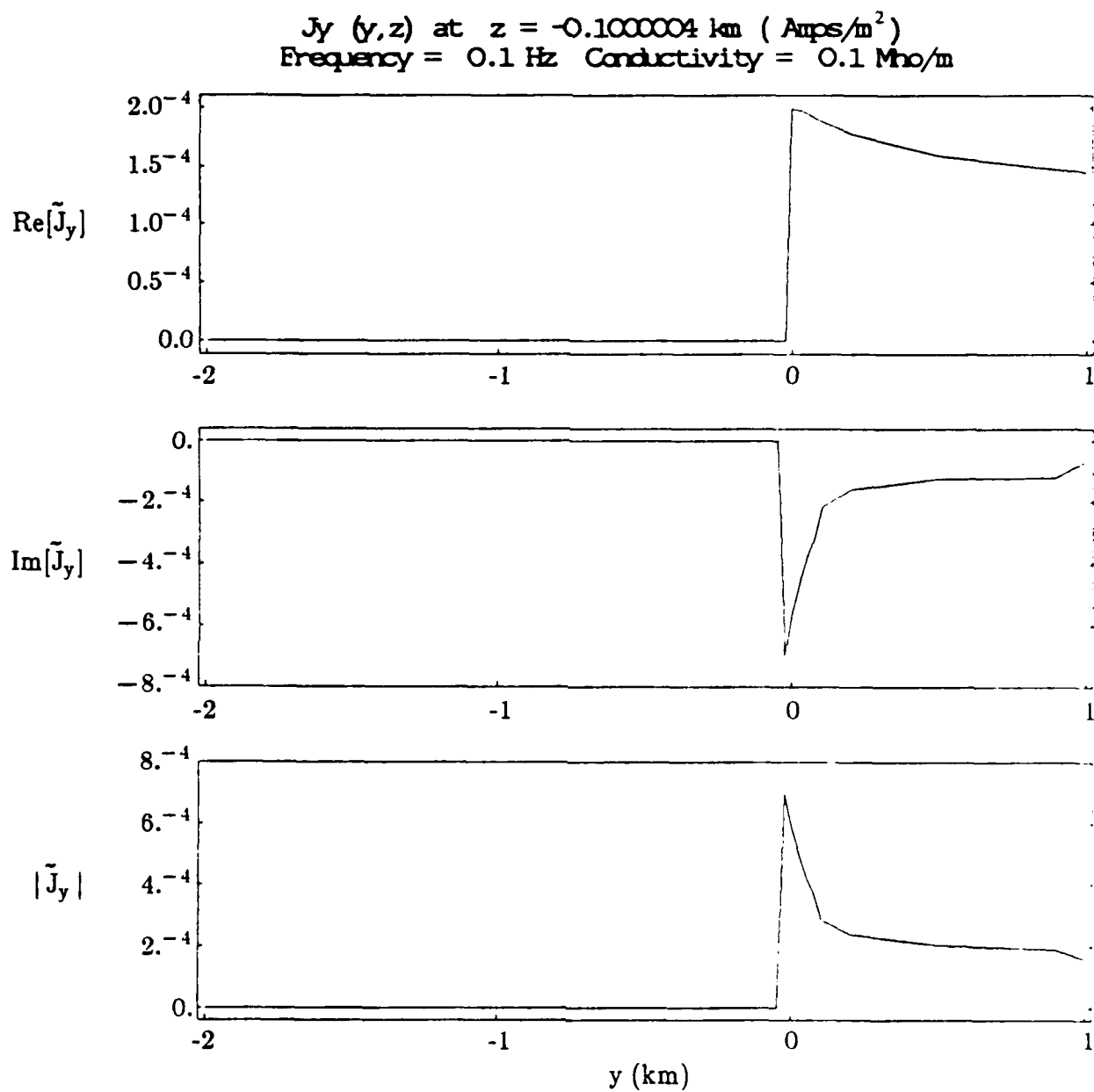


Fig. 6.22c. The total current  $\tilde{J}_y$  from the finite element code at  $z = -0.1$  km.

## CHAPTER 7

### A WORST-CASE SCENARIO FOR SUBMARINE CABLES

A simple worst-case scenario for the submarine cable system is readily available. The idea is to compare the effective resistivity obtained for the L4/L5 system [Ref. 1] with the maximum value of the effective resistivity obtained here. Recall that, at least for frequencies above 0.01 Hz only the part of the submarine cable on the continental shelf experiences appreciable coupling. Since the lengths of the submarine cable on the continental shelf and the L4/L5 land-based cable system are similar, a comparison of the threats can be made. This discussion will not address a comparison of the system response for a submarine and land-based cable for a given threat, which is system-equipment dependent. A discussion of system equipment for a submarine cable is given in Chapter 8, and a detailed evaluation of the threat to submarine cable systems is presented in Volume II (classified) of this report.

The implications from the above data analysis for the submarine cable as compared to the L4/L5 cable are roughly as follows. Take, for example, the maximum value of the effective resistivity for the TAT-6 225-km data, around  $10 \Omega\text{-m}$ . This number is about 50 times less than the average effective resistivity of around  $500 \Omega\text{-m}$  found in the L4/L5 study as exhibited in Fig. 7.1. Recall that the voltage fluctuations induced on the system vary as the square root of the effective resistivity. The above factor of 50 is thus really a factor of 7 for the system response. Given the uncertainties in the absence of experimental information at the desired frequency range up to 1 Hz, a conservative approach would be to identify a "worst-case-scenario" by ignoring this factor. Thus, this scenario would simply envision that the maximal threat

to a submarine cable would be similar to the threat for the L4/L5 system.

Now, because the effective resistivity is observed to decrease with frequency for submarine cables at least out to 0.05 Hz, the voltage fluctuations actually induced on submarine cables at the 0 - 1 Hz frequency range of interest for the MHD HABW (High altitude Blast Wave) effect [2] are plausibly considerably less than in this simple worst-case-scenario. This would assume that the extrapolation out to around 1 Hz does not encounter a rising behavior of the transfer function with increasing frequency. Such effects cannot be excluded (and physical situations are known where transfer functions do indeed rise locally with frequency). Nonetheless, suppose that an upper bound trial extrapolation for the effective resistivity at around 0.1 - 1 Hz is taken as 1 ohm-m. This value is above all values of effective resistivities deduced from all experiments at their Nyquist frequencies and above the extrapolations from the modeling as well. Then, the threat HABW-induced voltage fluctuations would be reduced for a submarine cable system from this worst-case-scenario by at least a factor of  $\sqrt{500} = 22$  relative to the HABW threat to the L4/L5 system. The MHD Heave effect takes place over longer times and involves less extrapolation; a value of the effective resistivity of 1 ohm-m would be consistent with these data, again leading to a factor of around 20 smaller response from a submarine cable system relative to the L4/L5 system.

At very low frequencies (say around 0.001 Hz), the coupling to the cable at the ocean bottom becomes more appreciable. However, this potential enhancement of the coupling of the lowest-frequency MHD fields (due primarily to the MHD Heave effect) onto a longer cable length is largely offset by taking into account

the variation of the field strength with distance from the source region of the fields. This analysis is discussed further in Volume 2 of this report.

In summary, although a "worst-case-scenario" identifies the MHD threat to a submarine cable system as being similar to the threat to the L4/L5 system, the observed decrease of the effective resistivity data with frequency over the available frequency range may be optimistically interpreted to imply that the threat to a submarine cable system is actually substantially less.

#### REFERENCES (Chapter 7)

1. D. L. Lin, "Solar-Induced and Nuclear Magnetohydrodynamic Effects on Coaxial Carrier Transmission Systems", 1984.
2. N. J. Carron and C. L. Longmire, "Magnetohydrodynamic EMP Environments (U)", Mission Research Corporation Report MRC-R-724 Revised, DNA-TR-82-25 (February, 1982).

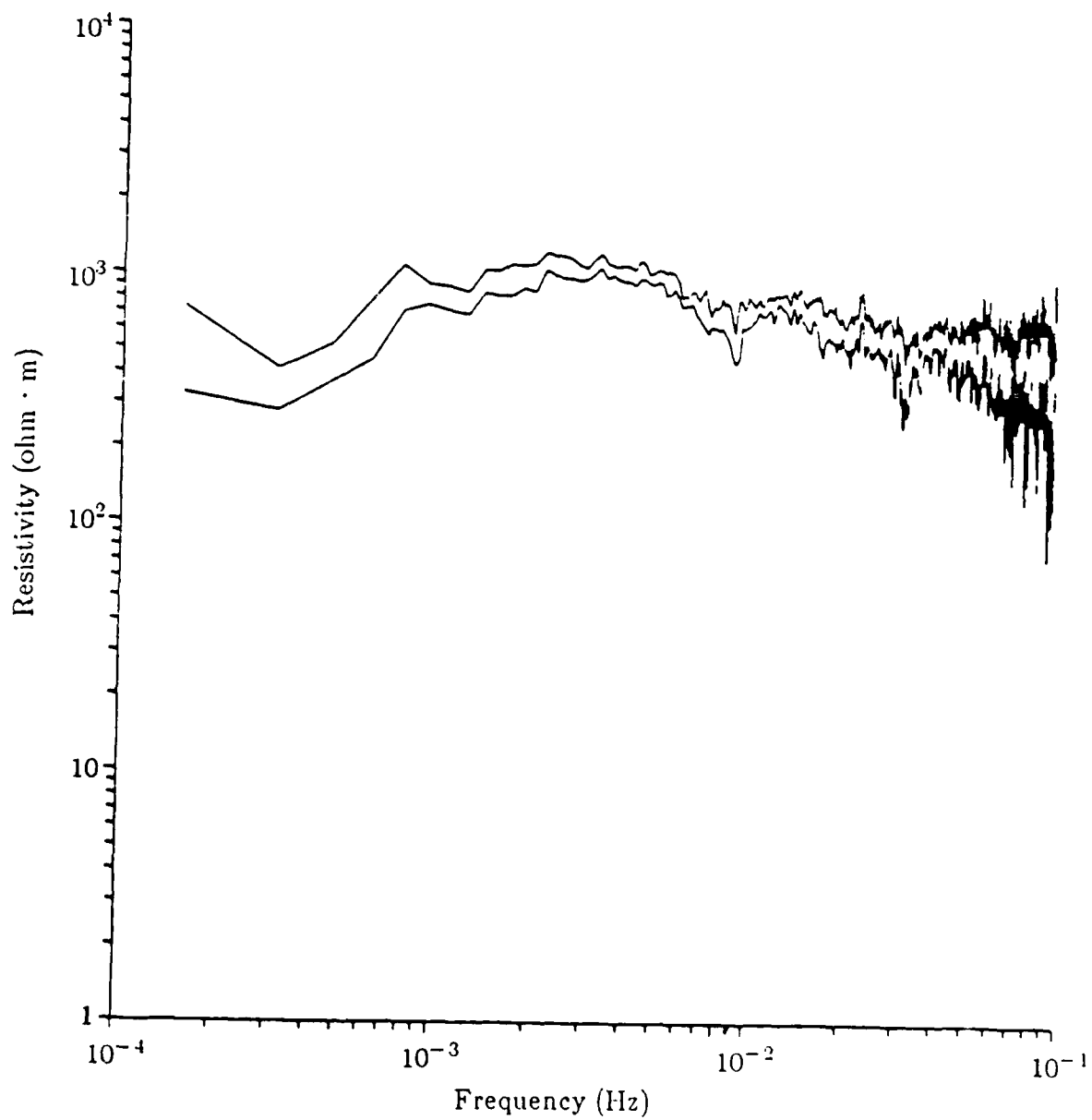


Fig. 7.1. Effective resistivity found in Ref. [1] for the L4/L5 land-based system. The two lines are 95% confidence bounds.



## CHAPTER 8

### EQUIVALENT MHD COUPLING AND CIRCUIT THEORY

#### 8.1 - GENERAL REMARKS

This section presents the quasi-static circuit theory including the power supply characteristics, assuming that the earth potential is given for a specified cable configuration and at the desired frequency. Appendix C contains some formalism relevant to this issue. For time scales on the order of 1 second or more, the circuit limit of the transmission line formalism is relevant. Consider first [1,2] the equivalent circuit shown in Fig. 8.1. The power supply voltage  $V_{ps}$  actually consists of two additive terms,  $V_{ps}^{(1)} + V_{ps}^{(2)}$  corresponding to the power supplies in the U.S. and in Europe for a transatlantic cable. We consider two cases, a net earth potential aiding  $V_{earth}^{(+)}$  and opposing or "bucking"  $V_{earth}^{(-)}$  the power supply voltage  $V_{ps}$ . Denoting the effective impedance of the cable system (including repeaters) by  $R_{eff}$  and assuming an aiding earth potential,

$$V_{ps}(I) + V_{earth}^{(+)} = IR_{eff}(I) \quad (8.1)$$

and for an opposing earth potential

$$V_{ps}(I) - V_{earth}^{(-)} = IR_{eff}(I) \quad (8.2)$$

Note that  $V_{ps}$  depends on the current  $I$  through the V-I characteristics of the power supply. An approximate straight-line-segment V-I curve for the U.S.

power supply [1] of a submarine cable is given in Fig. 8.2. The normal operating point is along the high resistance ( $80 \text{ k}\Omega$ ) segment at a typical point marked  $P_{op}$  where  $V_{ps} = V_0$ ,  $I = I_0$ . As the power supply voltage varies between  $V_{ps} = 0$ ,  $V_{ps} = V_1$ , the current  $I$  varies very little, as desired for a current-regulating power supply. A voltage-regulating power supply with additional current regulation for fluctuations of the line current over 3% of the nominal value may be deployed on the European side [1]. Now the earth potential will change the total current in the equivalent circuit unless the power supply voltage changes in the opposite direction to cancel it. Generally, the nominal current (about 1.6 amperes) is maintained by the power supplies within tight limits, and no problem with the system occurs. An earth potential of 1500 volts can be tolerated. However, if the earth potential and thus  $V_{ps}$  changes too much, the limits on the normal operating segment will be exceeded.

Consider first the case when the earth potential is opposing the power supplies, i.e.  $V_{earth} = -V_{earth}^{(-)}$ . Now  $V_{ps}$  must increase. For large  $V_{earth}^{(-)}$ ,  $V_{ps}$  will eventually pass  $V_1$  and the power supplies will no longer be in normal operation. For  $V_{ps}$  between  $V_1$  and  $V_2$  the power supply resistance decreases, and a much larger fluctuation in the current will result for a given fluctuation in  $V_{ps}$  than in normal operation. In this case the current varies between  $I_1$  and  $I_2$ . As  $V_{ps}$  increases still further, it eventually passes the points  $V_2$  and finally  $V_c$ , where the regulation ceases to be operative and the power supply experiences an overvoltage shutdown.

For the case of the aiding earth potential  $V_{earth} = V_{earth}^{(+)}$ , the power supply voltage must decrease in order to attempt to maintain constant current.

However, eventually again the normal operation is destroyed and the current passes  $I_3$ , eventually rising to  $I_c$ , at which point the power supply has an over-current shutdown.

In the event that an over-current or over-voltage shutdown occurs, the power supply system can be reactivated using a ramp generator. The ramp generator controls the up/down rate of the power supply output voltage as a function of time. The controller for the power supply responds to a manual command and issues up/down signals after passing conditional tests on alarms and status signals before a ramp-up is allowed. The ramp rate is 60 volts per second to permit gradual equalization of charge in cable capacitance. A fast ramp rate (1000 volts per second) is available for both up and down ramps when activated with a momentary pushbutton.

Further details on the operation of the power supplies which are relevant to the overcurrent and overvoltage shutdowns are as follows.

On an overcurrent shutdown where the current is above 3.2 amperes for at least one second, caused by an aiding induced voltage, the power supply does nothing to limit the further increase of current if the aiding induced voltage continues to increase. The output of the power supply remains as a short circuit across the cable for cable currents in the normal direction, as shown in Fig. 8.3. Note that nothing limits the current in the normal direction to less than 3.2 amperes.

On an overvoltage shutdown at 6900 volts lasting at least one second, caused by a bucking induced voltage, the power supply becomes an open circuit

- until the bucking induced voltage increases the power supply voltage to 9000 volts. At 9000 volts, shunt gas tubes fire and operate a relay that connects 1000 ohms in parallel with the power supply output. The relay will drop out when the voltage drops to about 100 volts, as shown in Fig. 8.4. After the gas tube fires, the main thing that will limit the reverse current in the cable is the 5200 ohms of resistance in the cable conductor plus the above 1000 ohms.

## 8.2 - BRANCHING POWER SUPPLIES

Assuming a configuration where a branching of the cable system into several branches occurs, the earth potential effects on the various power supplies would depend on the details of the branching. Consider the configuration illustrated in Fig. 8.5. The power supplies marked  $V_{ps}^{(1)}$ ,  $V_{ps}^{(2)}$ , and  $V_{ps}^{(3)}$  are branched at the branching unit marked BU. Suppose that  $V_{ps}^{(1)}$ , powered positive with respect to local ground, is connected through the BU to  $V_{ps}^{(2)}$ , which is powered negative with respect to its local ground. The current  $I_1$  is generated, and the earth potential acts on the equivalent circuit formed by  $V_{ps}^{(1)}$  and  $V_{ps}^{(2)}$  as if the other power supply  $V_{ps}^{(3)}$  were not present. If the BU is close to Europe, the voltage is low, and  $V_{ps}^{(3)}$ , powered negative with respect to its local ground has its circuit completed by a sea ground of the power conductor at the position of the BU. Only the signal information is transferred from the U.S. to this second branch. Hence the earth potential effects on this second branch from the BU to  $V_{ps}^{(3)}$  are due only to coupling on the European side of the BU to the magnetic field fluctuations. The power supply  $V_{ps}^{(1)}$  feels the effects of the entire magnetic field between the U.S. and Europe. If, on the U.S. side, branching units are envisioned, similar considerations apply. A power

supply connected to a branch on the U.S. side similar to  $V_{ps}^{(3)}$  would experience disturbances due only to the earth potential induced between that branching unit and the power supply position. The power supply powering the current through the transatlantic system would experience a disturbance due to the entire earth potential.

Typical operating values for a submarine cable system are [3]: length = 7400 km, cable resistance =  $0.7 \Omega/\text{km}$ , repeater voltage drop = (21 volts/repeater) x (120 repeaters) = 2520 volts, cable I-R drop = (7400 km) x ( $0.7 \Omega/\text{km}$ ) x (1.6 amps) = 8290 volts, and nominal earth potential allowance = 1500 volts (aiding or opposing). Assuming that the European and U.S. power supplies are identical, the budget of 8.3 kV (cable) + 2.5 kV (repeaters)  $\pm$  1.5 kV (earth potential) would produce  $V_{ps}^{(1)}$  in the range of 4.7-6.2 kV with a nominal value of 5.4 kV. This is consistent with the nominal power supply voltage of 5.6 kV in Fig. 8.2.

### 8.3 - REPEATER POWERING AND FAILURE [3]

For the repeaters, Zener diodes provide the regulated voltage across the transmitter arrays and across the regenerators. The regenerator requires that the voltage be regulated to better than around 10%. The diodes provide protection against surges to the repeaters. A 35% increase is allowed during surges such as those due to cable fault.

#### 8.4 - ZENER DIODE OPERATION

Normal operation of a diode as a voltage regulator means that the diode should operate in reverse bias where breakdown occurs. Then, regardless of the current flowing through the diode, the voltage across it is virtually equal to the breakdown voltage, and is therefore fixed. The value for submarine cable diodes is 6.8 volts. Thus the diodes act as voltage regulators against current fluctuations in normal operation. The crucial parameter determining deviations from normal operation is the amount of power that the diode can handle before internal damage occurs to the diode due to heat transfer problems. The nominal diode rating of say, 10 watts, is the continuous power maximum before such damage occurs. However, this value is not what is required for surges of limited time duration. The characteristics of a submarine cable diode (peak reverse surge power vs pulse width) for ambient temperature of 25 degrees C are shown in Fig. 8.6. The pulses are square for these data and are rather different from the shape of actual pulses from a fault [3], say, but give the right order of magnitude. For a surge of 1 second, appropriate for the HABW effect, the maximum power for the diode is around 80 watts. For the Heave effect, an estimate can be obtained from an average of the DC value of 10 watts and 25 watts for a 10-second surge, or around 17 watts. Thus, for a nominal reverse bias voltage of 6.8 volts, the maximum surge current allowed is around 10 amps for the HABW effect and around 2 amps for the Heave effect. In fact, the actual reverse bias voltage depends slightly on the current; typically  $\Delta V/\Delta I = 0.012$ , so the bias voltage is actually around 7.0 volts. This is well within the voltage regulation limits tolerated by the repeater.

Under the power-supply overvoltage shutdown situation discussed in Sect. 8.1 where gas tubes fire, the Zener diodes in the repeaters will be forward biased. The resulting repeater bias would then be about 6 volts in the opposite direction to the usual repeater bias of 21 volts from three diodes in series each reversed-biased at 7 volts. The dissipation in the forward-biased Zener diodes will be lower, for a given current, than if they were reversed biased, which is desirable from the point of view of the diodes. However, such a case would imply that the electronic integrated circuits would no longer be biased normally, presenting potential problems for the electronics following this power-supply overvoltage shutdown.

#### 8.5 - REPEATER OPERATION TOLERANCE

If the repeater has a parallel configuration of two strings of diodes, as illustrated in Fig. 8.7, the maximum current surge would be multiplied by two. Thus, for such a configuration,  $I_{\max} = 20$  amps would be allowed for a pulse width of 1 sec. For a pulse width of over 10 sec, the maximum current allowed would be around  $I_{\max} = 4$  amps for two diodes in parallel.

The nominal operation for the submarine cable system is 1.6 amp for the logic circuits and 0.34 amp for the diodes. The repeater voltage of 21 volts is obtained by stringing together three diodes in series, each with nominal 6.8 volts regulated voltage. The nominal operating current of 1.6 amps is divided between 6 regenerators (200 milliamps each), 60 milliamps for supervision, and 340 milliamps for the string of diodes. In shallow water, it is expected that two strings of diodes will be connected in parallel for added protection.

Using the illustrative value for the maximum current as the overcurrent shutdown value of 3.2 amps, the values of over 4 amps described above for the maximum currents allowed for repeaters on the continental shelf would imply sufficient protection. Still, the power supply shutdown only yields a short circuit, and does not prevent current flow above the 3.2-amp shutdown value. Further, the time for the shutdowns to take effect is on the order of 1 second, during which time the repeaters could be exposed to extra transient current. The dynamic response time of the power supplies around the normal operating point to changes in the earth potential is around 0.1 second [1].

The "worst case surge current" scenario of the repeater designers [3] is for the cable to be charged to 10 kV with subsequent failure. The system is designed to survive the transient currents that would result.

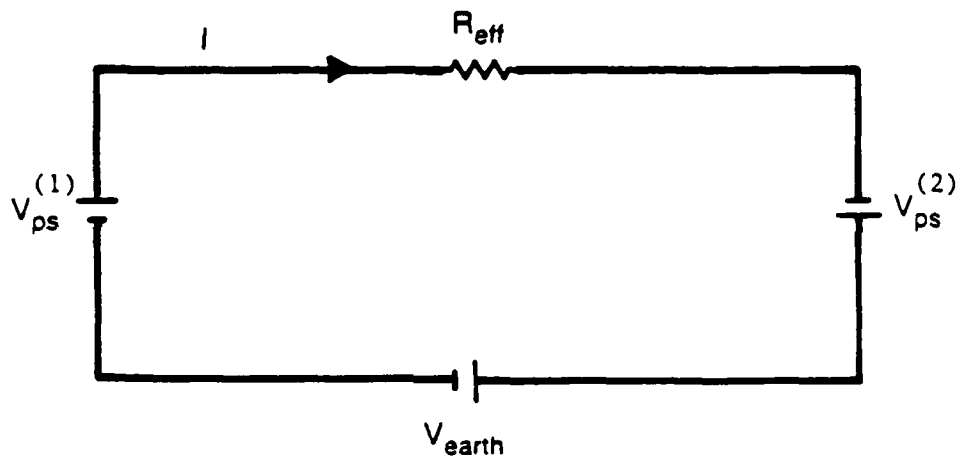
#### 8.8 - STEEL ARMOR

Steel armor is installed to add protection to a submarine cable across the continental shelf for protection against breakage by trawlers. For a thickness  $t = 3.3$  cm and at a frequency of 1 Hz, the skin depth for stainless steel is about  $t$ , while for cold rolled steel it is about  $t/3$ . Hence stainless steel armor is transparent to 1 Hz MHD excitation, while cold rolled steel would provide attenuation of about an order of magnitude. Less attenuation would occur at lower frequencies.



## REFERENCES (Chapter 8)

1. B. H. Hamilton, AT&T Bell Laboratories, private communication.
2. D. L. Lin, AT&T Bell Laboratories, private communication.
3. C. D. Anderson, AT&T Bell Laboratories, private communication.



EQUIVALENT CIRCUIT

Fig. 8.1. Equivalent circuit for a submarine cable communications system with an earth potential present.

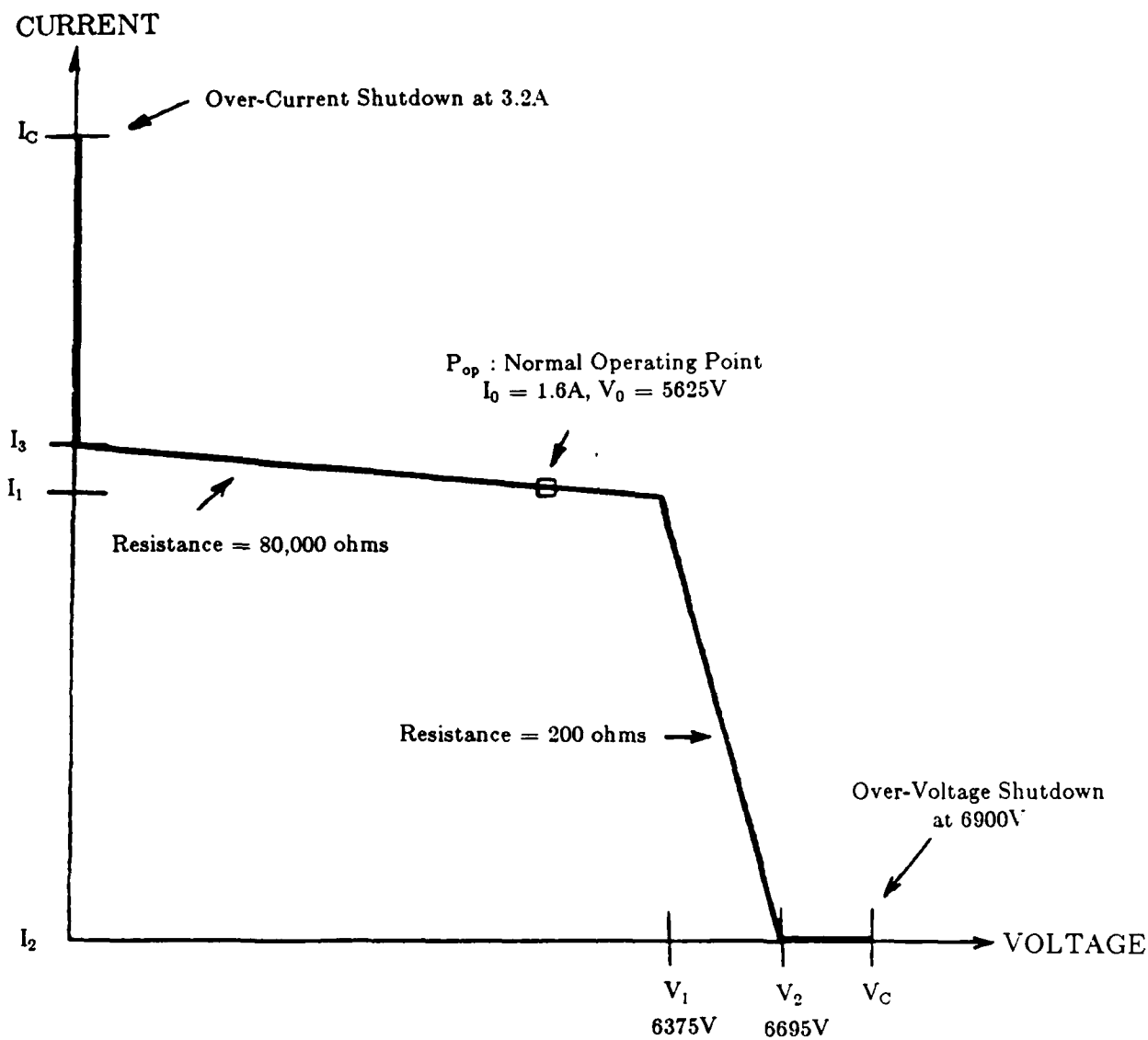


Fig. 8.2. The approximate straight-line-segment V-I curve for the power supply of a submarine cable.

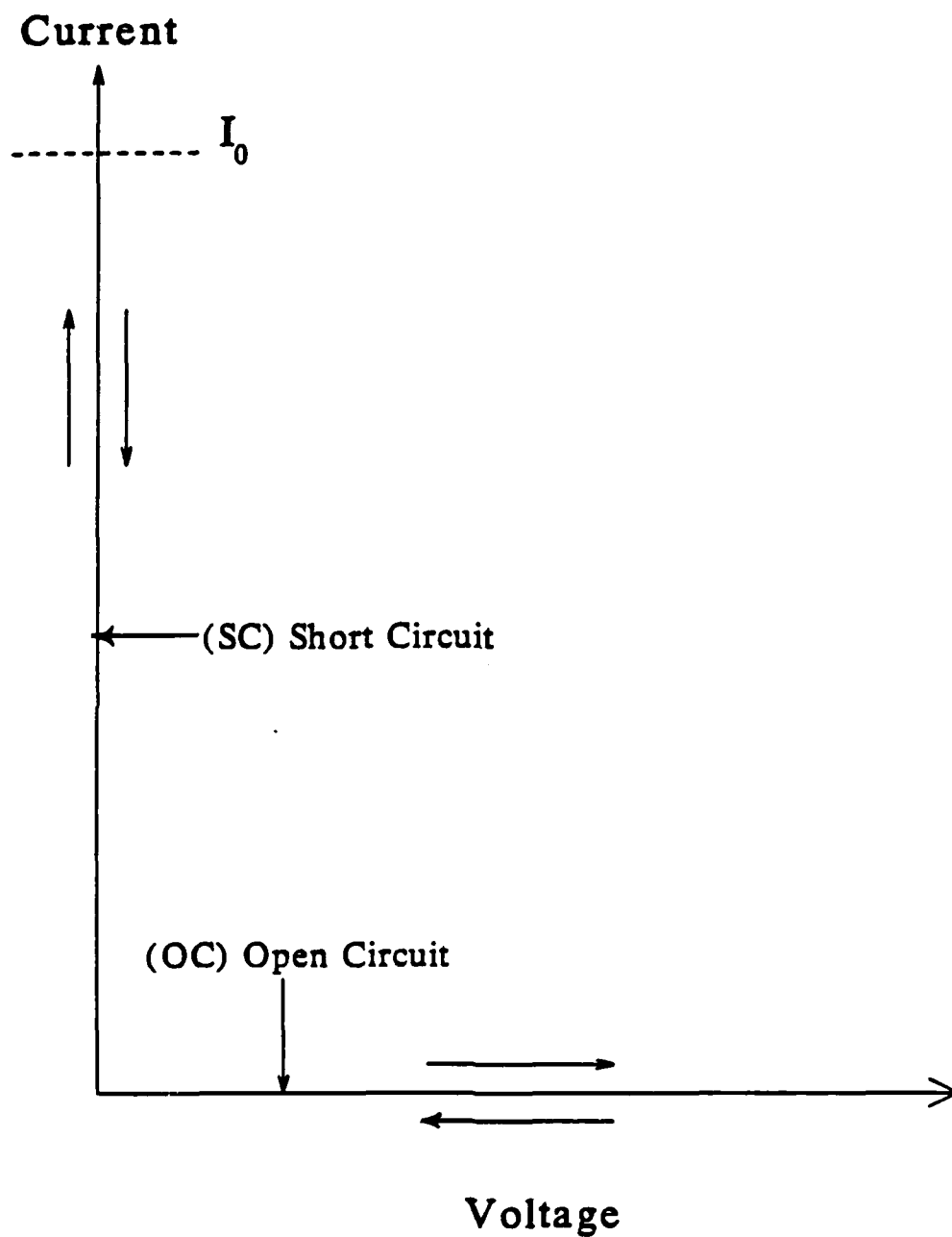


Fig. 8.3. The power supply characteristics after shutdown occurs. On the vertical segment marked (SC), a short circuit overcurrent shutdown situation for aiding earth potential voltages occurs. On the horizontal segment marked (OC) an open circuit overvoltage shutdown situation occurs for bucking earth potential voltages.

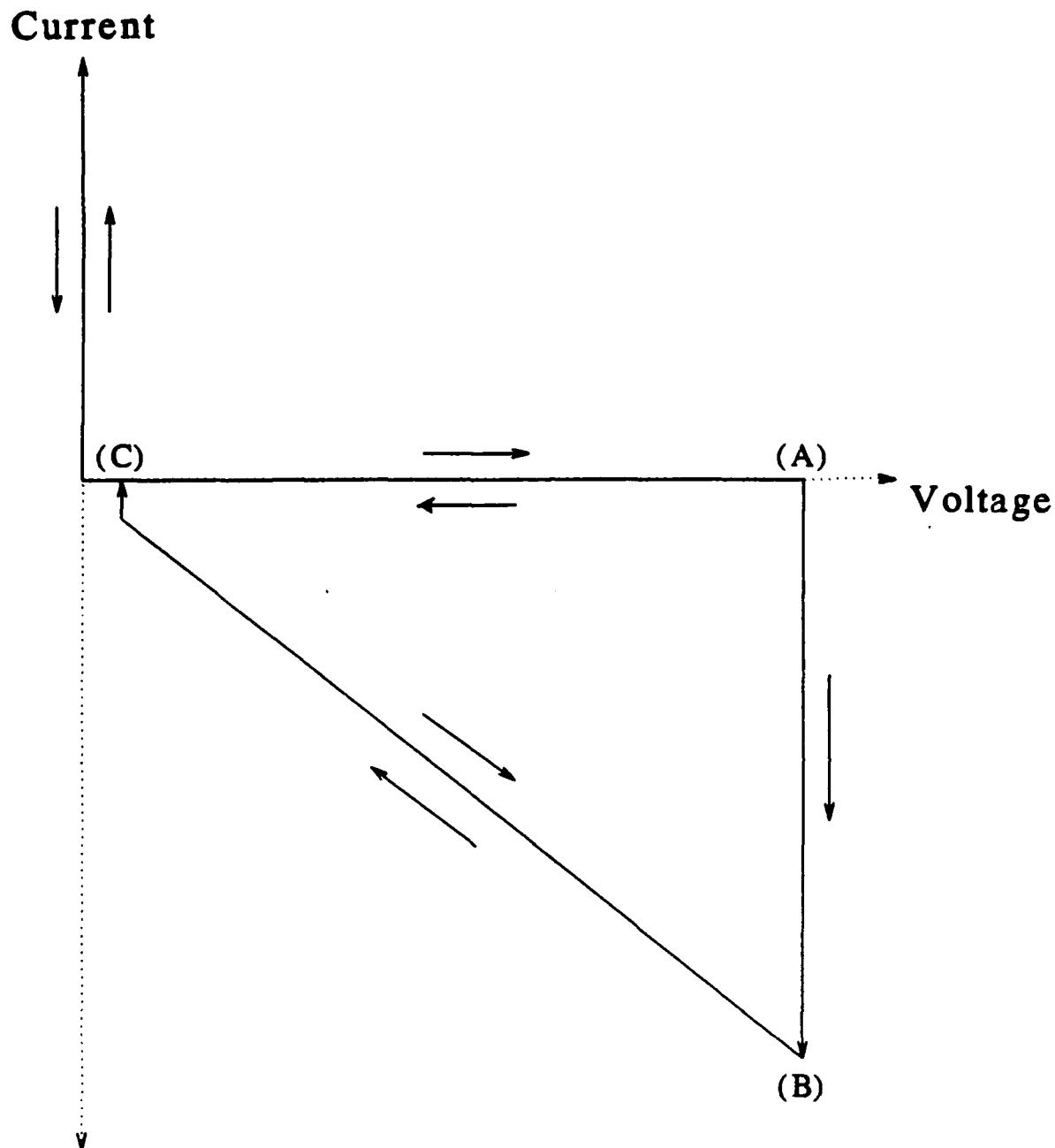


Fig. 8.4. The power-supply characteristics for a fast overvoltage shutdown. At point (A), shunt gas tubes fire at a power-supply voltage of 9000 volts, thereby connecting 1000 ohms in parallel with the power output. At point (B), 9 amperes of current exist in the reverse direction. At point (C), the power supply voltage is 100 volts. A 1000-ohm slope connects points (B) and (C). In the quadrant (ABC) the reverse current is limited mainly by the resistance of the cable power conductor.

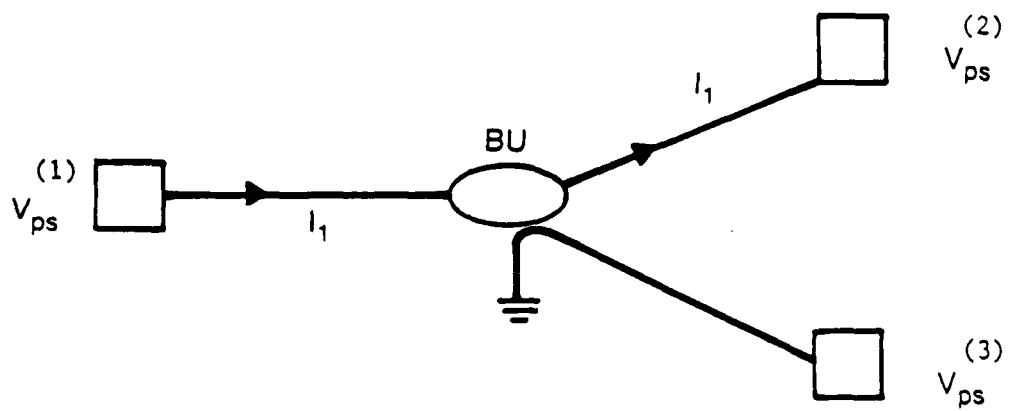


Fig. 8.5. A configuration of a branching into two legs with a total of three power supplies.

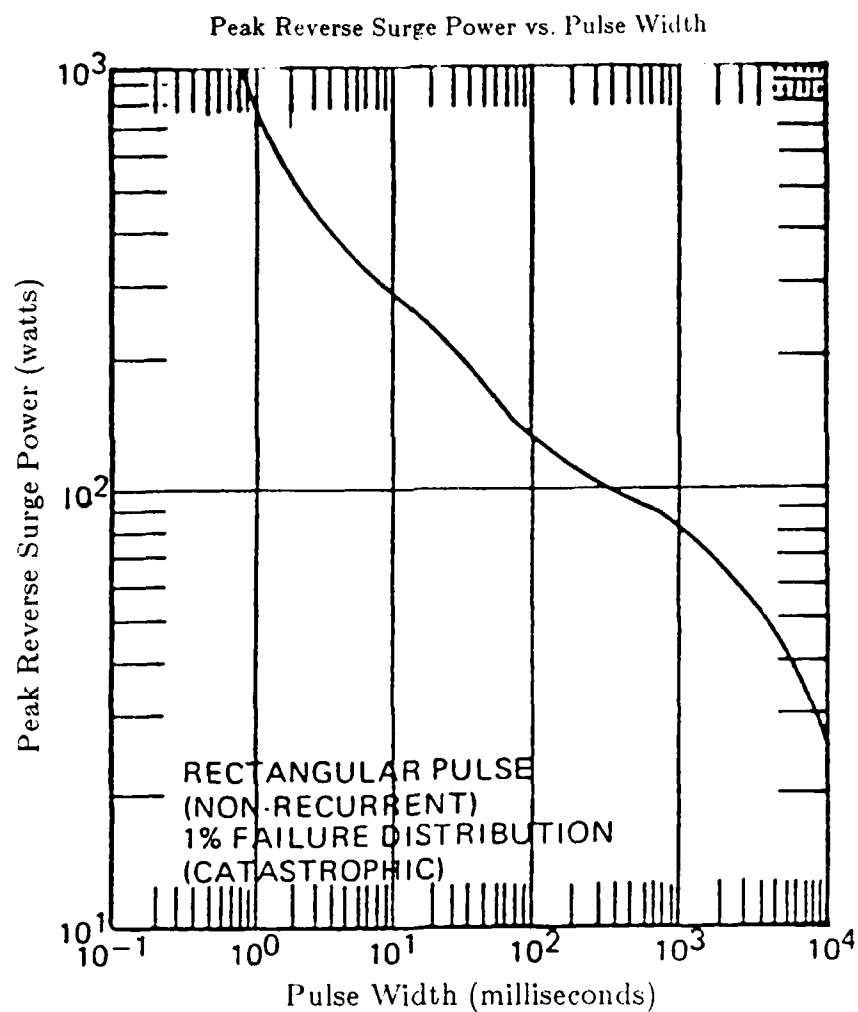


Fig. 8.6. The characteristics of a Zener diode in a submarine cable repeater. The maximum allowable surge power is plotted vs. pulse width of the surge. The surges are assumed to be square pulses. The DC power rating is 10 watts.

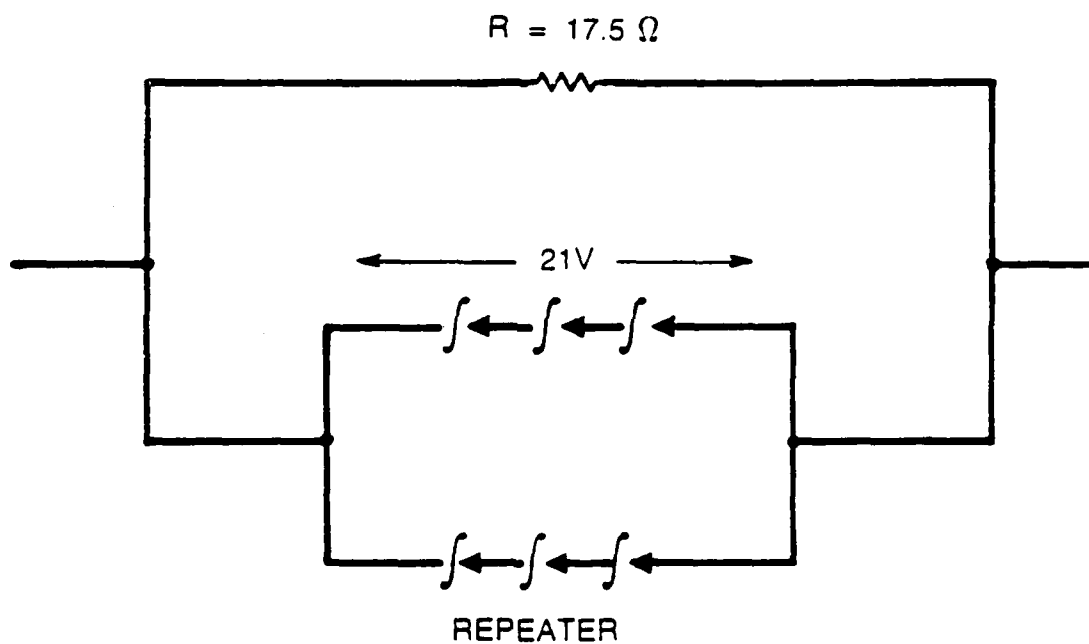


Fig. 8.7. The equivalent circuit for a repeater on the continental shelf with two strings of diodes.



## CHAPTER 9

### PROTECTION

From the results of the analysis of the experiments described in previous sections of this report, it appears that submarine cable systems are less susceptible to an MHD threat than their land based counterparts. The decrease of the effective resistivity with frequency over the available experimental range, coupled with the model results, leads to quite small effective resistivities at the MHD-HABW and Heave characteristic frequencies, and hence projections of small earth potential differentials.

If it were necessary to further enhance repeater protection for submarine cable systems, the approach would be to add extra Zener diodes to each repeater, of the type discussed in Chapter 8. Such diodes already form the protective mechanism against anomalous fluctuations for the repeaters, and extra diodes would provide further protection. Of course, modifications to repeaters already in place could not be considered lightly.

The discussion of the quite substantial protective mechanisms already provided for the power supplies has been presented in Chapter 8.

## SUMMARY AND RECOMMENDATIONS

This first volume of the report has presented the methodology for the evaluation of the MHD threat to a submarine cable system. Experiments and their analyses were presented along with modeling for a given geometry. Some submarine cable system characteristics were also given. A second volume (classified) deals with the threat and a detailed evaluation for submarine cable systems.

One objective of this report has been to highlight the difference between the MHD threat to land based cables and submarine undersea cables. While the effective resistivity which measures the system response is roughly constant on land out to available measured frequencies of 0.1 Hz, the effective resistivity for submarine cables decreases significantly with frequency. This indicates that a submarine cable is inherently less vulnerable than a land-based cable.

The application of the methodology of this report is general. However, the specific numerical results for a given situation will depend on the geometry as well as the geological features that happen to be present.

A characteristic difficulty present in the analysis is that no direct experimental information is yet available at the  $1/4$  - 1 Hz frequency range of interest for the MHD-HABW effect. Therefore it is a primary recommendation and conclusion of this work that measurements be performed at sampling rates faster than 1 measurement per second to allow information to be obtained at these frequencies. Such experiments are difficult since the spectra for both the cable voltage and the earth's magnetic field are anticipated to drop off with frequency, necessitating sensitive equipment to distinguish signal from noise.

Moreover the cable cannot be too short; otherwise stochastic contact potential noise corrupts the induced voltage signal.

A new generation of fiber-optic submarine cables (TAT-8, TAT-9 being the first) are coming on line. It would seem desirable to perform measurements on these systems or on parts of these systems as they become available, especially in the unpowered state, supplementing the measurements on existing coaxial cable systems (TAT-4,6,7). Making such measurements constitutes a second recommendation.

## APPENDIX A

### SEMI-ANALYTIC MODEL

#### A.1. INTRODUCTION

As stressed in the text, the available experimental information [1] is confined to low frequencies, mostly less than 0.1 Hz. Since higher frequencies are needed to describe MHD effects, it is necessary to formulate a model which, without too much effort or complication, would be available to extrapolate the results of such experiments to higher frequencies. This appendix deals with this issue.

Specifically, this appendix presents the theory of electromagnetic field penetration into an ocean/land environment resulting from an incident plane wave from above in the air, taking account of the important boundary conditions that occur at the continents. First, the reader is reminded of results for problems with layers, but without vertical boundaries. Some formalism is then presented to include vertical boundaries. The theory is then approximated by a modification of the ideas presented in Ref. [2] (the idealized island problem) to the geometry relevant to this application. Next it is shown how to implement the approximate theory numerically in order to obtain qualitatively correct results.

The geometry is presented in Fig. A1. Translation invariance in the  $x$ -direction (along the coastline) is assumed. This enables the EM fields to be broken up into two classes (usually called E and H polarization), corresponding to the case where the electric or magnetic field is parallel to the coast. The transverse ( $y,z$ ) plane can, on the other hand, present arbitrarily complicated

geometry. It is assumed that there is a continental shelf of depth  $d_c$  and width  $L_c$  on each side of the ocean which has of depth  $d_o$  and width  $L_o$ , and a mantle starting a depth  $z = -d_m$  inside the earth. The critical point to observe is that the ocean has a large conductivity compared with the land. The frequency range of interest is low enough so that the land acts to some extent as an insulator (that is, the skin depth in the land is large compared to the depth of the ocean). In addition to penetrating directly through the ocean, which strongly attenuates the fields, the land the fields can propagate through the land from the surface  $z = 0$  to the bottom of the ocean ("leakage fields").

In Section A.2 the problem is defined and the reader is oriented with some elementary background information, including the solutions to simple layered problems. For more details, the reader is encouraged to consult Chapters 7,8 and problems 7.2, 7.13-7.15 of Ref. [3]. Section A.3 presents the formalism for our approximation, while in Section A.4 it is shown how the numerical application of the theory is performed for this project.

## A.2 - GENERAL REMARKS

In this section, the reader is reminded of some well-known results from elementary electromagnetic theory to set the stage for our model. For a region with constant constitutive parameters (conductivity  $\sigma$ , dielectric constant  $\epsilon$ , permeability  $\mu$ ) and for a given (radian) frequency  $\omega$ , the Maxwell equations can be shown to produce the Helmholtz equation for each component of the magnetic field, for example  $(\nabla^2 + k^2)H_x = 0$  where  $k$  is the wave number. The appropriate boundary conditions are  $B_{\text{normal}}$  continuous and  $H_{\text{tangential}}$  continuous where  $\vec{B} = \mu\vec{H}$ . The electric field also satisfies the Helmholtz equation with the boundary conditions  $E_{\text{tangential}}$  continuous and  $D_{\text{normal}}$  continuous, where  $\vec{D} = \tilde{\epsilon}\vec{E}$ . Here  $\tilde{\epsilon}$  is the complex dielectric constant defined as  $\tilde{\epsilon} = \epsilon + i\sigma/\omega$ . Ohm's law for the conduction current reads  $\vec{J} = \sigma\vec{E}$ . It is useful to define the total (conduction plus displacement) current

$$(\tilde{J}_x, \tilde{J}_y, \tilde{J}_z) = \tilde{\sigma}(E_x, E_y, E_z) = -i\omega(D_x, D_y, D_z)$$

for simplicity of notation. Here the complex conductivity is  $\tilde{\sigma} = \sigma - i\omega\epsilon = -i\omega\tilde{\epsilon}$ . In a good conductor, the displacement current due to the second term in  $\tilde{\sigma}$  is small at low frequencies. The total current satisfies  $\tilde{J}_{\text{normal}}$  continuous and so  $D_{\text{normal}}$  is also continuous. Also, the "quasi-static" limit is relevant here, where the charge density  $\rho_{\text{ch}}(\vec{x}, t) = 0$ , which means charges redistribute themselves on very small time scales compared with the relaxation time  $\epsilon/\sigma$ , which for typical land values is 10 ns and for seawater much shorter. Still, surface charges will appear at interfaces between materials of different conductivities.

A remark which should help clarify the  $\tilde{J}_{\text{normal}}, D_{\text{normal}}$  boundary conditions is as follows. We have defined  $\vec{D}$  as  $\tilde{\epsilon}\vec{E}$ . Another possibility would be to define it simply as  $\epsilon\vec{E}$ ; in that case  $D_{\text{normal}}$  would no longer be continuous at

boundaries where the conductivity changes discontinuously, and the Poisson equation  $\vec{\nabla} \cdot \vec{D} = \rho_{ch}$  with this definition of  $\vec{D}$  is satisfied by the appearance of the surface charges at the interface. Needless to say, the normal electric field is not continuous at interfaces either. However  $\tilde{J}_{normal}$  is always continuous, even across interfaces. This can be seen by taking the divergence of the Maxwell equation  $\vec{\nabla} \times \vec{H} = \vec{\sigma} \vec{E} = \vec{J}$  to see that the total current is divergenceless, and using the Gauss volume theorem at the interface as usual. Note that the Helmholtz/p equation does not hold exactly at such an interface. Instead one can show that an extra term enters, given for  $H_x$  for example by the x component of  $\vec{\nabla} \tilde{\sigma} \times \vec{E}$ . This enters in the finite element code in a crucial manner.

A compendium of other details, which also serves to introduce notation, is as follows. The time dependence for the fields is taken as  $\exp(-i\omega t)$ . For a given region, Maxwell's equations produce  $k^2 = i\omega\mu\sigma + \mu\epsilon\omega^2$  where  $k$  is the wave number (complex for conductors and equal to  $\omega/c$  for the air where  $c$  is the speed of light). In terms of the complex conductivity,  $k^2 = i\omega\mu\tilde{\sigma}$ . The complex index of refraction is  $\tilde{n} = c(\mu\tilde{\epsilon})^{1/2}$ . Further, the wave impedance  $Z = (\mu/\tilde{\epsilon})^{1/2} = \mu c/\tilde{n}$  and the (complex) skin depth  $\delta = [2/(\mu\omega\tilde{\sigma})]^{1/2}$ ; hence  $Z = (1 - i)/(\tilde{\sigma}\delta) = -ik/\tilde{\sigma}$  and  $k = (1 + i)/\delta = \omega\tilde{n}/c$ . Also,  $|\tilde{\sigma}| = \mu\omega/|Z|^2$ . or defining the complex resistivity  $\tilde{\rho} = 1/\tilde{\sigma}$ , then  $|\tilde{\rho}| = |Z|^2/(\mu\omega)$ . In the air.  $Z$  is taken as the free space impedance,  $Z = 377\Omega$ .

#### A.2a - THE TEXTBOOK "TRIVIAL SOLUTIONS"

Consider first the textbook [3] example of a normally incident plane wave on a semi-infinite conductor in the half-space  $z \leq 0$ . The air above the conductor is labeled by "a" and the conductor by "c". Then, assuming that the incident wave has its magnetic field along the x direction, taking account of the reflected and transmitted wave produces the form for the magnetic field as

$$H_x(z) = H_0 \left[ e^{-ik_a z} + R_{ac}^{(0)} e^{ik_a z} \right] \quad (z \geq 0) \quad (A2.1a)$$

$$= H_0 T_{ac}^{(0)} e^{-ik_c z} \quad (z \leq 0) \quad (A2.1b)$$

The corresponding expression for the electric field is

$$E_y(z) = Z_a H_0 \left[ e^{-ik_a z} - R_{ac}^{(0)} e^{ik_a z} \right] \quad (z \geq 0) \quad (A2.2a)$$

$$= Z_c H_0 T_{ac}^{(0)} e^{-ik_c z} \quad (z \leq 0) \quad (A2.2b)$$

Here, the conductor c would represent the extreme cases of an infinite ocean (with no land) or an infinite continent (with no ocean). Although it will ultimately turn out that the land acts rather like an insulator as far as the ocean goes, the conductivity is kept general. In the above equations,  $T_{ac}^{(0)}$  is the transmission coefficient into the conductor through the boundary ac and  $R_{ac}^{(0)}$  the reflection coefficient back upwards into the air. The superscript (0) indicates that this is a zeroth-order result when compared to a multi-layered problem, as shall be seen in a moment. Write  $Z_a$ ,  $Z_c$  as the impedances for the air and conductor (see below) in terms of which  $T_{ac}^{(0)} = 2Z_a/(Z_a + Z_c)$  and



$R_{ac}^{(0)} = (Z_a - Z_c)/(Z_a + Z_c)$ . Note that  $R_{ac}^{(0)} = T_{ac}^{(0)} - 1$  and  $[R_{ac}^{(0)}]^2 + (Z_c/Z_a)[T_{ac}^{(0)}]^2 = 1$ . Finally  $H_0$  is a normalization constant with units of amps/meter.

The next simplest textbook case is one in which the conducting medium has a layered structure, as shown in Fig. A2. Still any continental boundary structure is ignored. This is the model treated in Ref. [4]. Now the tangential magnetic and electric field continuity equations at each boundary must be satisfied (again there are no fields perpendicular to the surfaces, i.e. in the vertical  $z$  direction). Reflections and transmissions through each layer are present. The fields in the air, ocean, and land now have the form in eqns. A2.1a, A2.2a with both transmission and reflection coefficients while those in the mantle have the form in eqns. A2.1b, A2.2b. In the limit as the land and mantle layers move downward to  $z = -\infty$  allowing the ocean to fill the half-space  $z \leq 0$  or in the limit as the land and mantle parameters are taken equal to those of the ocean this model reduces to the example just discussed.

The results for the reflection and transmission coefficients are standard. For illustration the three layer solution is presented. This corresponds to the degenerate case when the mantle and the land materials are set equal, or equivalently when the land region is the entire region from  $z = -\infty$  to  $z = 0$ . Addition of more layers is obtained by straightforward algebra. One may either match boundary conditions or get the result with a ray technique keeping track of multiple reflections and transmissions. Calling the three layers a (air), b (ocean), c (land) with the ab boundary at  $z = 0$  and the bc boundary at  $z = -d$  produces

$$T_{ab} = T_{ab}^{(0)} / D_{ab}^{(0)} \quad (A2.3a)$$

$$T_{bc} = T_{ab} T_{bc}^{(0)} \quad (A2.3b)$$

$$R_{ab} = [R_{ab}^{(0)} + R_{bc}^{(0)}] / D_{ab}^{(0)} = R_{ab}^{(0)} + R_{bc}^{(0)} (Z_b / Z_a) T_{ab}^{(0)} \quad (A2.3c)$$

$$R_{bc} = T_{ab} R_{bc}^{(0)} \quad (A2.3d)$$

Here  $R_{ab}^{(0)} = (Z_a - Z_b) / (Z_a + Z_b)$ ,  $T_{ab}^{(0)} = 2Z_a / (Z_a + Z_b)$  are the zeroth order reflection and transmission coefficients from region a to region b. (To get the corresponding quantities from region b to region a, interchange  $Z_a$  and  $Z_b$ ). The corresponding quantities at the bc boundary are  $R_{bc}^{(0)} = e^{2i\xi_b} (Z_b - Z_c) / (Z_b + Z_c)$ ,  $T_{bc}^{(0)} = e^{i(\xi_b - \xi_c)} 2Z_b / (Z_b + Z_c)$  with  $\xi_b = k_b d$ ,  $\xi_c = k_c d$ . Finally,  $D_{ab}^{(0)} = 1 + R_{ab}^{(0)} R_{bc}^{(0)}$ . The factor  $1 / D_{ab}^{(0)}$  can be seen to account for multiple reflections between the ab and bc boundaries.

The fields in each region are

$$\begin{aligned} H_x^{(a)}(z) &= H_0 [ e^{-ik_a z} + R_{ab} e^{ik_a z} ] \\ E_y^{(a)}(z) &= Z_a H_0 [ e^{-ik_a z} - R_{ab} e^{ik_a z} ] \end{aligned} \quad \text{Region a} \quad (A2.4a)$$

$$\begin{aligned} H_x^{(b)}(z) &= H_0 [ T_{ab} e^{-ik_b z} + R_{bc} e^{ik_b z} ] \\ E_y^{(b)}(z) &= Z_b H_0 [ T_{ab} e^{-ik_b z} - R_{bc} e^{ik_b z} ] \end{aligned} \quad \text{Region b} \quad (A2.4b)$$

$$\begin{aligned} H_x^{(c)}(z) &= H_0 [ T_{bc} e^{-ik_c z} ] \\ E_y^{(c)}(z) &= Z_c H_0 [ T_{bc} e^{-ik_c z} ] \end{aligned} \quad \text{Region c} \quad (A2.4c)$$

## A.2b - INCLUSION OF VERTICAL BOUNDARIES

Now the above case does not include boundary effects between the ocean and continent. A potential source of fields at the ocean bottom could occur through "leakage", as illustrated in Fig. A3, namely field penetration down through the land and around the bottom of the ocean basin. At the same time, reflections can occur off the mantle of the earth, which has high conductivity, as well as from the ocean at the various boundaries defining the continental shelf and abyssal plane. These effects are further complicated by effects such as the east coast magnetic anomaly [5], the mid-Atlantic ridge, and so on. Specific features in the land could be introduced, such as possible leakage field barriers in the land due to faults, conductivity discontinuities, etc. An example of this sort of complication is shown in Fig. A4. Specific geophysical information, especially under the continental shelf, is not readily available [6]. However, some additional structure in what has been called the land is present in reality.

It is clear that in the limit as the continents move off to  $\pm\infty$  in the coordinate  $y$ , this model should reduce to the simpler layered model discussed above and pictured in Fig. A2.

In order to treat this very complicated problem the following essential, but standard, assumption retained from the above models is made. It is assumed that the geometry is translation invariant parallel to the coast. That is, any transverse ( $y, z$ ) - plane cut (east-west and up-down) looks the same as any other cut. Planar geometry (flat earth) is also taken, and the incoming field is taken as before as a normally incident plane wave with  $\vec{H}$  along the  $x$ -axis.

In practice, the model exhibited in Fig. A5 was investigated in this report.

From the Maxwell equations with  $\frac{\partial}{\partial x}$  replaced by zero the two sets of decoupled equations are obtained,

$$\tilde{J}_y(y,z) = \tilde{\sigma} E_y(y,z) = \frac{\partial}{\partial z} H_x(y,z) \quad (A2.5a)$$

$$\tilde{J}_z(y,z) = \tilde{\sigma} E_z(y,z) = - \frac{\partial}{\partial y} H_x(y,z) \quad (A2.5b)$$

$$k^2 H_x(y,z) = \tilde{\sigma} \left( \frac{\partial}{\partial y} E_z(y,z) - \frac{\partial}{\partial z} E_y(y,z) \right) \quad (A2.5c)$$

(the H-polarization case) and

$$\tilde{J}_x(y,z) = \tilde{\sigma} E_x(y,z) = \frac{\partial}{\partial y} H_z(y,z) - \frac{\partial}{\partial z} H_y(y,z) \quad (A2.6a)$$

$$k^2 H_y(y,z) = \tilde{\sigma} \frac{\partial}{\partial z} E_x(y,z) \quad (A2.6b)$$

$$k^2 H_z(y,z) = - \tilde{\sigma} \frac{\partial}{\partial y} E_x(y,z) \quad (A2.6c)$$

(the E-polarization case). Since the submarine cables of interest do run primarily in the  $(y,z)$  plane and since the coupling to a metallic cable is always through the tangential electric field, the H-polarization case is of interest.

The above simplification is not enough to make progress without a model which reasonably well approximates the physics. This is the subject to be considered next.

### A.3 - FORMALISM FOR THE APPROXIMATION

The approximation used is based on the results of Ref. [2], the "idealized island problem". There, an asymptotic expansion in the distance perpendicular to a conducting right cylindrical island ( $z$ ) was introduced, following a careful theoretical study of a specific model for that problem. In this section it is shown how to modify the ansatz of Ref. [2] to the case at hand. The H-polarization case is treated; the less interesting (from our point of view) E-polarization case is similar.

The regions are labeled with a generic index  $\zeta$ . Different regions would be defined by different materials (air, ocean, land, mantle, etc.), but also may have to be defined geometrically as subregions within a given material region. For example, different subregions within the land may be defined with boundaries ending on the various horizontal and vertical components of the overall boundary.

For each region  $\zeta$  the wave number  $k_\zeta$  becomes

$$k_\zeta^2 = i\omega\mu_\zeta\sigma_\zeta + \mu_\zeta\epsilon_\zeta\omega^2 \quad (\text{A3.1})$$

Then write

$$H_x^{(\zeta)}(y, z) = \sum_{\alpha, \eta_y, \eta_z} H_x^{(\zeta, \alpha, \eta_y, \eta_z)}(y, z) \quad (\text{A3.2})$$

where

$$H_x^{(\zeta, \alpha, \eta_y, \eta_z)}(y, z) = H_0^{(\zeta, \alpha, \eta_y, \eta_z)} e^{i\eta_z k^{(\zeta, \alpha)} z} e^{\eta_y \gamma^{(\zeta, \alpha)} y} \quad (A3.3)$$

Here  $k^{(\zeta, \alpha)}$  is the complex wave number parameter for term  $\alpha$  in region  $\zeta$ . Also  $\gamma^{(\zeta, \alpha)}$  is obtained from the solution of the Helmholtz equation

$$(\nabla^2 + k_\zeta^2) H_x^{(\zeta)}(y, z) = 0 \quad (A3.4)$$

namely

$$\gamma^{(\zeta, \alpha)^2} = k^{(\zeta, \alpha)^2} - k_\zeta^2 \quad (A3.5)$$

The reader should note that the model specifies the fields everywhere once the parameters  $H_0^{(\zeta, \alpha, \eta_y, \eta_z)}$ ,  $k^{(\zeta, \alpha)}$  are given. If the boundary conditions were easy to implement, these parameters would be determined by simple relations. Our geometry is sufficiently complicated that no simple relations exist, and we shall be forced to implement the determination of the parameters with a method such as described in the next section.

In the simplest textbook cases discussed above,  $\gamma^{(\zeta, \alpha)} = 0$ , so  $k^{(\zeta, \alpha)} = k_\zeta$  and the  $y$  dependence disappears. The coefficients  $H_0^{(\zeta, \alpha, \eta_y, \eta_z)}$  are then just the various reflection or transmission coefficients, depending on the region.

In the above equations,  $\eta_y$  ,  $\eta_z$  are numbers equal to  $\pm 1$ .  $\eta_z = \pm 1$  gives the possibility of reflected and transmitted waves from the various horizontal boundaries. Also, with  $\text{Re}(\gamma^{(\zeta, \alpha)}) > 0$   $\eta_y = \pm 1$  implies terms increasing (decreasing) respectively with increasing  $y$ . This would be relevant, for example, in satisfying the physical requirement that terms other than the simple  $\gamma^{(\zeta, \alpha)} = 0$  term just discussed go to zero far away from the ocean boundary in the land, so that the solution reduces to the simpler layered case with no vertical boundary effects.

The total current and electric fields are given by

$$\tilde{J}_y^{(\zeta)}(y, z) = \tilde{\sigma}_\zeta E_y^{(\zeta)}(y, z) = \frac{\partial}{\partial z} H_x^{(\zeta)}(y, z) = i \sum_{\alpha, \eta_y, \eta_z} \eta_z k^{(\zeta, \alpha)} H_x^{(\zeta, \alpha, \eta_y, \eta_z)}(y, z)$$

$$\tilde{J}_z^{(\zeta)}(y, z) = \tilde{\sigma}_\zeta E_z^{(\zeta)}(y, z) = - \frac{\partial}{\partial y} H_x^{(\zeta)}(y, z) = - \sum_{\alpha, \eta_y, \eta_z} \eta_y \gamma^{(\zeta, \alpha)} H_x^{(\zeta, \alpha, \eta_y, \eta_z)}(y, z)$$

The boundary conditions of continuous  $E_{\text{tangential}}$  ,  $H_{\text{tangential}}$  ,  $D_{\text{normal}}$  or  $\tilde{J}_{\text{normal}}$  between any two regions  $\zeta$  ,  $\zeta'$  are then:

*HORIZONTAL BOUNDARY:*  $H_x$  ,  $E_y$  ,  $\tilde{J}_z$  continuous.

*VERTICAL BOUNDARY:*  $H_x$  ,  $\tilde{J}_y$  ,  $E_z$  continuous.

This specifies the model. The procedure to evaluate the consequences is examined next.

#### A.4. NUMERICAL EVALUATION PROCEDURE

The numerical evaluation of the model proceeds from a suggestion made in Ref. [2]. Specifically, for boundary  $B_{mn}$  between regions  $\zeta_m$ ,  $\zeta_n$ , the generic boundary condition for field  $F_j$  ( $F_j = H_x, E_y, E_z, \tilde{J}_y, \tilde{J}_z$  depending on the situation) is written as

$$F_j^{(\zeta_m)} = F_j^{(\zeta_n)} \quad \text{on } B_{mn} \quad (\text{A4.1})$$

Then the following sum is formed

$$\chi^2(B_{mn}) = \sum_{j, p_{m,n}} w_j(p_{m,n}) |F_j^{(\zeta_m)} - F_j^{(\zeta_n)}|^2_{\text{model}} \quad (\text{A4.2})$$

and  $\chi^2(B_{mn})$  is minimized with respect to the parameters  $k^{(\zeta, \alpha)}$ ,  $H_0^{(\zeta, \alpha, \eta_y, \eta_z)}$  for  $(y, z)$  set equal to a number of points  $p_{m,n}$  along the boundary  $B_{mn}$  between  $\zeta_m$ ,  $\zeta_n$ . Note that the sum does depend on the boundary. Here  $w_j(p_{m,n})$  are weights which are at the liberty of the programmer to choose in such a way that the matching of the fields is in some sense optimal. The  $w_j(p_{m,n})$  were chosen to maximize the efficiency of the least squares program in fitting the boundary conditions. The program Minuit [7] was chosen as the least-squares routine. The initial parameters were specified along with the geometry and the material parameters.

The model as exhibited in Fig. A5 was examined in this report, as described in detail in the text.



## REFERENCES (Appendix A)

1. See, e.g., A. Meloni, L. J. Lanzerotti, and G. P. Gregori, Reviews of Geophysics and Space Physics, Vol. 21, 795 (1983) and L. V. Medford, A. Meloni, L. J. Lanzerotti, and G. P. Gregori, Nature, Vol. 290, p. 329 (1981).
2. A. Beilis, J. W. Dash, and A. Farrow, "Analytic " $\alpha$  - Pole" Approach to an Electromagnetic Scattering Problem", IEEE Transactions EMC Vol. 29 , No. 2, pp. 175-185 (1987).
3. J. D. Jackson, "Classical Electrodynamics", 2nd edition, John Wiley & Sons, N.Y. (1975).
4. N. J. Carron and C. L. Longmire, Mission Research Corporation Report MRC-R-741 (1982). See also I. I. Rokityansky, "Goelectromagnetic Investigation of the Earth's Crust and Mantle", Springer-Verlag, Berlin (1982), especially p. 57.
5. See, e.g., L. J. Lanzerotti, D. J. Thomson, A. Meloni, L. V. Medford, and C. G. MacLennan, J. Geoph. Res., Vol 91, pp 7417-27 (1986).
6. A. Chave, private communication.
7. F. James and M. Roos, Computer Physics Communications 10, 343 (1975).

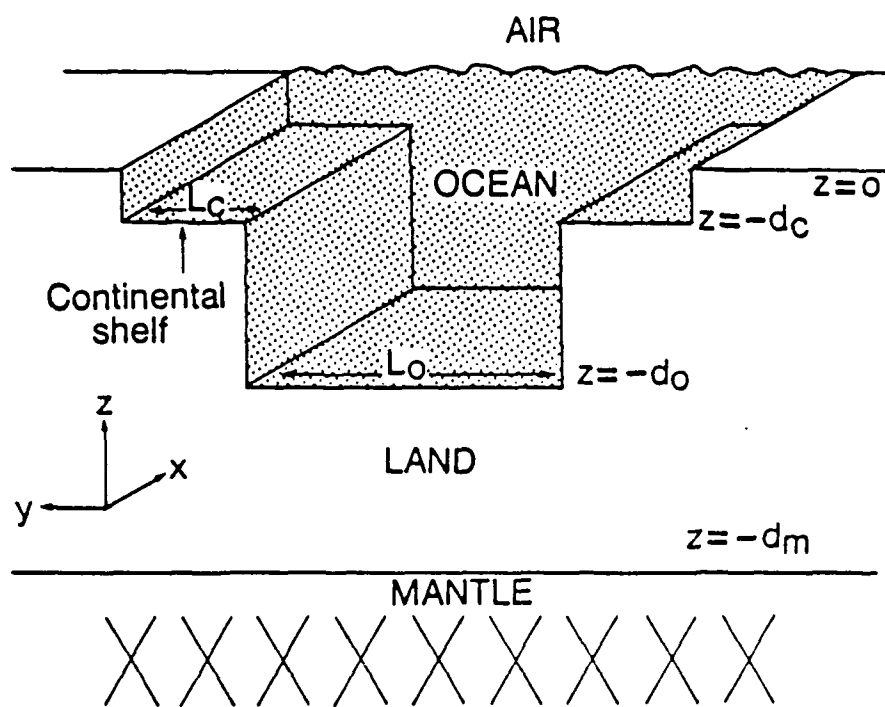


Fig. A1. Idealized geometry for the land/ocean model treated in the text.

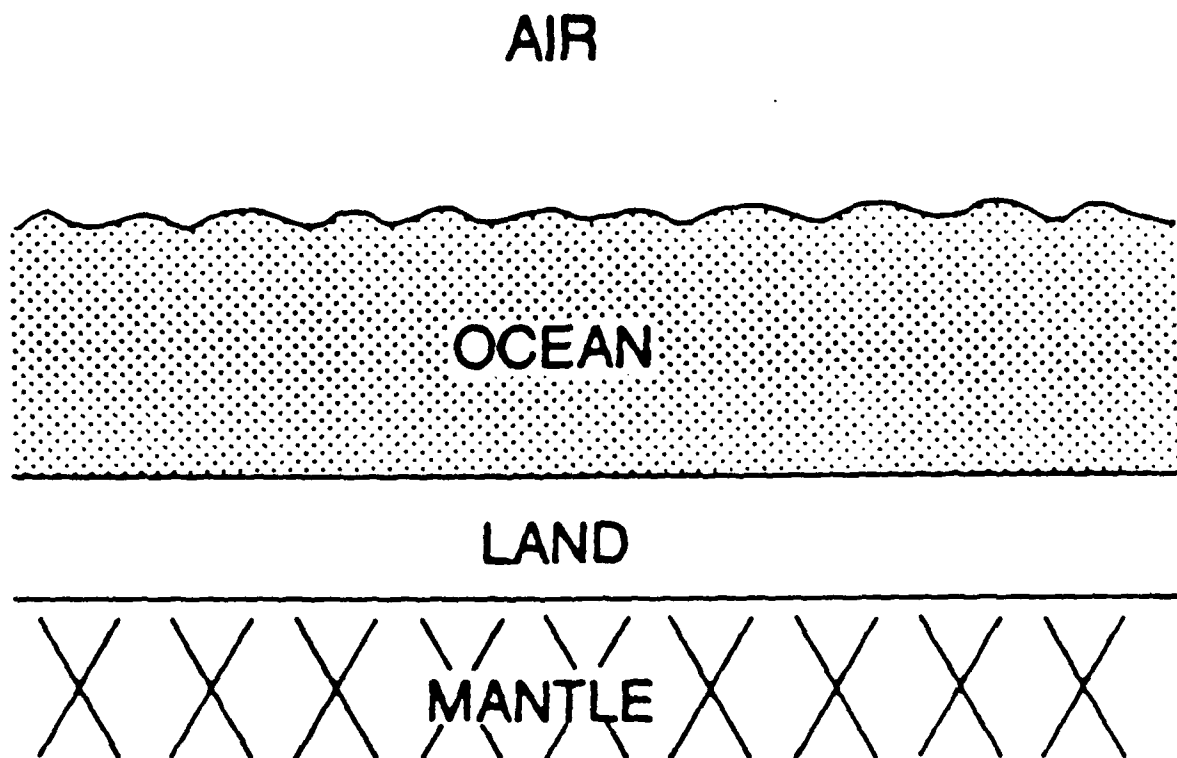


Fig. A2. A simpler version of Fig. A1 containing several layers, but without the complications of the continental edge effects.

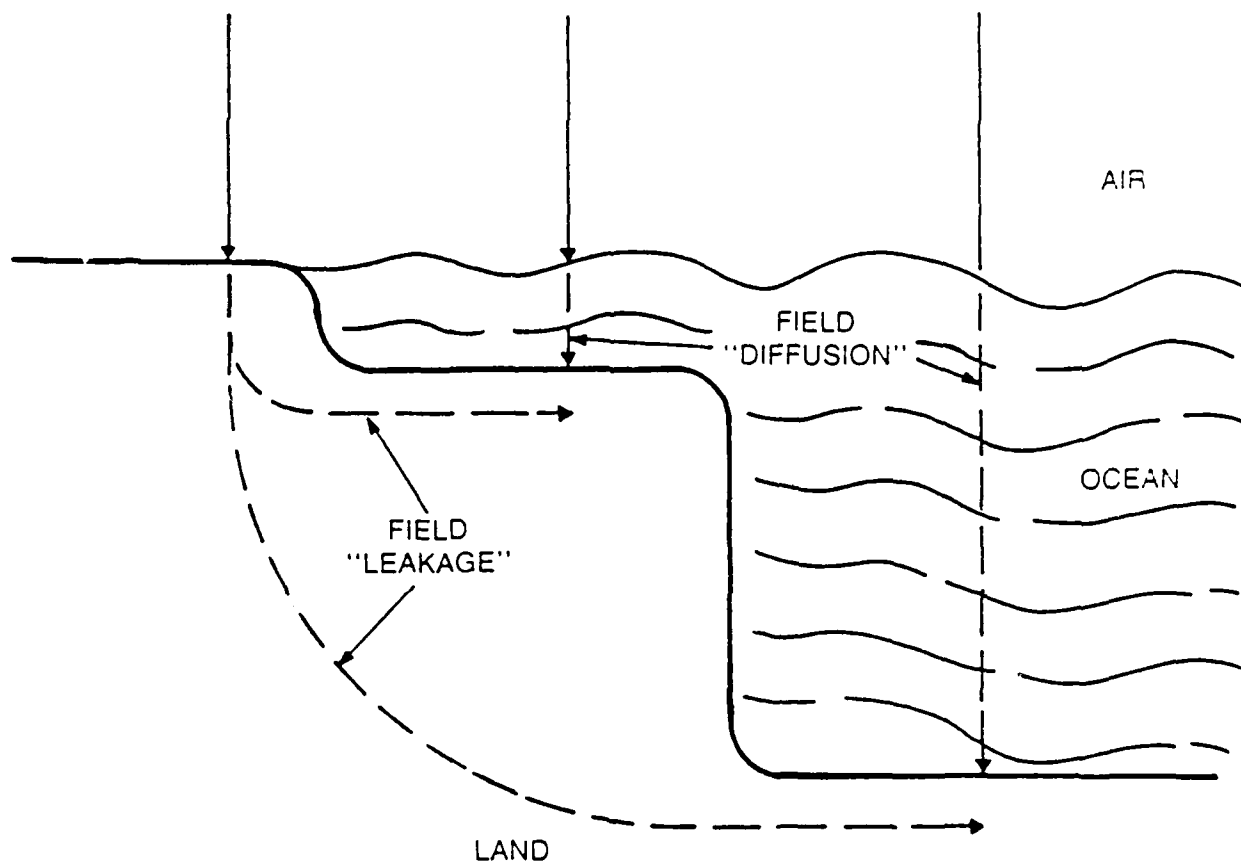


Fig. A3. An idealized land/ocean geometry showing the possibility of leakage fields coming down through the land and around to the bottom of the ocean floor as well as diffusion fields coming down through the ocean.

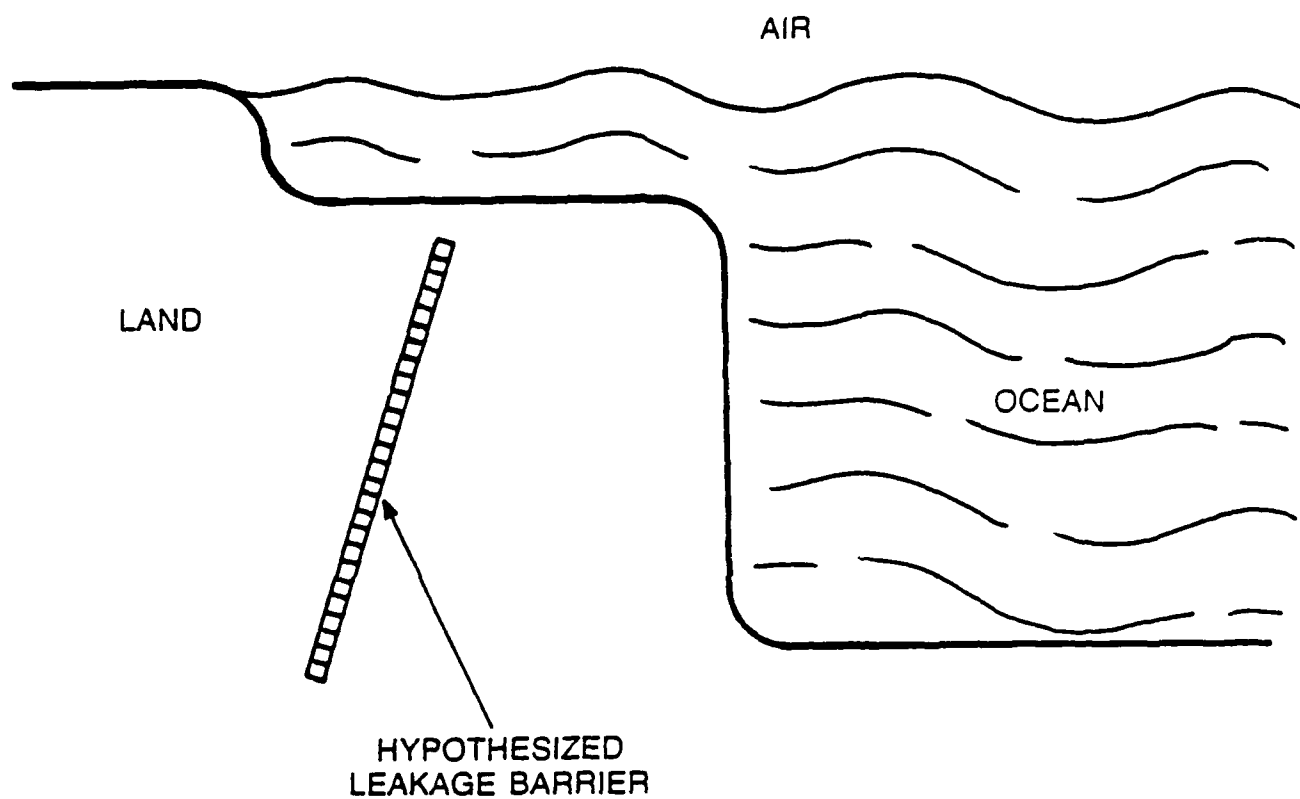


Fig. A4. The hypothesized leakage barrier which serves to help attenuate the leakage fields at higher frequencies, consistent with the falloff in the effective resistivity with frequency.

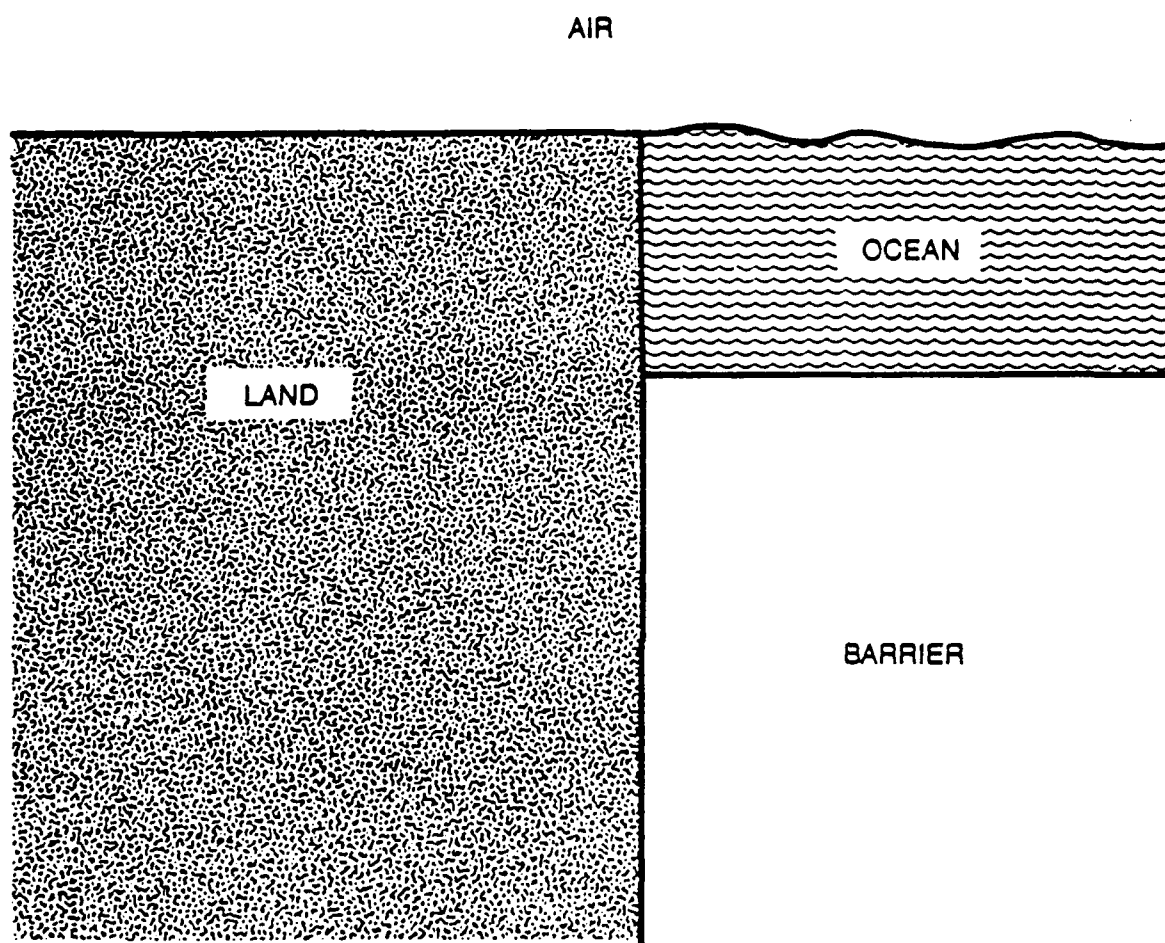


Fig. A5. The model evaluated in this report with a homogeneous barrier substance beneath the ocean on the continental shelf.

## APPENDIX B

### FINITE ELEMENT CODE

This appendix deals with the finite element code results for the calculation of the fields in the ocean/land environment corresponding to the approximations described in sections A.1, A.2 of appendix A. However, the semi-analytic model of sections A.2, A.3 is replaced by a finite element code.

#### B.1 - REMARKS ON THE FINITE ELEMENT METHOD

The finite element method used consisted of the code TTGR [1] supplemented by a front-end program and a separate linear solver routine [2]. TTGR stands for Transient Tensor Galerkin for partial differential equations on Rectangles. The rectangles form a grid on the  $(y,z)$  plane where the solution is being found, and constitute a set of "finite elements". The front-end program [2] consisted of the specification of the equation to be solved by TTGR along with the appropriate geometry, the mesh on which the calculation is performed, and the boundary conditions.

As described in more detail below, the numerical solution technique employs Galerkin's method [3] in the two-dimensional space  $(y,z)$  for fixed frequency. B-splines are used [4] to approximate the solution locally. Thus, each real function (here the real or imaginary part of  $H_x$ ) is approximated by a piecewise polynomial function of some degree specified in advance locally on the desired geometry. Then the Galerkin method (a method employing a variational minimization technique) is employed to determine the coefficients in these local polynomials in such a way that the original continuous equation is satisfied along with the boundary condition to some accuracy. The accuracy depends on

the order of the polynomials employed along with the size of the mesh elements, especially near places where singular behavior of some sort is encountered. Such places here correspond to the interface boundaries between the regions of the land/ocean/barrier geometry.

The equation used is the Helmholtz equation for  $H_x$  discussed in Appendix A in each region along with the boundary conditions (continuous  $H_x$ , tangential electric field and normal total current). However, the Helmholtz equation valid in regions with constant constitutive parameters does not hold right at an interface. The equation that is true everywhere is a generalized Helmholtz equation,

$$\vec{\nabla}_T \cdot \left( \frac{1}{\tilde{\sigma}} \vec{\nabla}_T H_x(y,z) \right) + \frac{k^2}{\tilde{\sigma}} H_x(y,z) = 0 \quad (B.1)$$

where  $\tilde{\sigma}$ ,  $k^2$  are defined in Appendix A and  $\vec{\nabla}_T$  refers to the gradient in the (y,z) plane. This equation is demonstrated in the present case of translation invariance in x for H-polarization by considering  $-\nabla \cdot \vec{E} = \vec{\nabla}_x (\vec{\nabla}_x \vec{H})$   
 $= \tilde{\sigma} \vec{\nabla}_x \vec{E} + (\vec{\nabla} \tilde{\sigma})_x \vec{E} = \tilde{\sigma} \vec{\nabla}_x \vec{E} - \frac{\hat{e}_x}{\tilde{\sigma}} (\vec{\nabla} \tilde{\sigma}) \cdot (\vec{\nabla} H_x)$  where  $\hat{e}_x$  is the x-unit vector, and noting that  $\vec{\nabla} = \vec{\nabla}_T$ .

Once  $H_x$  has been obtained,  $E_y$ ,  $E_z$  are obtained by differentiation as explained in Appendix A, and these results are then used to obtain the model effective resistivity at a given frequency.



The basis functions (B-splines) in terms of which the trial solutions are to be expanded are defined as follows. Picking the variable  $z$  first (the variable  $y$  will be treated similarly), for a given mesh point  $z_i$  write  $B_i^{(n)}(z)$  as the real valued function

$$B_i^{(n)}(z) = \sum_{j=i-n-1}^i \frac{(z_j - z)^n \Theta(z_j - z)}{D[\omega_{ni}(z_j)]} \quad (\text{B.2})$$

where

$$D[\omega_{ni}(z_j)] = \frac{\partial}{\partial z} \prod_{j=i-n-1}^i (z - z_j) \text{ at } z = z_i \quad (\text{B.3})$$

and  $\Theta(z_j - z)$  (the Heaviside function) is defined as 1 for positive argument and 0 for negative argument.

Two properties of the B-splines are important. First, each spline is a polynomial of degree  $n$  over a finite region and zero outside of that region. Second, the spline has a single maximum in that region.

The function to be expanded (call it  $f(z)$ ) is then written as

$$f(z) \approx \sum_{i=1}^{N+n+1} a_i B_i^{(n)}(z) \equiv \vec{A} \cdot \vec{B} \quad (\text{B.4})$$

where the  $\{a_i\}$  are coefficients to be determined,  $N$  is the number of mesh points,  $\vec{A}$  is the vector of coefficients, and  $\vec{B}$  is the vector of splines. The idea can be generalized to include a multiplicity of a mesh point  $z_i$ .

Given the above form of the approximation of the desired function  $f(z)$  in terms of the B-splines, the next task is to determine the coefficients  $\{a_i\}$ . This is done using the following method. First, a scalar inner product is defined for two real functions  $g_1(z)$ ,  $g_2(z)$  over a domain  $D$  as

$$\langle g_1(z), g_2(z) \rangle = \int_D g_1(z)g_2(z)dz \quad (B.5)$$

or its discrete equivalent. Next,  $g_1(z)$  is chosen in turn as each of the B-spline basis functions  $B_i^{(n)}(z)$  for  $n$  fixed and with  $i = 1, 2, 3, \dots$ . Also  $g_2(z)$  is chosen as the residual  $[f(z) - \vec{A} \cdot \vec{B}]$ . Galerkin's method corresponds to setting each resulting scalar product equal to zero, viz

$$\langle B_i^{(n)}(z), [f(z) - \vec{A} \cdot \vec{B}] \rangle = 0 \quad i = 1, 2, 3, \dots \quad (B.6)$$

This yields a set of linear equations of the form

$$\vec{A} \cdot \langle \vec{B}, B_i^{(n)}(z) \rangle = \langle f(z), B_i^{(n)}(z) \rangle \quad i = 1, 2, 3, \dots \quad (B.7)$$

Then linear solver routines are used to find the coefficient vector  $\vec{A}$ . The results can be shown to be optimal as approximations relative to the inner product in the space of basis functions used. The accuracy of the approximation is discussed in Ref. 4. The whole idea is very closely related to standard energy minimization (Rayleigh-Ritz) procedures in physics.

For the problem at hand, a tensor product of the basis functions in  $y$  and in  $z$  was used. One attractive feature of the method is that the boundary conditions at interfaces described above can be shown to be automatically satisfied in the continuum limit, although with numerical differentiation some error is incurred. Specifically,  $H_x$  and  $-\frac{1}{\tilde{\sigma}} \vec{\nabla}_T H_x \cdot \hat{n}$  are guaranteed continuous, where  $\hat{n}$  is the normal to the interface. The latter quantity is just the tangential electric field  $\hat{n} \times \vec{E} \cdot \hat{e}_x$ . With high enough order splines, other derivatives are also continuous, namely  $\partial H_x / \partial z$  at vertical boundaries and  $\partial H_x / \partial y$  at horizontal boundaries; these are the normal total current continuity conditions.

The conditions on the computer generated boundary of the area in which the equation is being solved were specified in the following way. To the left of the vertical boundary between the land and the water/barrier ( $y = 0$ ) the computer generated boundary conditions were set equal to those of the trivial 2-layer air-land solution and to the right of the vertical  $y = 0$  boundary the trivial 3-layer air/water/barrier solution was used. Then the finite element method was employed to generate the results in the interior of the computer generated boundary, as shown in the graphs specified in Chapter 6.

## REFERENCES (Appendix B)

1. N. L. Schryer, private communication.
2. M. A. Driscoll, private communication.
3. See, e.g., G. Dahlquist and A. Bjorck, "Numerical Methods", Prentice-Hall, Inc. (1974), Section 8.6.4 ff
4. G. A. Watson, "Approximation Theory and Numerical Methods", J. Wiley, 1980. See Chapter 8.

## APPENDIX C

### THE EARTH POTENTIAL AND THE MHD CIRCUIT LIMIT

MHD coupling to a cable is usually treated in a circuit limit. This involves the concept of the "earth potential" induced by the magnetic field fluctuations. In order to clarify these concepts, it is desirable to begin with a more fundamental posture, namely the transmission line formalism, and take the circuit limit. In this appendix some details of the transmission line formalism are presented along with the quasistatic limit necessary to understand how a circuit formalism can be used to describe the nature of the earth potential and the consequent coupling of MHD to a submarine cable.

#### C.1 - REVIEW OF TRANSMISSION LINE FORMALISM

The one-dimensional transmission line equations in the spatial variable  $y$  at a given frequency  $\omega$  for the transmission line voltage and effective current are [1,2]

$$\frac{d}{dy}V(y) + ZI(y) = V^{(s)}(y) \quad (C.1a)$$

$$\frac{d}{dy}I(y) + YV(y) = I^{(s)}(y) \quad (C.1b)$$

The interpretation of the quantities in these equations is somewhat subtle. First, the axial incident electric field induces common-mode currents which propagate in the same direction. Thus the actual currents on the two conductors are

$$I_1 = I_0 + I_c \quad (C.2a)$$

$$I_2 = -I_0 + I_c \quad (C.2b)$$

where  $I_c$  ( $I_0$ ) is the common-mode (differential-mode) current. The quantity  $I$  appearing above then depends on the geometry. Most coupling to a submarine cable would be in the common mode. This is because the MHD excitation would create electric fields and currents, some of which would get picked up by a cable, and thus the cable current would be in the same direction as the current in the surrounding medium. Thinking of the cable and surrounding medium as forming a transmission line, the current flows in the same direction and is thus common mode. There is a small differential-mode current due to the magnetic flux linking the cable and surrounding medium as well, but this is negligible [3,4]. For the common-mode current, the current return evidently must occur well within the earth, presumably in the mantle under the ocean seabed, but the details of this have not been investigated. A pictorial representation of this equivalent circuit is in Fig. C1. In this report these complicating features will be ignored.

The quantity  $V(y)$  is the voltage difference between the conductors at point  $y$ . The voltage source per unit length  $V^{(s)}(y)$  is actually  $-j\omega\phi_{inc}$  where  $\phi_{inc}$  is the flux through a small loop due to the incident  $H$  field transverse to the  $y$  axis. (In this appendix,  $j$  is the usual electrical engineering symbol for  $\sqrt{-1}$ ). The small loop is formed by the two conductors of the transmission line parallel to the  $y$  axis along with two perpendicular lines between the conductors spaced

one unit apart. By Faraday's law this is related to the axial incident electric field. The current source  $I^{(s)}(y)$  arises physically from the incident electric field perpendicular to the axes of the conductors. This generates extra (opposite) charges on the conductors and is related to the transverse incident electric field [5,6].

The impedance and admittance of the transmission line per unit length are  $Z$  and  $Y$ , in general of the form  $Z = R + j\omega L$  and  $Y = G + j\omega C$ . The inductance per unit length  $L$  arises from the flux linking the small loop if the exciting field (and therefore the common-mode currents) were zero. The resistance per unit length of the conductor is  $R$ . The conductance per unit length  $G$  arises from any current physically transported between the two conductors at  $y$  due to the voltage difference  $V(y)$ . The capacitance per unit length  $C$  is due to opposite charges on the two conductors due to the TEM potential difference in the absence of any transverse incident electric field. The parameters  $R, L, G, C$  are not given and must be obtained from the problem to which the transmission line formalism is assumed to be an approximation [1,7].

Now if  $Z$  and  $Y$  are independent of  $y$ , the two equations for  $V(y)$  and  $I(y)$  are easily solved. Define  $\gamma = \sqrt{ZY}$ . It is the propagation constant determining the attenuation and the speed of propagation of the wave along the transmission line (at the given frequency  $\omega$ ). Also, define  $Z_0 = \sqrt{Z/Y}$ , the characteristic impedance. Explicitly, the solutions for the voltage and current are

$$V(y) = Z_0 e^{\gamma y} [Q_-(y) + \alpha_-] + Z_0 e^{-\gamma y} [Q_+(y) + \alpha_+] \quad (C.3a)$$

$$I(y) = -e^{\gamma y} [Q_-(y) + \alpha_-] + e^{-\gamma y} [Q_+(y) + \alpha_+] \quad (C.3b)$$

where the functions  $Q_+(y)$  and  $Q_-(y)$  are given by

$$Q_-(y) = \frac{1}{2Z_0} \int_{y_+}^y d\hat{y} e^{-\gamma \hat{y}} [V^{(s)}(\hat{y}) - Z_0 I^{(s)}(\hat{y})] \quad (C.4)$$

$$Q_+(y) = \frac{1}{2Z_0} \int_{y_-}^y d\hat{y} e^{\gamma \hat{y}} [V^{(s)}(\hat{y}) + Z_0 I^{(s)}(\hat{y})] \quad (C.5)$$

The constants  $\alpha_-$  and  $\alpha_+$  from the homogeneous equation solutions are to be determined by the boundary conditions between  $V$  and  $I$  at the endpoints  $y_a$  and  $y_b > y_a$  of the transmission line. The lower limits of integration in the expressions for  $Q_-(y)$  and  $Q_+(y)$  can be chosen as  $y_a$  and  $y_b$  without loss of generality.

The physical interpretation of these equations is clear. Reinstating the time dependence  $e^{j\omega t}$ , one sees that a source at point  $y$  of frequency  $\omega$  generates both positive and negative travelling waves given by the two exponentials  $e^{\gamma y}$  and  $e^{-\gamma y}$ . An incident electric field pulse is then treated by specifying the dependence of  $V^{(s)}(y)$  on  $\omega$  (which is implicit in the above formalism), and integrating over  $\omega$ .



The details of the common-mode transmission line formalism may be found in Refs. [5,6].

## C.2 - THE EARTH POTENTIAL AND THE CIRCUIT LIMIT

The coupling of a submarine (or other) cable to an ambient (incident) electromagnetic field in the presence of a conducting medium (here the ocean/land environment) should be treated with transmission line theory, as detailed above and in Vance's book for example [2]. Transmission line theory is valid in a long wavelength limit, which is satisfied here. This means that the transit time for electromagnetic pulses around the system should be small compared to the time scales of the pulse itself, so that the entire system responds instead of just a local piece of the system. For a submarine cable system, typical transit times are less than 1 second. Hence, for MHD time scales on the order of 1-1000 seconds, the circuit limit is applicable. However, it is profitable to keep the more fundamental transmission line formalism in mind to avoid confusion when dealing with an extended medium, such as the ocean/land environment, where one is essentially "looking inside the circuit components". In particular, the so-called "earth potential", an equivalent battery placed in the effective circuit, can be a confusing concept. Let us review the relevant concepts (see also [4,8]).

An ambient or other externally originated electric field parallel to a segment of the cable will couple to the cable according to the transmission line formalism. This makes it obvious that the relevant electric field is the field at the undersea position of the cable. The integrated electric field along the cable

length is then the appropriate equivalent "earth potential" battery to be placed in the equivalent circuit, assuming that the equivalent transmission line was terminated on both ends by grounding. Notice that the line integral of the electric field does depend on the path, since this is not a static problem. If the cable were to run along a different path, the equivalent "earth potential" battery would be different. To picture this, imagine the hypothetical case where the cable was made to follow a path that rose to the ocean surface in the middle of the ocean. The coupling to ambient electromagnetic fields would clearly be much larger, since the attenuation of the fields by the highly conducting ocean would no longer be present. Finally, the net earth potential also implicitly includes an I-R drop across an "earth impedance", which in general is also unknown, and which can only be derived in conjunction with the line integral of the electric field along the cable position through the solution of the overall boundary value problem of the land/ocean environment including the cable. A transfer function to couple the electric field into the cable system is also needed.

Thus the derivation from fundamental principles of the value of the earth potential for a given cable configuration is a highly nontrivial task. If one is interested only in scaling up ambient fluctuations to threat fluctuations on a given cable at a given frequency, one need not be concerned with this issue. If, however, one tries to derive the threat fluctuations on one cable from the ambient fluctuations on another cable, or if the ambient fluctuations are not available at the desired frequency, then attention must be paid to the nature of the earth potential.

Finally we exhibit the traditional argument [8] which links a measurement of the voltage across one end of a cable and the local ground to the line integral of the electric field along the cable. The argument assumes that the other cable end is grounded at its own local ground. The argument proceeds in two stages.

Consider Fig. C2 which exhibits a cable conductor running from point A (not grounded) to point B (grounded, e.g., in seawater for a partial submarine cable, such as the partial TAT-6 cable on which measurements were reported elsewhere in this report). The voltage between point A and the local ground point C near point A is called  $V_{ac}$ . This is the voltage actually measured on a voltmeter by the experimentalists.

Now let us model this quantity. We define a "hypothetical circuit" path (the "equivalent circuit" of the geophysicists) which we call  $C_{hyp}$  exhibited in Fig. C3, running from point A to B back to C and up to A. The part of the path  $C_{BC}$  from B to C is defined to be "close" to the actual cable path  $C_{AB}$  from A to B, but not "too close". "Close" means that the time derivative of the magnetic flux through the surface  $S_{ABC}$  spanned by  $C_{hyp}$  is small because that surface has small area. "Not too close" means that we insist that the electric field locally tangent to  $C_{BC}$  is in fact the same that would exist in the absence of the cable; that is, if the cable were not there at all. Thus the complex coupling feedback problem of the cable on the neighboring environment is finessed. Finally we ignore the coupling problem of the electric flux at the grounded end of the cable with the seawater; i.e., the electrochemical potential due to the fact that there are dissimilar materials in contact.

With these approximations in hand, we now consider the line integral of the electric field around  $C_{hyp}$ . The first assumption (small surface  $S_{ABC}$  bounding  $C_{hyp}$ ) means that this line integral is approximately zero,

$$\int_{C_{hyp}} \vec{E} \cdot d\vec{l} \approx 0 \quad (C.6)$$

Now break up this line integral into three pieces. The first, along  $C_{AB}$  is zero because the tangential electric field next to a good conductor is negligible. The second piece, along  $C_{BC}$  is approximately the line integral "close" to the actual cable path, of the electric field in the absence of the cable. This integral is in fact DEFINED as the earth potential  $V_{earth}$ . The last piece, along  $C_{CA}$ , is just the voltage  $V_{ac}$  measured experimentally. So we get

$$V_{ac}^{ext} \approx \int_{C_{BC}} \vec{E}_{cable\ absent} \cdot d\vec{l} \approx V_{earth} \quad (C.7)$$

We hope that this discussion has clarified some aspects of the concepts of the equivalent circuit and earth potential in the literature.

### C.3 - MHD COUPLING TO A SUBMARINE CABLE

In this section the details of the coupling of electromagnetic energy into a submarine cable are given in more detail. Such considerations would be necessary for corrections to the above argument relating the measured cable

voltage fluctuations to the earth potential which neglected the coupling details. This coupling depends on the Schelkunoff transfer impedance [9] which in turn depends on the values of the cable parameters. For a typical submarine coaxial cable the static capacitance  $C$  and space inductance  $L$  are [10]:

$$C = \frac{\epsilon_r}{18 \ln \left( \frac{a}{b} \right)} (\mu F / km) \quad (8.3)$$

$$L = 0.2 \ln \left( \frac{a}{b} \right) (mH / km) \quad (8.4)$$

Here  $\epsilon_r = 2.28$  for polyethylene dielectric,  $a = 1$  cm, and  $b = 0.5$  cm for the outer and inner radii.

The total impedance is  $Z = j\omega L + Z_{\text{ocean}} + R_{\text{cable}}$  while the admittance is  $Y = j\omega C$ . The cable resistance can be taken as the DC resistance. The sea impedance is given by solving a boundary value problem. For the simple case of a buried cable in a uniform medium stretching to infinity (taken as the ocean), the result is

$$Z_{\text{ocean}} = \frac{j\omega\mu_0}{2\pi a \sqrt{j\omega\mu_0\sigma}} \frac{K_0 \left( \sqrt{j\omega\mu_0\sigma} a \right)}{K_1 \left( \sqrt{j\omega\mu_0\sigma} a \right)} \quad (C.8)$$

Here,  $K_0$  and  $K_1$  are modified Bessel functions. The characteristic impedance  $Z_0$  for  $f = 1$  Hz is given by  $|Z_0| = 753 \Omega$ ,  $\arg(Z_0) = -44.4^\circ$  while the propagation constant is  $\gamma = \alpha + j\beta$  with  $\alpha = 5.26 \times 10^{-3}$  (dB / km) and  $\beta/\omega = 9.83 \times 10^{-5}$  (sec / km) being the "delay". The velocity is the inverse  $\omega/\beta = 10^4$  km/sec. The time delay for propagation over a distance of 200 km (the width of the continental shelf) is then 0.02 sec. Since this is small compared to the characteristic time scale of around 1-1000 sec for MHD effects, the circuit concept applies. Ref. [11] reaches similar conclusions.

## REFERENCES (Appendix C)

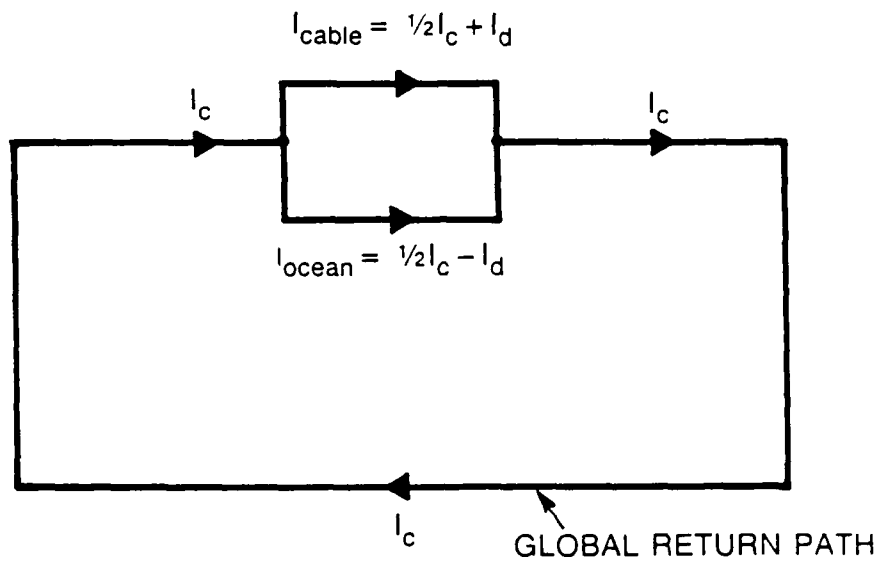
1. See, e.g., "EMP Interaction: Principles, Techniques, and Reference Data (A Compleat Concatenation) ", K.S.H. Lee, editor , Air Force Weapons Laboratory Report TR-80-402, Kirtland AFB, NM (1980).
2. E. Vance, "Coupling to Shielded Cables", John Wiley & Sons, NY (1978).
3. G. A. Axe, "The Effects of the Earth's Magnetism on Submarine Cables", The Post Office Electrical Engineers' Journal, Vol. 61, 37-43 (1968).
4. N. J. Carron and C. L. Longmire, "MHD EMP Threat on Trans-Oceanic Cables (U)", Mission Research Corporation Report MRC-R-741 (December, 1982).
5. K. S. H. Lee, "Two Parallel Terminated Conductors in External Fields", IEEE Transactions on Electromagnetic Compatibility, Vol 20, No. 2, pp 288-296 (1978).
6. C. D. Taylor, R. S. Satterwhite and C. W. Harrison, "The Response of a Terminated Two-Wire Transmission Line Excited by a Nonuniform Electromagnetic Field". IEEE Trans. Ant. Prop., Vol 13, pp 987-989 (1965).
7. J. D. Jackson, "Classical Electrodynamics", 2nd Ed., J. Wiley. NY. (1975).
8. M. L. Van Blaricum and C. L. Longmire, "Coupling of MHD-EMP to Submarine Cables (U)", Mission Research Corporation Report MRC-R-306 (February, 1977).

9. S.A. Schelkunoff, "The Electromagnetic Theory of Coaxial Transmission Lines and Cylindrical Shields", Bell System Tech. Journal, pp. 532-579 (Oct., 1934).

10. C. D. Anderson, private communication.

11. M. L. Van Blaricum and C. L. Longmire, "Coupling of MHD-EMP to Submarine Cables (U)", Mission Research Corporation Report MRC-R-306 (February, 1977). See p. 6.





$I_c$ : COMMON MODE

$I_d$ : DIFFERENTIAL MODE

Fig. C1. The equivalent circuit for the cable and ocean along with a global return path deep in the earth. The common-mode current for the cable and ocean is called  $I_c$  and the small differential-mode current is  $I_d$ .

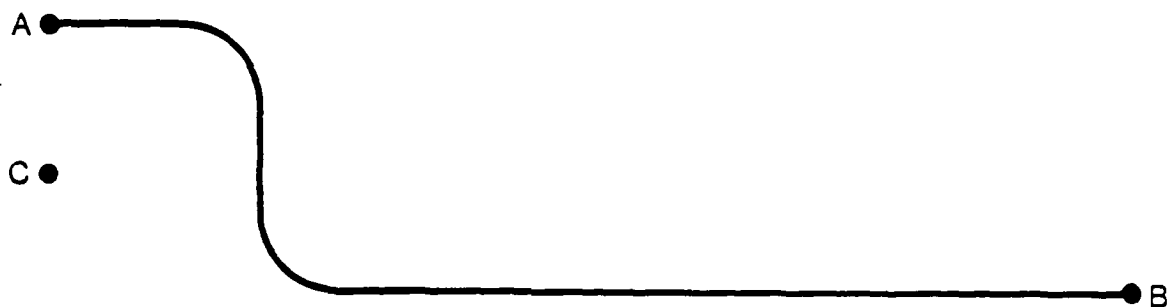


Fig. C2. The path of a submarine cable from point A (earth station) to point B (sea ground or other ground). Point C represents the local ground at the earth station.

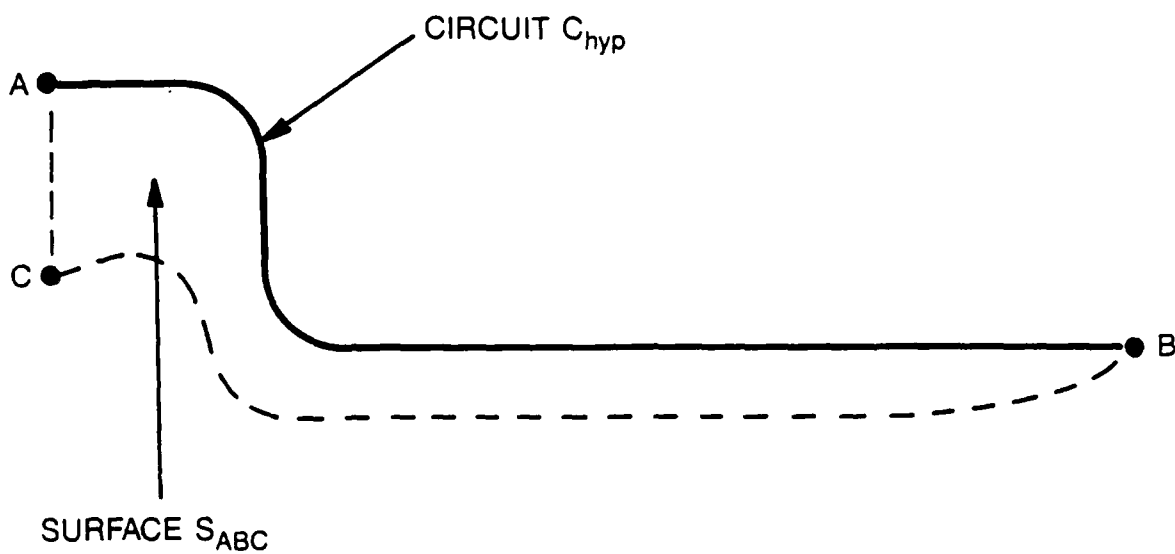


Fig. C3. The hypothetical circuit path ABCA used to deduce the approximate result that the voltage measured at the earth station between the cable end point A and the local ground point C is equal to the line integral of the unperturbed electric field along the path of the cable from point A to point B.